Understanding and Controlling Dynamically-Induced Stochastic Domain Wall Behaviours in Magnetic Nanowires

By:

Khalid AbdelMajid Omari

A thesis submitted in partial fulfilment of the requirements for the degree of
Doctor of Philosophy

Faculty of Materials Science and Engineering
The University of Sheffield
January, 2016

Abstract

Stochastic pinning of domain walls (DWs) in Permalloy (Py) nanowires is a significant challenge that needs to be overcome to produce reliable magnetic nanowire-based devices for memory/logic applications. In this study, stochastic interactions of vortex DWs (VDWs) with intrinsic defects and artificial notch-shaped defects have been studied with the aim of understanding their complexity and proposing methods to control them.

VDW pinning/depinning behaviour in double and single notches showed complex behaviour in real measurements when compared with quasi-static simulations. Systematic study was performed on VDW interactions with double and single notches with a range of depths and nanowires' thicknesses. Results showed that multi-mode stochastic pinning/depinning behaviour occurred for the vast majority of systems. However, for large single notches in thick nanowires (t=40nm), single-mode depinning-field-distributions were observed. It was shown that convergence to single depinning-mode was due to the nature of Walker-breakdown transformations that preserve the vortex shape of VDWs, and to the specifics of DWs interaction with notch and edge roughness.

The dependence of stochastic pinning/depinning behaviours on DW injection processes was also studied. It was found that DWs injected into nanowires using pulses through orthogonal current-line nucleation exhibited more deterministic pinning/depinning behaviour than those injected from nucleation pads. This may be attributed to the process by which DWs depin from the nucleation pad junction.

Additionally, it is shown that pinning/depinning stochasticity can be mitigated by passing VDWs through sharp bends that act as chirality rectifiers. For certain nanowire/notch geometries, this reduces the number of accessible pinned DW configurations to a single configuration; thus, producing a single-mode depinning-field-distribution.

Finally, micromagnetic simulations are used to demonstrate feasibility of DW logic architecture where bits are encoded using VDW chirality. Designs are proposed for NAND, AND, NOR, OR and FAN-OUT gates. All gates work by manipulating the interaction of VDWs with Y-shaped junctions and/or notches.

Acknowledgement

I start by thanking my family, my mother and father for their never-ending support since the day I was born. Their fountain of love and blessing is the reason for any success I make. I would like also to thank my sisters for their support, love and encouragement.

Secondly, I would like to thank my awesome supervisor Dr. Thomas Hayward for his guidance, remarks and for tolerating my "unexpected" questions and discussions. I've learned immensely from him and from his professional scientific meticulousness. I congratulate him for his success in tutoring his first PhD student, and I hope that despite all the challenges he might have faced, that he had enjoyed this teaching journey.

I'm extremely grateful to Professor Dan Allwood for his support, advises, and most importantly for recommending me for this amazing educational opportunity. I hope that I was as he expected me to be. Also I would like to thank the SCAMMD group for their friendliness and nice caring atmosphere. Special thanks go to the team whom I worked with at the ALS in Berkeley, who worked extra hard and collectively succeeded at the end!

Of course I wouldn't have made it through this journey without the company, friendly spirit, support, socials, fiery discussions, laughs, arguments and definitely the amazing food of my amazing friends in Sheffield Musheer, Hasan, Ahmad, Kareem, Omar and all the rest.

I would never forget to acknowledge my friends and family in Palestine who continue to emanate hope and inspiration for a better life and a just future, regardless of the difficulties they face every day.

Finally I hope that the findings of this research would contribute in any way and in any gigantic or infinitesimal amount to the benefit and justice of humanity!

10th of January, 2016

Amman - Jordan

List of Publications and Contributions

1. K. Omari and T. Hayward, "Chirality-based vortex domain-wall logic gates," Physical Review Applied, vol. 2, p. 044001, 2014.

2. K. Omari, R. Bradley, T. Broomhall, M. Hodges, M. Rosamond, E. Linfield, et al., "Ballistic rectification of vortex domain wall chirality at nanowire corners," Applied Physics Letters, vol. 107, p. 222403, 2015.

3. MMM – InterMag Conference, 2013   Denver, Colorado – USA: "Chirality-based vortex domain-wall logic gates" (Poster)

This thesis contains the work done by Khalid AbdelMajid Omari as part of his PhD degree requirements. All the fabrication, modelling, SEM imaging and work analysis presented in this thesis have been done by the author (Khalid AbdelMajid Omari). The MTXM imaging was done by the author supported by co-workers from SCAMMD group and ALS/Berkely collaborators.

Nomenclature

α	Gilbert damping coefficient
Δ	DW width parameter
σ_d	Standard deviation of depinning field
δ_{DW}	Domain all width
$\bar{\sigma}_{inj}$	Average standard deviation of injected fields
ħ	Dirac's constant (1.055×10^{-34})
γ_{dw}	Domain wall energy
γ	Gyromagnetic ratio
χ	Magnetic susceptibility
μ	Domain wall mobility
μ_0	Vacuum permeability ($4\pi \times 10^{-7}$ T.m/A)
μ_B	Bohr's magneton constant (9.274×10^{-24} J/T)
τ	Switching time of a thermally activated event
τ_1	Torque
$\boldsymbol{\tau}_0$	Characteristic mean switching time
θ_K	Kerr angle of rotation
A	Exchange stiffness constant
ACW	Anti-clockwise
AFM	Atomic force microscope
CCD	Charged-coupled device (camera)
CN	Current-induced nucleation
CW	Clockwise
D_{AREA}	Exposed area dose
DFD	Depinning field distribution
DOS	Density of state
DN	Downward
DW	Domain wall
e	Electron charge (1.602×10^{-19} coulombs)

E	Electric field
E_b	Energy barrier
E-Beam	Electron beam
E_{an}	Magnetocrystalline anisotropy energy density
EBL	Electron beam lithography
E_{ex}	Exchange energy density
$E_{exchange}$	Exchange energy
E_{ms}	Magnetostatic energy density
E_{total}	Total magnetic energy density
FDM	Finite difference method
FM	Ferromagnetic
g	g-factor
g_e	Landé g-factor
H	Magnetic field
H_d	Depinning field
H_{dem}	Demagnetising field
H_{eff}	Effective field
H_{ext}	External magnetic field
H_{inj}	Injection magnetic field
$\bar{H}_{inj}$	Average injection field
H_N	Nucleation field
H_p	Propagation field
H_s	Switching Field
H_{SW}^0	Switching field at T= 0 K
H_{WB}	Walker-breakdown field
IFD	Injection field distribution
IPA	Isopropyl alcohol
J	Total angular momentum
$\mathcal{J}$	Exchange integral
K_1	Anisotropy constant

k_B	Boltzmann constant (1.381×10^{-23} m^2 kg s^{-2} K^{-1})
l	Length
L	Orbital angular momentum
L$_{ex}$	Exchange length
LLG	Landau-Lifschitz Gilbert equation
m	Magnetic moment
M	Magnetisation
m_e	Mass of electron (9.109×10^{-31} kilograms)
m_J	Total magnetic quantum number
m_l	Orbital magnetic quantum number
m_{orbit}	Orbital magnetic moment
m_s	Spin magnetic quantum number
m_{spin}	Spin magnetic moment
M$_s$	Material Saturation magnetisation
m_{tot}	Total magnetic moment
MTXM	Magnetic transmission X-ray microscope
M$_z$	Out of plane magnetisation
N$_d$	Notch depth
PMA	Perpendicular magnetic anisotropy
PMMA	Poly(methyl methacrylate)
PN	Pad nucleation
P$_P$	DW pinning percentage
Py	Permalloy
r	radius
RM	Race-track memory
r_{sd}	Radius of single domain particle
$R_{superpara}$	Radius of superparamagnetic particle
S	Spin angular momentum
S_{an}	Shape anisotropy factor
SEM	Scanning Electron Microscope

t	Thickness
T	Temperature
TDW	Transverse domain wall
UP	Upward
VDW	Vortex domain wall
WB	Walker-breakdown
w,W	Width

Table of Contents

Chapter 1

Introduction

Uniquely among all materials, ferromagnetic (FM) materials possess a spontaneous magnetic moment, making them ideal for the non-volatile storage of information. With the emergence of the field of nanotechnology, FM materials can now be patterned into devices with length scales similar to those of the magnetism itself, thus creating new functionality that can be exploited in devices. For example, when FM materials with in-plane magnetisation are formed into elongated planar nanowires, the complex competition between the magnetic energies at the nanoscale, favours the formation of single domain magnetisation states, where the nanowire's magnetisation is oriented along the long axis of the nanowire. For magnetic switching of such nanowire to occur, a domain wall (DW) can be nucleated at one end and propagated to the other end by either an applied magnetic field [1, 2] or spin polarized current [3].

In recent decades, extensive amount of research has been directed towards studying the behaviour and motion of DWs in nanowires [4-19]. Promising results including high DW propagation velocities and the non-volatility of magnetisation information have made FM nanowires an exceptional candidate for memory storage and information processing applications [5, 20]. This has resulted in proposals for novel spintronic applications that use spins of the magnetic domains to store binary information including solid-state computer memories [21-25] and a complete logic architecture [26].

Further to utilizing the spin alignment of domains to represent data, the spin structure of DWs themselves has also been proposed as a medium to carry and process binary information via their internal degrees of freedom, their 'chirality' [27-31]. Moreover, biotechnological

applications for nanowires have been proposed including cell trapping [32], drug delivery and micro-beads transportation where a micro-bead is pinned on a DW, and is propagated on a nanowire [33]. Additionally, DWs in nanowires have been proposed for use as magnetic sensors [21, 34], rotation sensors in vehicles [35, 36] and high-frequency oscillators [37].

Nevertheless, these applications and devices face some challenges that need to be overcome in order to obtain reliable performances. This thesis tackles one of these in particular: the problem of stochastic DW pinning and depinning behaviour.

When nanowire switching occurs through DW propagation, several external and intrinsic parameters add significant elements of randomness to the DW propagation resulting in stochastic behaviour. For instance, DW motion has been shown to become complex or even chaotic when they are propagating above a critical field known as the Walker-breakdown field [38-41]. This irregular motion can become very problematic, as the associated DW spin structure transformations result in lower DW velocities, the loss of chirality information, and the interaction with artificial pinning sites that vary from instance to instance, thus creating a variety of pinning/depinning modes [39, 42, 43]. Moreover, the existence of edge roughness at nanowire edges, due to fabrication limitations, produces random and undesired pinning sites that can hinder the motion of DWs. Additionally, thermal perturbation can alter DW depinning behaviours by assisting them in overcoming energy barriers, resulting in a further component of probabilistic behaviour. Although thermal stochasticity alone can be modelled in simple nanomagnetic systems [44-46], in reality all the stochasticity factors interact together to form a complex array of stochastic behaviours that are very difficult to model [4].

In this thesis, I aim to:

1. Gain a comprehensive understanding of stochastic DWs pinning in Permalloy (Py) nanowires by performing both simulations and experimental studies of vortex DW (VDW) pinning behaviours in Py nanowires; both, with and without artificial defect sites.

2. Use the results of this study to develop methods to mitigate stochastic DW behaviour.

3. Propose a DW-based logic architecture where data is stored using the chirality of VDWs. This represents the kind of technology that could be realised if stochastic DW behaviour could be fully overcome.

The thesis will be presented in the following manner: In Chapter 2, a brief background of general magnetism theory, with a particular focus on nanomagnetism will be provided as the theoretical basis for the reader. Chapter 3 will present a literature review of the topics that will be discussed in subsequent chapters, starting with an explanation of the origin and significance of the novel magnetic properties found at the nanoscale, and introducing essential nanomagnetic terms and concepts before moving on to a review of the most important studies relating to DW behaviour and applications. Chapter 4 will then present details of the fabrication, measurement and modelling techniques used in studies described in this thesis.

Chapter 5 will be the results chapter and will present the initial studies performed to understand the basic pinning/depinning behaviour of DWs in simple Py nanowires. Chapter 6 will then present systematic study of VDW pinning/depinning at both symmetric (double notches) and asymmetric (single notches) pinning sites with a range of depths and in nanowires with a variety of thicknesses. Using a combination of experimental measurements and micromagnetic simulations, this study will unravel many of the complexities seen in the stochastic pinning/depinning of DWs in Py nanowires. Chapter 7 will investigate the role of the method

used to nucleate DWs on the stochasticity of their behaviour, by comparing systems in which DWs are injected using micrometer scale current lines, to those in which they are injected from nucleation pads. In Chapter 8, a VDW chirality rectifier device will be introduced and its operation will be demonstrated and explained using a combination of magnetic imaging experiments and micromagnetic simulations. A method to mitigate DW stochasticity using the vortex DW rectifier will then be introduced. Finally, Chapter 9 will use micromagnetic simulations to propose a novel chirality-based DW logic architecture that uses the internal magnetisation structure of VDWs to store information.

Finally, Chapter 10 will present the conclusion of the thesis and will sum up the key points made in the preceding chapters.

1.1 References

[1]   F. Nasirpouri and A. Nogaret, *Nanomagnetism and spintronics: fabrication, materials, characterization and applications*: World Scientific, 2011.

[2]   A. P. Guimarães, *Principles of nanomagnetism*: Springer Science & Business Media, 2009.

[3]   D. Ralph and M. D. Stiles, "Spin transfer torques," *Journal of Magnetism and Magnetic Materials,* vol. 320, pp. 1190-1216, 2008.

[4]   T. J. Hayward, "Intrinsic Nature of Stochastic Domain Wall Pinning Phenomena in Magnetic Nanowire Devices," *Scientific Reports,* vol. 5, p. 13279, 08/25/online 2015.

[5]   G. Hrkac, J. Dean, and D. Allwood, "Nanowire spintronics for storage class memories and logic," *Philosophical Transactions of the Royal Society of London A: Mathematical, Physical and Engineering Sciences,* vol. 369, pp. 3214-3228, 2011.

[6]   G. S. Beach, C. Nistor, C. Knutson, M. Tsoi, and J. L. Erskine, "Dynamics of field-driven domain-wall propagation in ferromagnetic nanowires," *Nature materials,* vol. 4, pp. 741-744, 2005.

[7]   L. Bogart, D. Eastwood, and D. Atkinson, "The effect of geometrical confinement and chirality on domain wall pinning behavior in planar nanowires," *Journal of Applied Physics,* vol. 104, p. 033904, 2008.

[8]   L. K. Bogart, D. Atkinson, K. O'Shea, D. McGrouther, and S. McVitie, "Dependence of domain wall pinning potential landscapes on domain wall chirality and pinning site geometry in planar nanowires," *Physical Review B,* vol. 79, Feb 2009.

[9]   J. Brandao, R. L. Novak, H. Lozano, P. R. Soledade, A. Mello, F. Garcia*, et al.*, "Control of the magnetic vortex chirality in Permalloy nanowires with asymmetric notches," *Journal of Applied Physics,* vol. 116, Nov 21 2014.

[10]   M. Bryan, D. Atkinson, and D. Allwood, "Multimode switching induced by a transverse field in planar magnetic nanowires," *Applied physics letters,* vol. 88, p. 032505, 2006.

[11]   M. Bryan, T. Schrefl, and D. Allwood, "Symmetric and asymmetric domain wall diodes in magnetic nanowires," *Applied Physics Letters,* vol. 91, p. 142502, 2007.

[12]   D. Eastwood, L. Bogart, and D. Atkinson, "Scaling Behaviour of Chirality Dependent Domain Wall Pinning in Planar Nanowires," *memory,* vol. 3, p. 11, 2010.

[13]   D. Eastwood, J. King, L. Bogart, H. Cramman, and D. Atkinson, "Chirality-dependent domain wall pinning in a multinotched planar nanowire and chirality preservation using transverse magnetic fields," *Journal of Applied Physics,* vol. 109, p. 013903, 2011.

[14]   C. C. Faulkner, M. D. Cooke, D. A. Allwood, D. Petit, D. Atkinson, and R. P. Cowburn, "Artificial domain wall nanotraps in Ni81Fe19 wires," *Journal of Applied Physics,* vol. 95, pp. 6717-6719, 2004.

[15]   M.-Y. Im, L. Bocklage, P. Fischer, and G. Meier, "Direct Observation of Stochastic Domain-Wall Depinning in Magnetic Nanowires," *Physical Review Letters,* vol. 102, Apr 10 2009.

[16]   D. McGrouther, S. McVitie, J. Chapman, and A. Gentils, "Controlled domain wall injection into ferromagnetic nanowires from an optimized pad geometry," *Applied physics letters,* vol. 91, p. 022506, 2007.

[17]   D. Petit, A.-V. Jausovec, D. Read, and R. P. Cowburn, "Domain wall pinning and potential landscapes created by constrictions and protrusions in ferromagnetic nanowires," *Journal of Applied Physics,* vol. 103, p. 114307, 2008.

[18]   J. Yang, C. Nistor, G. S. D. Beach, and J. L. Erskine, "Magnetic domain-wall velocity oscillations in permalloy nanowires," *Physical Review B,* vol. 77, Jan 2008.

[19] Y. Nakatani, A. Thiaville, and J. Miltat, "Faster magnetic walls in rough wires," *Nature materials,* vol. 2, pp. 521-523, 2003.

[20] D. Atkinson, D. A. Allwood, G. Xiong, M. D. Cooke, C. C. Faulkner, and R. P. Cowburn, "Magnetic domain-wall dynamics in a submicrometre ferromagnetic structure," *Nature materials,* vol. 2, pp. 85-87, 2003.

[21] J. Slaughter, "Materials for magnetoresistive random access memory," *Annual Review of Materials Research,* vol. 39, pp. 277-296, 2009.

[22] S. Parkin and S.-H. Yang, "Memory on the racetrack," *Nature nanotechnology,* vol. 10, pp. 195-198, 2015.

[23] S. S. Parkin, M. Hayashi, and L. Thomas, "Magnetic domain-wall racetrack memory," *Science,* vol. 320, pp. 190-194, 2008.

[24] J. King, D. Eastwood, L. Bogart, H. Armstrong, M. Bath, and D. Atkinson, "ChiralMEM: A novel concept for high density magnetic memory technology," in *Nanotech Conference and Exposition*, 2009, pp. 623-635.

[25] J. Franken, H. Swagten, and B. Koopmans, "Shift registers based on magnetic domain wall ratchets with perpendicular anisotropy," *Nature nanotechnology,* vol. 7, pp. 499-503, 2012.

[26] D. A. Allwood, G. Xiong, C. Faulkner, D. Atkinson, D. Petit, and R. Cowburn, "Magnetic domain-wall logic," *Science,* vol. 309, pp. 1688-1692, 2005.

[27] B. Behin-Aein, D. Datta, S. Salahuddin, and S. Datta, "Proposal for an all-spin logic device with built-in memory," *Nature nanotechnology,* vol. 5, pp. 266-270, 2010.

[28] K. Omari and T. Hayward, "Chirality-based vortex domain-wall logic gates," *Physical Review Applied,* vol. 2, p. 044001, 2014.

[29] A. Pushp, T. Phung, C. Rettner, B. P. Hughes, S.-H. Yang, L. Thomas*, et al.*, "Domain wall trajectory determined by its fractional topological edge defects," *Nat Phys,* vol. 9, pp. 505-511, 08//print 2013.

[30] J. Vandermeulen, B. Van de Wiele, L. Dupré, and B. Van Waeyenberge, "Logic and memory concepts for all-magnetic computing based on transverse domain walls," *Journal of Physics D: Applied Physics,* vol. 48, p. 275003, 2015.

[31] S. Walton, K. Zeissler, D. Burn, S. Ladak, D. Read, T. Tyliszczak*, et al.*, "Limitations in artificial spin ice path selectivity: the challenges beyond topological control," *New Journal of Physics,* vol. 17, p. 013054, 2015.

[32] M. T. Bryan, K. H. Smith, M. E. Real, M. Bashir, P. W. Fry, P. Fischer*, et al.*, "Switchable cell trapping using superparamagnetic beads," *Magnetics Letters, IEEE,* vol. 1, pp. 1500104-1500104, 2010.

[33] E. Rapoport and G. S. Beach, "Dynamics of superparamagnetic microbead transport along magnetic nanotracks by magnetic domain walls," *Applied Physics Letters,* vol. 100, p. 082401, 2012.

[34] H. Corte-Leon, P. Krzysteczko, H. W. Schumacher, A. Manzin, V. Antonov, and O. Kazakova, "Tailoring of Domain Wall Devices for Sensing Applications," *Magnetics, IEEE Transactions on,* vol. 50, pp. 1-4, 2014.

[35] M. Diegel, S. Glathe, R. Mattheis, M. Scherzinger, and E. Halder, "A New Four Bit Magnetic Domain Wall Based Multiturn Counter," *Magnetics, IEEE Transactions on,* vol. 45, pp. 3792-3795, 2009.

[36] M. Diegel, R. Mattheis, and E. Halder, "360 domain wall investigation for sensor applications," *Magnetics, IEEE Transactions on,* vol. 40, pp. 2655-2657, 2004.

[37] O. Teruo and N. Yoshinobu, "Magnetic Domain Wall Oscillator," *Applied Physics Express,* vol. 1, p. 061301, 2008.

[38] M. Munoz and J. L. Prieto, "Suppression of the intrinsic stochastic pinning of domain walls in magnetic nanostripes," *Nature Communications,* vol. 2, Nov 2011.

[39] J.-Y. Lee, K.-S. Lee, S. Choi, K. Y. Guslienko, and S.-K. Kim, "Dynamic transformations of the internal structure of a moving domain wall in magnetic nanostripes," *Physical Review B,* vol. 76, Nov 2007.

[40] S.-M. Seo, K.-J. Lee, W. Kim, and T.-D. Lee, "Effect of shape anisotropy on threshold current density for current-induced domain wall motion," *Applied physics letters,* vol. 90, p. 252508, 2007.

[41] N. L. Schryer and L. R. Walker, "The motion of 180 domain walls in uniform dc magnetic fields," *Journal of Applied Physics,* vol. 45, pp. 5406-5421, 1974.

[42] J. Akerman, M. Muñoz, M. Maicas, and J. L. Prieto, "Selective injection of magnetic domain walls in Permalloy nanostripes," *Journal of Applied Physics,* vol. 115, p. 183909, 2014.

[43] M. T. Bryan, T. Schrefl, D. Atkinson, and D. A. Allwood, "Magnetic domain wall propagation in nanowires under transverse magnetic fields," *Journal of Applied Physics,* vol. 103, p. 073906, 2008.

[44] W. Wernsdorfer, B. Doudin, D. Mailly, K. Hasselbach, A. Benoit, J. Meier*, et al.*, "Nucleation of magnetization reversal in individual nanosized nickel wires," *Physical Review Letters,* vol. 77, pp. 1873-1876, Aug 26 1996.

[45] W. Wernsdorfer, E. B. Orozco, B. Barbara, K. Hasselbach, A. Benoit, D. Mailly*, et al.*, "Mesoscopic effects in magnetism: Submicron to nanometer size single particle measurements," *Journal of applied physics,* vol. 81, pp. 5543-5545, 1997.

[46] W. Wernsdorfer, E. B. Orozco, K. Hasselbach, A. Benoit, B. Barbara, N. Demoncy*, et al.*, "Experimental evidence of the Neel-Brown model of magnetization reversal," *Physical Review Letters,* vol. 78, pp. 1791-1794, Mar 3 1997.

Chapter 2:

Theoretical Background of Magnetism

2.1. Origin of Magnetism

The source of magnetism in materials can be generally attributed to the quantized atomic magnetic moments that stems from the restricted spin and the orbital motions of electrons in their atoms [3, 4]. The quantization calculated from the Schrodinger equation [5], dictates the spatial distribution of electron wavefunctions as well as the allowed values and orientation of the angular momenta. The electron orbital motion around the nucleus produces the orbital angular momentum **L** that results in the angular magnetic quantum number m_l. More significantly, the spin motion of the electron produces a spin angular momentum **S**, that results in spin magnetic quantum number m_s. Both momenta couple via the spin-orbit interaction to form the total angular momentum **J** and the total atomic magnetic quantum number m_j.

The magnetic moment produced by the orbital angular momentum **L** can be calculated using the Bohr classical model of an atom by visualizing the angular magnetic moment as the product of an electron orbiting a circular path of radius r around the nucleus. This creates a magnetic moment analogous to the magnetic moment **m** produced from an electric current I in a circular loop of area A, (i.e. *m=IA*), the moment of an electron orbiting a circular path, can be defined as [4]:

$$\mathbf{m} = -\frac{ev}{2\pi r}\pi r^2 = -\frac{ev}{2}r \qquad\qquad (eq. 2.1)$$

where *-e* is electron charge, v is the electron velocity, r is radius of orbit.

Since angular momentum is equivalent to the general product of mass (of electron) m_e times velocity v times distance r, it can be written in a form that equates it with $m_l\hbar$, the component of the angular moment along the field, as:

$$m_e v r = m_l \hbar \qquad \text{(eq. 2.2)}$$

where $\hbar$ is Dirac constant (1.054×10^{-34} J.s).

From eq. 2.1 and eq. 2.2, the orbital angular magnetic moment, m_{orbit}, can be expressed as:

$$m_{orbit} = -\frac{e\hbar}{2m_e} m_l = -\mu_B m_l \qquad \text{(eq. 2.3)}$$

where μ_B is defined as the Bohr magneton constant (9.274×10^{-24} J/T).

The same approach can be followed to derive the magnetic contribution from the spin angular momentum. The result is expressed as:

$$m_{spin} = -g\,\mu_B m_S \qquad \text{(eq. 2.4)}$$

where g is termed the g-factor and is approximately equal to 2. The g-factor is present in the equation since the electron spin does not have a classical analogue, its moment derivation from the relativistic Dirac equation will result in twice the classical value when the spin moment is taken in analogous with the orbital angular moment (that has a classical analogy) [5].

Similarly, the total magnetic moment which emerges from the spin-orbit coupling is found to be equal to:

$$m_{tot} = -g_e\,\mu_B m_J \qquad \text{(eq. 2.5)}$$

where g_e, the Lande g-factor which depends on the spin and angular momenta, is equal to:

$$g_e = \frac{J(J+1)+S(S+1)-L(L+1)}{2J(J+1)} + 1 \qquad \text{(eq. 2.6)}$$

In 3d metals the contribution to the total magnetic moment comes mainly from the spin moment as the orbital angular momentum is quenched due to coupling with the electric field of nearby atoms in the crystal lattice [3, 4].

The values of the quantum numbers **L**, **S** and **J** are determined by the occupancy of the electronic states in an atom which can be predicted by applying the Hund's rules and Pauli exclusion principle to identify the lowest energy configuration of partially filled electron shells [4, 6].

The resultant spin and orbital magnetic moment of an atom are the vector sum of contributions of all of it electrons. This produces one of two outcomes: 1. Magnetic moments are aligned in a manner to cancel out each other producing a zero net magnetic moment. These materials are known to be 'diamagnetic materials', or 2. The summation of magnetic moments leads only to partial cancellation, leaving an overall net magnetic moment. These ' magnetic' materials can be either paramagnetic, ferromagnetic, anti-ferromagnetic or ferrimagnetic [1]. In magnetic materials, the net total moment is usually represented over the whole volume (V) of the material by the term, magnetisation **M**, such that:

$$\mathbf{M} = \frac{m}{V} \qquad \text{(eq. 2.7)}$$

2.1.1. Diamagnetic Materials

In diamagnetic materials, there is zero net magnetic moment in the absence of applied field. However, when a magnetic field (**H**) is applied, a moment is induced to cancel the applied field. This can be understood as a consequence of Lenz's law. When a magnetic field is applied to an orbiting electron, a change in flux occurs resulting in inducing an electromotive force that acts to oppose this change. The induced force acts to decelerate/accelerate the electron causing

a change in the magnetic moment it produces, which is seen as the diamagnetic effect. The change in magnetic moment due to the application of field **H** is expressed as:

$$\Delta \mathbf{m} = -\frac{e^2 r^2 \mu_0}{4m_e} \mathbf{H}$$

(eq. 2.8)

where μ_0 is the vacuum permeability constant ($4\pi \times 10^{-7}$ T.m/A). The opposition of the induced moment to the applied field is indicated by the negative sign and is proportional to **H**. Hence, the susceptibility ($\chi = \mathbf{M}/\mathbf{H}$) is negative ($\chi < 0$).

It is important to mention that the diamagnetic effect occurs in all atoms; however, in paramagnetic and ferromagnetic atoms, the diamagnetic effect is overshadowed by stronger interactions [4], and is not easily measurable.

2.1.2. Paramagnetic Materials

In paramagnetic materials, the magnetic moments are oriented only in the presence of magnetic field. However, in the absence of magnetic field thermal energy is sufficient to break their magnetic ordering, and randomly align their moments.

When **H** is applied, the magnetic moments in paramagnetic materials tend to align parallel to the field forming a net magnetic moment. This behaviour can be explained by considering the *energy-band* model which applies to the 'itinerant electron' model that can explain paramagnetic metals as follows: When atoms are brought together, the wave-function of their valence electrons overlap. This causes their discrete orbitals to interact to form continuous energy bands (Figure 2.1(a)). The number of possible energy states at a particular energy is known as the density of state (DOS) [2]. The energy bands are then occupied by electrons starting from the lowest energy level to the highest. The highest filled energy level at 0 K is known as the Fermi level. In paramagnetic materials, spin-up and spin-down sub-bands have the same energy, and hence, both their bands have the same occupancy (Figure 2.1(b) left).
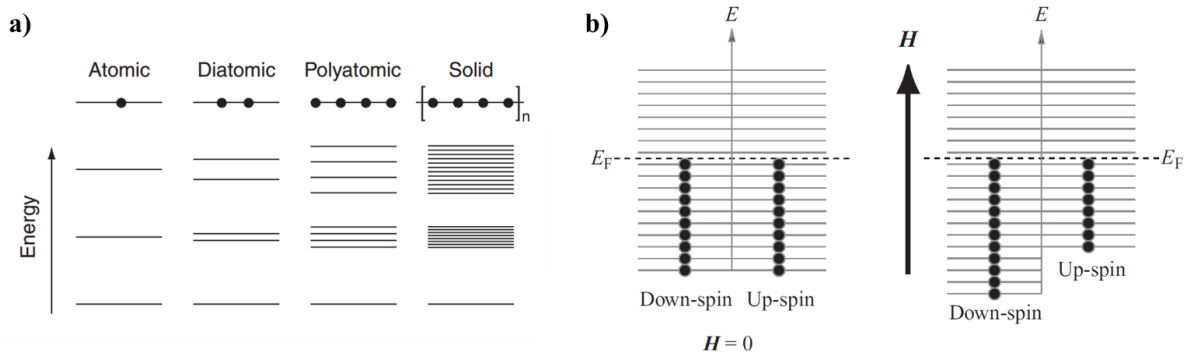
Figure 2.1: (a): Schematic showing the formation of energy bands from interacting energy levels of the same energy from neighbouring atoms. (b): schematic of valence energy band showing distribution of electron spin at H=0 (left) and at H > 0 (right) [2].

Upon applying **H**, electrons with magnetic moment aligned parallel to **H** (represented by spin anti-parallel to **H** due to the negative charge of the electron) will have lower energy than electrons with anti-parallel magnetic moments. This is reflected in a downward shift of the spin-down energy bands and an upward shift of the spin-up energy bands, as shown in Figure 2.1(b). This creates vacancies in spin-down band, and spin-up electrons will prefer to transfer to it to lower their energy. However, only electrons near the Fermi level are energetically capable of transferring. As a result, a majority of electron spins are in the spin-down band, resulting in a net magnetic moment aligned along **H**. When **H** is removed, the energy bands become degenerate and the band population for up and down spins equalise resulting in losing their overall magnetic moment [4]. In paramagnetic materials $\chi > 0$.

2.1.3. Ferromagnetic Materials

In ferromagnetic materials, a 'spontaneous magnetisation' occurs due to a strong interaction between magnetic moments that orders them in spite of the presence of thermal perturbations. This ordering occurs because of a quantum mechanical coupling between electron spins known as the exchange interaction.

In ferromagnetic materials the exchange interaction tends to orient electron spins in atoms parallel to each other. The exchange interaction can be understood as a consequence of both

the Pauli Exclusion Principle and Hund's first rule. Hund's first rule states that when electrons occupy the energy orbitals, they tend to maximize their spins. This results in electrons occupying orbitals, such that one electron occupies one orbital. When there are no more vacant orbitals, electrons start to pair up, but with an electron of opposite spin. The former principle states that if two electrons occupy the same electronic orbital, they must have anti-parallel spins, and hence if they have parallel spin moments they must occupy different orbitals. However, if one electron is promoted to an empty orbital with a parallel spin motion to the first, then the electrons' spatial wave-functions will overlap less and there will be lower coulomb interactions between them than in the anti-parallel state, resulting in a more energetically favourable configuration in some conditions. Consequently, in ferromagnetic material electrons will 'tend' to align their spins parallel to each other to minimise total energy.

Promoting an electron also costs energy as it must be accommodated in the vacant levels at the top of the sub-band. In non-ferromagnetic metals, this energy cost prevents electrons from re-aligning their spins by the exchange interaction. However, in ferromagnetic transition metals (Fe, Ni and Co), the Fermi level is within both the 3d and 4s orbitals (Figure 2.2), and so the valence electrons partially occupy both the 3d and 4s bands. In the case of 4s band, the DOS is narrow making it energetically expensive for electrons to re-align their spins. However the 3d
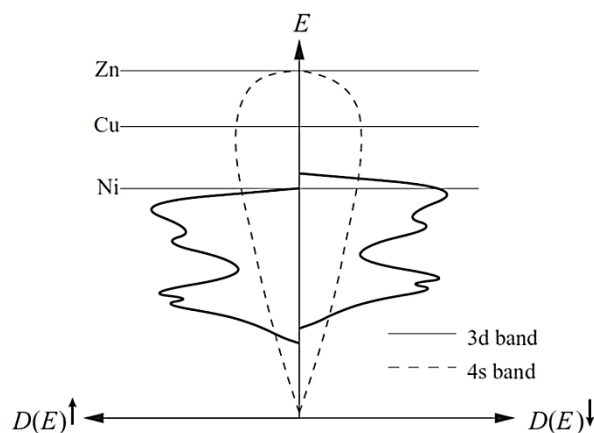

Figure 2.2: Schematic showing the hybridization of the 3d and 4s band in transition metals. Horizontal lines intersecting the bands indicate the Fermi levels. Zn and Cu are non-ferromagnetic with full 3d band while Ni is ferromagnetic with partially filled 3d and 4s bands.

band has a high DOS at the Fermi level (Figure 2.2), and so less energy is required for an electron to be promoted to a vacant orbital and reverse its spin. As a result, the splitting of the sub-bands due to the exchange interaction dominates, and a spontaneous magnetic moment is formed in the absence of an external field [4]. Other metals such as Cu and Zn have similar band structure, but are non-ferromagnetic as their 3d band is fully occupied. In ferromagnetic materials $\chi \gg 0$.

2.2. Magnetic Energies

Having provided an overview of the origins of atomic magnetic moments and the spontaneous magnetisation observed in ferromagnetic material, it is important to discuss how magnetic moments interact with each other, with the crystal lattice and with external stimuli, thus allowing the magnetisation states formed by ferromagnetic materials to be understood. These magnetisation states are a product of the minimisation of four magnetic energy terms, namely, the exchange energy, the magnetocrystalline anisotropy energy, the magnetostatic energy and the Zeeman energy.

2.2.1. Exchange Interaction

As explained above, the exchange interaction arises from Pauli exclusion principle and is responsible for the magnetic ordering of electrons' spins parallel to each other in ferromagnetic materials. If two electron spins are not aligned perfectly parallel to each other, their energy can be calculated using the total exchange energy, $E_{exchange}$, equation [2]:

$$E_{exchange} = -2\,\mathcal{J}\,\boldsymbol{S_i S_j} \; = \; -2\,\mathcal{J}\,S^2\,cos(\theta) \qquad\qquad \text{(eq. 2.9)}$$

where $\mathcal{J}$ is the exchange integral, $\boldsymbol{S_i S_j}$ are the spin quantum numbers for the two electrons and θ is the angle between the two spins. If $\mathcal{J} > 0$, then the system energy decreases when spins of

electrons align parallel to each other (ferromagnetic order). However, if $\mathcal{J} < 0$, the system energy decreases when spins are aligned anti-parallel, as in anti-ferromagnetic materials [4].

The above equation is for two electron spins, however, for the more general case of multiple electron spins, a sum is taken over $\mathcal{J}$ and is divided by two to avoid counting the contribution of pairs twice, resulting in an expression [4, 7] :

$$E_{exchange} = - \sum_{i,j} \mathcal{J}_{i,j} \ \boldsymbol{S_i} \cdot \boldsymbol{S_j} \qquad \text{(eq. 2.10)}$$

The strength of the exchange interaction, or how difficult it is to "twist" the spin configuration of a cubic lattice can be given by the exchange stiffness constant, A, according to the expression [7]:

$$A = \frac{N\mathcal{J}S^2}{a} \qquad \text{(eq. 2.11)}$$

where $\mathcal{J}$ and S are the exchange integral and spin operator, respectively (predefined in eq. 2.9 and eq 2.10), a is the cubic lattice length and N = 1 for simple cubic lattice, N = 2 for body-centered-cubic and N = 4 for face-centered-cubic lattice. A has units of J/m.

The exchange energy per unit volume (energy density), E_{ex} can hence be calculated as [7, 8]:

$$E_{ex} = \frac{E_{exchange}}{V} = A \ (\nabla \boldsymbol{M})^2 \qquad \text{(eq. 2.12)}$$

Where V is the volume of the magnetic system and $\nabla \boldsymbol{M}$ is the divergence of the normalized magnetisation vector. E_{ex} is in J/m^3.

2.2.2. Magnetocrystalline Anisotropy

When the magnetic moments energetically prefer to be aligned in a certain direction as opposed to another, then the ferromagnetic materials is said to possess magnetic 'anisotropy' [7].
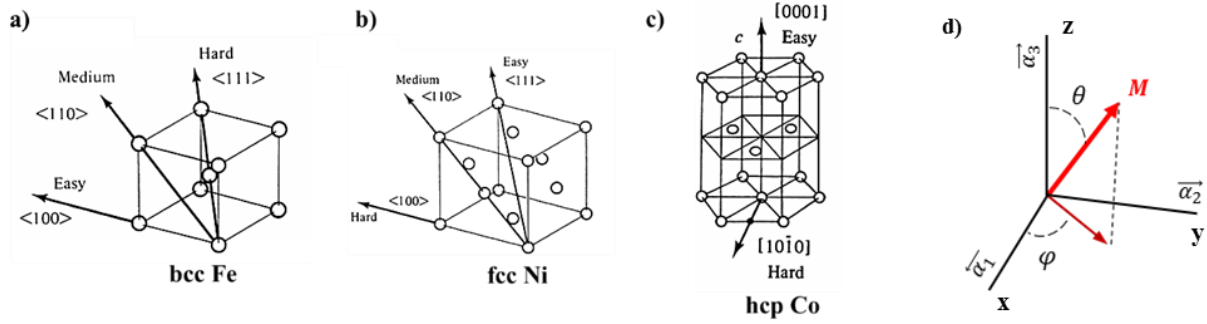
Figure 2.3: Crystal structure showing the easy and hard axes for bcc Fe (a), fcc Ni (b) and hcp Co (c) [1]. (d): Representation of directional cosines (α) and angles of magnetisation M along the axes of the cubic structure.

In crystalline ferromagnetic materials, spins interact with the crystal lattice via the spin-orbit interaction creating a "magnetocrystalline" anisotropy [1]. This creates specific crystal 'easy' axes which the spins prefer to align to. When an external field is applied to force the magnetic moments to align away from the easy axes, the anisotropy energy is increased, with it reaching a maximum when spins are aligned along a 'hard' axis.

For the case of Fe with body-centered-cubic (bcc) structure, the easy axes are <100> directions and the hard axes are <111> directions. Conversely, for face-centered-cubic (fcc) structures, such as Ni, the easy axes lie along <111> directions, while the hard axes lie along <100> directions. For Co hexagonal close packed (hcp), the <0001> directions (i.e. c-axis) are easy axes, while any direction in the basal plane is a hard axis (Figure 2.3) [1].

For a material with uniaxial anisotropy, such as Co, the magnetocrystalline energy can be expressed as an expansion in terms of anisotropy constants K_i and powers of $\sin^2 \theta$, where θ is the angle between the easy uniaxial axis and the aligned magnetic moment. Hence magnetocrystalline anisotropy energy density, E_{an} can be expressed as [2]:

$$E_{an} = K_0 + K_1 sin^2\theta + K_2 sin^4\theta + \cdots \qquad \text{(eq. 2.13)}$$

The equation is usually approximated to the second term only (i.e. $E_{an} = K_1 sin^2\theta$) since the term K_0 is ignored as the change in energy is the point of interest. The other terms are small to affect the approximated energy value.

As for materials with cubic crystalline structure like Fe, Ni and Permalloy ($Ni_{80}Fe_{20}$), the magnetocrystalline anisotropy can be defined as set of polynomials represented by directional cosines α_1, α_2 and α_3 that reflect the three axes of the cubic structure (as indicated in Figure 2.3(d)). The anisotropy energy can then be expressed as [2, 9]:

$$E_{an} = K_1(\alpha_1^2\alpha_2^2 + \alpha_2^2\alpha_3^2 + \alpha_3^2\alpha_1^2) + K_2(\alpha_1^2\alpha_2^2\alpha_3^2) \qquad \text{(eq. 2.14)}$$

Where $\alpha_1 = \sin\theta\cos\varphi$, $\alpha_2 = \sin\theta\sin\varphi$, and $\alpha_3 = \cos\theta$, and where angle θ and φ are the angles defined in Figure 2.3(d). For the case where the easy axes lie along <100> directions, such as in bcc Fe, K_1 is of positive value (usually for Fe at room temperature, $K_1 = 4.8 \times 10^4$ J/m^3). Whereas, in the other case, where the easy axes lie along the <111> directions, such as in the case of fcc Ni or Permalloy, then the value of K_1 is negative indicating a different energy surface. The values of K_1 for Ni and Permalloy (at room temperature) are -4.5×10^4 and -3×10^3 J/m^3, respectively [9]. E_{an} is in J/m^3.

2.2.3. Magnetostatic (Demagnetising) Energy

When all the magnetic moments align parallel to each other in a ferromagnetic structure of a certain geometry, their total alignment forms the material's macroscopic magnetisation **M**. The magnetisation emanates closed magnetic flux (Figure 2.4(a)). The field produced acts to reverse, or self-demagnetise, the direction of the magnetisation in a manner similar to an external field applied anti-parallel to **M** (Figure 2.4(b)).

The demagnetising field (**H**$_{dem}$) is created by magnetic poles or "charges" at the surface of the magnet. These charges are the result of magnetic poles that were not cancelled by nearby moments inside the material, as indicated by red poles in Figure 2.4(a). Hence, the distribution of these 'free poles' depend on the alignment of the magnetic moment dipoles with respect to the shape of the structure [8].
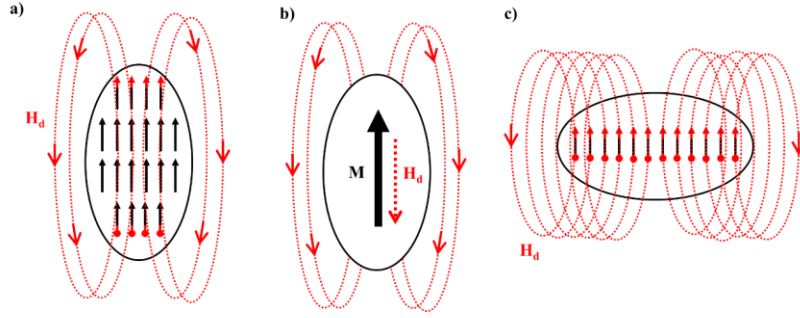
Figure 2.4: Schematic illustrating the demagnetising field in an elongated magnetic structure. (a): Moments aligned along the long axis produce few free poles (in red). (b): Moments forming single domain magnetisation, producing demagnetising field H_d. (c): Moments aligned along the short axis producing more number of free poles at the edges, resulting in high H_d.

If dipoles are aligned perpendicular to the long axis of an elongated structure, then more magnetic charges are accumulated at the surface producing stronger $\mathbf{H_{dem}}$ (Figure 2.4(c)), and so a greater magnetostatic energy. Thus, the shape of the structure plays an important role in determining the preferred alignment of magnetic moments, giving rise to the concept of 'shape anisotropy', where a magnet's magnetisation will preferentially align along its longest axis.

Since $\mathbf{H_{dem}}$ is proportional to the magnetisation $\mathbf{M}$ and in the opposite direction, it can be expressed as [6]:

$$H_{dem} = -N_d\,\mathbf{M} \qquad\qquad \text{(eq. 2.15)}$$

where N_d is a direction specific demagnetising factor (between 0 and 1) that depends on the shape of the structure, such that, it is smallest at the long axis and greatest at the short axis. For a spherical shape, $N_d = 1/3$ in any direction [4].

Since field is applied on a magnetisation $\mathbf{M}$, an energy product can be calculated from their interaction. The demagnetising energy density equation is expressed as [6]:

$$E_{ms} = -\mu_0 \int \mathbf{H_d}\,.\,d\mathbf{M} \qquad\qquad \text{(eq. 2.16)}$$

From eq. 2.15, eq. 2.16 can be rewritten as:

$$E_{ms} = -\frac{1}{2}\,\mu_0\,N_d\,M^2 \qquad\qquad \text{(eq. 2.17)}$$

where E_{ms} is in J/m^3.

In order for a material to reduce its magnetostatic energy, it may form a multi-domain structure to reduce the demagnetising field. This will be discussed further in the section 3.2.

2.2.4. Zeeman Energy

When a magnetic field **H** is applied to a magnetic moment **m** a potential energy arises due to their interaction [8]. This energy can be thought of as the work needed to rotate a magnetic moment an angle θ away from direction of the magnetic field. This energy is expressed as [4]:

$$U = -\mu_0 m H \cos(\theta) \qquad \text{(eq. 2.18)}$$

From eq. 2.7, the Zeeman energy can be written in terms of energy density as:

$$E_Z = -\mu_0 \, \boldsymbol{M}.\boldsymbol{H} = = -\mu_0 M H \cos(\theta) \qquad \text{(eq. 2.19)}$$

where E_Z is in J/m^3.

2.3. Magnetisation Dynamics (LLG equation)

In the previous section the various energy terms that affect the state of a magnetic system were outlined. In reality, the magnetisation of the magnetic system will attempt to form a state that minimises the total energy density, E$_{total}$, as given by:

$$E_{total} = E_{ex} + E_{an} + E_{dem} + E_z \qquad \text{(eq. 2.20)}$$

In order to understand the process by which a system evolves between states, a micromagnetic approach based on the Landau-Lifschitz Gilbert equation (LLG) equation of motion must be used. An explanation of the formulation of this equation is given below.

In the simple case where a magnetic moment is subjected to an external applied field **H**, a torque is produced that causes the moment to precess around the field vector **H**. This torque is equivalent to the rate of change of total angular momentum **J** [4], and can be defined as:

$$\tau_1 = \frac{dJ}{dt} = M \times H \qquad\qquad\text{(eq. 2.21)}$$

From eq 2.5 and eq 2.7 we can define **M** as ($M = -n\, g_e\, \mu_B\, J$), hence we can rewrite eq 2.21 in terms of $\dfrac{dM}{dt}$ as [10]:

$$\frac{dM}{dt} = -n\, g_e\, \mu_B\, \frac{dJ}{dt} = -\gamma_0\,(M \times H) \qquad\qquad\text{(eq. 2.22)}$$

where $\boldsymbol{\gamma_0}$ is the gyromagnetic ratio of a spin (1.75882×10^7 $\text{Oe}^{-1}\,\text{s}^{-1}$).

This equation represents the rate of change of magnetisation with respect to a simple applied field. However, in order to incorporate the effects of the various other energy terms on the magnetisation in a real system, an effective field **H**eff is introduced to the dynamic equation (eq. 2.22), such that:

$$\boldsymbol{H_{eff}} = \frac{1}{\mu_0}\frac{dE_{tot}}{d\boldsymbol{M}} \qquad\qquad\text{(eq. 2.23)}$$

Hence, we can re-write eq. 2.22 to include the effective field as:

$$\frac{dM}{dt} = -\gamma_0\,(M \times H_{eff}) \qquad\qquad\text{(eq. 2.24)}$$

This equation represents the precession motion of the moment around the effective field in a gyroscopic manner (Figure 2.5(a)). This equation includes no terms to account for energy dissipation, which means that the moment vector will precess continuously at an angular frequency of $-\gamma_0 H_{eff}$ [11]. However, in reality, the magnetic moment would rapidly reach an equilibrium state with the moment becoming aligned in the same direction as $\boldsymbol{H_{eff}}$ and no net torque being exerted. Therefore, a damping term proportional to the rate of change of magnetic moment must be introduced to represent the dissipation of energy that brings the moment into equilibrium with $\boldsymbol{H_{eff}}$. This term is represented as $-\alpha\dfrac{d\boldsymbol{M}}{dt}$, where α is termed the Gilbert

damping coefficient and is analogous to the classical coefficient of friction. The equation of motion then becomes [10]:

$$\frac{d\boldsymbol{M}}{dt} = -\gamma\,\boldsymbol{M} \times \boldsymbol{H}_{eff} - \gamma\,\alpha\,\frac{d\boldsymbol{M}}{dt} \times (\boldsymbol{M} \times \boldsymbol{H}_{eff}) \qquad\qquad \text{(eq. 2.25)}$$

Following the addition of the damping coefficient term, the equation of motion models the damped precession of the moment around $\mathbf{H}_{eff}$. When the moment becomes aligned parallel with the direction of $\mathbf{H}_{eff}$, the system reaches equilibrium [11]. Figure 2.5(b) shows a schematic of the motion of a magnetic moment both with and without the damping term included.

In this thesis, the LLG equation is used in the micromagnetic modelling of the magnetisation dynamics of Py nanowires using the software packages described in section 4.4.
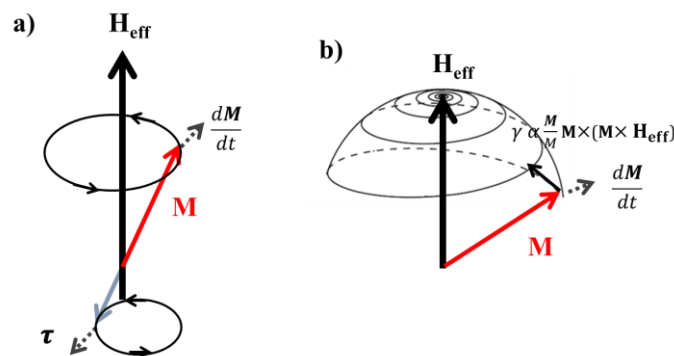
Figure 2.5: Schematic showing the precession of the magnetic dipole around H$_{eff}$ without the damping factor (a) and with the introduced damping factor (b).

2.4. References

[1]   B. D. Cullity and C. D. Graham, *Introduction to magnetic materials*: John Wiley & Sons, 2011.
[2]   R. Kelsall, I. W. Hamley, and M. Geoghegan, *Nanoscale science and technology*: John Wiley & Sons, 2005.
[3]   D. J. Sellmyer and R. Skomski, *Advanced magnetic nanostructures*: Springer Science & Business Media, 2006.
[4]   N. A. Spaldin, *Magnetic materials: fundamentals and applications*: Cambridge University Press, 2010.
[5]   P. W. Atkins and R. S. Friedman, *Molecular quantum mechanics*: Oxford university press, 2011.
[6]   D. C. Jiles, *Introduction to magnetism and magnetic materials*: CRC press, 1998.
[7]   A. P. Guimarães, *Principles of nanomagnetism*: Springer Science & Business Media, 2009.
[8]   A. Hubert and R. Schäfer, *Magnetic domains: the analysis of magnetic microstructures*: Springer Science & Business Media, 2008.
[9]   R. C. O'handley, *Modern magnetic materials: principles and applications* vol. 830622677: Wiley New York, 2000.
[10]   D. Wei, *Micromagnetics and Recording Materials*: Springer Science & Business Media, 2012.
[11]   T. J. Hayward, "Exquisitely Balanced Magnetic Switching in Microscopic Ferromagnetic Rings," PhD Dissertation, Sidney Sussex College, University of Cambridge, 2007.

3. Literature Review

3.1. Introduction

Nanomagnetism is defined as the science involved in the fabrication and characterisation of magnetic materials and devices that have one or more dimensions in the nano-scale (from 1-1000 nm). Its importance arises from the novel magnetic properties that offer levels of control that are not possible in bulk magnetic materials. Promising nanomagnetic applications in different disciplines, but mainly in the data storage/processing fields have made this field of study extremely important [1-3].

The continuous need to miniaturize magnetic grains used in magnetic storage device in order to increase areal density as well as improve signal-to-noise ratio have resulted in an evolutionary reduction of magnetic grain size. This has resulted in an exponential growth of the number of bits stored in a magnetic storage device, as seen in the last few decades (refer to Figure 3.1). With the continuous reduction of magnetic grains, magnetisation becomes unstable as grain size approaches the superparamagnetic size (discussed in section 3.2). At that stage, new technological methods are needed for stabilizing the grains' magnetisation and for developing methods for reading/writing their magnetic information [2].
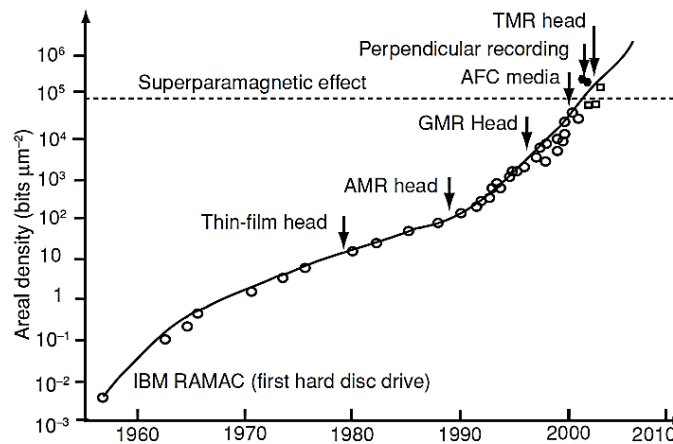

Figure 3.1: Plot showing the evolution of areal density due to the reduction of grain size in magnetic storage devices. Advancement in nanotechnology allowed for new reading head technologies to emerge [6].

In order to meet these challenges, it is essential that a substantial level of understanding of the new magnetic switching behaviours, how they occur, and how they can be controlled and utilized be attained. As will be demonstrated in the following sections, magnetic nanowires play a very critical role in providing solutions to many of these challenges.

In addition to the field of magnetic data storage and processing, magnetic nanowires have been utilized in different novel biomedical applications such as in drug delivery, cell trapping, biosensing and tissue engineering [15, 31-33].

This chapter will provide the basic knowledge required to understand the behaviour of magnetism at the nanoscale, and the unique challenges that appear when attempting to engineer devices that exploit these behaviours. The chapter will then move on to provide a detailed review of the most significant publications related to the behaviour and applications of domain walls (DWs) in Permalloy (Py) nanowires, as these systems are the primary focus of this thesis.

3.2. Nanomagnetism

As seen in section 2.2, the magnetisation states formed by ferromagnetic materials arise due to complex interactions of magnetic energies. Magnetic domains are formed for the purpose of reducing the magnetostatic energy of a system. These domains are separated by DWs with sizes governed by the interplay between exchange and anisotropy/magnetostatic energies.

When the dimension of magnetic materials reach the nanoscale, they approach the characteristic lengths that control their magnetic behaviours [34]. These include the exchange length, DW widths, the single domain limit, the superparamagnetic limit, and other characteristic lengths shown in Table 3.1 [4].

Table 3.1: Characteristic Lengths for nanomagnetic materials [4]

Length	Typical magnitude (nm)
Interatomic distance (Fe)	2.5×10^{-1}
Range of exchange interaction	$\sim 10^{-1} - \sim 1$
Range of RKKY interaction	$\sim 10^{-1} - \sim 10$
Domain size	$10 - 10^4$
Superparamagnetic critical diameter	$\sim 1 - \sim 10^2$
Critical single-domain size	$\sim 10 - \sim 10^3$
Domain wall width	$\sim 1 - \sim 10^2$
Exchange length	$\sim 1 - \sim 10^2$
Spin diffusion length	$\sim 10 - 10^2$
Electron mean free path	$\sim 1 - 10^2$
Superconducting coherence length	$\sim 1 - 10^3$
Fermi wavelength/metal	$\sim 10^{-1}$
Fermi wavelength/semiconductor	$\sim 10^2$

One of the most important characteristic lengths is the exchange length (L_{ex}). This is defined as the longest distance over which it is always energetically favourable for magnetic moments to be parallel [35], or the shortest distance over which magnetisation can be twisted to reduce dipolar interaction [6]. In materials dominated by competition between exchange and demagnetising energy, L_{ex} can be calculated using the equation [36]:

$$L_{ex} = \sqrt{\frac{2A}{\mu_0 M_s^2}} \qquad (eq\ 3.1)$$

where A is the exchange constant and M_s is the material saturation magnetisation. For Py material, L_{ex} is estimated to be around 5.7 nm.

L_{ex} is important as it governs the width of the transitional region between two anti-parallel domains, or in other words it is the width of an idealised DW.

Alternately, in materials dominated by the competition between exchange and anisotropy energies, the DW width (δ_{DW}) can be estimated by the equation [4]:

$$\delta_{DW} = \pi \sqrt{\frac{A}{K_1}} \qquad (eq\ 3.2)$$

where K_1 is the anisotropy constant and δ_{DW} is in SI units. δ_{DW} is in the range of 10-100 nm [6]. It is the competition between the exchange energy, that favours a wide DW with gradual change in spins orientation, and the anisotropy/magnetostatic energies that favour narrow walls with abrupt changes in orientation, that determines the DW width [3].

In other nanostructures, such as in magnetic thin films, film thickness also plays a major role in determining the structure of DWs. In thick films, DW's spins rotate perpendicular to the plane of the structure across its thickness creating almost no surface or volume charges, in what is known as Bloch DWs. This is favourable in thick nanowires where t > DW width. On the other hand, in thin films (t < DW width), the spins of the DW rotate in the plane of the film as rotating across its small thickness would create a strong demagnetising field which is energetically unfavourable [6]. These are known as Néel DWs.

In order for a DW to be nucleated, an amount of energy is required. This can be intuitively understood by considering the case of a material with uniaxial anisotropy. Here, forming a DW causes an increase in the exchange energy, as well as an increase in anisotropy energy as DW internal spins will be oriented away from the easy axis [37]. The DW energy per unit area can be found by the minimization of its total exchange and anisotropy energy density with respect to DW thickness [1]. The yielded DW energy per unit area is given by [4]:

$$\gamma_{dw} = 4\sqrt{AK_1} \qquad \text{(eq 3.3)}$$

where γ_{dw} is in SI unit, and is in the range of 0.001 J/m^2 for transitional metals.

Therefore, in a small spherical particle of radius r, the total DW energy is proportional to its cross-sectional area r^2; whereas the total magnetostatic energy that favours the creation of domains is proportional to r^3. This implies that for a spherical ferromagnetic material, below a certain radius, r_{sd}, the energy needed to create a DW will exceed the saving in the magnetostatic

energy that would result if domains and DWs are created. As a result, it becomes unfavourable to create a DW, and below r_{sd} the magnet becomes a single-domain particle.

r_{sd} can be derived by equating the magnetostatic energy with the DW energy of an elliptic particle of radius r. r_{sd} is, hence, equal to [2, 4]:

$$r_{sd} = 36 \frac{\sqrt{AK}}{\mu_0 M_S^2} \qquad \text{(eq 3.4)}$$

r_{sd} ranges from 10-1000 nm [4] depending on type and shape of material.

In single-domain spherical ferromagnetic particles (where there is no shape anisotropy) the magnetisation will align along the easy axis in order to reduce the total energy by reducing E_{an}. Since total E_{an} is the product of the anisotropy constant (K) and volume (V), total E_{an} is proportional to volume of the particle (i.e. r^3), hence as the size of the particle is reduced, its E_{an} will also be decreased. With the presence of thermal energy ($k_B T$), at a certain small particle volume ($V_{superpara}$), it will be possible for thermal energy to exceed E_{an} ($K_1 V$) resulting in a spontaneous magnetisation reversal of the ferromagnetic particle with a zero net magnetisation. This phenomenon is known as superparamagnetism [38].

Typically superparamagnetic switching occurs through coherent reversal of magnetisation and not through DW nucleation. The radius below which superparamagnetism occurs can be calculated according to the equation [6]:

$$R_{superpara} = \sqrt[3]{\frac{k_B T}{K_1}} \qquad \text{(eq 3.5)}$$

The magnetisation reversal becomes governed by the probabilistic attempt of the thermal energy to surpass the anisotropy energy barrier, as characterised by the Arrhenius-Neel law:

$$f = f_0 \, e^{\frac{-Eb}{k_B T}} \qquad \text{(eq 3.6)}$$

26

where f is inverse of the characteristic switching timescale of a thermally activated event and f_0 is the characteristic attempt frequency [6]. Thermally activated behaviour will be described further in section 3.4.2.

In summary, for ferromagnetic spherical particles with $r \leq R_{superpara}$, a particle is in the superparamagnetic regime where it is constantly switching due to thermal energy. In particles with $R_{superpara} < r \leq r_{sd}$, a particle is single domain and has its magnetisation stably aligned along one of its long (easy) axis. However, when the particle radius size r exceeds r_{sd}, the magnetostatic energy exceeds the DW energy and the single-domain particle can split into thermally stable multi-domain states in order to reduce the strength of the demagnetising field and the magnetostatic energy. At this point a particle's coercivity is reduced. This represents the mesoscopic regime, which lies between the bulk regime, with highly complex multi-domain states, and the single domain regime with simple uniform states. For example, in magnetic nanodisks a 'vortex-state' can occur between the single-domain and the multi-domain regime; in which magnetisation align in a vortex shape in order to reduce the magnetostatic energy (Figure 3.2) [4].

The Py nanowires studied in this thesis represent another excellent example of a magnetic system in the mesoscopic regime. In Py nanowires with submicron width and tens of
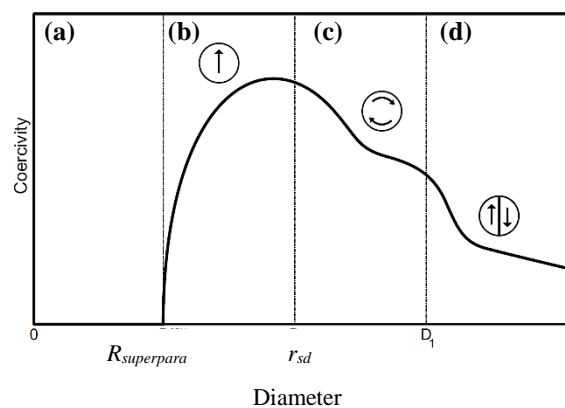

Figure 3.2: Curve showing how coercivity and magnetisation change with increase in particle diameter. (a): Superparamagnetic region for $r \leq R_{superpapra}$. (b): Single-domain region at $R_{superpara} < r \leq r_{sd}$. (c): Vortex state for diameter between single-domain and before multi-domain region. (d): Multi-domain region, for $r > r_{sd}$ [4].

nanometres in thickness, the lowest energy states calculated by Ramstock [39] indicate that domains will align along the long axis of the nanowires to reduce the magnetostatic energy [4, 38]. States where a 180° DW is created parallel to the edges of a nanowire and between two antiparallel domains is unfavourable as the DW will have very high energy as it extends along the whole length of the nanowire [40].

Since there are two easy directions in Py nanowires, magnetisation switching can only occur when applied field is sufficient enough to overcome the magnetostatic energy barrier between the two anti-parallel alignments. If the field is applied along the hard axis, magnetisation will rotate in the same direction as the field, but will return back to the easy axis with no hysteresis (Figure 3.3(b)). Hence, a well-defined field equal to the coercivity of the nanowire is required to switch the magnetisation between the two possible easy axis directions. The outcome of this is a nanomagnetic system with a sharp hysteresis loop that would not be seen in bulk materials (Figure 3.3(a)). Such sharp hysteresis switching behaviour is ideal for magnetic recording applications [38]. The single domain states and the sharp switching of nanowires demonstrate two important examples of how low-dimensionality can create new magnetic features that would not be present in bulk materials.
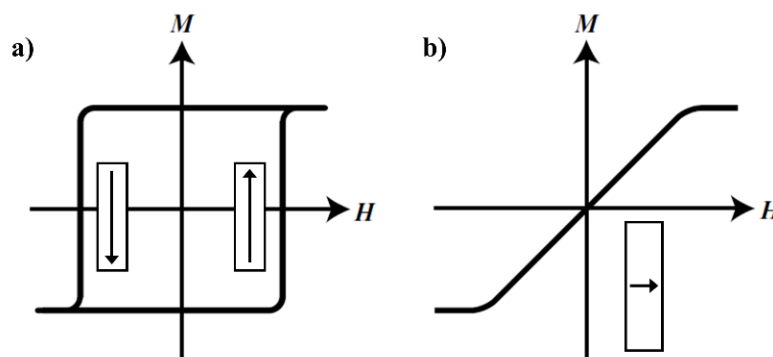

Figure 3.3: M-H curve for nanomagnetic structures with high shape anisotropy. (a): Sharp hysteresis loops when magnetisation is switched along the easy axis (long axis). (b): No magnetic hysteresis when magnetisation is switched along the hard axis (short axis).

3.3. Domain walls in Py nanowires

3.3.1. Types of DWs

In ferromagnetic nanowires the presence of DWs at remanence is energetically metastable or unfavourable. Instead, two bi-stable magnetisation states can occur in which spins prefer to align parallel to the edges of the nanowire in either direction along its long axis. This alignment is always energetically favourable in soft magnetic materials with no perpendicular magnetic anisotropy (PMA) due to the nanowire high shape anisotropy. One such material that has been extensively studied is Permalloy (Py) ($Ni_{80}Fe_{20}$) soft magnetic material.

Py nanowires have been widely used in nanomagnetic studies due to their low coercivity, near zero magnetocrystalline and magnetoelastic anisotropies, high Curie temperature, high magnetoresistance effect and high magnetic permeability (hence the name). Such properties yielded an easily magnetisable material suitable for magnetic recording and reading sensors[34, 41].

The length scales for Py nanowires usually range between 3-50 nm in thickness and 50-1000nm in width [3]. Within these geometries, Py nanowires possess single domain magnetisation across both their widths and thicknesses.

Magnetisation reversal under an external magnetic field in isolated nanowires occurs through DW nucleation and propagation. When sufficient external field is applied anti-parallel to the nanowire magnetisation, DWs nucleate either at imperfections or at the ends of the nanowire. These are then propagated along the nanowire expanding magnetic domains that have spins oriented parallel to the external magnetic field. Switching is completed once these reversed magnetic domains expands over the whole length of the nanowire. The amount of field needed to switch the magnetisation of the nanowire is known as the coercive field (H_c) and depends

mainly on the thickness and width of the nanowire. According to the analysis of Yuan *et al,* an upper bound of H_c can be estimated in Py nanowires according to the following equation [42]:

$$H_c = \frac{8\,M_S\,t}{w}\,S_{an} \qquad \text{(eq 3.7)}$$

where t is thickness, *w* is width and S_{an} is shape anisotropy factor related to the aspect ratio of the nanowire, and can be calculated as:

$$S_{an} = \frac{\frac{l}{w} - \frac{w}{l}}{\sqrt{1 + (\frac{l}{w})^2}} \qquad \text{(eq 3.8)}$$

where *l* is the length of the nanowire.

DWs in soft magnetic nanowires typically have one of two main internal magnetisation configurations namely the vortex and transverse DWs. In vortex DWs (VDWs), the internal magnetisation rotates in a 360° around a vortex core; whereas in transverse DWs (TDWs), the internal magnetisation of the DWs aligns in a direction transverse to the domain magnetisation (Figure 3.4). Depending on the initial orientation of the magnetisation in the nanowire, the DW can either represent a head-to-head (H2H) or a tail-to-tail (T2T) boundary.

The magnetisation inside the VDW can follow, either a clock-wise (CW) or anti-clock wise (ACW) sense of circulation or 'chirality'. Similarly, the direction of magnetisation of the TDW
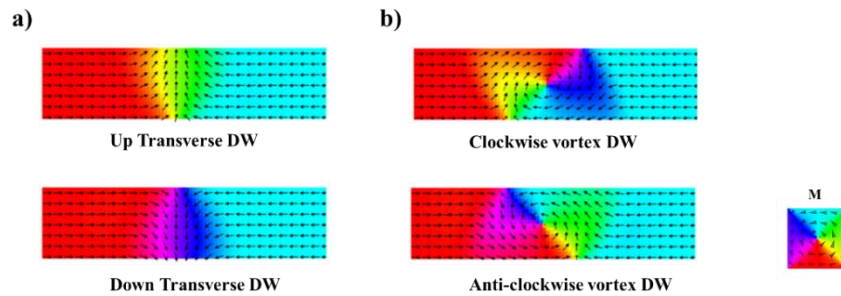

Figure 3.4: Simulation snapshot showing transverse (a) and vortex DW chiralities (b) in a H2H magnetic configuration.
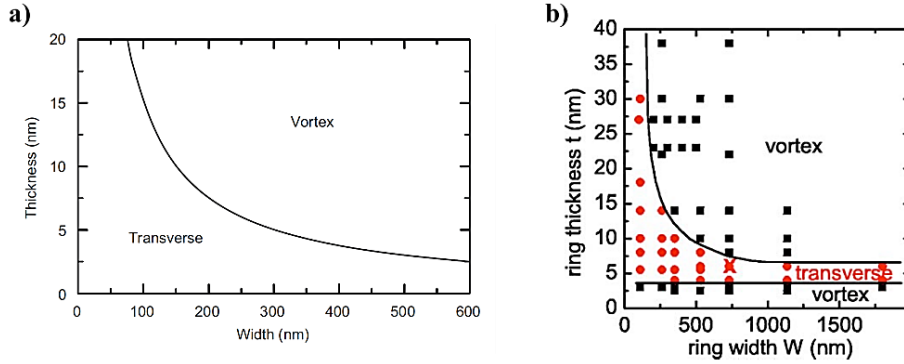
Figure 3.5: Phase diagram of transverse and vortex DWs in (a): Py nanowire (calculated) [8], (b): Py ring (experimental) [19]. Curved lines represent the boundary between the two DW types.

can also be aligned either in an upward or downward direction chirality (refer to Figure 3.4)[3]. The DW chiralities also depend on the magnetisation configuration types (H2H or T2T) since the symmetry of the DW structure depends on the monopole direction at the DW as well as its internal magnetisation orientation. Hence a CW T2T chirality is equivalent to the ACW H2H chirality in a VDW, and the 'up' T2T TDW is equivalent to the 'down' H2H TDW [43].

The type of DW formed also affects its internal energy. For instance, in the TDW structure, the spins are all aligned parallel to each other but perpendicular to the edge of the nanowire. This results in having a relatively low exchange energy but high magnetostatic energy. As for VDWs, the spins are aligned in a circular manner, which reduces the magnetostatic energy. However, this will be in the cost of increasing the exchange energy since the VDW structure is highly non-uniform rather than quasi-uniform like for TDWs [3, 40].

It has been reported that with an increase in nanowire thickness, the exchange energy increases linearly, while the magnetostatic energy increases quadratically. Moreover, increasing the width of the nanowire results in a stronger increase in the magnetostatic energy than in exchange energy [44]. Therefore, it is energetically favourable to stabilize TDW in thin nanowires; whereas thick nanowires will favour the creation of VDWs. A phase diagram has been estimated and refined by Nakatani *et al* [8] for Py nanowire that shows the boundary between the two DW types with respect to nanowires' widths and thicknesses (Figure 3.5(a)).

31

Later, experimental imaging done by Laufenberge *et al* [19] on Py rings with different widths and thicknesses was used to produce a similar phase diagram based on the experimental results (Figure 3.5(b)) .

Mathematically, the boundary relationship between the TDWs and VDWs has been estimated as [17]:

$$t.w = CL_{ex}^2 \qquad \text{(eq 3.9)}$$

where t is thickness, w is width and C is a material dependant constant, and is equal to 128 for Py material [4].

3.3.2. DW nucleation in nanowires

As mentioned previously, during the magnetisation reversal of a magnetic nanowire, an external field with direction opposite to the nanowire's magnetisation is increased until a DW is nucleated and propagates along the nanowire, reversing its magnetisation. In principle, DWs should nucleate from both ends of the nanowire simultaneously if the nanowire is assumed to be perfectly symmetrical, or favourably at imperfections in real nanowires. In both cases, the switching field is relatively high and is equal to the nanowire's coercivity. Moreover, such method does not allow for control over DW propagation; and would dramatically limit the scope of many spintronic applications. Hence, other methods for DW nucleation have been innovated.

One method of controlling DW nucleation works by attaching a wide pad to one of the nanowire ends [45-47]. From (eq 3.7) it can be deduced that increasing the width of the nanowire will reduce H_c. This may be understood as wide magnetic structures have low shape anisotropy as opposed to narrow wires that have high shape anisotropy [46]. Therefore, upon applying field to a nanowire with a nucleation pad, the low coercivity pad switches first creating
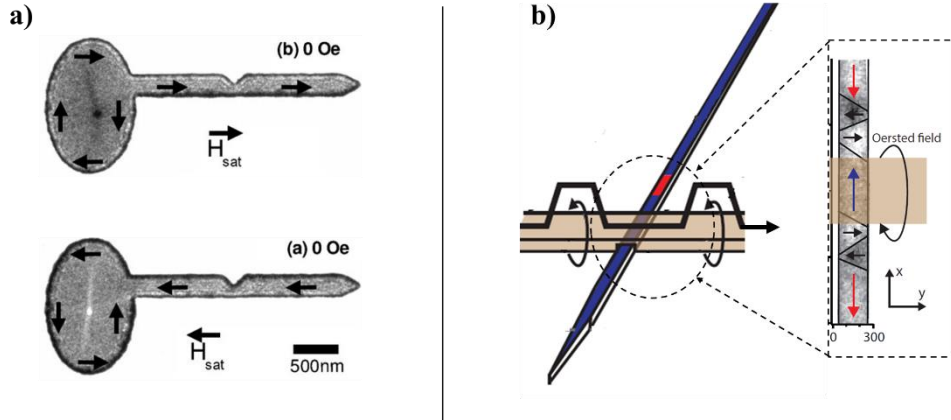
Figure 3.6: DW nucleation methods. (a): Controlled pad nucleation. When nanowire is saturated to the right (left), pad becomes CW (ACW) [10]. (b): Current-induced DW nucleation. Current pulse produces a reversed domain between two DWs at each side of current line [24].

a DW that pins at the junction of the nanowire. The pinning occurs because the DW encounters a pinning potential at the junction. The pinning potential can be attributed to exchange and magnetostatic energy barriers created by the necessity of the DW to change its structure to propagate into the narrow nanowire. Eventually, the DW is injected into the nanowire as long as the field applied is above the required injection field (H_{inj}) [48]. H_{inj} is lower than the nanowire H_c and so the pad acts as well-defined source of domain walls. [45, 46].

It is important to mention that H_{inj} will have an associated field distribution due to the effects of thermal perturbations that can assist DW depinning [49]. Moreover, Bryan *et al* [50] have shown that the nucleation pad geometry as well as the closure domains formed in the pad at remanence can also affect the distribution of H_{inj}, making it even less well defined.

In addition to using a nucleation pad for lowering the injection field, the nucleation pad can also be utilized to bias the chirality of nucleated DWs. McGrowther *et al* [10] demonstrated one such method by creating an asymmetrical nucleation pad. This was done by offsetting the pad in a transverse direction to the nanowire (Figure 3.6(a)). It was found that upon saturating the nanowire and then leaving the system to relax, the spins of the nanowire determined the magnetisation state of the nucleation pad. Since it was observed that the injected DW always

had the same chirality as the closure domains of the nucleation pad, the asymmetric pad design results in biasing the chirality of VDWs (Figure 3.6(a)).

Another method used to inject DWs into nanowires, involves inducing a strong local magnetic field by applying electric pulses through a current line perpendicular to the direction of the nanowire as shown in Figure 3.6(b). In accordance with Ampere's law, a circular magnetic field is induced around the strip, and if it is large enough it will switch the nanowire segment below the strip by creating two DWs, as indicated in the enlarged segment of Figure 3.6(b). The field induced should be higher than H_c, and the polarity of the current should be set to induce a magnetic field anti-parallel to the nanowire's initial magnetisation for switching to occur. The equation indicating the strength of the field induced can be derived from Bio-Savart law [51] and has the following form [52]:

$$ H = \frac{I}{2w} \qquad \text{(eq. 3.10)} $$

where I is the electric current and w is the width of the current line.

DW nucleation using this method is considered to contain elements of stochasticity that can be explained by Arrhenius-Neel model. This is because DW nucleation depends on the reversal of a certain activation volume [53]. However, with proper optimization of field amplitude and pulse width, DW nucleation can become deterministic with nucleation times of less than 3 ns [54]. After the two DWs have been nucleated, an external field is used to propagate the DWs to the opposite sides of a nanowire leading to completion of its switching.

Similar to nucleation pad method, the current induced nucleation can be modified to generate DWs with defined chirality. One method proposed and verified by Sentker *et* al [14] used a tilted strip line rather than a purely perpendicular one. The strip line was tilted at an angle of 30º, in order to utilize the y-component of the induced magnetic field to bias the structure of
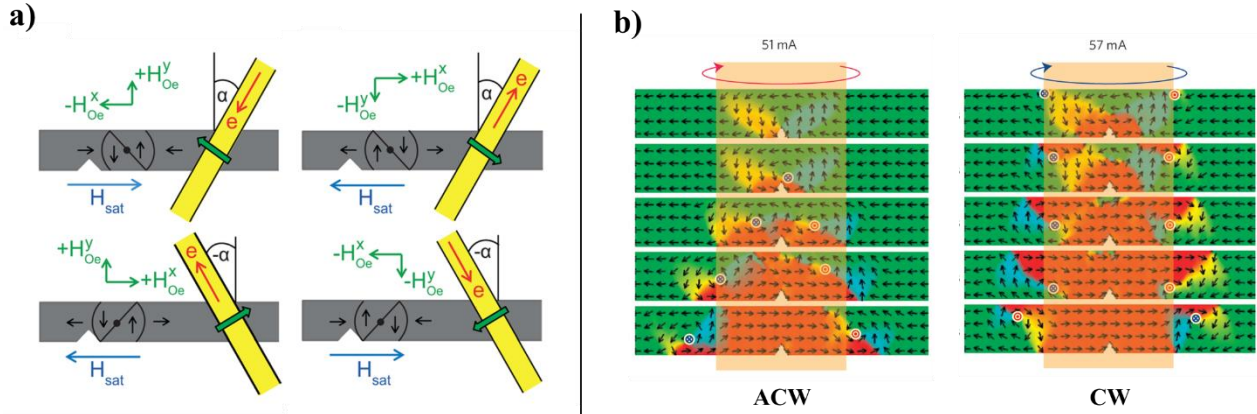
Figure 3.7: Controlled current-induced DW nucleation. (a): Tilted current line biasing the VDW chirality depending on the y-component of the induced field [14]. (b): Asymmetric notch under current line biases chirality depending on amount of current pulse causing curling to occur at bottom (left) or top edge of nanowire (right) [30].

the nucleated VDW. The direction of the tilt strip can be set to determine the chirality of the DW as shown in Figure 3.7(a).

Another interesting method for biasing VDW chirality has been proposed and verified by Pushp *et al* [30]; in which, an asymmetric notch is fabricated below the strip line (Figure 3.7(b)).

When the pulsed field was anti-parallel to the saturated nanowire above the notch, DWs were nucleated by first creating a curling region of magnetisation around the notch. The curl nucleated a vortex core at the top edge of the nanowire or the bottom edge of the notch depending on the amplitude of the current pulse (Figure 3.7(b)). If the core was nucleated at the notch, ACW VDWs were nucleated; where as if the core was nucleated near the top edge of the nanowire, CW VDWs were nucleated [30]. Using this method the chirality of the VDW can be controlled by the current pulse amplitude.

3.3.3. Motion of DWs in nanowires

DWs in nanowires can be moved under the influence of an external magnetic field, or when a spin-polarized current passes through nanowire causing the transfer of angular momentum to the DW, pushing it along the current direction [55, 56]. The latter method is beyond the scope

of this thesis. (Reader may refer to mentioned references for further details of spin-transfer-torque method).
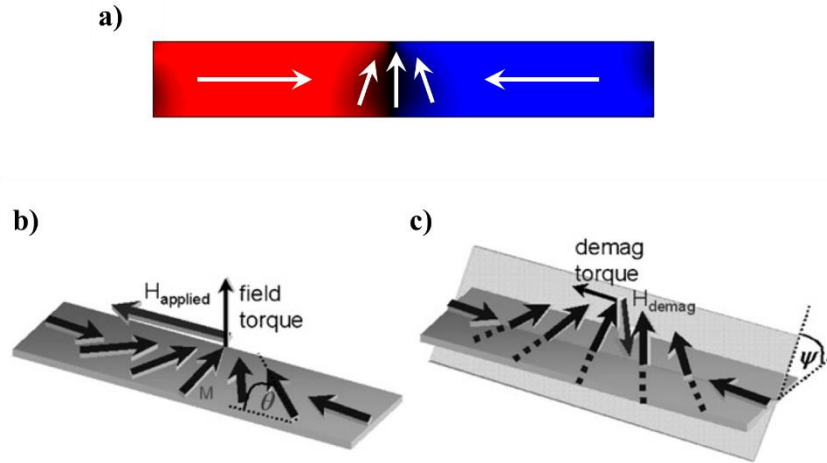
Motion of DW under external field

Figure 3.8: Schematic of one-dimensional wall. (a): Head-to-head TDW in nanowire. (b): Schematic showing DW when H is applied to the left. The field H results in an out-of-plane field torque (c): Schematic showing the out-of-plane offset at a canting angle ψ. A demagnetising field results which results in a demagnetising torque that moves the DW to the left [17].

When a magnetic field is applied to a DW in a nanowire (Figure 3.8(a)), the magnetic moments inside the DW tilt, thus creating an out-of-plane magnetisation component (Figure 3.8(b)). This creates a demagnetizing field perpendicular to the DW that produces a torque parallel to the external applied field (Figure 3.8(c)). This torque causes the displacement of DW; such that the domain parallel to the direction of the external field expands [4]. The movement of the DW under an applied field occurs in order to reduce the total Zeeman energy with propagating DWs dissipating energy through damping mechanisms [57].

The velocity of the DW propagation is proportional to the applied field **H**, according to the equation:

$$v = \mu H \qquad \text{(eq. 3.11)}$$

where μ is the 'mobility'. μ can be defined as the rate of change of velocity with **H** [5] and is expressed as:

$$\mu = \frac{\mu_0 \, \gamma \, \Delta}{\alpha} \qquad \text{(eq. 3.12)}$$

where γ is the gyromagnetic ratio, Δ is the DW width parameter (equal to $\sqrt{\frac{A}{K}}$) and α is damping coefficient . For Py material, the above material parameters are: α, ranging from 0.01 to 0.02, $\mu_0 \gamma = 2.2 \times 10^5$ m/A.s and assuming Δ ranges from 50 nm [58] up to size of nanowire width.

It can be deduced from the equation that increasing **H** will result in an increase in DW velocity. This is valid for values of **H** below a critical field value known as the walker-breakdown field (H_{WB}), and DWs propagating in this range of fields are said to be in the 'viscous' regime of motion. Velocities in the viscous regime have been measured to be 10 s to 100 s of m/s [58, 59].

When **H** exceeds H_{WB}, DWs start undergoing unique transformations of their internal structure due to a phenomenon known as 'Walker breakdown' (WB) transformation [60]. Following WB, the velocity of the DW dramatically decreases, and remains close to constant with applied field before increasing again when **H** exceeds a further field value (indicated as H_i in Figure 3.9(a)). This decrease in DW velocity has been attributed to the retrograde motion that starts to occur in the DW due to complicated structural transformations within the DW [58].

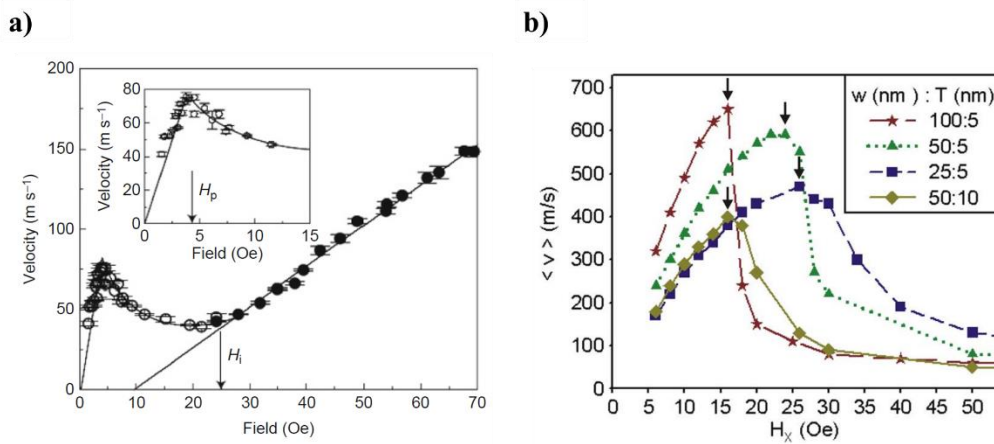
Figure 3.9: (a): Plot of DW velocity with respect to applied field in nanowires. Inset shows magnification near H_{WB}, here equal to H_p [5]. (b): Plot of DW velocity with respect to field for different nanowire widths and thickness [25]

These WB transformations can follow a certain periodic cycle of transformations as well as become turbulent and chaotic at very high fields.

The value of H_{WB} depends on the geometry of the nanowire, damping coefficient, magnetic anisotropy and edge roughness [61]. For instance, the relationship between H_{WB}, width and thickness of Py nanowire has been modelled by Bryan *et al* [25] (Figure 3.9(b)) to show that when width or thickness increases, H_{WB} decreases according to the following equation:

$$H_{WB} = 46\, e^{-0.007w - 0.09t} + 2 \qquad \text{(eq. 3.13)}$$

The WB transformation occurs when an applied field, exceeding H_{WB}, produces an out of plane demagnetizing torque that is sufficient to tilt the canting angle ψ of the DW (refer to Figure 3.8(c)), and results in producing DW transformations that are affected by the DW type (VDW or TDW).

In real nanowires the WB transformations depend on the type of the DW (whether TDW or VDW), the geometry of the nanowire and the value of the field applied [23, 25, 61]. For instance, when a field is applied in a nanowire containing a VDW, the tilt of the DWs spins creates an out-of-plane demagnetising field which both limits further tilting and causes the
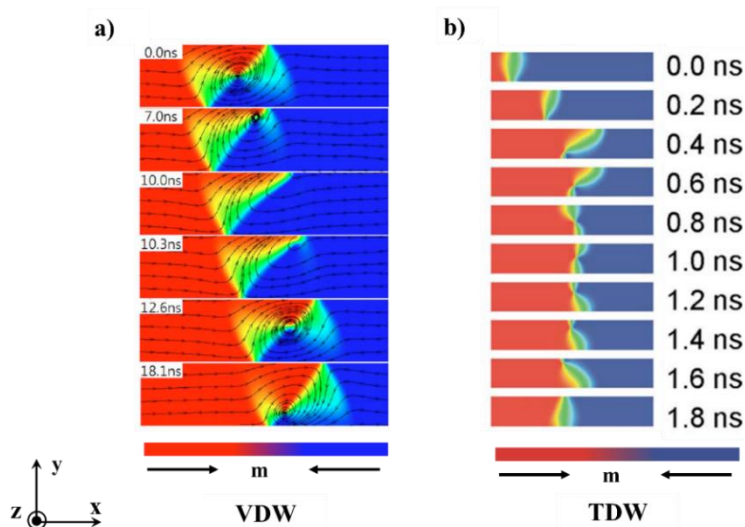

Figure 3.10: WB transformations in the oscillatory regime in Py nanowires. (a): VDW undergoing periodic oscillations transforming from VDW to UP TDW, VDW and DN TDW [13]. (b): TDW undergoing periodic oscillations and transforming between TDW/anti-vortex [28].

propagation of the DW. However, when **H**>H$_{WB}$ the DWs out-of-plane magnetisation component (**M$_z$**) (Figure 3.10(a)) becomes very high causing the VDW core to move in a transverse manner towards the edge of the nanowire where the VDW core gets annihilated (Figure 3.10(a)-10ns). This results in the transformation of the VDW to a transverse-lik DW structure that has a significant –**M$_z$** component that would reduce the overall out of plane demagnetising field [13, 62].

The movement of the core from the centre of the VDW to the edge of the nanowire results in a retrograde motion that pulls the DW structure backward causing a reduction in its velocity. The TDW-like structure is energetically unfavourable in thick nanowires and eventually transforms back to a VDW by nucleating a core with an opposite polarity to the original VDW core. The core is nucleated at the edge where it was annihilated (Figure 3.10(a)-10.3ns), and moves towards the centre of the DW creating a vortex shape while pushing the DW forward (Figure 3.10(a)-12.6ns). The forward motion exceeds the backward motion resulting in an overall DW forward propagation. The same process is then repeated once more but this time the VDW core moves to the other edge of the nanowire (bottom) and transforms to a TDW-like shape with opposite chirality to that formed in the previous cycle [13]. The DW continues to oscillate between CW VDW, up TDW, CW VDW and down TDW in a regular fashion, and hence this is known as the 'oscillatory' regime of motion.

For TDWs, a different cycle of transformations are observed: the high field causes the nucleation of an anti-vortex at the bottom of the TDW, which then moves in a transverse direction to the other edge of the nanowire (Figure 3.10(b)-0.4ns). As the movement of the core goes from the centre to the top edge, a retrograde motion ensues (Figure 3.10(b)-0.6ns to 1.6ns). The anti-vortex eventually annihilates on the other side causing the reversal of the TDW chirality. The process is repeated with the DW transforming between an up TDW, anti-vortex and down TDW [28, 47]. Other WB modes have also been reported for VDWs [61].

At **H**>H$_i$ (refer to Figure 3.9(a)), the DW can no more maintain a steady oscillatory motion due to the very high Zeeman energy, and it propagates in a chaotic turbulent motion at a velocity that increases with **H**. This is known as the 'turbulent regime' [5, 21, 63].

Stein *et al* [24] have managed to image the WB transformations in Py nanowire using magnetic X-ray microscopy. The DWs were generated using perpendicular current pulses and the DW was driven above H$_{WB}$. Figure 3.11 shows two DWs being generated and propagated along the long axis of the nanowire (in this case vertically). The DW type is indicated by white/black contrast which indicates the chirality of the transverse component of the DW. Figure 3.11(a) shows how two DWs were first nucleated as VDWs (at 2 ns) with a current pulse of 6 ns duration. After that each DW propagated away from the other one. The upper DW transforms into a transverse-like structure with (←) chirality (at 2.9 ns), then the DW started regaining its vortex shape as the (→) transverse component started to expand until the DW became transverse-like again with (→) chirality (from 5.7 ns to 7.2 ns), then it went back again to vortex shape, and the DW continued to oscillate in the same manner preserving the VDW chirality.

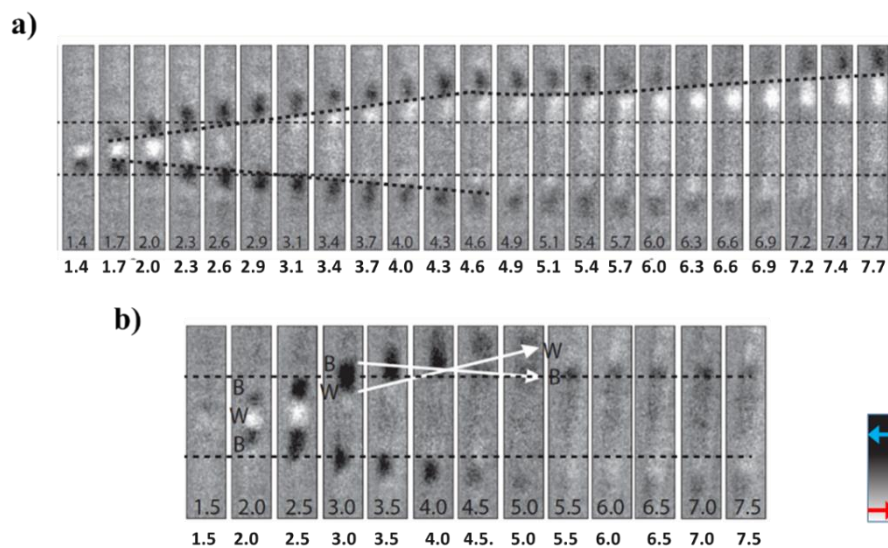**Figure 3.11: X-ray microscopy images showing the dynamic transformations of DW in Py nanowires of t=20 nm and w=200 nm. (a): DW nucleated with a 6 ns current pulse. The DW is transformed between VDW, (←) TDW-like, (→) TDW-like and VDW, while preserving the VDW chirality. (b): DW nucleated with an 8 ns current pulse. The VDW inverts its chirality in this transformation. H=60 Oe [24].**

Another period is seen in Figure 3.11(b) where the pulse duration was set to 8 ns. In this period, the upper DW is first nucleated as VDW, transforms into transverse like shape and then back to the VDW but with flipped chirality (at 5.5 ns). These results verify the WB transformation phenomenon explained earlier.

WB transformations present a limitation on device performance due to the reduction of DW propagation velocity, and also due to the changes it creates in the DW structure. Such changes can induce stochastic behaviours in spintronic applications [64], as well as the loss of any chirality-based information stored in the DWs [65]. Therefore, methods to suppress WB transformations or increase H_{WB} have been proposed. One method suggested by Nakatani *et al* [58] involves increasing edge roughness in nanowires in order to create a channel for energy dissipation in the form of spin waves; hence, supressing the nucleation of anti-vortices and thus WB. Other methods employ the application of an out-of-plane magnetic fields ($\mathbf{H_z}$) to the nanowire to reduce the demagnetising field that triggers the WB [62], or the application of transverse fields ($\mathbf{H_y}$) which hinder the nucleation of anti-vortices in TDW or separate them from the TDW structure after being nucleated [28].

3.3.4. DW pinning in nanowires

In perfect nanowires, a DW can propagate smoothly at any infinitesimally small field value above 0 Oe. However, in real nanowires where intrinsic defects such as edge roughness, material impurities and local variations of magnetic parameters (such as A and M_s) may exist, a minimum field is needed to allow the DW to depin from these defects and continue its propagation [5]. This field is known as propagation field (H_p).

DW pinning due to these intrinsic imperfections has been investigated due to its importance in describing and explaining the hysteresis and coercive responses of switching behaviour in ferromagnetic materials [66]. On the other hand, artificially designed defects in nanowires in

the form of constrictions, notches or protrusions have been widely introduced in order to manipulate and study nanowire switching. For instance, in order to study and model the effect of thermal perturbation on nanowire switching, a DW pinning site in the form of a notch was introduced and the switching field was measured at different temperatures [67-70]. Other experiments have utilized asymmetric pinning sites to investigate their interaction with DWs in order to understand the different internal DW spin configurations [20, 23, 71]. Furthermore, huge interest is being directed towards nanowires with pinning sites for information storage applications [26, 72], as well as for performing logical operations [16].

DW pinning can be explained in terms of a DW encountering different energy potentials [20]. When a propagating DW encounters a different geometrical section of the nanowire such as a constriction, protrusion or curved region, it will have to change its structure and area in order to continue its propagation. Such changes will result in altering its energy, thus creating an energy well/barrier that causes the DW to pin [9, 73-75].

The nature of the energy landscape formed depends mainly on the DW chirality. Hayashi *et al* [20] conducted a study for the energy potential encountered by transverse and vortex DWs when reaching an asymmetric triangular notch. For H2H magnetisation orientation it was found that an energy well is formed when a downward TDW or a CW VDW reaches the notch, as seen in Figure 3.12(a). On the other hand, an energy barrier is encountered if an upward TDW
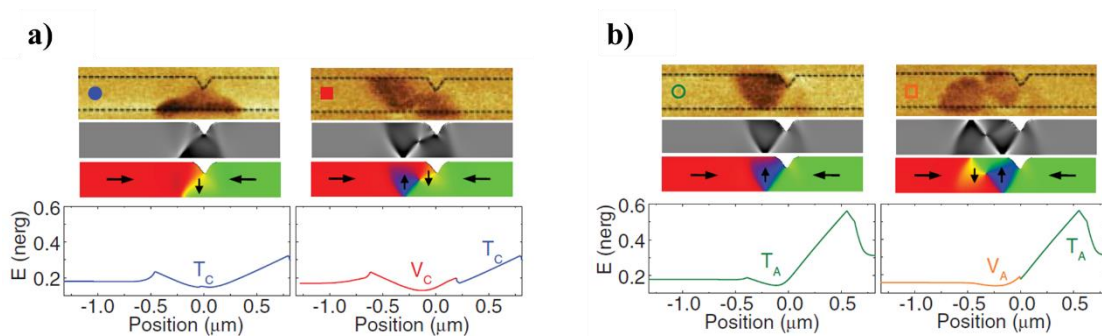

Figure 3.12: MFM, simulation and DW pinning energy landscape images of pinned DWs in nanowires. (a): An energy well is formed for downward TDW and CW VDW in H2H magnetic configuration. (b): An energy barrier is formed for upward TDW and ACW VDW in H2H magnetic configuration [20].

or an ACW VDW reaches the notch, as shown in Figure 3.12(b). The reason behind these two behaviours can be understood as follows: in the first case, the spin alignment of the two domains as well as the spins of the DW (aligned downward in Figure 3.12(a)) can align themselves inside the constricted region continuously along the edge of the triangular notch without creating regions of magnetic frustration. This yields a reduction in the energy of the DW when it is pinned inside the constricted region, thus creating an energy well. However, for an upward TDW or ACW VDW (Figure 3.12(b)), the spins of the DW can not align parallel with the edge of the notch when passed into the constricted region without forming regions of magnetic frustration with the two domains' spins. Instead, the DW spins are forced to align perpendicular to the notch, accumulating magnetic charges and increasing the magnetostatic energy of the system. This is energetically unfavourable, hence, the DW pins outside the notch before an energy barrier.

The geometry of a notch is an important factor in determining the strength of the DW pinning. Experimental results [48, 76, 77] have indicated that increasing the depth of a notch will result in an increase in depinning field (H_d). This is understandable as it will require more energy for a DW to deform its structure in order to pass through a deeper constricted region leading to an increase in H_d [48]. However, the increase in H_d eventually reaches a saturation value (estimated at notch depth ~60% of nanowire width [77]) as the switching mechanism changes such that the pinned DW remains pinned while a new DW is nucleated on the other side of the notch [48].

As for the effect of geometrical shape of the notch on pinning strength, Bogart *et al* [78] has compared the pinning potential for a triangular and rectangular notch shape and concluded that very similar depinning fields result for both shapes, thus indicating that the overall geometrical shape of the notch does not play a significant role in affecting the pinning strength.
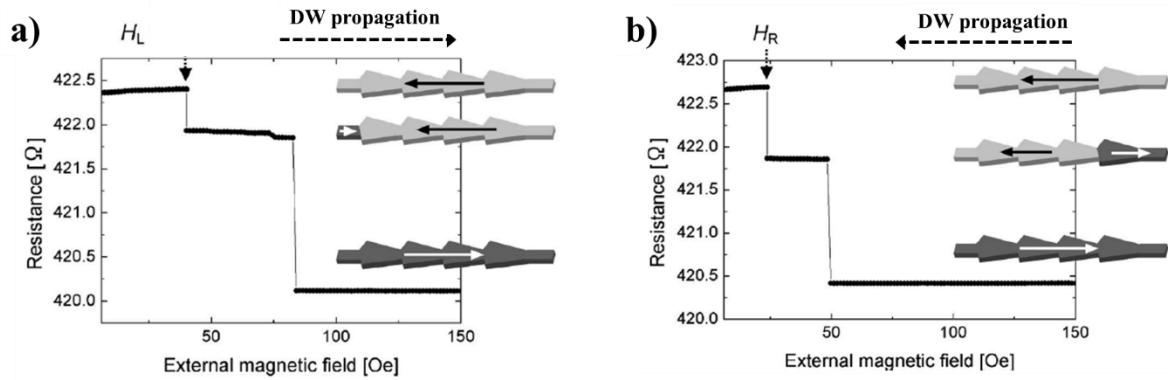
Figure 3.13: Plot showing the asymmetry in propagation field for a DW moving Py nanowires with diode-like structure when moving from narrow to wide region (left to right) (a), and when moving from wide to narrow region (right to left) (b) [12].

On the other hand, Cheo *et al* [79] conducted a simulation study for the depinning of DWs from triangular notches with asymmetrical edges. It was suggested that only the slope of the notch in the direction the DW exists can affect the depinning process. Prior to that, Himeno *et al* [12] demonstrated that the slope of double notches with asymmetric edges creates asymmetry in H_d depending on pinning direction. This was used to create a DW propagation diode (Figure 3.13): In the presence of double notches with asymmetric edges, the DW depins at small field when propagating from the wide notch region to the narrow region (Figure 3.13(b)) compared with its propagation from the narrow to the wide notch region (Figure 3.13(a)). This behaviour can be understood in terms of a gradient in the energy of a DW. As the DW energy is proportional to its area, when a DW propagates to a wider region, it has to cross an energy potential as wider nanowire region requires the DW to expand its area and its energy. This change in DW energy is more rapid than the change required when a DW propagates from wide to narrow position, hence, larger field is required [79, 80].

Another important aspect to consider in DW pinning/depinning is the fact that there are two types of DW depinning mechanisms: static depinning and the dynamic (kinetic) depinning. In the static depinning, the DW is initially pinned and relaxed at a potential well/barrier or is propagated to the pinning site by applying very low field (below WB) and allowing it to fully relax at the pinning site prior to applying an external field to depin it. Whereas in the dynamic

case the DW is propagated towards the defect site at constant field, and H_d is measured to find the field at which the DW passes the defect site [23].

It has been experimentally observed that a static H_d is higher than the dynamic H_d for the same pinning site. This has been attributed to the different energy landscapes encountered by a moving DW compared with a static DW [23, 81]. The latter has a more relaxed state within a deeper pinning potential, as energy has been dissipated during its relaxation. On the other hand, a moving DW encounters a shallower pinning potential resulting in weaker pinning. This concept is analogous to static and kinetic friction that occurs in classical mechanics [81].

Equally important is the fact that in the dynamic pinning case, the propagating DWs can undergo WB transformations when moving above H_{WB}. This results in probabilistic and stochastic dynamic pinning/depinning as DWs can arrive the pinning site with different internal spin structures depending on their initial state and the WB period [23].

3.4. Stochastic depinning in nanowires

The depinning of DWs in ferromagnetic nanowires depends mainly on the nature of the encountered pinning energy landscape. This is dictated by the shape of the pinning site, the spin structure of the DW and the depinning mechanism. The two latter factors are affected by both dynamical and thermal effects resulting in stochastic pinning/depinning behaviour where H_d changes from one field cycle to the next. Hence, two different forms of stochasticity exist, dynamically-induced stochasticity and thermally-induced stochasticity.

3.4.1. Dynamic stochasticity

As mentioned in the previous section, DWs propagating above H_{WB} undergo internal spin structural changes when in the oscillatory or turbulent regimes of motion. This can dramatically affect their interaction with defect sites and the energy potential they encounter. As a result,

DWs can exhibit a variety of different switching modes and different H_d for the same defect site.

Since H_{WB} for Py nanowires ranges from 3-50 Oe [25, 82-84], depending on nanowire geometry, the DW is very likely to be propagating above H_{WB} due to the presence of intrinsic defects. It is only in high quality nanowires (where DW nucleation occurs via means other than nucleation pad, such as nucleating DW in L-shaped corners [74, 85] or via current lines [51, 54, 86]) that DW propagation and nanowire switching can occur below H_{WB}. Hence, for the majority of nanowires when switching is measured multiple times, the outcome will be stochastic with a probabilistic value of H_d.

Pi *et al* [23] have attempted to explore stochastic DW pinning by modelling the different DW structures that arrived to the same pinning site when the applied field was changed by only few Oersteds. Their results showed that a DW can arrive to the pinning site and pin as either a VDW or a TDW depending on the transverse position of the DW core with respect to the defect (refer to Figure 3.14).
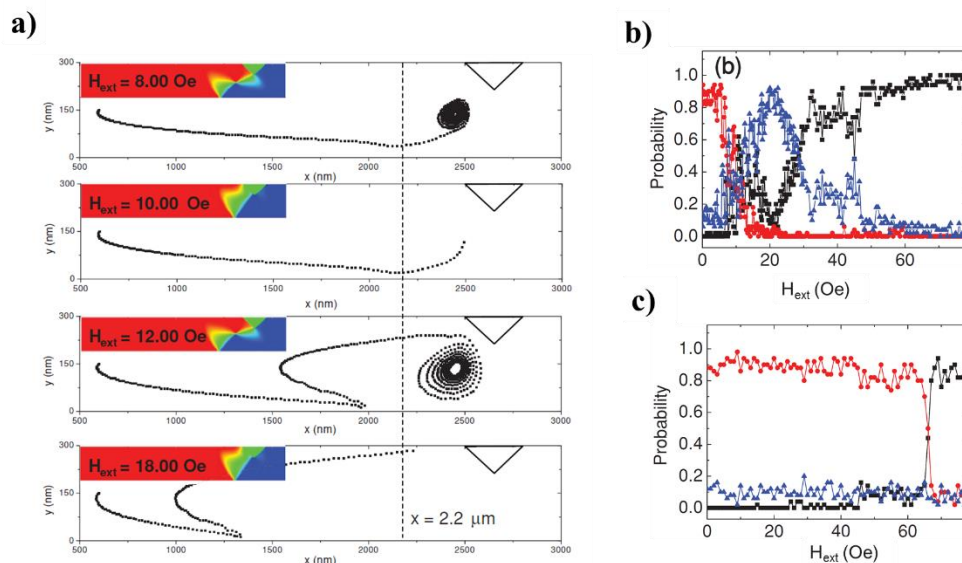

Figure 3.14: (a): Schematic showing trajectory of DW core reaching notch at different locations. Inset shows the DW structure when pinning at the notch after undergoing WB transformations. (b): Probability plot for dynamic depinning. (c): Probability plot for static depinning. Black: DW passing. Red: VDW pinned. Blue: TDW pinned [23].

Each DW is expected to encounter a different pinning potential and hence would have a different H_d [20]. In Pi *et al* measurements, some DWs passed the defect without pinning indicating that there may have been more than the two pinning modes revealed in the simulation (Figure 3.14(b)-red). Moreover, the authors compared pinning in the static and dynamic regimes. In the static case, the DW was propagated to the defect below H_{WB} and was allowed to relax before its depinning probability was studied at different external fields. In the dynamic case, the DW was propagated above H_{WB}.

The results of the static depinning case, where DW propagated below H_{WB}, showed a more deterministic behaviour (Figure 3.14(c)). The vast majority of DW propagation incidents resulted in a VDW being pinned at the notch, up until $H_{ext}= 65$ Oe; at which the vast majority of incidents passed without pinning. However in the dynamic case, where DW propagated above H_{WB} (estimated at 6 Oe), (Figure 3.13 (b)), multiple pinning modes were seen at $H_{ext}>6$Oe indicating stochastic pinning behaviour [23].

In a similar experiment conducted by Akerman *et al* [71], nucleated DWs were propagated to a defect site both below H_{WB}, and above H_{WB}. Results indicated that below H_{WB} two types of DW pinned at the notch (CW or ACW VDWs) reflecting only poorly defined initial chiralities of the DWs, however, when propagating above H_{WB}, four types of DW structure pinned at the notch. These four types were interpreted to be upward TDW, downward TDW, CW VDW and ACW VDW, and were formed due to dynamic WB transformations.

In another attempt to investigate DW switching stochasticity, Im *et al* [87, 88] investigated the role of nanowire and notch geometries in affecting depinning stochasticity by imaging nanowire pinning/depinning using X-ray microscopy. It was deduced that small notches in nanowires with large widths (w $\geq$ 500 nm) and thickness (t= 50 nm) produced the least stochastic switching behaviours. This has been generally suggested to be attributed to the few

DW structures that occur at the vicinity of the notch in these geometries. However, further studies were needed to verify that.

3.4.2. Thermal stochasticity

Another critical factor that induces DW depinning stochasticity is thermal activation/perturbations that assists DW depinning process [67, 68, 70]. Equally critical is the fact that thermal perturbations can also affect DW motion when propagating above H_{WB} creating another layer of complexity to the DW pinning/depinning stochasticity [21].

The switching behaviour of superparamagnetic materials by thermal fluctuations was hypothesised by Néel to follow some form of Brownian motion [89]. This has later been experimentally verified for single-domain ferromagnetic nanostructures with single energy barrier [22].

For instance, Wernsdorfer *et al* [22] have shown that switching behaviour of high quality Co nanowires followed a probabilistic distribution in the presence of thermal energy (T>0 K). This occurred when an external field **H** close to the nanowire's switching field at T = 0 K (donated as H_{SW}^0) was applied. The probability of switching after time t was deduced to be given as:

$$P(t) = 1 - e^{\frac{-t}{\tau}} \qquad \text{(eq. 3.14)}$$

where τ is the characteristic switching time of a thermally activated event, expressed in the Arrhenius form as:

$$\tau = \tau_0 \, e^{\frac{E_b(H)}{k_B T}} \qquad \text{(eq. 3.15)}$$

where τ_0 is the characteristic mean switching time, k_B is Boltzmann constant, T is temperature and E(H) is the energy barrier against switching that can be approximated as:

$$E(H) = E_0 \left(1 - \frac{H}{H_{SW}^0}\right)^\alpha \qquad \text{(eq. 3.16)}$$

where H is the external applied field, H_{SW}^0 is switching field at T=0 K, E_0 is the extrapolation of energy barrier at zero field and α is equal to 1.5 [90].

In order to verify that nanostructures follow the above equations, Wernsdorfer *et* al performed an experiment [22] where they fixed the temperature at T value and applied a sweeping field between 0.001 to 100 mT at a specific rate of **v**. The field at which the Co nanowire switched and the time taken for switching were recorded. The experiment was performed at different temperature values between 0.1 to 6 K. Each time measurements were repeated 100-2000 times in order to construct a histogram.

Results have indicated a Gaussian distribution of switching fields at each temperature value. The width of the distribution increased with increasing temperature. Moreover, the average switching field showed an increasing trend with reduced T (refer to Figure 3.15(a)). Both observations were expected, as reducing T will reduce thermal energy that assists in surpassing the switching energy barrier; hence, the field needed to switch the system increased, and thermal stochasticity was reduced [22] (Figure 3.15(a)).

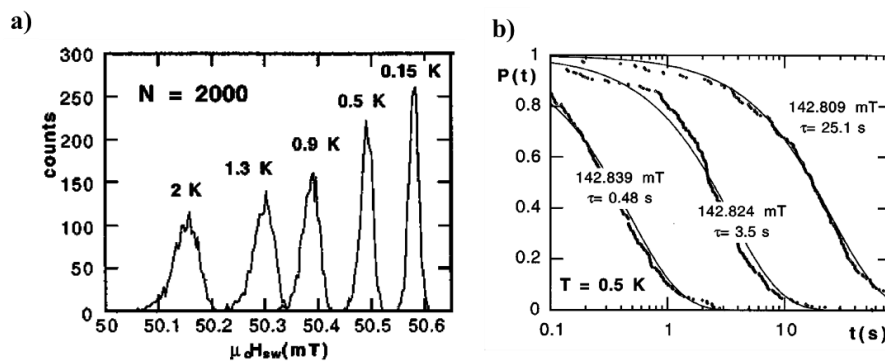Moreover, in many of the cases, the values of switching field followed the Kurkijarvi model [91]:

Figure 3.15: (a): Plot showing the Gaussian distribution of switching field at different temperatures. (b): Plot showing the probability of not switching as function of time at different fields at T=0.5K. Both results are for 20 nm Co particle [22].

$$H_{sw} \approx H_{SW}^0 \left[1 - \sqrt[\alpha]{\frac{k_B T}{E_0} \ln(\frac{CT}{v \varepsilon^{\alpha-1}})} \right] \qquad \text{(eq. 3.17)}$$

where H_{sw} is the switching field and is equal to H_c, H_{SW}^0 is the switching field at T=0 K,

$C = \frac{k_B H_0}{\alpha \tau_0 E_0}$ and v is the field sweep rate.

An interesting observation was seen in the relationship between the field sweep rate **v** and H_{SW}, and was indicated in eq. 3.17. Results indicated an increase in H_{SW} with increasing **v**. Such unintuitive result can be explained by analogy to the time-dependence of the magnetisation changes in the remnant magnetisation observed in permanent magnets [92]. When a constant external magnetic field is applied in opposition to the magnetisation of a ferromagnetic material for a long time, time-dependant fractional loss of the magnetisation starts to occur. This is due to thermally activated magnetisation reversal attempts. This phenomenon is known as *magnetic viscosity* or *magnetic after effect*, and results in an exponential decay of the magnetisation with time [66]. Similarly, increasing the sweep rate will create a lagging response in the thermally assisted magnetic reversal attempts resulting in an increase in H_{SW}.

In addition to assisting in switching, thermal energy can also play a role in changing the spin configuration of DWs, and in some cases affecting the magnetisation configuration of domains, producing further stochasticity. For instance, it was observed by Laufenberg *et* al [19] that relaxed TDWs in Py nanowire rings can transform into VDWs when T is increased above a critical value (refer to Figure 3.16(a)). This has been explained by the fact that an energy barrier exists between TDW, that are favoured in thin nanostructures, and VDW that are favoured in thicker structures according to the normal phase diagram (refer to Figure 3.5(b)). However, metastable TDWs are often formed as rings are relaxed from saturation even when they are not in the ground state DW, and thermal perturbation can assist in surmounting this energy barrier
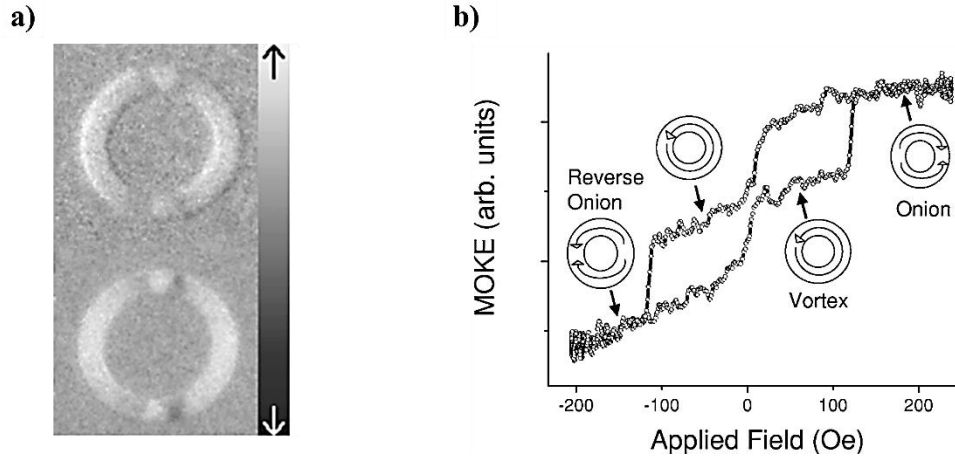
Figure 3.16: (a): XMCD-PEEM images of Py nanowires of w=730 nm and t=7 nm showing TDWs at T=260ºC (top) transformed to VDW at T=310ºC before retaining its type at T=20ºC [19]. (b): Hysteresis loop and schematic diagram of Py rings of diameter 5 μm and t=45 nm showing magnetisation transformation between 'onion' and 'vortex' configurations due to thermal perturbation [29].

in a stochastic manner. Such thermally assisted transformation creates an additional stochastic element that would affect magnetic switching behaviour of the rings.

In a slightly similar experimental observations, Hayward *et al* [29] and Moore *et al* [93] have reported changes in the magnetisation states of Py rings between 'vortex state' and 'onion' shape magnetisation due to thermal fluctuations (refer to Figure 3.16(b)).

In addition to changes in magnetisation states, thermal perturbations can also play a major role in influencing the dynamics of DW movement. It was recently reported by Hayward [21] (in his simulation studies) that while thermal effects can only alter DW motion slightly in the viscous regime, it can have much more dramatic effects on behaviour of domain walls propagating at fields above WB (refer to Figure 3.17).

For instance, in the oscillatory regime, it was observed that the nature of WB cycle stays the same at finite temperature, however, the timing of the transformation between DW configurations was either delayed or occurred earlier [21] (indicated by two curves run at different T 'seed value' in Figure 3.17(b)). This was then shown to produce significant stochasticity in the depinning of DWs from a pinning site due to sensitivity of DW profile/notch
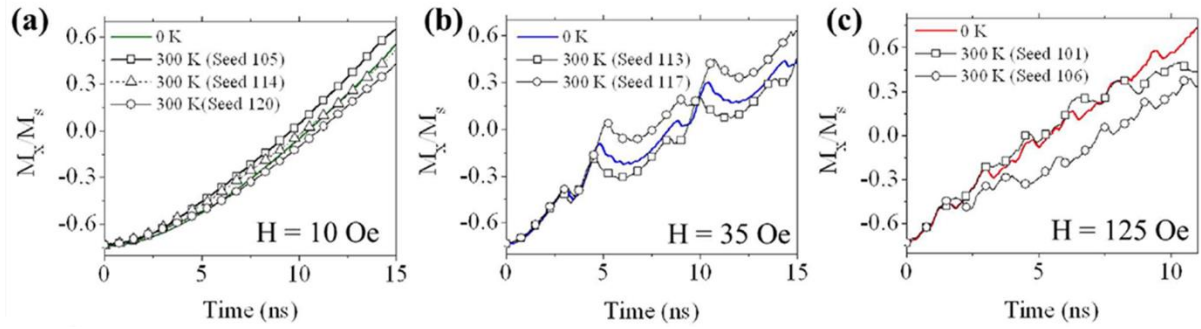
Figure 3.17: Simulated propagation behaviour of DW in Py nanowire at T=0 and T=300 K (seed 101 (open square)) and (seed 106 (open circle) when propagating at the viscous regime (a), oscillatory regime (b) and turbulent regime (c) [21].

interaction [94]. Even more significant effects were noted in the turbulent regime. Here, thermal perturbation caused not only changes in the timing of the DW transformations, but also randomised the position at which new vortex/anti-vortex cores nucleated, introducing a new and substantial stochastic element to the DW dynamics (Figure 3.17(c)).

The complexity of DW dynamics thus combines with thermal perturbations to create a strong stochastic element in DW propagation [21, 70]. These effects seem to be an intrinsic feature of DW propagation at finite temperatures and may not be possible to completely suppress them[21].

3.5. DW-based nanomagnetic applications

The novel behaviours and controllability of DWs and magnetisation states gained at the nanoscale have opened the door for a range of applications. Ferromagnetic nanowires can have bi-stable (non-volatile) magnetisation states, in which switching between them can be achieved relatively easily. Moreover, these bi-stable magnetisation states can be exploited to represent binary information by creating DWs that separate them into small domains to create trains of data along the nanowire (as will be explained in sec 3.6 below).

Nucleated DWs can be propagated in forward and backward directions at high speeds of 100s m/s [59], and their movement can be controlled using engineered pining sites. Furthermore,

DWs have two spin structures (chiralities) that can provide an additional degree of freedom for encoding data. All these features can potentially be utilized to build fast (running at clock speed greater than 100 MHz [95]) and low power consumption (less than 10^{-2} pJ per logical operation [7]) devices in areas such as magnetic recording, information processing, magnetic sensing and biotechnological applications.

3.5.1. Logic gates

DW Logic gates

Several DW logic schemes have been proposed in the last decade [7, 65, 96-98]. One major scheme proposed and implemented by Allwood *et al* [7] uses the direction of magnetisation of domains in Py nanowires of width 200 nm to represent bits of '1s' and '0s'. The AND, NOT, FAN-OUT, and Cross-over gates (Figure 3.18(a)) were successfully implemented and demonstrated as proof of concepts.

In this scheme, binary '1' is represented by domain magnetisation that points in the same direction as the direction of DW propagation, while binary '0' is represented by the opposite magnetisation direction. The propagation of DWs, and thus data trains, around the logic circuits
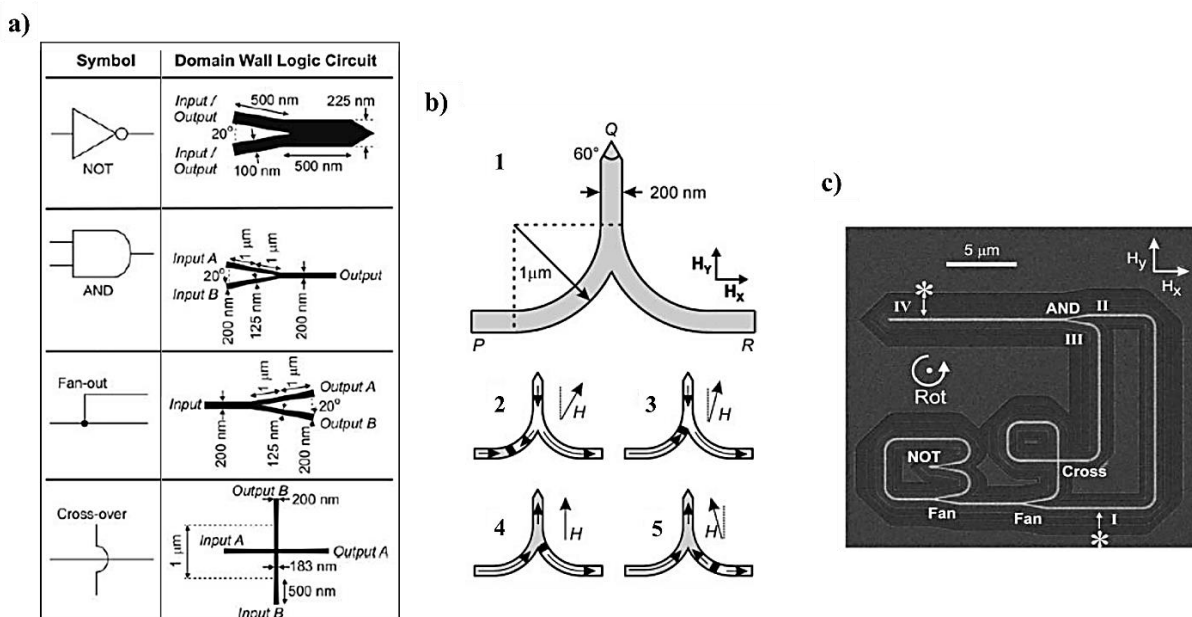

Figure 3.18: (a): Schematic design of DW logic gates next to their symbols [7]. (b): Schematic showing NOT gate functionality [27]. (c): FIB image showing tested logic gates interconnected together [7].

were driven by an external rotating magnetic field that acted as both a power supply and a system clock.

For instance, the NOT gate (inverter) was composed of a cusp-shaped nanowire with two interchangeable channels; where one channel acts as the input and other as the output. The NOT gate will always contain one DW during its operation. In order to demonstrate its operation, it was first assumed that the rotating magnetic field (clock) rotates in an anti-clockwise direction. The inversion process ran as follows: when a DW entered the input channel P (Figure 3.18(b)), the external field started with Hx= +ve and Hy= +ve (refer to Figure 3.18(b)-2). The magnetisation at the input channel was thus pointing in the same direction as the DW propagation direction. The external field continued to rotate causing the switching of terminal Q, as shown in Figure 3.18(b)3&4). When the clock reached half the cycle, the DW propagated to the output channel R switching its magnetisation to the direction anti-parallel to the direction of DW propagation, which is also the inversion of the input magnetisation (Figure 3.18(b)-5). The output was therefore an inversion of the input, and the DW can continue its propagation across the other gates [27].

In the AND gate, the process was more straight forward (Figure 3.18(a)). It had been previously demonstrated that in a Y-interconnected network of nanowires, similar to the AND gate, switching of the junction and the output channel could occur at low field if both input channels have switched and two DWs were pinned at the junction (Figure 3.19(c)). However, if only one DW arrived to the junction (only one channel switched), it would require high field to switch the junction (20% higher in the experiment done in [18]).
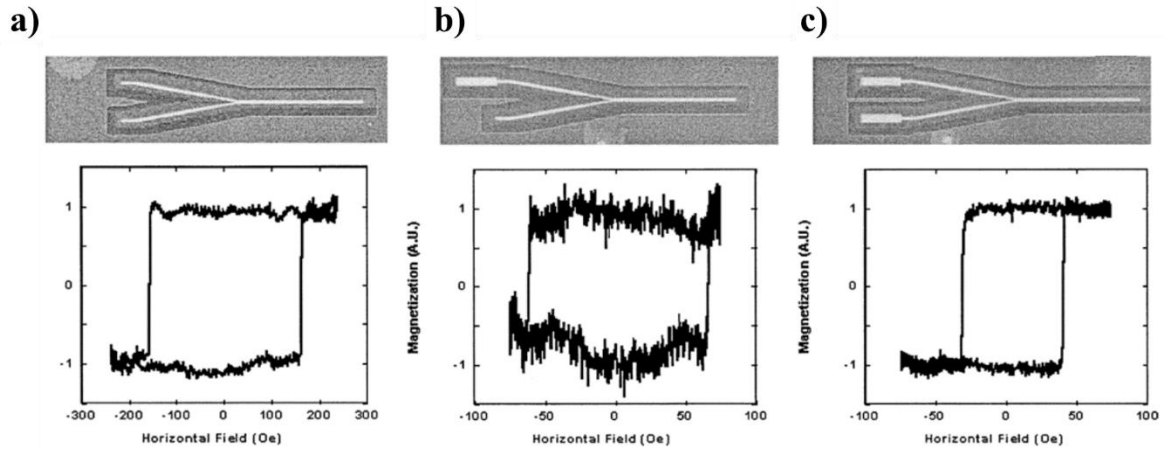
Figure 3.19: FIB images of AND gate along with hysteresis loop indicating switching of output terminal at highest field when no DWs at input (a), at lowered field when one DW is at input (b) or at minimum filed when two DWs at the two inputs (c) [18].

Thus for a certain range of applied field, the junction would only switch if both input channels had switched and two DWs were at the junction. Such behaviour resembled the operation of an AND gate where both inputs are required to be '1' for the output to be '1' [18].

The FAN_OUT functioned in a very straight forward manner (Figure 3.18(a)). As the input channel was switched, a DW propagated across the junction and expanded into the two output channels producing (cloning) two DWs, one in each output channel and switching them both [5].

As for the Cross-Over, it was shown that DWs could propagate across the 4-terminal cross (Figure 3.18(a)) along the direction of the applied external field. The DWs first expanded at the junction, but eventually propagated horizontally parallel to the applied field.

Allwood *et. al.* showed that all of these logic gates could be cascaded together as shown in Figure 3.18(c) [7].

TDW Chirality Logic Gates

In another recent DW logic concept modelled by Vandermeulen *et al* [16], the chiralities of TDWs were utilized in order to represent binary '1' and '0'. The gates worked by manipulating

the dynamics and velocity of the DWs. These were controlled by locally modifying the damping coefficient in certain sections of the nanowires, which the authors suggested could be achieved by increasing/reducing the doping concentration of rare-earth metals [99]. In the simulations, TDWs were moved using a spin-polarized current of current density (J), where J was below WB current density (J_{WB}) at α = 0.02.

In order to achieve a NOT gate, the damping coefficient α of a straight segment of nanowire was lowered to 0.01. Due to lowering the value of α, the current density J was above the new J_{WB} limit of the modified segment j_{WB}^{NOT} and TDWs underwent WB transformations causing the TDW to flip its chirality. The length of the segment was chosen such that the TDW would undergo only one chirality flipping cycle, resulting in reliable inversion of its chirality. Figure 3.20(a) shows the simulation of the process.

For AND/OR gates, a similar Y-interconnected network to that used by Allwood *et al'*s AND logic gate was used. The simulations showed that the output DW chirality depends on : 1. whether the two inputs are the same or different, 2. the arrival sequence of the TDWs. For instance, when two *opposite* TDW chiralities were propagated into the Y-shaped network (i.e: (upward, downward), the chirality of the output TDW will only depended on the arrival sequence of the two input DWs, such that if a DW arrived to the junction first from top channel, a TDW of downward chirality was produced at the output. However, if the DW arrived first from bottom channel, a TDW of upward chirality was produced at the output. This condition applies only to TDWs of opposite chiralities. However when the two TDWs are of the same chirality, then the arrival sequence is irrelevant and the output TDW will be of the same chirality of the two input TDW.
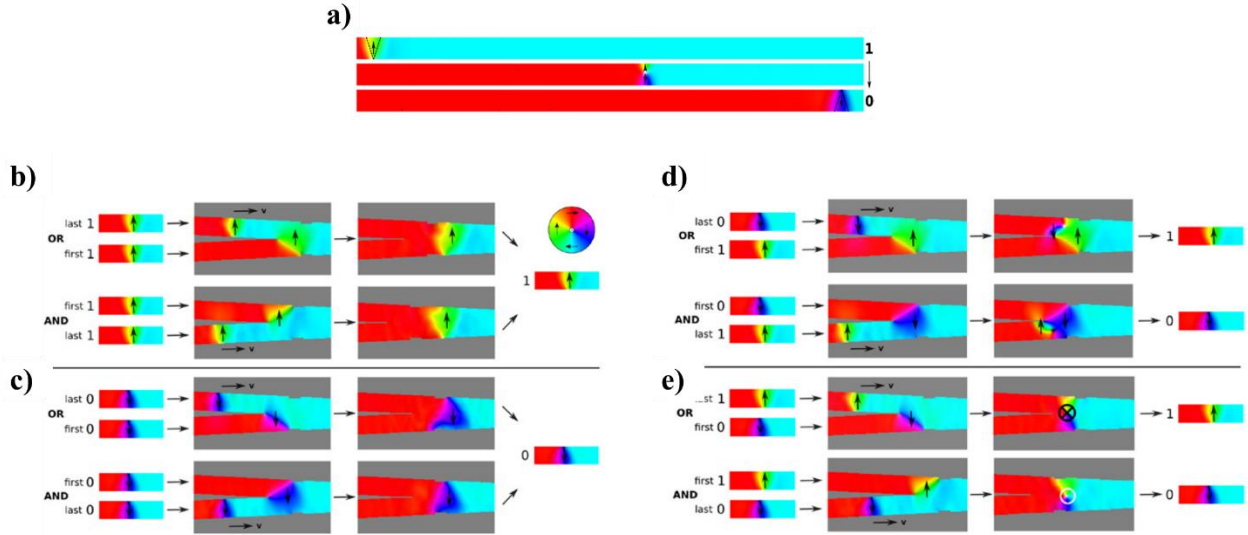
Figure 3.20: TDW logic gate. (a): NOT gate based on WB transformations. (b-e): AND/OR gate designed based on DW arrival sequence. In AND gate, TDW should always arrive from top channel. In OR gate TDW should always arrive from bottom channel [16].

The truth table in Figure 3.20 showed that for the AND gate to function in this scheme, the DW at the top input channel should always arrive first. On the other hand, for the OR gate to function, the DW at the bottom input channel should always arrive first (refer to Figure 3.20(b-d)).

In order to achieve this desired arrival sequence, the velocity of DWs in the bottom (top) input needed to be reduced to obtain an AND (OR) gate. This was done by increasing the damping of the bottom (top) input channels to $\alpha=0.03$ resulting in a reduction in the velocity of DWs in that channel, and achieving the functionality of the AND and OR gates [16].

Despite the number of challenges facing the TDW logic gate, the above proposed scheme can be miniaturized while maintaining a TDW structure. Moreover, since DWs are moved using spin-polarized current, the scheme can be integrated with race-track memory devices, which will be described below. An earlier publication [65] (that is the topic of chapter 9) has discussed a similar full chirality-based logic architecture that works for vortex DWs.

3.5.2. Race-Track memory

The concept of Race-track Memory (RM) proposed by Parkin *et al* [26] stems from the idea of using small domains separated by DWs as bits in long ferromagnetic nanowires. These domains will have one of the two bi-stable magnetisation states, and can be written by nucleating DWs using current pulses of opposite polarities as illustrated in Figure 3.21(b). RM can be envisaged to use 3D nanowire networks (Figure 3.21(a)), however, 2D devices (such as the devices studied in this thesis) are likely to be easier to create in the short-term.

In RM, the formed domains can move in forward and backward direction along the nanowire in order for the reading sensor (usually a magnetic tunnelling junction (MTJ) (refer to Appendix 1) for explanation)) to access each domain individually (Figure 3.21(c)). This can be done using the spin-transfer-torque method; in which DWs are moved in the same direction as the direction of the current. Using an external field would result in annihilating the DWs, as domains with the parallel magnetisation direction to the external field will expand causing neighbouring DWs to propagate in opposite directions and annihilate each other.

In order to control the spacing and movement of DWs as well as increase their stability against thermal fluctuations, pinning sites are introduced to stabilise DWs. These pinning sites can be in the form of notches or through modulating the material parameter at fixed spaces. In the case of using notches, the problem of stochastic pinning/depinning behaviour of DWs can arise (as
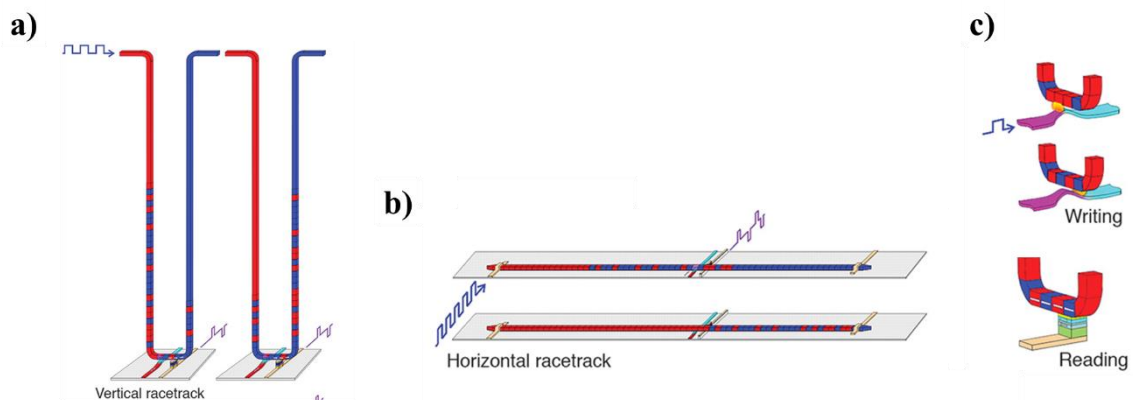

Figure 3.21: (a): Schematic of Race-track memory with vertical (3D structure) (b): Race-track memory with horizontal architecture (2D structure). (c): Schematic of writing and reading head [26].

discussed in section 3.4) which requires methods to circumvent it (one of the aims of this thesis is to tackle this problem).

The current density needed to move DWs/domains between engineered pinning sites is in the range of 10^8 A/cm^2, and this would result in DW velocities of around 100m/s. However, high current densities such as this could cause Joule heating that would result in undesired magnetic reversal and DW depinning events. In order to tackle this challenge, current pulses instead of continuous current can be used to drive DWs and surpass the pinning potential [26]. It was reported by Thomas *et al* [100] that using short length pulses (with frequency matching the internal precession frequency of the pinned DWs) can result in resonant amplification of DW dynamics, resulting in a reduction in the current density needed to depin DWs [26].

In RM devices made up from Py nanowires, DWs can be very flexible and unstable. This has led scientists to develop and evolve the materials used for RM nanowires in three further stages (refer to Figure 3.22).

The second stage of RM (Race-track memory 2.0) involved the use of materials with perpendicular anisotropy, such as Co/Ni super-lattices instead of Py. In Co/Ni the DWs will have a more robust structure than in Py material due to the perpendicular magnetic anisotropy. Later it was discovered that DWs in ultrathin layer of Co nanowires deposited on Pt can propagate faster even faster than those in RM 2.0. This was attributed to a complicated spin-
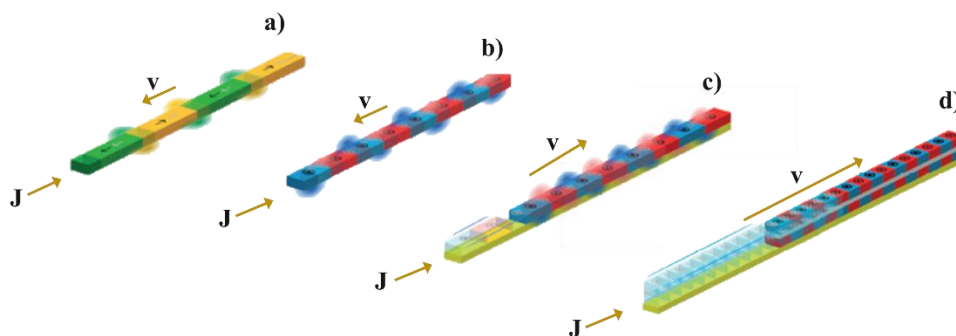

Figure 3.22: Evolution of Race-track memory. (a): Race-track 1.0 with in-plane magnetisation, (b): Race-track 2.0 that uses materials with PMA (c): Race-track 3.0 with giant exchange coupling effect, (d):Race-track 4.0 with synthesized antiferromagnetic coupling [11].

orbit coupling-based effect known as the 'chiral spin-torque' mechanism. This mechanism is based on the interplay of four different magnetic features: Perpendicular magnetic anisotropy, Dzyaloshinsky– oriya interaction (DMI), exchange coupling, proximity-induced magnetisation, and the Hall spin effect. This was labelled as Race-track memory 3.0.

In the latest and most promising stage, Race-track memory 4.0, ferromagnetic materials coupled antiferromagnetically through an ultrathin ruthenium layer are used. This material is known as synthetic antiferromagnetic material. In this material, DWs are driven at very high velocities that can reach up to 1000 m/s due to the presence of giant exchange coupling torque. Moreover, in this material the demagnetising field of DWs is minimized due to the nature of the exchange coupling; resulting in the ability to pack DWs closer together and raise data densities. These features are expected to make Race-track memory 4.0 a very promising technology that can compete in areal density, speed, power and cost with current RAM technology as well as magnetic hard disks [11].

3.5.3. Ratchet memory

The ratchet memory proposed by Franken *et al* [9] is a very similar concept to the RM described above, however in a ratchet memory, DWs can be moved using an external magnetic field (unlike RM where spin-transfer-torque method is used).

The concept of the ratchet memory works by engineering the energy landscapes of specific lengths of a nanowire with varying levels of PMA in order to control the direction of flow of DWs, in a ratchet-like movement manner. A similar effect could be obtained in soft Py nanowires by employing the concept of DW diodes [12, 80] explained in Figure 3.13.

Modifying energy landscapes can be done by tuning the PMA of materials such as Co in a Pt/Co/Pt structure by modulating the ion irradiation during the focussed ion beam (FIB) fabrication process [101]. The aim is to tune the energy landscapes in a manner similar to the

one shown in Figure 3.23; in which, the two consecutive domains of the same magnetisation are separated by at least two energy potential steps.

When such energy landscape is achieved, DWs motion in nanowire loops can be done by applying an oscillating magnetic field pulses of opposite polarity and controlled pulse duration (Figure 3.23(c)).

The ratchet-like movement process of DWs can be demonstrated as follows: when a first pulse is applied in the (+ve) direction, the left and right domains will expand causing the two DWs to start moving towards each other. However, their movement will stop when the left DW reaches an energy step (high PMA); whereas the right DW will stop after stepping one downward step (one ratchet period) (Figure 3.23(b)). The latter can be achieved by accurately tuning the time of the current pulse. After this, a (–ve) pulse is applied. This will cause the intermediate domain with downward magnetisation to expand pushing the DWs away from each other. In this case, the right DW will move until encountering a potential step, and the left DW will move until it passes one downward step (one ratchet period) (Figure 3.23(b)-bottom). The overall motion is a movement of the two DWs to the left in a manner exploiting magnetic behaviour which is analogous to the movement of a ratchet [9].

Ratchet memory (and similar concepts of DW diode described previously for Py nanowires) provides a solution to propagating trains of domains/DWs using magnetic fields. This has the
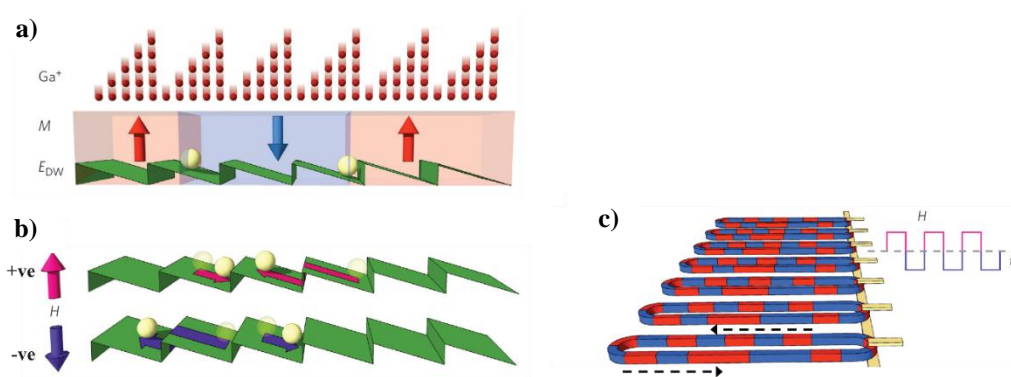

Figure 3.23: (a-b): Schematic depicting the tuned energy landscape by tuning the PMA level through irradiation. (c): Schematic of the ratchet memory architecture [9].

advantage of providing an alternative method to the spin-transfer-torque approach used in the RM technology, which may lead to a reduction in power consumption and higher durability. This is because electric currents can create undesirable joule heating as well as limited device life due to the self-diffusion of atoms [9], via a phenomenon known as 'electromigration' [102].

3.5.4. Bionanomagnetic applications: biological nanomagnetic beads

Magnetic nanoparticles can be fabricated with sizes that are comparable to biological building blocks such as cells (10-100 μm), proteins (5-50 nm), genes (2 nm wide by 10-100 nm long) as well as viruses (20-450 nm). In combination to their ability to be remotely controlled by magnetic fields this has made magnetic nanoparticles to be major candidates for many *in vivo* and *in vitro* biological applications. Their small dimensionality and biocompatibility allows them to access and migrate into normally inaccessible places inside the human body without disrupting its functionality. Moreover, the fact that cells can dramatically react to changes occurring on their own surfaces (which can induce their death or stimulate their growth) provides a new level of control over cells attached to magnetic nanoparticles [2].

Many bio-nanomagnetic applications are based on the idea of introducing single domain magnetic beads engulfed inside biocompatible material into the blood stream. The aim of this is to target specific cells or biomolecules such as DNA and RNA. Once these beads are attached to the targeted object, different functions can be achieved.

For instance, targeted cells/biomolecules can be labelled and then detected *in vitro* by detecting their stray field, for diagnostic purposes [2]. Other labelled cells/biomolecules can be separated and filtered from blood stream using magnetic tweezers or external magnetic field [6, 103].

Methods have been proposed to transport nanomagnetic beads on ferromagnetic nanowires [15, 33]. This has been mainly achieved by magnetically pinning the bead to a DW via its stray
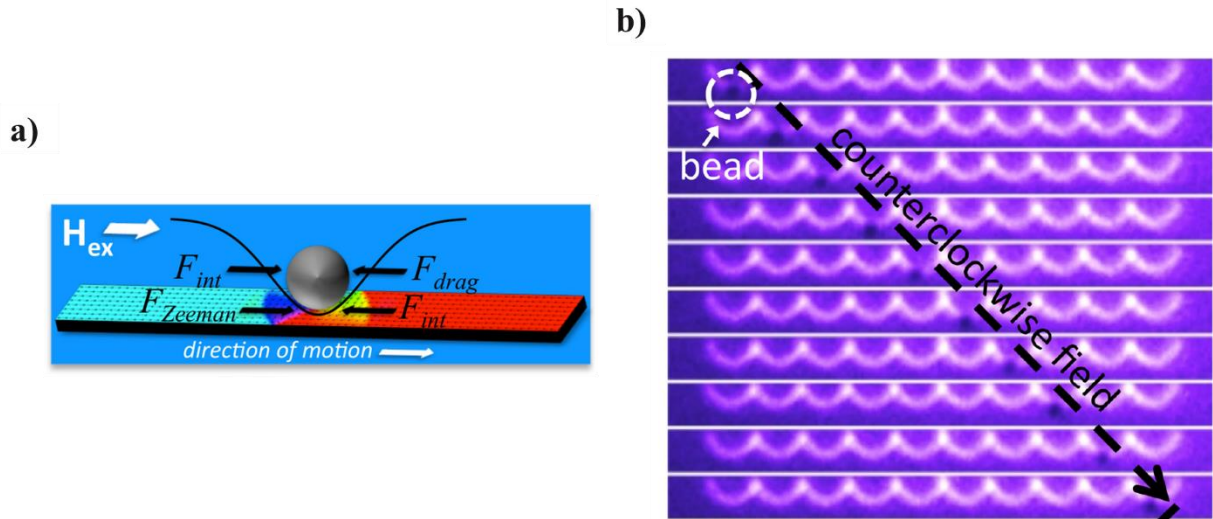
Figure 3.24: (a): Schematic showing the micromagnetic bead fixed on a VDW to be transported as VDW propagates. (b): Experimental results showing superparamagnetic beads pinned on VDWs on a track of Py nanowire being transported using rotating magnetic field [15].

field. Subsequently, the bead can be moved when the DW is moved by the effect of an external field or spin-polarized current (Figure 3.24).

These forms of controlled transportation can be utilized to controllably transport magnetic beads in numerous biomedical applications such as cell separating, drug delivery, cell diagnostics and bio-sensing [104].

From the above section it can be seen that many of the DW-based applications work by exploiting DW motion and DW pinning in order for the devices to function as designed. Therefore, further understanding of DW behaviour will indeed contribute towards solving many of the existing challenges. The coming chapters aim on presenting deeper understanding of the DW stochastic behaviour and may provide experimentally verified methods that can help in overcoming some of these challenges.

3.6. References

[1]   R. Kelsall, I. W. Hamley, and M. Geoghegan, *Nanoscale science and technology*: John Wiley & Sons, 2005.

[2]   D. J. Sellmyer and R. Skomski, *Advanced magnetic nanostructures*: Springer Science & Business Media, 2006.

[3]   G. Hrkac, J. Dean, and D. Allwood, "Nanowire spintronics for storage class memories and logic," *Philosophical Transactions of the Royal Society of London A: Mathematical, Physical and Engineering Sciences,* vol. 369, pp. 3214-3228, 2011.

[4]   A. P. Guimarães, *Principles of nanomagnetism*: Springer Science & Business Media, 2009.

[5]   T. Shinjo, *Nanomagnetism and spintronics*: Elsevier, 2009.

[6]   J. M. Coey, *Magnetism and magnetic materials*: Cambridge University Press, 2010.

[7]   D. A. Allwood, G. Xiong, C. Faulkner, D. Atkinson, D. Petit, and R. Cowburn, "Magnetic domain-wall logic," *Science,* vol. 309, pp. 1688-1692, 2005.

[8]   Y. Nakatani, A. Thiaville, and J. Miltat, "Head-to-head domain walls in soft nano-strips: a refined phase diagram," *Journal of magnetism and magnetic materials,* vol. 290, pp. 750-753, 2005.

[9]   J. Franken, H. Swagten, and B. Koopmans, "Shift registers based on magnetic domain wall ratchets with perpendicular anisotropy," *Nature nanotechnology,* vol. 7, pp. 499-503, 2012.

[10]   D. McGrouther, S. McVitie, J. Chapman, and A. Gentils, "Controlled domain wall injection into ferromagnetic nanowires from an optimized pad geometry," *Applied physics letters,* vol. 91, p. 022506, 2007.

[11]   S. Parkin and S.-H. Yang, "Memory on the racetrack," *Nature nanotechnology,* vol. 10, pp. 195-198, 2015.

[12]   A. Himeno, S. Kasai, and T. Ono, "Depinning fields of a magnetic domain wall from asymmetric notches," *Journal of applied physics,* vol. 99, p. 08G304, 2006.

[13]   S.-M. Seo, K.-J. Lee, W. Kim, and T.-D. Lee, "Effect of shape anisotropy on threshold current density for current-induced domain wall motion," *Applied physics letters,* vol. 90, p. 252508, 2007.

[14]   K. Sentker, F.-U. Stein, L. Bocklage, T. Matsuyama, M.-Y. Im, P. Fischer*, et al.*, "Fast generation of domain walls with defined chirality in nanowires," *Applied Physics Letters,* vol. 104, p. 172404, 2014.

[15]   E. Rapoport and G. S. Beach, "Dynamics of superparamagnetic microbead transport along magnetic nanotracks by magnetic domain walls," *Applied Physics Letters,* vol. 100, p. 082401, 2012.

[16]   J. Vandermeulen, B. Van de Wiele, L. Dupré, and B. Van Waeyenberge, "Logic and memory concepts for all-magnetic computing based on transverse domain walls," *Journal of Physics D: Applied Physics,* vol. 48, p. 275003, 2015.

[17]   G. Beach, M. Tsoi, and J. Erskine, "Current-induced domain wall motion," *Journal of magnetism and magnetic materials,* vol. 320, pp. 1272-1281, 2008.

[18]   C. C. Faulkner, D. Allwood, M. D. Cooke, G. Xiong, D. Atkinson, and R. P. Cowburn, "Controlled switching of ferromagnetic wire junctions by domain wall injection," *Magnetics, IEEE Transactions on,* vol. 39, pp. 2860-2862, 2003.

[19]   M. Laufenberg, D. Backes, W. Bührer, D. Bedau, M. Kläui, U. Rüdiger*, et al.*, "Observation of thermally activated domain wall transformations," *Applied physics letters,* vol. 88, p. 052507, 2006.

[20] M. Hayashi, L. Thomas, C. Rettner, R. Moriya, X. Jiang, and S. S. Parkin, "Dependence of current and field driven depinning of domain walls on their structure and chirality in permalloy nanowires," *Physical review letters,* vol. 97, p. 207205, 2006.

[21] T. J. Hayward, "Intrinsic Nature of Stochastic Domain Wall Pinning Phenomena in Magnetic Nanowire Devices," *Scientific Reports,* vol. 5, p. 13279, 08/25/online 2015.

[22] W. Wernsdorfer, E. B. Orozco, B. Barbara, K. Hasselbach, A. Benoit, D. Mailly*, et al.*, "Mesoscopic effects in magnetism: Submicron to nanometer size single particle measurements," *Journal of applied physics,* vol. 81, pp. 5543-5545, 1997.

[23] U.-H. Pi, Y.-J. Cho, J.-Y. Bae, S.-C. Lee, S. Seo, W. Kim*, et al.*, "Static and dynamic depinning processes of a magnetic domain wall from a pinning potential," *Physical Review B,* vol. 84, p. 024426, 2011.

[24] F.-U. Stein, L. Bocklage, M. Weigand, and G. Meier, "Time-resolved imaging of nonlinear magnetic domain-wall dynamics in ferromagnetic nanowires," *Scientific Reports,* vol. 3, p. 1737, 04/26/online 2013.

[25] M. T. Bryan, T. Schrefl, and D. Allwood, "Dependence of transverse domain wall dynamics on permalloy nanowire dimensions," *Magnetics, IEEE Transactions on,* vol. 46, pp. 1135-1138, 2010.

[26] S. S. Parkin, M. Hayashi, and L. Thomas, "Magnetic domain-wall racetrack memory," *Science,* vol. 320, pp. 190-194, 2008.

[27] D. Allwood, G. Xiong, M. Cooke, C. Faulkner, D. Atkinson, N. Vernier*, et al.*, "Submicrometer ferromagnetic NOT gate and shift register," *Science,* vol. 296, pp. 2003-2006, 2002.

[28] M. T. Bryan, T. Schrefl, D. Atkinson, and D. A. Allwood, "Magnetic domain wall propagation in nanowires under transverse magnetic fields," *Journal of Applied Physics,* vol. 103, p. 073906, 2008.

[29] T. J. Hayward, T. A. Moore, D. H. Y. Tse, J. A. C. Bland, F. J. Castaño, and C. A. Ross, "Exquisitely balanced thermal sensitivity of the stochastic switching process in macroscopic ferromagnetic ring elements," *Physical Review B,* vol. 72, p. 184430, 11/28/ 2005.

[30] A. Pushp, T. Phung, C. Rettner, B. P. Hughes, S.-H. Yang, L. Thomas*, et al.*, "Domain wall trajectory determined by its fractional topological edge defects," *Nat Phys,* vol. 9, pp. 505-511, 08//print 2013.

[31] D. Fayol, G. Frasca, C. Le Visage, F. Gazeau, N. Luciani, and C. Wilhelm, "Use of magnetic forces to promote stem cell aggregation during differentiation, and cartilage tissue modeling," *Advanced Materials,* vol. 25, pp. 2611-2616, 2013.

[32] J. Rife, M. Miller, P. Sheehan, C. Tamanaha, M. Tondra, and L. Whitman, "Design and performance of GMR sensors for the detection of magnetic microbeads in biosensors," *Sensors and Actuators A: Physical,* vol. 107, pp. 209-218, 2003.

[33] M. T. Bryan, J. Dean, T. Schrefl, F. E. Thompson, J. Haycock, and D. A. Allwood, "The effect of trapping superparamagnetic beads on domain wall motion," *Applied physics letters,* vol. 96, p. 192503, 2010.

[34] F. Nasirpouri and A. Nogaret, *Nanomagnetism and spintronics: fabrication, materials, characterization and applications*: World Scientific, 2011.

[35] C. Dennis, R. Borges, L. Buda, U. Ebels, J. Gregg, M. Hehn*, et al.*, "The defining length scales of mesomagnetism: a review," *Journal of Physics: Condensed Matter,* vol. 14, p. R1175, 2002.

[36] G. S. Abo, Y.-K. Hong, J. Park, J. Lee, W. Lee, and B.-C. Choi, "Definition of magnetic exchange length," *Magnetics, IEEE Transactions on,* vol. 49, pp. 4937-4939, 2013.

[37] R. C. O'handley, *Modern magnetic materials: principles and applications* vol. 830622677: Wiley New York, 2000.

[38]   N. A. Spaldin, *Magnetic materials: fundamentals and applications*: Cambridge University Press, 2010.

[39]   K. Ramstöck, W. Hartung, and A. Hubert, "The phase diagram of domain walls in narrow magnetic strips," *physica status solidi (a),* vol. 155, pp. 505-518, 1996.

[40]   R. D. McMichael and M. J. Donahue, "Head to head domain wall structures in thin magnetic strips," *Ieee Transactions on Magnetics,* vol. 33, pp. 4167-4169, Sep 1997.

[41]   I. Hashim, "Microstructural and Magnetic Properties of Polycrystalline and Epitaxial Permalloy (Ni80Fe20) Multilayered Thin Films," PhD Doctor of Philosophy, California Institute of Technology, 1994.

[42]   S. W. Yuan, H. N. Bertram, J. F. Smyth, and S. Schultz, "Size effects of switching fields of thin permalloy particles," *Magnetics, IEEE Transactions on,* vol. 28, pp. 3171-3173, 1992.

[43]   T. Hayward, M. Bryan, P. Fry, P. Fundi, M. Gibbs, D. Allwood*, et al.*, "Direct imaging of domain-wall interactions in Ni 80 Fe 20 planar nanowires," *Physical Review B,* vol. 81, p. 020410, 2010.

[44]   M. Kläui, C. A. Vaz, J. A. C. Bland, L. J. Heyderman, F. Nolting, A. Pavlovska*, et al.*, "Head-to-head domain-wall phase diagram in mesoscopic ring magnets," *Applied physics letters,* vol. 85, pp. 5637-5639, 2004.

[45]   R. P. Cowburn, D. A. Allwood, G. Xiong, and M. D. Cooke, "Domain wall injection and propagation in planar Permalloy nanowires," *Journal of Applied Physics,* vol. 91, pp. 6949-6951, 2002.

[46]   K. Shigeto, T. Shinjo, and T. Ono, "Injection of a magnetic domain wall into a submicron magnetic wire," *Applied Physics Letters,* vol. 75, pp. 2815-2817, 1999.

[47]   M. T. bryan, "Nucleation and propagation of domain walls in Permalloy nanowires," PhD, Department of Engineering Materials, University of Sheffield, 2008.

[48]   D. Eastwood, L. Bogart, and D. Atkinson, "Scaling Behaviour of Chirality Dependent Domain Wall Pinning in Planar Nanowires," *memory,* vol. 3, p. 11, 2010.

[49]   K. Shigeto, K. Miyake, T. Okuno, K. Mibu, T. Ono, Y. Yokoyama*, et al.*, "Temperature dependence of switching field distribution in a NiFe wire with a pad," *Journal of magnetism and magnetic materials,* vol. 240, pp. 301-304, 2002.

[50]   M. T. Bryan, P. W. Fry, T. Schrefl, M. R. Gibbs, D. Allwood, M.-Y. Im*, et al.*, "Transverse field-induced nucleation pad switching modes during domain wall injection," *Magnetics, IEEE Transactions on,* vol. 46, pp. 963-967, 2010.

[51]   J. L. Prieto, M. Muñoz, and E. Martínez, "Structural characterization of magnetic nanostripes by fast domain wall injection," *Physical Review B,* vol. 83, p. 104425, 2011.

[52]   T. Silva, C. Lee, T. Crawford, and C. Rogers, "Inductive measurement of ultrafast magnetization dynamics in thin-film Permalloy," *Journal of Applied Physics,* vol. 85, pp. 7849-7862, 1999.

[53]   L. O'Brien, D. Read, D. Petit, and R. Cowburn, "Dynamic propagation and nucleation in domain wall nanowire devices," *Journal of Physics: Condensed Matter,* vol. 24, p. 024222, 2012.

[54]   L. Bocklage, F.-U. Stein, M. Martens, T. Matsuyama, and G. Meier, "Time structure of fast domain wall creation by localized fields in a magnetic nanowire," *Applied physics letters,* vol. 103, p. 092406, 2013.

[55]   D. Ralph and M. D. Stiles, "Spin transfer torques," *Journal of Magnetism and Magnetic Materials,* vol. 320, pp. 1190-1216, 2008.

[56]   G. Beach, C. Knutson, C. Nistor, M. Tsoi, and J. Erskine, "Nonlinear domain-wall velocity enhancement by spin-polarized electric current," *Physical review letters,* vol. 97, p. 057203, 2006.

[57] X. Wang, P. Yan, J. Lu, and C. He, "Magnetic field driven domain-wall propagation in magnetic nanowires," *Annals of Physics,* vol. 324, pp. 1815-1820, 2009.

[58] Y. Nakatani, A. Thiaville, and J. Miltat, "Faster magnetic walls in rough wires," *Nature materials,* vol. 2, pp. 521-523, 2003.

[59] D. Atkinson, D. A. Allwood, G. Xiong, M. D. Cooke, C. C. Faulkner, and R. P. Cowburn, "Magnetic domain-wall dynamics in a submicrometre ferromagnetic structure," *Nature materials,* vol. 2, pp. 85-87, 2003.

[60] N. L. Schryer and L. R. Walker, "The motion of 180 domain walls in uniform dc magnetic fields," *Journal of Applied Physics,* vol. 45, pp. 5406-5421, 1974.

[61] J.-Y. Lee, K.-S. Lee, S. Choi, K. Y. Guslienko, and S.-K. Kim, "Dynamic transformations of the internal structure of a moving domain wall in magnetic nanostripes," *Physical Review B,* vol. 76, Nov 2007.

[62] K.-C. Hu, H.-Y. Lu, C.-C. Chang, H.-H. Chen, F.-S. Wu, C.-H. Huang*, et al.*, "Adjustment of Demagnetizing Field in Permalloy Nanowires to Control Domain Wall Motion," *Magnetics, IEEE Transactions on,* vol. 50, pp. 1-3, 2014.

[63] G. S. Beach, C. Nistor, C. Knutson, M. Tsoi, and J. L. Erskine, "Dynamics of field-driven domain-wall propagation in ferromagnetic nanowires," *Nature materials,* vol. 4, pp. 741-744, 2005.

[64] M. Munoz and J. L. Prieto, "Suppression of the intrinsic stochastic pinning of domain walls in magnetic nanostripes," *Nature Communications,* vol. 2, Nov 2011.

[65] K. Omari and T. Hayward, "Chirality-based vortex domain-wall logic gates," *Physical Review Applied,* vol. 2, p. 044001, 2014.

[66] R. Skomski, *Simple models of magnetism*: Oxford Univ. Press, 2008.

[67] P. Lendecke, R. Eiselt, G. Meier, and U. Merkt, "Temperature dependence of domain-wall depinning fields in constricted Permalloy nanowires," *Journal of Applied Physics,* vol. 103, p. 3909, 2008.

[68] A. Himeno, T. Okuno, T. Ono, K. Mibu, S. Nasu, and T. Shinjo, "Temperature dependence of depinning fields in submicron magnetic wires with an artificial neck," *Journal of magnetism and magnetic materials,* vol. 286, pp. 167-170, 2005.

[69] A. Mihai, F. Garcia-Sanchez, L. Vila, A. Marty, L. Buda-Prejbeanu, J. Pillet*, et al.*, "Stochastic domain-wall depinning under current in FePt spin valves and single layers," *Physical Review B,* vol. 84, p. 014411, 2011.

[70] C. Wuth, P. Lendecke, and G. Meier, "Temperature-dependent dynamics of stochastic domain-wall depinning in nanowires," *Journal of Physics-Condensed Matter,* vol. 24, Jan 18 2012.

[71] J. Akerman, M. Muñoz, M. Maicas, and J. L. Prieto, "Selective injection of magnetic domain walls in Permalloy nanostripes," *Journal of Applied Physics,* vol. 115, p. 183909, 2014.

[72] H. Cramman, D. S. Eastwood, J. King, and D. Atkinson, "Multilevel 3 bit-per-cell magnetic random access memory concepts and their associated control circuit architectures," *Nanotechnology, IEEE Transactions on,* vol. 11, pp. 63-70, 2012.

[73] P. Bruno, "Geometrically constrained magnetic wall," *Physical Review Letters,* vol. 83, p. 2425, 1999.

[74] D. Petit, A.-V. Jausovec, D. Read, and R. P. Cowburn, "Domain wall pinning and potential landscapes created by constrictions and protrusions in ferromagnetic nanowires," *Journal of Applied Physics,* vol. 103, p. 114307, 2008.

[75] D.-T. Ngo, M. Hickey, D. McGrouther, S. McVitie, C. Marrows, J. Chapman*, et al.*, "Formation of Magnetic Structure by Domain Wall Confinement in Nanoconstriction," *Magnetics, IEEE Transactions on,* vol. 47, pp. 2511-2514, 2011.

[76] C. C. Faulkner, M. D. Cooke, D. A. Allwood, D. Petit, D. Atkinson, and R. P. Cowburn, "Artificial domain wall nanotraps in Ni81Fe19 wires," *Journal of applied physics,* vol. 95, pp. 6717-6719, 2004.

[77] L. Bogart, D. Eastwood, and D. Atkinson, "The effect of geometrical confinement and chirality on domain wall pinning behavior in planar nanowires," *Journal of Applied Physics,* vol. 104, p. 033904, 2008.

[78] L. K. Bogart, D. Atkinson, K. O'Shea, D. McGrouther, and S. McVitie, "Dependence of domain wall pinning potential landscapes on domain wall chirality and pinning site geometry in planar nanowires," *Physical Review B,* vol. 79, Feb 2009.

[79] S.-B. Choe, "Unique depinning fields at symmetric double notches in a ferromagnetic permalloy nanowire," *Journal of Magnetism and Magnetic Materials,* vol. 320, pp. 1112-1114, 2008.

[80] M. Bryan, T. Schrefl, and D. Allwood, "Symmetric and asymmetric domain wall diodes in magnetic nanowires," *Applied Physics Letters,* vol. 91, p. 142502, 2007.

[81] S.-M. Ahn, D.-H. Kim, and S.-B. Choe, "Kinetic and static domain-wall pinning at notches on ferromagnetic nanowires," *Magnetics, IEEE Transactions on,* vol. 45, pp. 2478-2480, 2009.

[82] G. S. D. Beach, C. Knutson, C. Nistor, M. Tsoi, and J. L. Erskine, "Nonlinear domain-wall velocity enhancement by spin-polarized electric current," *Physical Review Letters,* vol. 97, Aug 4 2006.

[83] J. Yang, C. Nistor, G. S. D. Beach, and J. L. Erskine, "Magnetic domain-wall velocity oscillations in permalloy nanowires," *Physical Review B,* vol. 77, Jan 2008.

[84] D. Porter and M. Donahue, "Velocity of transverse domain wall motion along thin, narrow strips," *Journal of applied physics,* vol. 95, pp. 6729-6731, 2004.

[85] E. Lewis, D. Petit, L. O'Brien, A.-V. Jausovec, H. Zeng, D. Read*, et al.*, "Kinetic depinning of a magnetic domain wall above the Walker field," *Applied Physics Letters,* vol. 98, p. 042502, 2011.

[86] F.-U. Stein, L. Bocklage, T. Matsuyama, and G. Meier, "Generation and annihilation of domain walls in nanowires by localized fields," *Applied Physics Letters,* vol. 100, p. 192403, 2012.

[87] M.-Y. Im, L. Bocklage, P. Fischer, and G. Meier, "Direct Observation of Stochastic Domain-Wall Depinning in Magnetic Nanowires," *Physical Review Letters,* vol. 102, Apr 10 2009.

[88] M.-Y. Im, L. Bocklage, G. Meier, and P. Fischer, "Magnetic soft x-ray microscopy of the domain wall depinning process in permalloy magnetic nanowires," *Journal of Physics: Condensed Matter,* vol. 24, p. 024203, 2012.

[89] W. T. Coffey and Y. P. Kalmykov, "Thermal fluctuations of magnetic nanoparticles: Fifty years after Brown," *Journal of Applied Physics,* vol. 112, p. 121301, 2012.

[90] R. Victora, "Predicted time dependence of the switching field for magnetic materials," *Physical review letters,* vol. 63, p. 457, 1989.

[91] W. Wernsdorfer, E. B. Orozco, K. Hasselbach, A. Benoit, B. Barbara, N. Demoncy*, et al.*, "Experimental evidence of the Néel-Brown model of magnetization reversal," *Physical Review Letters,* vol. 78, p. 1791, 1997.

[92] W. F. Brown Jr, "Thermal fluctuations of a single-domain particle," *Journal of Applied Physics,* vol. 34, pp. 1319-1320, 1963.

[93] T. Moore, T. Hayward, D. Tse, J. Bland, F. Castaño, and C. Ross, "Magnetization reversal in individual micrometer-sized polycrystalline Permalloy rings," *Journal of applied physics,* vol. 97, p. 063910, 2005.

[94]   J. Akerman, M. Munoz, M. Maicas, and J. L. Prieto, "Stochastic nature of the domain wall depinning in permalloy magnetic nanowires," *Physical Review B,* vol. 82, Aug 31 2010.

[95]   W. Zhao and G. Prenat, Eds., *Spintronic-based Computing*. Springer, 2015, p.^pp. Pages.

[96]   S. Goolaup, M. Ramu, C. Murapaka, and W. Lew, "Transverse domain wall profile for spin logic applications," *Scientific reports,* vol. 5, 2015.

[97]   B. Behin-Aein, D. Datta, S. Salahuddin, and S. Datta, "Proposal for an all-spin logic device with built-in memory," *Nature nanotechnology,* vol. 5, pp. 266-270, 2010.

[98]   H. K. Teoh, G. Sarjoosing, and W. S. Lew, "Programmable logic operation via Domain Wall Profile Manipulation."

[99]   W. Bailey, P. Kabos, F. Mancoff, and S. Russek, "Control of magnetization dynamics in Ni 81 Fe 19 thin films through the use of rare-earth dopants," *Magnetics, IEEE Transactions on,* vol. 37, pp. 1749-1754, 2001.

[100]   L. Thomas, M. Hayashi, X. Jiang, R. Moriya, C. Rettner, and S. S. Parkin, "Oscillatory dependence of current-driven magnetic domain wall motion on current pulse length," *Nature,* vol. 443, pp. 197-200, 2006.

[101]   C. Chappert, H. Bernas, J. Ferré, V. Kottler, J.-P. Jamet, Y. Chen*, et al.*, "Planar patterned magnetic media obtained by ion irradiation," *Science,* vol. 280, pp. 1919-1922, 1998.

[102]   C. M. Tan and A. Roy, "Electromigration in ULSI interconnects," *Materials Science and Engineering: R: Reports,* vol. 58, pp. 1-75, 2007.

[103]   N. Walter, C. Selhuber, H. Kessler, and J. P. Spatz, "Cellular unbinding forces of initial adhesion processes on nanopatterned surfaces probed with magnetic tweezers," *Nano letters,* vol. 6, pp. 398-402, 2006.

[104]   R. Ramanujan, "Magnetic Particles for Biomedical Applications," in *Biomedical Materials*, R. Narayan, Ed., ed: Springer US, 2009, pp. 477-491.

4. Experimental Techniques

4.1. Introduction

Throughout this study, different instruments and techniques have been used to fabricate, characterise, image and model the magnetic material under study. In all of the experiments done in this thesis, Py material was used as the only magnetic material under study.

The fabrication processes for nanowire magnetic systems were done using Electron Beam Lithography and thermal evaporation. The electric contacts were fabricated using UV photolithography, thermal evaporation and wire bonding in cleanrooms. Most of the sample imaging was done using Scanning Electron Microscope.

The magnetic characterisation and modelling work was done using focussed Magneto-Optic Kerr Effect magnetometer and magnetic transmission X-ray microscopy (MTXM). The simulation packages used were the OOMMF [4] and MuMax^3 [5] . Simulation jobs were run via special university computer clusters that allow for parallel job executions.

In the following sections, an explanation of the fabrication, topographical characterisation, imaging and modelling techniques used in the following chapters will be provided. These techniques are explained in the context of their usage in this study.

4.2. Fabrication techniques

The following section explains the electron beam lithography, UV lithography and thermal evaporation techniques used to fabricate Py nanowires and gold contacts.

4.2.1. Electron Beam Lithography

The Electron Beam Lithography (EBL) has been used in this project to fabricate all the different Py nanowire patterns that were characterized and studied.

The EBL is considered one of most highly used techniques for fabricating nanoscale patterns. This is due to its high resolution, which allows features down to 10 nm [6, 7] to be patterned, its multi-layer alignment accuracy and large depth of focus [6]. Moreover, in EBL, the desired pattern is directly written from a design made in a computer-aided design (CAD) software package without the need for a pre-fabricated mask. This provides the ability for a researcher to easily fabricate almost any desired shape and pattern on a one off bespoke basis.

Fabrication using EBL goes through several steps that include pattern designing, substrate/photoresist preparation, E-beam exposure, developing, metal deposition and lift-off.

The EBL fabrication technique works by creating sub-micron patterns by exposing a beam of electrons on a photoresist polymer surface. The exposed regions of the polymer react photochemically with the electron beam. The photochemical reaction alters the solubility of the exposed regions of the photoresist making them more or less soluble than the rest of the unexposed polymer regions depending on whether the photoresist is a 'positive' or 'negative' type, respectively. For instance, in a positive resist, the E-beam causes the carbon-chains in the photoresist to break in a process known as chain-scission, which makes the exposed regions more soluble. On the other hand, in case a negative resist was used, the opposite reaction occurs; in which, polymer chains are combined together in a process known as polymer cross-linking, making the exposed region less soluble in solvent [6].

The exposed sample is, then, developed to dissolve the more soluble regions resulting in a pattern ready to be used as a growth template. After growing the metal on the template, the sample is immersed in a solvent to lift-off the remaining photoresist template, leaving the grown metal deposited with the desired pattern. Figure 4.1 summarises the process.

The amount of radiation a section of resist is exposed to can be quantified by calculating the amount of incident charge per unit area, a parameter known as the area dose (D_{area}). The area dose can be calculated using the following equation:

$$D_{Area} = \frac{I_{Beam}}{S^2} \cdot t_{dwell} \qquad\qquad (eq\ 6.1)$$

where I_{beam} is the beam current, t_{dwell} is the time duration spent by the E-beam at each exposure point, and S is the unit step size taken by the E-beam to write a pattern. Usually the current and step size parameters are set to a default value, with t_{dwell} being used to control the area D_{area} in a given section of pattern [6, 8].

For the samples fabricated in this study, a RAITH 150 EBL system was used, which allowed the writing of patterns with features as small as ~20 nm. An accelerating voltage of 10 kV and aperture size of 10 μm were used in all cases.

The patterns (usually nanowires) were first designed using the RAITH CAD software package with a write field sizes of 25 x 25 μm^2 or 50 x50 μm^2, depending on the size of the features that needed to be accommodated. It was experimentally noticed that the resolution of the nanoscale features are more accurately resolved as the size of the writing field was reduced.
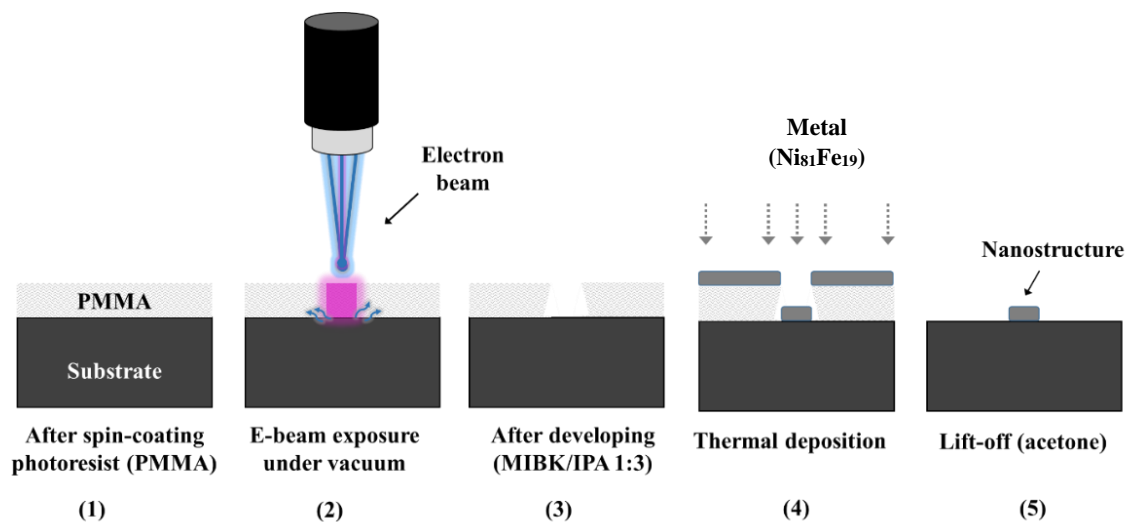

Figure 4.1: Schematic illustrating the EBL process for fabricating a nanostructure starting with photoresist spin coating (1), E-beam exposure (2), developing (3), metallization (4) and lift-off (5).

This was noticed after imaging fabricated samples that were designed using different write fields, and observing that small features (down to 50 nm) were resolved more accurately in the $25\text{x}25\mu\text{m}^2$ writing field.

To prepare the substrates, Si or Si_3N_4 substrates were first cleaned using acetone and then rinsed with isopropyl alcohol (IPA) chemical. The substrates were then spin-coated with the 'positive' photoresist of 495K Poly(methyl methacrylate) (PMMA) at a rotation speed of 4000rpm. The spin-coated sample was then baked at 180°C for 5 minutes in order to cross-link the PMMA molecules.

The spin-coated samples were transferred to the EBL system and exposed. The electron beam current was typically set at a value of ~10 pA. Using this small value had the advantages of limiting sample charging and producing a high depth of focus, but this came at the cost of increased exposure times and difficulty in focusing due to decreased signal-to-noise ratio [6].

The samples were developed with MIBK:IPA (1:3) in order to dissolve the exposed region of the positive resist. The samples were immersed in the solution for 30 s at a temperature of 23°C, and then transferred to a beaker of IPA for 30 s to wash away any remaining developer solvent and prevent the development process from continuing. The immersion time and developer temperature needed to be adjusted carefully to ensure that only the exposed regions of the photoresist were dissolved with minimal effects on the unexposed regions of the sample.

Following development the resist templates were metallised by thermal evaporation, and the fabrication was completed using lift-off processing. This was achieved by immersing the samples in acetone for a couple of minutes. For samples on Si an ultrasonic bath was used to promote the lift-off. For Si_3N_4 substrate, the sample was instead immersed in acetone at 50° C for 15 min, to avoid ultrasonic vibrations damaging the Si_3N_4 membranes.

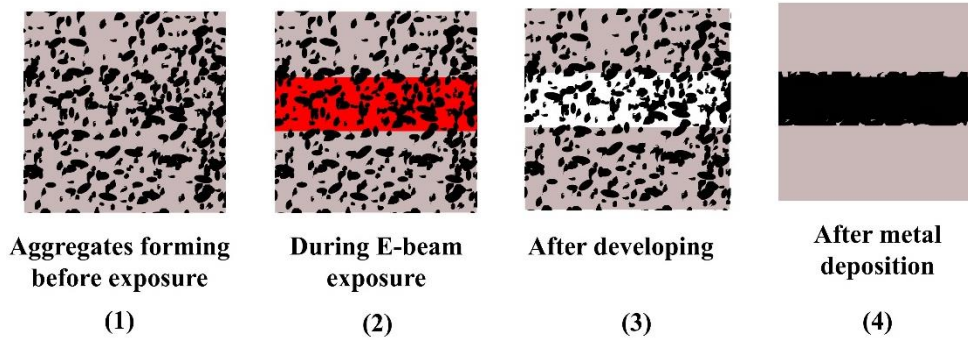| Aggregates forming before exposure	During E-beam exposure	After developing	After metal deposition
(1)	(2)	(3)	(4)

Figure 4.2: Schematic illustrating the process that results in the formation of edge roughness due to the presence of polymer aggregates on the surface of the photoresist before the exposure stage.

As the electron beam irradiated and penetrated the photoresist, parts of the electron beam suffered unavoidable scattering; where electrons were reflected back through elastic and/or inelastic scattering. In elastic scattering the energy of the scattered electrons is conserved while the scattering angle changes considerably [6]. An unavoidable fabrication error occurs when the elastic scattering of electrons from the resist as well as backscattering of electrons from substrate causes the formation of secondary electrons (electrons excited from scattered electrons). These electrons may irradiate the photoresist outside the desired region, and would have undesired contribution to the dose area. This effect is known as the 'proximity effect' and is minimized by implementing a proximity effect correction algorithm to the EBL device.

Another important effect that occurs during EBL lithography is the introduction of edge roughness to the nanostructures. This can occur due to the creation of random polymer aggregates (granules structures) that create line width fluctuations on the edges of the nanostructure [9]. These aggregates are believed to be caused by the interpenetration and entanglement of the polymer chains, and their interaction due to Van der Waal forces [10]. Such aggregates are believed to have been formed during spin-coating even before the baking process. During exposure, the aggregates bonds are insufficiently fragmented resulting in having a slower dissolution rate than the exposed polymer chains. Therefore, at the development stage, only some of the aggregates that were fully surrounded by exposed soluble polymers will be easily dissolved, while those at the edges of the nanostructures will be left on

the edges of the surface without dissolving [9]. After metal deposition and lift-off processes, the aggregates will be removed leaving a rough edge surface behind. Figure 4.2 illustrates the process.

Finally, it is believed that controlling polymer size of the resist and its developing properties will help reduce or increase edge roughness [10].

4.2.2. UV Photolithography

The basic process of ultra-violet (UV) photolithography is very similar to that of EBL; however UV photons (instead of electrons) are used to modify the resist layers. Since UV light has a longer wavelength (λ) ranging from 100 nm - 400 nm compared to electron De Broglie wavelengths $\lambda < 10nm$, its resolution limits it to the patterning of micron-scale features. Furthermore, unlike EBL, UV light exposure is done through a reflective mask, allowing it to expose a full sample simultaneously. Therefore, this method is ideal for patterning features with dimensions ranging from 0.5 µm to 100s of µm. In the work described in this thesis photolithography was used to pattern current lines which were used to nucleate DWs into nanowires. A schematic diagram of the photolithography processes is shown in Figure 4.5.

UV lithography was performed in cleanroom environment to prevent contamination of the photomask and substrate. UV light of wavelength 300 nm was used, which allowed features with widths down to ~0.5µm to be resolved. To allow patterning of these very small features,
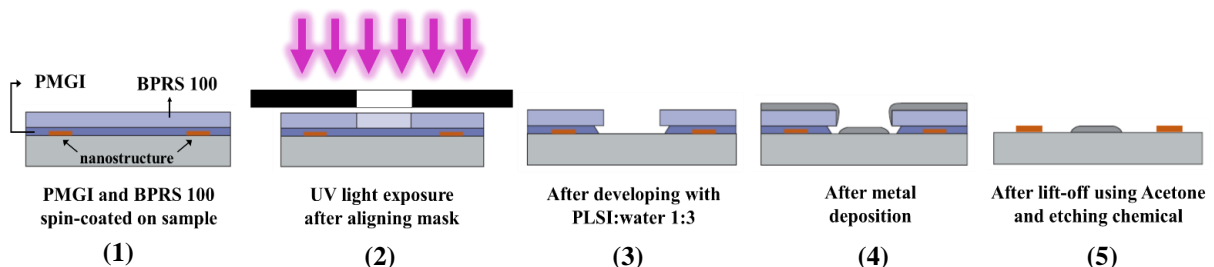

Figure 4.5: Schematic illustrating the UV lithography process with the added undercut layer. (1): PMGI is first spin coated above existed nano-pattern before spin-coating BPRS photoresist. (2): UV light is exposed above the patterned mask. (3): Developing with PLSI removes PMGI and BPRS (4): Deposition is done using thermal evaporation .(5): Lift-off is used to remove unexposed photoresist [3].

the exposure had to be done under the vacuum mode; in which, the small compartment holding the sample during UV exposure was sealed with ribbon gasket under vacuum before exposure was started. This ensures the minimum level of air molecules that might block the photons from reaching the sample.

Since the lithography process was highly sensitive to contamination, the mask had first to be cleaned to ensure that no particles were blocking the transparent pattern. Therefore, the mask was carefully cleaned using a corrosive solution of sulphuric acid and hydrogen peroxide.

Sample substrates were first cleaned with acetone and washed with IPA. Then the positive photoresist BPRS 100 was spin-coated at 4000 rpm and baked at 100°C for 1 minute. In some cases, an 'undercut' layer of PMGI-SF8 resist was first spin-coated on the sample and baked for 3 minutes at 180°C before spin-coating the BPRS photoresist. The undercut layer provided a spacer layer between the photoresist and the substrate, and allowed for a facilitated lift-off process by facilitating the diffusion of the lift-off solution to the photoresist layer.

 After spin-coating the photoresist, the sample was aligned under the pre-fabricated Cr/glass mask in a Karl Suss aligner by matching the markers on the mask with the markers fabricated near the nanowires. Upon ensuring perfect alignment, the compartment was sealed for vacuum level to be achieved, and the sample was exposed for 13 seconds. The sample was then developed using PLSI:water (1:3) developer for 1 minute before being rinsed with ionized water. The sample was then ready for the deposition of Ti/Au to create the contacts.

After the metal deposition process was done, the sample was immersed in acetone to lift-off the BRPS and metal from the unexposed region. Finally the sample was immersed in an etching solvent to remove the PMGI under cut layer.

4.2.3. Thermal Evaporation

All of the magnetic samples studied in this thesis were metallised using thermal evaporation. In this simple process a source material is placed in a refractory crucible in a high vacuum environment. The crucible is then heated by the application of current through an embedded tungsten wire causing the source material to melt and begin to evaporate. The evaporated vapour is then condensed onto a substrate to form a high quality film.

Thermal evaporation was performed using Edwards thermal evaporator, a schematic diagram of which is shown in Figure 4.3. Metal powder ($Ni_{81}Fe_{19}$ or Ti) was placed in an alumina crucible connected to electric terminals inside the evaporation chamber. The target substrate was mounted above the crucible in an upside-down orientation. The chamber was sealed and was pumped down to a base vacuum pressure of $1x10^{-7}$ mbar using a turbo molecular pump. Maintaining a high vacuum was essential in maintaining to avoid oxidation of the samples during growth.

Prior to depositing metal onto the substrate, a 'bake-out' process was performed in which a layer of the source metal (~10 nm) was evaporated and deposited on the inner walls of the evaporator while the substrate was protected by a shutter (Figure 4.3). This process removes
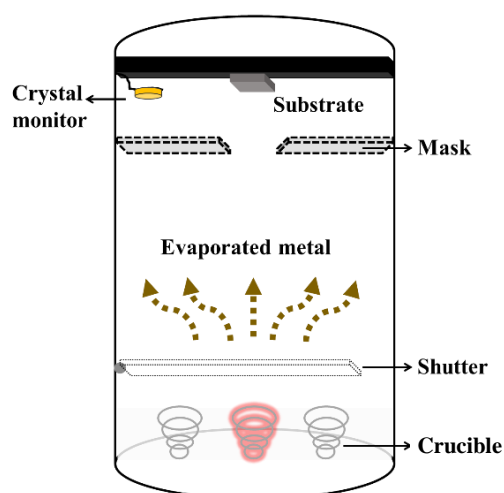

Figure 4.3: Schematic illustrating Edwards type thermal evaporator device used to deposit Py metal. The shutter and mask can be rotated to cover or expose the crucible and sample, respectively.

any contamination on the outer coils of the crucible, and also grows a layer on the inner walls of the evaporator that seals in contaminants on the chamber walls.

Growth of the films was measured using quartz crystal thickness monitor sensor placed near the sample holder. In all growths, the growth rate was maintained at 0.2-0.4 Å/s to maintain homogeneous growth of the metal layers. Finally the chamber was left to cool down before removing the sample.

For fabricating gold contacts, an evaporator was used inside the cleanroom. An adhesive layer of Ti of thickness 20 nm was first deposited to facilitate the adhesion of gold on the sample. A thickness of 200 nm of gold was then deposited to form the sample. The evaporation process was done under a base vacuum level of 1×10^{-6} mbar.

4.3. Topographical characterisation

In this section, the scanning electron microscope and the atomic force microscope will be explained.

4.3.1. Scanning Electron Microscope

All of the samples fabricated in this study were imaged using scanning electron microscopy (SEM) to characterise the topography of the fabricated pattern. This ensured that the geometry of the patterned nanostructure has been fabricated within tolerable error.

Imaging was performed in secondary electron mode, where secondary electrons generated from the surface of the sample are detected as a focused electron spot is scanned across the sample surface [11]. Secondary electrons have energy < 50 eV [6].

An SEM instrument is basically composed of a vacuum chamber containing an electron gun, condenser lens, objective lens, scan coil, aperture, scan generator, photon detector and display screen. Figure 4.6 shows the schematic diagram of a SEM system.
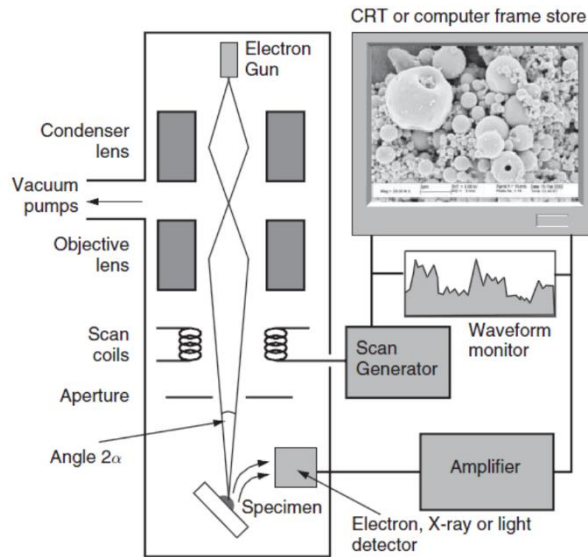
Figure 4.6 : Schematic diagram showing the SEM apparatus. [2]

In the electron gun, a tungsten or lanthanum-boron filament is heated by passing current thought it. This causes the thermal emission of electrons, which are passed through the condenser lens. The condensed electron beam is then passed through the objective lenses which focuses onto the sample with a focus radius of around 1-5 nm. The angular spread of the focused electron beam is limited by aperture lens (refer to Figure 4.6).

The scanning coils (controlled by the scan generator) control the motion of the focused beam causing it to raster-scan the specimen surface, generating secondary electrons [2]. The intensity of secondary electrons is related to the topography of the sample and to the distance between the surface and the detector. This provides contrast differences for surfaces that face the detector compared with tilted regions.

The secondary electrons are detected by the electron detector, and an electric signal containing the intensity information is amplified and then fed to a display monitor where the image is rasterized in real-time [2].

4.3.2. Atomic Force Microscopy

Atomic force microscopy (AFM) is a technique used to image the topography of surfaces down to the nanoscale by exploiting the atomic forces interactions between the specimen and a sharp tip. In this study AFM was only used in the initial stages of the project to image the first designs of nanowire structures, while SEM imaging was used to characterise the majority of samples fabricated.

A schematic diagram of an AFM system is shown in Figure 4.7. The AFM uses a piezoelectric scanner that positions a cantilever of length ~2 µm [2] connected to a sharp tip of length ~10nm [8] over the surface of a specimen. Atomic forces such as the attractive Van der Waal forces and repulsive electrostatic forces interact with the AFM tip causing the cantilever to deflect in response to the change in specimen topography. The deflection of the cantilever is detected optically by using a photodiode to measure the deflection of a laser beam that is continuously focussed on the back of the cantilever.

The AFM used has two modes of operation, 'contact mode' and 'tapping mode'. In contact mode, the AFM tip is in soft contact with the surface of the specimen. As the tip traces the surface, the cantilever deflects in response to the changes in the topography of the surface.
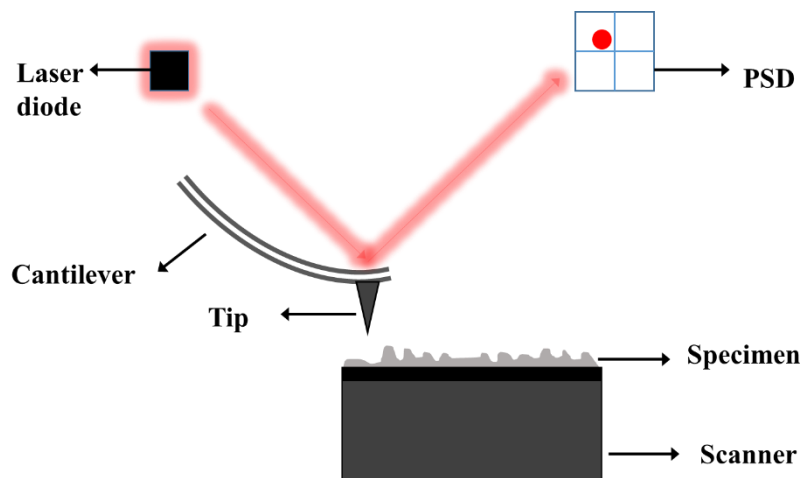

Figure 4.7: Schematic illustrating the imaging process of the AFM. Laser is reflected from the cantilever into the detector in response to movement of tip due to atomic interactions from specimen's surface atoms.

Hence, deflection reflects changes in topography, and can be translated into an image that reflects the shape of the surface.

In 'tapping mode', the cantilever is set to oscillate at its resonant frequency vertically above the surface of the specimen; such that the tip almost touches the surface. As the tip scans the surface, the amplitude of its oscillations change in response to attraction/repulsion from the atomic forces from the atoms at the surface, which modify its resonant frequency. This again reflects the topography of the sample, and can be translated into an image. In practise, the amplitude of the signal is kept constant by a feedback loop connecting the photodiode signal to the piezoelectric scanning stage, and displacements of the scanning stage are used to map the surface [2, 12].

If the cantilever spring is very stiff, the tip can deform/damage the specimen in the 'contact mode'. However, if controlled properly, it can be used to write patterns on a soft surface. The tapping mode, on the other hand, ensures scanning the specimen without contaminating or damaging the surface [2]. In this project AFM analysis was performed in tapping mode.

4.4. Magnetic characterization techniques

In the following section, the focused magneto-optic Kerr effect magnetometer and the magnetic transmission X-ray microscope techniques will be explained

4.4.1. Focused Magneto-Optic Kerr Effect Magnetometer

The focused magneto-optic Kerr effect magnetometer (MOKE) is used in this project as the primary technique in characterising the magnetic properties and magnetic switching behaviours of Py nanostructures.

The MOKE is an optical characterization system that uses a focused laser beam to locally characterize the magnetization of ferromagnetic materials by exploiting the Kerr effect. In the Kerr effect, the plane of polarization of linearly polarized light that is incident on a magnetic

surface, is rotated by an angle of θ_K with respect to the plane of polarization of its incident

beam (Figure 4.8). The magnitude and direction of θ_K depends on the magnetisation direction

of the reflecting surface, hence it can be used to measure magnetic switching behaviour. A

similar phenomenon occurs for light transmitting through a medium in the presence of a

magnetic field and is referred to as the Faraday effect [13, 14]. In addition to the rotation in the

plane of polarization, the electric field of reflected light can suffer a phase delay in its linear

polarization resulting in a slight ellipticity of its polarization.

The Kerr effect is due to circular birefringence phenomenon in which left-handed and right-

handed circularly polarized light have different permittivity in a magnetic material due to spin-

orbit coupling. This is because ferromagnetic materials are spin polarised which results in non-

equivalent spin-orbit interactions with circularly polarized light of different handedness. This

picture of the Kerr effect can be extended to the linearly polarized light when linear polarization

is treated as a superposition of left-handed and right-handed circular polarizations [15].

An alternative classical explanation attributes the Kerr effect to the Lorentz force. In this

picture it is imagined that the electric field component of the incident light causes the electrons

of the magnetic material to oscillate along a direction parallel to the electric field vector **E**. Due
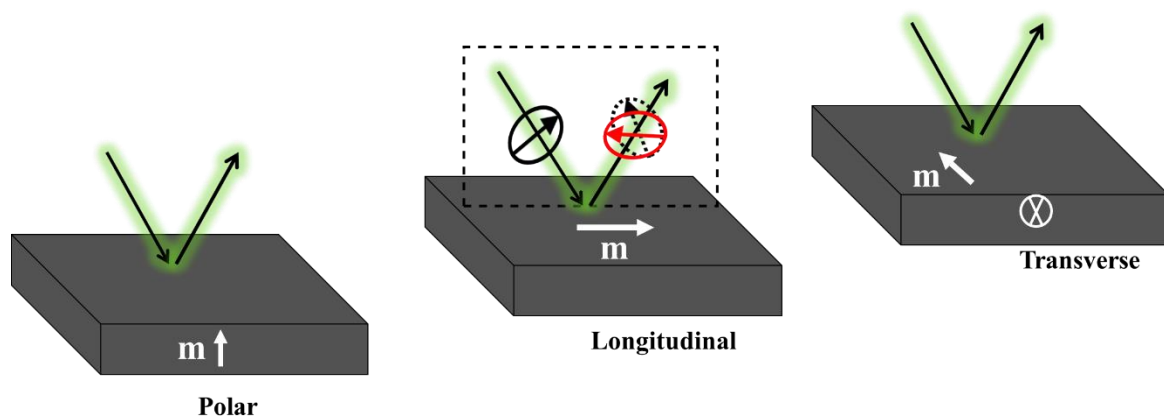

Figure 4.8: Schematic showing the three possible MOKE geometry. Green arrows represent the incident and reflected laser light. White arrows show the direction of magnetisation. Arrow in circle show the plane of polarization, red arrow shows rotated plane of polarization due to Kerr effect. Dashed rectangle shows the plane of incidence.

to the presence of the magnetisation **m** of the magnetic material, the electrons experience a Lorentz force orthogonal to both **E** and **m** which can be considered as an effective electric field component E_K. The reflected light then consists of both the original **E** and the orthogonal E_K component resulting in a slight rotation of its polarisation [14, 16].

MOKE systems are typically described by one of three geometries depending on the relative orientations of the samples magnetisation and the plane of reflection of the incident light, namely the polar, longitudinal and transverse MOKE geometries (Figure 4.8).

In the polar geometry, the magnetisation of the sample is perpendicular to its surface and thus parallel to the plane of light incidence. Kerr rotations are observed both for light with polarisation parallel (p-polarisation) and perpendicular (s-polarisation) to the plane of incidence. The polar effect produces larger Kerr rotations than the other two geometries. [14, 15].

In the longitudinal geometry, the magnetisation lies in the plane of the magnetic surface and parallel to the plane of incidence. Similar to the polar geometry, both s- and p-polarization components are rotated [14], however rotations are only observed for non-zero angles of incidence.

In the transverse geometry, the magnetisation lies in the plane of the magnetic surface and perpendicular to the plane of incidence. In this geometry a modification of intensity of p-polarised light occurs, and rotations of polarisation can only be produced by using light with mixed s-p character. [15]. Once again, the transverse effect is only observed for non-zero angles of incidence. Throughout this study the longitudinal MOKE geometry was used.

A schematic of the focused MOKE system is shown in Figure 4.9. The MOKE setup is basically composed of two optical systems. The first system focuses a polarised laser beam onto the
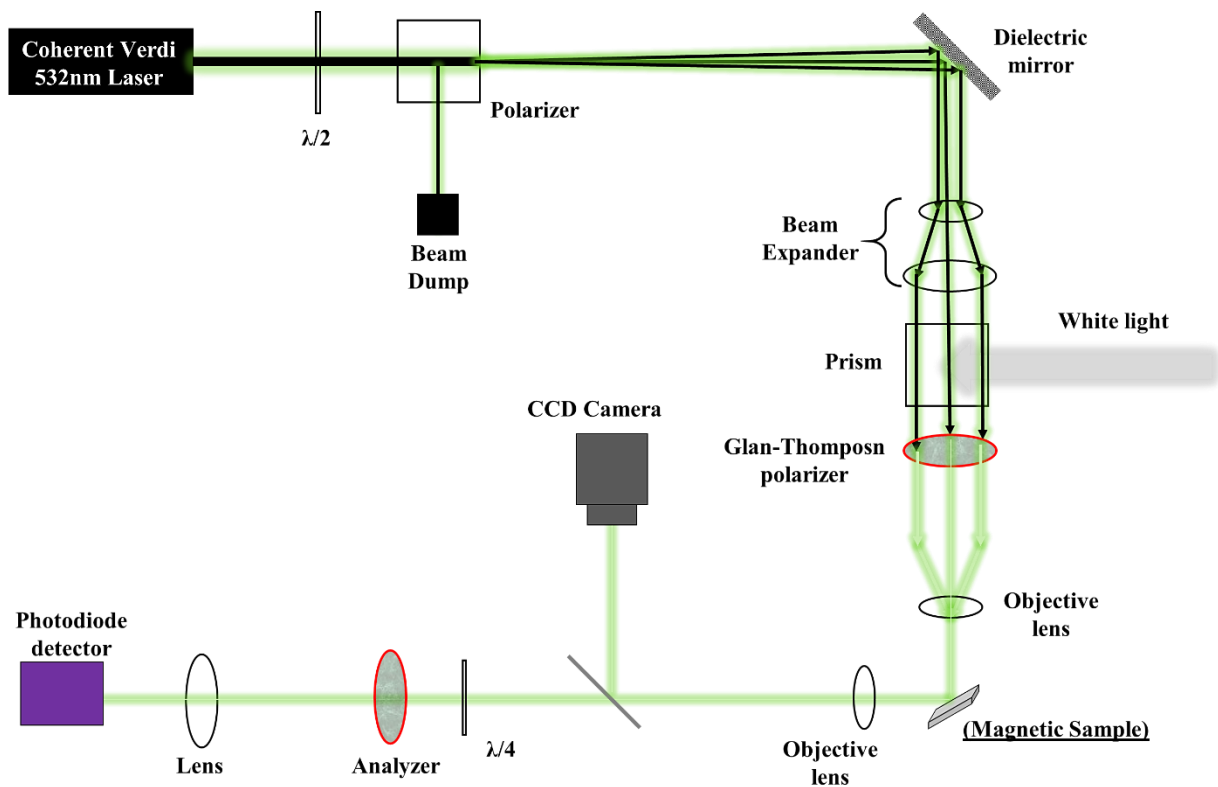
Figure 4.9: Schematic illustrating the MOKE setup. Green line represent the laser being generated, polarized, and reflected towards the magnetic sample placed inside the EM. White light is only used during sample alignment.

sample's surface and then analyses changes in its polarisation state. The second system is a

white light microscope that allows the MOKE laser spot to be aligned on the sample's surface.

Laser light was generated through a diode-pumped solid-state Coherent Verdi laser with

wavelength λ = 532 nm and a maximum output power of 2.2 W. The stability of the laser

increased with increasing power and therefore the power was set to its maximum output to

obtain the highest S/N ratio. However, very high laser powers can damage the sample, so the

laser power was attenuated to around 20-40 mW by rejecting a large fraction of the laser power

into a beam dump. The beam was then reflected through a beam expander and a beam splitter.

At the beam splitter, white light was added to the beam path to provide a light source for the

CCD camera that was used to view the sample and laser spot. The laser was then passed through

a Glan-Thompson polarizer (extinction ratio $<10^{-5}$) in order to create high purity p-polarized

light. The polarized laser beam then passed through an objective lens and onto the sample producing a focused laser spot size ~5μm. The sample was angled such that it was at 45° to the incident beam, and was placed inside a quadrupole electromagnet that could provide both horizontal and vertical magnetic field. The sample was mounted on a pair of Newport MFA-CC miniature linear stages that could be moved both horizontally and vertically with sub-micron resolution using a Newport ESP300 universal motion controller. The sample could also be rotated using Newport M-URM 80CC precision rotation stage.

The reflected beam from the sample was re-collimated by a second lens before passing through a beam-splitter that diverted a fraction of the beam and white light to a CCD camera used for imaging the sample surface. The laser beam was then passed through a quarter-wave plate, where any added elliptical polarization was converted back into linear polarization. The polarization of the beam was then converted into intensity by passing it through a second polarizer, known as the analyser [17], and detected by a photodiode.

The current generated by the photodiode depended on the intensity of light, which in turn depended on θ_K and thus the magnetisation of the sample. In order to maximise the S/N, the analyser and the quarter-wave plate were rotated iteratively until extinction (minimum transmitted intensity) was reached. The analyser was rotated back approximately 2° to reach to optimised signals [8]. For the samples measured in this thesis, S/N ratios were typically large enough to allow single-shot switching shot data to be produced, although the system also allowed multiple field-sweeps to be averaged together.

The electric signal from the photodiode was amplified using a pre-amplifier connected to a 1GHz sampling oscilloscope, which was in turn connected to a computer through a GPIB interface. The computer software captured the signal and plotted it against the magnetic field applied in the x-axis and/or y-axis directions, which was measured at the electromagnet using

an inductive coil. The electromagnet coils were driven by a pair of KEPCO power supplies one of which drove the x-axis field (in the plane of laser incidence) and the other the y-axis field (orthogonal to plane of laser incidence). The power supplies were controlled by custom computer software which could be used to create arbitrary biaxial magnetic field waveforms.

4.4.2. Magnetic Transmission X-ray Microscopy

Magnetic X-ray transmission microscopy (MTXM) is a method used to image magnetic domains in nanomagnetic materials with extremely high spatial resolution. In this thesis MTXM was performed at beamline 6.1.2, of the Advanced Light Source (ALS) which is part of the Lawrence Berkeley Laboratory in Berkeley, California [18]. This technique is used in chapter 8 where the chirality of vortex domain walls was measured.

The MTXM works by combining X-ray magnetic circular dichroism (X-MCD) with transmission X-ray microscopy (TXM) in order to obtain an image that shows magnetisation contrast. The technique can be used to probe magnetisation configurations with resolution as high as 25 nm [19]. X-MCD is an effect where the absorption of circular polarized X-ray photons by a ferromagnetic material depends on the projection of sample magnetisation along the light propagation direction, and the helicity of the X-ray photon. In other words, the degree of absorption of the X-ray photons by a magnetic material depends on the direction of its magnetisation and whether the emitted x-ray has left-handed or right-handed circular polarization. This effect is very similar to the bifringence effect exploited in the MOKE magnetometer.

A schematic diagram of MTXM system is shown in Figure 4.10. High intensity X-rays for MTXM are produced at a bending magnet [19, 20], where changes in the electron trajectory due to the Lorentz force result in the emission of polychromatic X-ray photons [20] along the beam line (Figure 4.10). Monochromatic circularly polarized X-rays can then be selected by

partly masking the beam using a 9 mm condenser zone plate and a tuneable 2 μm pinhole [19, 20]. Thus, the condenser and the pinhole act as a monochromator that only allows X-rays with a certain energies/wavelengths to pass onto the sample. Tuning is achieved by changing the distance between the pinhole and the condenser, with photon energies in the range 250 eV – 850 eV being selectable. The photon energy should be tuned to correspond to the absorption energy of the L-shell electrons of the magnetic material that will be studied on the sample (for Py nanowires characterized by MTXM in this thesis, the photon energy was tuned to Fe element L-shell electrons). The micro-zone plate acts as an objective lens that focuses photons into the X-ray CCD camera. A CCD camera with quantum detection efficiency of 70% is placed after the sample to capture the transmitted X-ray photons and produce an X-ray image [20].

In order to obtain maximum photon transmission, the samples used in MTXM imaging were fabricated on transparent thin (t = 100 nm) Si_3N_4 membranes. The sample was placed inside an electromagnet that was used to apply controlled, biaxial magnetic fields ($\mathbf{H_x}= \pm 1k$ Oe and $\mathbf{H_y}= \pm 150$ Oe). For measuring in-plane magnetic contrast, the samples were tilted at an angle of 30° in order to project a component of the in-plane magnetization of the sample along the X-ray
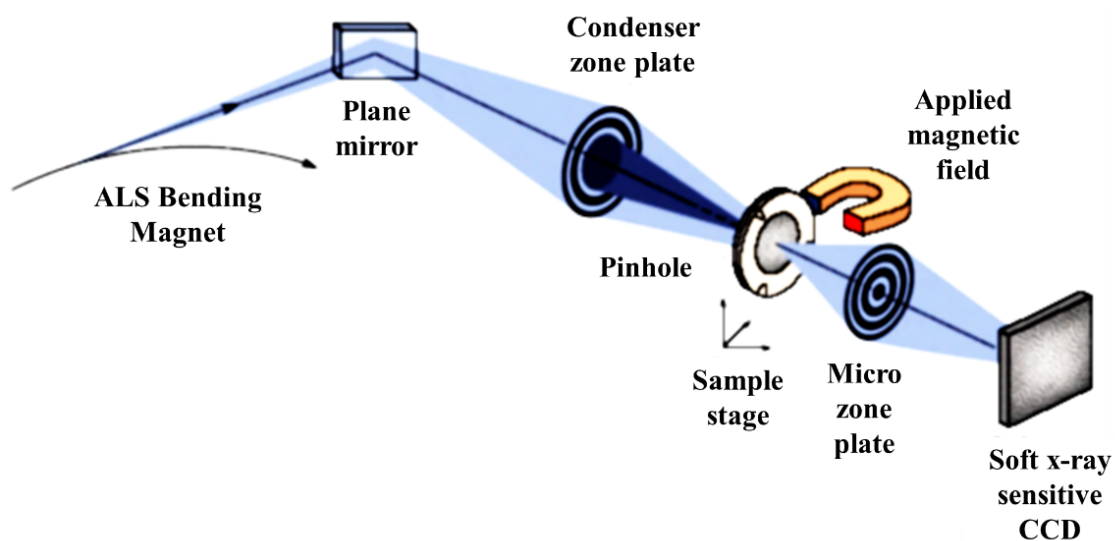
Figure 4.10: Schematic illustrating the MTXM setup of beamline 6.1.2 at ALS lab [1].

propagation direction. However, this had a negative effect of reducing the contrast by a factor of two when compared to polar contrast [19]. Therefore, in order to obtain clear images of samples' magnetisation configurations, the magnetic contrast needed to be enhanced. This was achieved in two ways: either by taking the same image with both left-handed and right-handed circularly polarized X-rays and dividing the two images or by dividing images by a reference taken at magnetic saturation.

4.5. Micromagnetic Modelling

Micromagnetic modelling is a method of predicting the behaviour of magnetic materials at sub-micron length scales. This is usually achieved by using numerical techniques to solve the Landau-Lifshitz-Gilbert equation.

Two open-source simulation packages were used in this study: the Object Oriented Micromagnetic Framework (OOMMF) software developed by National Institute of Standards and Technology (NIST) [4], and MuMax^3 developed by Ghent University [5].

Both OOMMF and MuMax^3 packages use the finite difference method (FDM) of simulation. The FDM works by meshing the simulation into regular cubic cells. This is in contrast to the finite element approach applied by other simulation packages [21-23] where a tetrahedral mesh is generated. The FDM is best suited for objects with rectangular (non-curved) geometries, but has higher performance and lower memory requirements [5] than finite element modelling.

In the OOMMF simulations the oxsii 3D solver module was used to perform both 2D and 3D simulations. Integration of the LLG equation was achieved using the Oxs_EulerEvolve function, which is based on Euler method for solving differential equations. The MuMax^3 software package is graphics processing unit (GPU) accelerated, making it 1 to 2 orders of magnitude faster than CPU-based simulation packages [5]. Hence, it was more efficient to use it for the majority of 3D simulations done in this study. For solving the LLG equation in

MuMax^3, the RK45 solver (based on Dorman-Prince method for solving differential equations) was used due to its accuracy and fast performance with magnetisation dynamics.

In this thesis simulations were only performed for samples composed of Py, and so the following material parameters were set in all of the simulations: exchange stiffness constant *A* = 13 ×10^{-12} J/m [24], saturation magnetization *Ms* = 860 kA/m [25] and magnetocrystalline anisotropy constant K = 0 J/m^3. Thermal effects were not included in any of the simulations. When simulating dynamic effects, the Gilbert damping parameter was set to realistic value of α = 0.02, but in cases where this was not required α = 0.5 or 1 was used in order to reduce computational time. For example α = 0.02 was used for all of the simulations of Walker breakdown phenomenon in chapters 6, 8 and 9, while α = 1 was used when relaxing initial DW configurations, or simulating the magnitude of quasi-static depinning fields.

As for the cell size of the mesh, it was important for this to be at equal to or smaller than the exchange length L_{ex} which defines the thickness of an idealised domain wall. For Py, which has very low magnetocrystalline anisotropy, the appropriate measure was calculated using eq. 3.1 which gives a measure of the relative strengths of exchange and magnetostatic interactions. For Py L_{ex} was calculated to be ~5.7 nm [26]. Therefore, the length and width of the cells were set to either 5 x 5 nm^2 or 2.5 x 2.5nm^2. For 3D simulations the thickness of the cells was 5 nm except for nanowires with thicknesses of t = 40 nm where cell thicknesses of 10 nm were used in order to reduce computational time (the validity of this approximation will be discussed in section 6).

4.6. References

[1] *Beamline 6.1.2 (XM-1)*. Available: http://cxro.lbl.gov//XM1

[2] R. Kelsall, I. W. Hamley, and M. Geoghegan, *Nanoscale science and technology*: John Wiley & Sons, 2005.

[3] MichroChem. *Nano PMGI Resist*. Available: https://www.seas.upenn.edu/~nanosop/documents/Data_PMGI.pdf

[4] *Object Orientated Micromagnetic Framework (OOMMF)* Available: http://math.nist.gov/oommf/.

[5] A. Vansteenkiste, J. Leliaert, M. Dvornik, M. Helsen, F. Garcia-Sanchez, and B. Van Waeyenberge, "The design and verification of mumax3," *AIP Advances,* vol. 4, p. 107133, 2014.

[6] I. Utke, S. Moshkalev, and P. Russell, *Nanofabrication Using Focused Ion and Electron Beams*: Oxford University Press, 2011.

[7] V. R. Manfrinato, L. Zhang, D. Su, H. Duan, R. G. Hobbs, E. A. Stach*, et al.*, "Resolution limits of electron-beam lithography toward the atomic scale," *Nano letters,* vol. 13, pp. 1555-1558, 2013.

[8] M. T. bryan, "Nucleation and propagation of domain walls in Permalloy nanowires," PhD, Department of Engineering Materials, University of Sheffield, 2008.

[9] T. Yamaguchi, H. Namatsu, M. Nagase, K. Yamazaki, and K. Kurihara, "Nanometer-scale linewidth fluctuations caused by polymer aggregates in resist films," *Applied physics letters,* vol. 71, pp. 2388-2390, 1997.

[10] H. Namatsu, Y. Takahashi, K. Yamazaki, T. Yamaguchi, M. Nagase, and K. Kurihara, "Three-dimensional siloxane resist for the formation of nanopatterns with minimum linewidth fluctuations," *Journal of Vacuum Science & Technology B,* vol. 16, pp. 69-76, 1998.

[11] H. Inada, D. Su, R. Egerton, M. Konno, L. Wu, J. Ciston*, et al.*, "Atomic imaging using secondary electrons in a scanning transmission electron microscope: experimental observations and possible mechanisms," *Ultramicroscopy,* vol. 111, pp. 865-876, 2011.

[12] L. Zang. Basics of Atomic Force Microscope (AFM) [Online]. Available: http://www.eng.utah.edu/~lzang/images/Lecture_10_AFM.pdf

[13] P. N. Argyres, "Theory of the Faraday and Kerr effects in ferromagnetics," *Physical Review,* vol. 97, p. 334, 1955.

[14] J. M. Coey, *Magnetism and magnetic materials*: Cambridge University Press, 2010.

[15] T. J. Hayward, "Exquisitely Balanced Magnetic Switching in Microscopic Ferromagnetic Rings," PhD Dissertation, Sidney Sussex College, University of Cambridge, 2007.

[16] A. Hubert and R. Schäfer, *Magnetic domains: the analysis of magnetic microstructures*: Springer Science & Business Media, 2008.

[17] D. Allwood, G. Xiong, M. Cooke, and R. Cowburn, "Magneto-optical Kerr effect analysis of magnetic nanostructures," *Journal of Physics D: Applied Physics,* vol. 36, p. 2175, 2003.

[18] *ALS* Available: http://www.cxro.lbl.gov/BL612/

[19] T. Eimüller, P. Fischer, M. Köhler, M. Scholz, P. Guttmann, G. Denbeaux*, et al.*, "Transmission X-ray microscopy using X-ray magnetic circular dichroism," *Applied Physics A,* vol. 73, pp. 697-701, 2001.

[20] P. Fischer, G. Schütz, G. Schmahl, P. Guttmann, and D. Raasch, "Imaging of magnetic domains with the X-ray microscope at BESSY using X-ray magnetic circular dichroism," *Zeitschrift für Physik B Condensed Matter,* vol. 101, pp. 313-316, 1997.

[21]   T. Fischbacher, M. Franchin, G. Bordignon, and H. Fangohr, "A systematic approach to multiphysics extensions of finite-element-based micromagnetic simulations: Nmag," *Magnetics, IEEE Transactions on,* vol. 43, pp. 2896-2898, 2007.

[22]   A. Kakay, E. Westphal, and R. Hertel, "Speedup of FEM micromagnetic simulations with graphical processing units," *Magnetics, IEEE Transactions on,* vol. 46, pp. 2303-2306, 2010.

[23]   R. Chang, S. Li, M. Lubarda, B. Livshitz, and V. Lomakin, "FastMag: Fast micromagnetic simulator for complex magnetic structures," *Journal of Applied Physics,* vol. 109, p. 07D358, 2011.

[24]   N. Smith, D. Markham, and D. LaTourette, "Magnetoresistive measurement of the exchange constant in varied-thickness permalloy films," *Journal of applied physics,* vol. 65, pp. 4362-4365, 1989.

[25]   R. M. Bozorth, "Ferromagnetism. Hoboken," ed: NJ: Wiley, 2003.

[26]   G. S. Abo, Y.-K. Hong, J. Park, J. Lee, W. Lee, and B.-C. Choi, "Definition of magnetic exchange length," *Magnetics, IEEE Transactions on,* vol. 49, pp. 4937-4939, 2013.

Chapter 5:

In Search for a Single-Mode Domain Wall Depinning Field Distribution

The main aim of this thesis is to perform a thorough study of the stochasticity of DWs in Py nanowires, in order to understand it and explore ways to control it in device applications. Therefore it is important to begin by investigating how DWs with different spin structures pin and depin in simple nanowire systems.

In most of the published literature, magnetic stochasticity in nano/mesoscopic ferromagnetic nanowires has been explored by studying DW pinning and depinning at artificial defect sites[1-9]. The results of these studies have indicated that stochasticity can arise due to:

1   Thermal activation effects that assist magnetic switching as the applied field approaches H_s, resulting in Gaussian depinning field distributions (DFD) [10-12].

2   DWs pinning with different internal magnetisation configurations, resulting in multi-mode depinning field distribution. These configurations can be DWs with different overall structure (i.e. transverse/vortex), chiralities or a variety deformations of these [3]. The variety of observed DW structures can be due to the injection method [2], or due to them undergoing dynamic transformations and deformations as they propagate above the H_{WB} [4].

3   DWs undertaking multiple depinning paths or passing through intermediate states during the depinning process. This can create stochasticity when small perturbations, (e.g. from thermal excitations), cause different switching routes to be taken in each reversal [13-15].

In this chapter the nature of DW pinning from symmetrical and asymmetrical defects using micromagnetic simulations and experimental measurements is investigated. The simulations are performed quasi-statically using high damping in order to investigate the fundamental nature of the energy landscape encountered by vortex and transverse DWs at defects. The experiments are performed using focused magneto-optic Kerr effect microscopy and use single shot measurements to deduce the depinning field distributions of DWs pinned at similar defect sites.

Both studies will contribute to the basis for exploring the complexity of DW stochasticity in magnetic nanowire systems, through analysing and comparing the results of the two studies in the light of the three stochasticity factors mentioned above. In particular, the comparison between the (low damping) experimental measurements and (high damping) simulated results will shed light on influence of complex magnetisation dynamics on DW depinning behaviours. Furthermore, an attempt to study a method that uses an extrinsic approach (externally applied transverse field) for manipulating DW stochasticity and improving DW motion has been done.

The studies presented in this chapter work towards finding a geometry of nanowire and defect site that exhibits single-mode/single-energy-barrier magnetic switching. Such a device can be used for further studies of complex magnetic stochasticity. Moreover, having good understanding of such device would be a step forward in producing sub-micron nanowire system that have highly reproducible magnetic behaviour which will be essential in building nanomagnetic applications.

5.1 Simulation of DW pinning/depinning in Py nanowires

The aim of this section is to get a qualitative understanding of the shape and nature of energy landscapes that are formed when transverse (TDW) and vortex DWs (VDWs) of different spin structures pin at pinning sites.

As mentioned previously, a careful choice of nanowire geometry can result in energetically favouring one DW type over the other. For instance, in nanowires of thicknesses > 10nm, VDWs are typically favoured in order to minimize the magnetostatic energy. Whereas in nanowires of thicknesses < 10nm TDWs are favoured in order to minimize the exchange energy due to the relatively low magnetostatic energy [16]. Therefore, in the following simulation study two nanowire geometries were studied; one with thickness t = 5 nm which was expected to support TDWs, while the other had thickness t = 40 nm and was expected to support VDWs.

In each nanowire two different defect geometries are studied. The first of these was an asymmetrical pinning site in the shape of a single triangular notch, while the second was a symmetrical pinning site in the shape of a double triangular notch. The width (w) and length (l) of the rectangular nanowires were: w= 150 nm and l= 1500 nm. Triangular notches of depth and length N_w=N_d=50 nm (0.33W (i.e. 33% of nanowire width)) were added to the nanowire. Figure 5.1 shows the schematic of both nanowires.

Two different defect geometries were chosen to allow chirality-related effects to be explored: The single triangular notch was expected to be sensitive to the DW chirality, and would thus unravel the difference in the energy barrier/well formed when a vortex or transverse DW of one chirality gets pinned compared to the energy landscape formed for the opposite chirality.
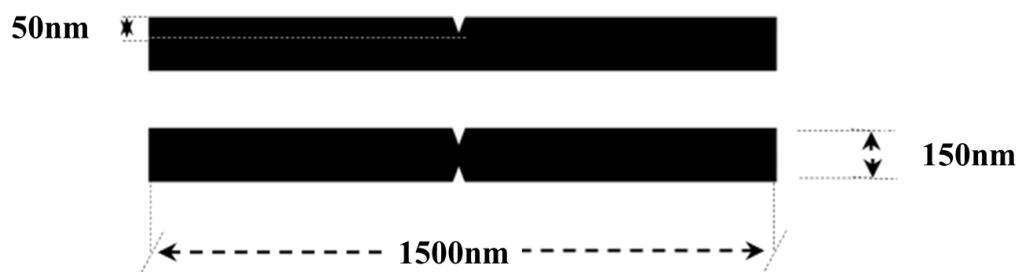
Figure 5.1: Schematic of the nanowire geometries used in simulations. The top nanowire has an asymmetric defect in the form of a single notch of depth N_d= 50 nm (0.33W). The bottom nanowire has symmetrical double triangular notches of depth N_d= 50 nm each.

On the other hand, the nanowires with double triangular notches were expected to show insensitivity to DW chirality. This insensitivity might be a step towards obtaining a system, which exhibits a single mode depinning field distribution.

5.1.1 Injecting and relaxing DWs

Micromagnetic simulations were performed using the OOMMF 3D solver [17]. Cell sizes were chosen to be 5 x 5 x 5 nm^3 and 5 x 5 x 40 nm^3 for nanowire systems with t= 5nm and t= 40nm, respectively. The damping coefficient was $\alpha = 0.5$, much higher than the expected value for Py (of $\alpha = 0.02$). This was imposed to supress complex DW dynamics as the aim here was to study the energy landscape presented by the defect sites. Dynamic effects will be studied extensively in the next chapter. All simulation were performed at Temperature, T = 0 K.

In the first stage of the simulation procedure, DWs were initialised, moved to the notches and then relaxed. The simulations initialised TDWs in the nanowires with t = 5 nm, and VDWs in the nanowires with t = 40 nm, at ~60 nm before notch in a tail-to-tail (T2T) magnetisation configuration. An applied field of $\mathbf{H_x}$ = 5 Oe was then applied to move the DW to the notch. The field was then reduced to 0 Oe to allow the DW to relax.
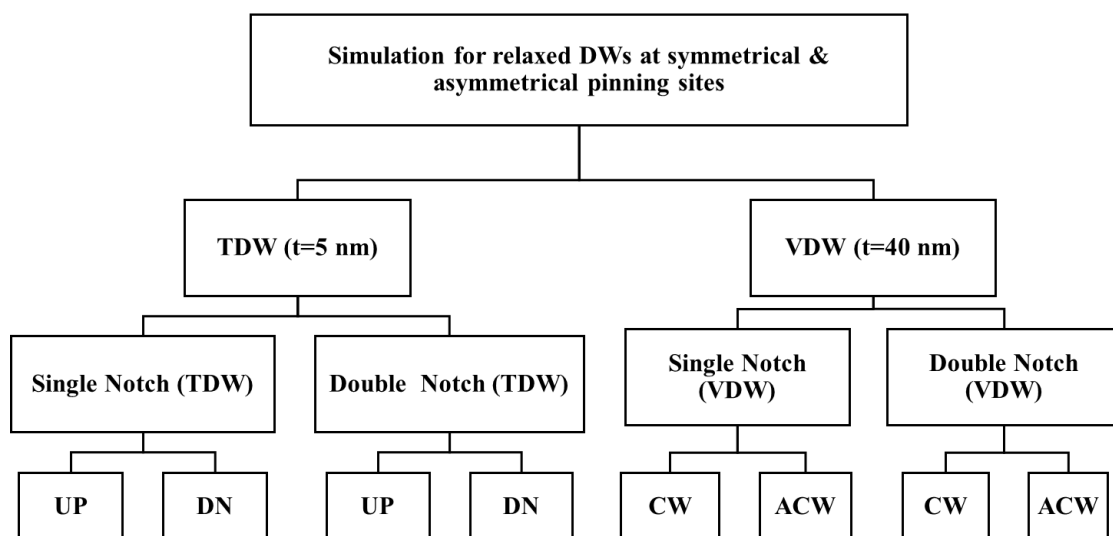
Figure 5.2: Flow chart summarizing the simulation scheme. The simulations aimed to relaxing the four possible DW configurations at the symmetric and asymmetric pinning sites.

Simulations were performed for both DW chiralities (Vortex: clockwise (CW) and anti-clockwise (ACW), Transverse: upwards (UP) and downwards (DN)). Figure 5.2 above summarises the simulation scheme.

Results and Discussion of relaxed DW simulation

Figure 5.3 shows the states of the simulated nanowire systems after the DWs were initialised, propagated and pinned.
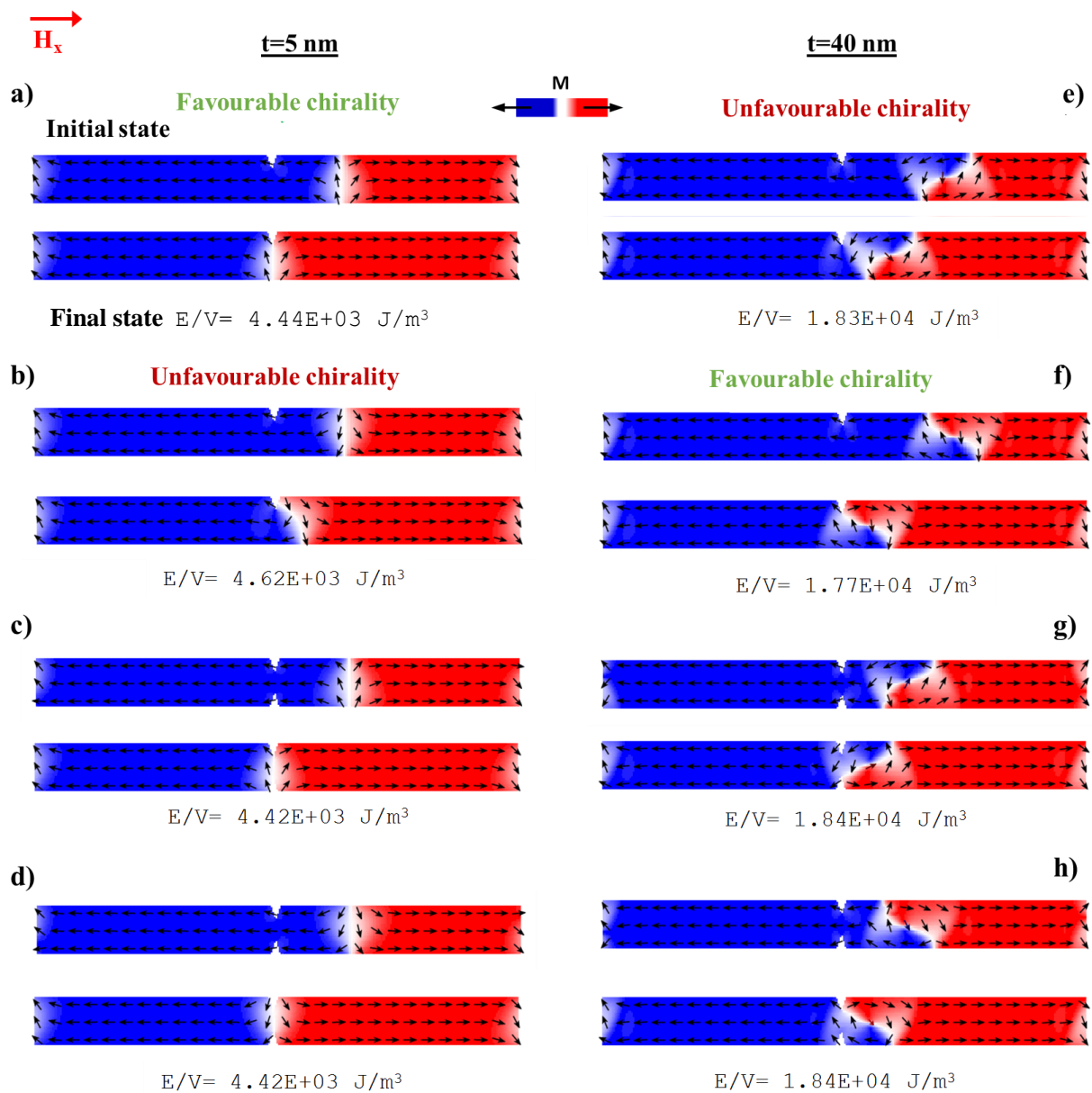

Figure 5.3. Simulated DW configurations for nanowires with t =5 nm (a-d) and t =40 nm (e-f) with T2T configuration. Initial (relaxed) DW states (top) and pinning states (bottom) were simulated for both TDWs and VDWs.

As the DWs approached the defect sites, they encountered a change in the energy landscape as the shape of the magnetic material changes. The narrow shape of the defect will force the DW to deform and the magnetic spins to alter their alignment in order to reach an energetically favourable state that would minimise the DW's energy [18]. This will cause the DW to pin as it has to overcome an energy barrier/well. The pinning barrier may exist just before the notch causing the DW to pin outside the notch, or an energy well can exist at the notch causing the DW to pin inside the notch. The shape of the pinning landscape will depend on the DW chirality (as will be discussed next). The DW remains pinned until the applied field exceeds the depinning field ($\mathbf{H_d}$) and the high Zeeman energy forces the DW to move across the constricted region.

Results showed that, in the nanowires with single notch (Figure 5.3 (a,b,e,f)), there were two possible pinning states for each DW type, one for each chirality. The different spin orientation in the two chiralities will results in different spin alignment with the asymmetric notch, in order to minimize DW's energy [3]. For instance, in the case of the TDW with upward (UP) chirality (Figure 5.3(a)), the DW pinned and relaxed inside the notch. This was not the case for the downward (DN) chirality where the DW pinned on the right edge of the notch (Figure 5.3(b)). This behaviour can be explained from the way the spins of the DW oriented themselves in order to lower their magnetostatic energy. In Py nanowire, the magnetostatic energy is dominant over the other anisotropy energies. This is due to the high shape anisotropy present in the nanowire geometry, and the low magnetocrystalline anisotropy of the Py material. The exchange is thus the only magnetic energy competing with the high magnetostatic energy. The magnetostatic energy is expected to increase as the nanowire width gets constricted at the notch. Therefore, magnetisation of the DW is expected to evolve in a manner that would reduce the demagnetising field produced by the system when magnetic charges accumulate at the
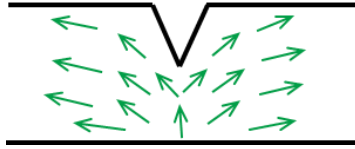
Figure 5.4: Schematic showing the spin alignment of an UP TDW in a T2T magnetic configuration when pinned inside the notch (Favourable chirality). Green arrows represent the TDW spins

surface of the notch, i.e. when the nanowires' spins have a component perpendicular to its edges.

In the case of the T2T UP TDW, the DW's spins were able to both; orient themselves parallel with the edges of the triangular notch and in-line with the magnetic dipoles of the two opposite domains (Figure 5.4). Therefore the TDW can pin inside the notch without increasing its magnetostatic energy. Such coherent orientation is only possible in an UP TDW in a T2T configuration, and when the triangular notch is on the upper edge of the wire. For the T2T DN TDW, the situation was different. The orientation of the spins of the DN TDW could not align with the two domains without accumulating magnetic charge at the edges of the notch (Figure 5.5(a)). This would have been energetically unfavourable as it would have increased the demagnetising field leading to an increase in the magnetostatic energy of the system. Instead, the DN TDW pinned outside the notch so fewer spins would need to align perpendicular to the notch and wire edges (Figure 5.5(b)). Moreover, the high energy state seen in Figure 5.5(a) justifies the existence of an energy barrier that causes the pinning before the notch. Results are in agreement with published literature [3, 19].

Since DN TDW pinned state had a higher total energy density ($E = 4.62 \times 10^3$ J/m^3) than the UP TDW ($E = 4.44 \times 10^3$ J/m^3), and since the UP TDW was able to enter the notch rather than pin
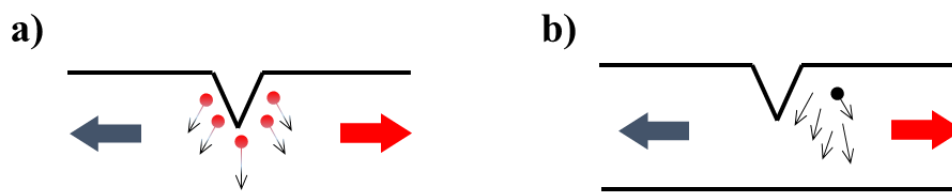
Figure 5.5: Schematic showing the alignment of spins in a T2T DN TDW. (a): High magnetostatic energy sate for DW pinned inside the notch (hypothetical). (b): Low magnetostatic energy state of DW pinned outside the notch (actual). The red circles show locations at which magnetic charges/poles accumulate.

outside of it, it is reasonable to classify the UP TDW as the "favourable" chirality for this defect and the DN TDW as the "unfavourable" chirality.

The VDWs in the t = 40 nm nanowires always pinned outside the notches independent of their chiralities. However, similar analysis to that applied above could also be used to explain whether their leading edges pinned at the apex of the notch as in the case of the CW VDW ('favourable' chirality, Figure 5.3(f)) or outside of it as for the ACW VDW ('unfavourable' chirality, Figure 5.3(e)). Here the DWs position was determined by the spin orientation of the leading edge of the VDW, making it analogous to the cases of the TDWs, once it is recognised that a VDW closely resembles two combined antiparallel TDWs. The results presented here for VDWs pinned at single notches agree very well with similar published studies [3, 19, 20].

For the symmetric double notches, the pinning behaviour was the same for both chiralities of TDW and VDW. Thus, the final state is the same for DWs of both chiralities, yielding a chirality-independent behaviour. This is clearly seen in the t= 40 nm nanowire, where the CW VDW pinned at the apex of the bottom notch while the ACW VDW pinned at the apex of the upper notch. In the case of the TDWs, both chiralities pinned inside the notches (Figure 5.6), such that the final configuration was reflective of a combination of those shown in Figure 5.4 and Figure 5.5(a). This suggests that the increase in energy that would have been required to avoid creating surface charges in one of the notches (e.g. by forming a combination of Figure 5.4 and Figure 5.5(b)) was offset by the energy cost of lengthening the DW; such that one side
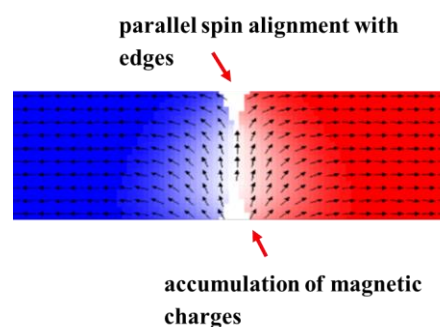

Figure 5.6: Schematic showing the spin configuration of a TDW pinned at the double notch. Magnetic spins align parallel with the top notch, while magnetic charges accumulate at the bottom notch.

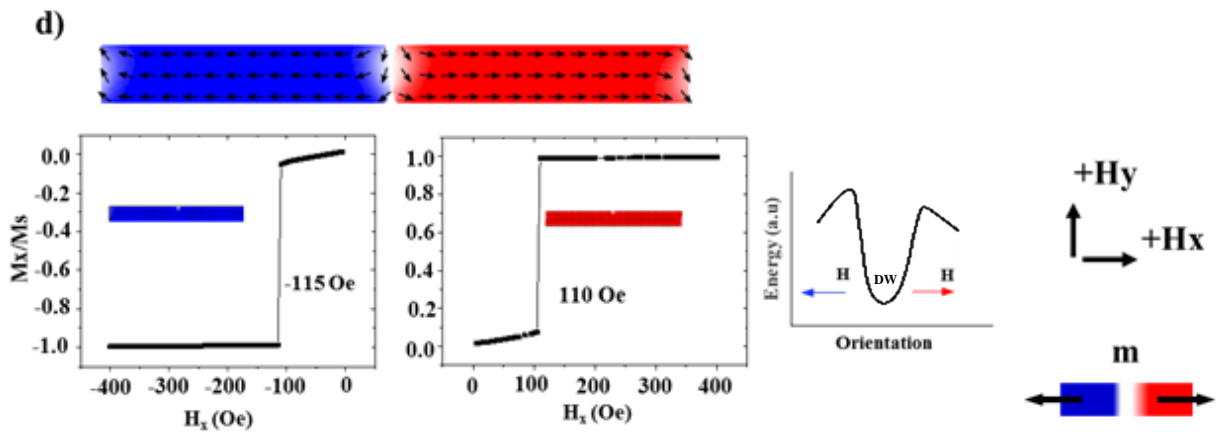was pinned inside while the other was pinned outside as might have been expected from the discussion above.
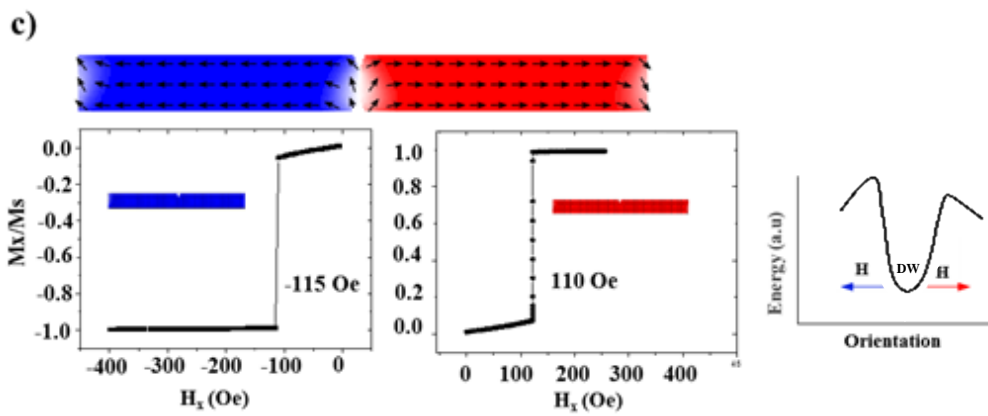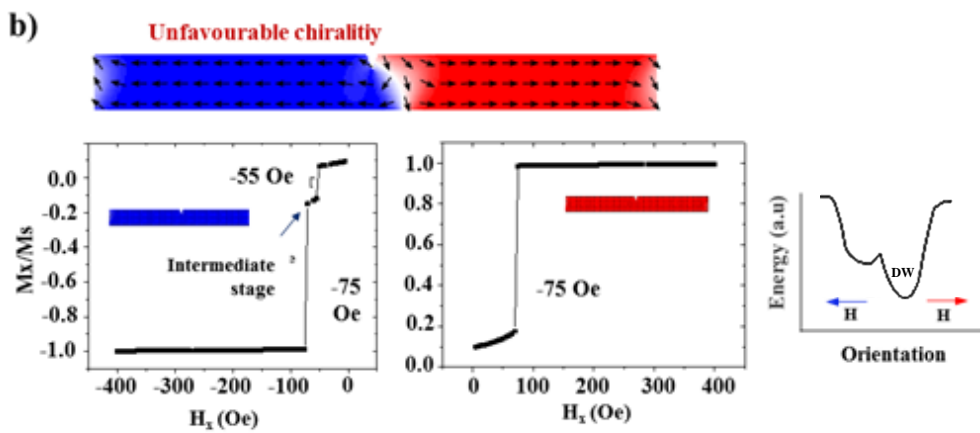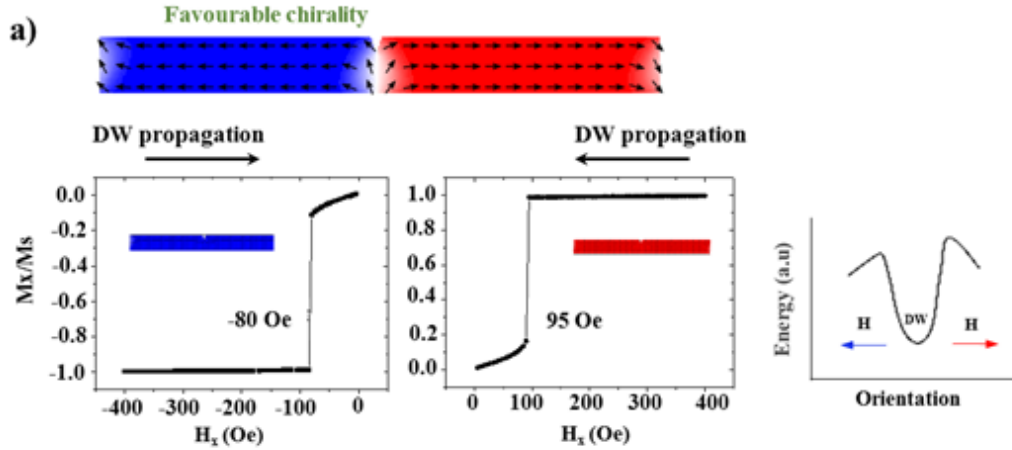
5.1.2   Quasi-static depinning of DWs

The next step in obtaining a *qualitative* sense of the energy landscape presented to the DWs by the notches was to simulate the depinning process of the eight pinned DW states described above. The depinning was simulated in both the forward and backward directions with respect to the direction the DW was initially pinned from. This was achieved by applying enough field to overcome the energy gradient at the notch, and depin the DW. The magnitudes of the fields required to depin the DWs in the two directions can then be used to approximate the shape of the energy potential for each DW chirality.

H_x was increased from 0 - 400 Oe in increments of 5 Oe. The simulation was performed in a quasi-static manner where each time the magnetic field was incremented, the magnetization state was allowed to relax in each field step before any further increment. The exact same simulation was then repeated, but with the field incremented in the opposite direction i.e: from 0 to -400 Oe. Figure 5.7 shows the results of depinning simulations for both depinning directions.

The figure also shows the approximate shapes of the notches' energy barriers/wells deduced from the depinning behaviour. In each set of results, the left **M-H** curves show the applied field needed to depin the DW to the right (i.e away from notches) while the curves on the right show the field needed to depin the DW to the left (i.e through the notches). The **M-H** curves indicate the nature of the notches pinning potential and whether or not an intermediate metastable state was formed during depinning.
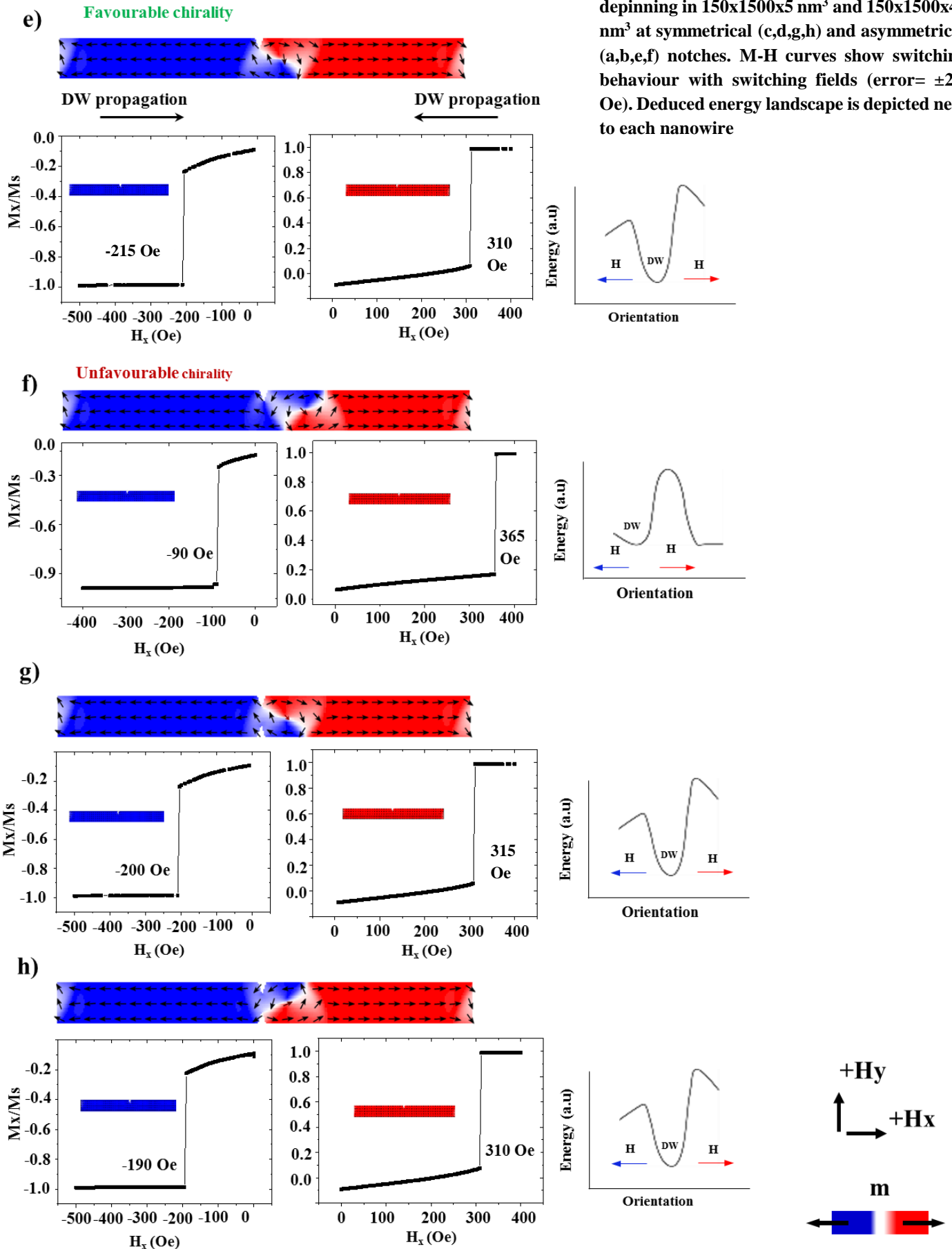
t= 5 nm

a)

Favourable chirality

DW propagation →

← DW propagation

−80 Oe

95 Oe

b)

Unfavourable chiralitiy

−55 Oe

Intermediate stage

−75 Oe

−75 Oe

c)

−115 Oe

110 Oe

d)

−115 Oe

110 Oe

+Hy

+Hx

m

Figure 5.7: Micromagnetic Simulation of DW depinning in 150x1500x5 nm³ and 150x1500x40 nm³ at symmetrical (c,d,g,h) and asymmetrical (a,b,e,f) notches. M-H curves show switching behaviour with switching fields (error= ±2.5 Oe). Deduced energy landscape is depicted next to each nanowire

For the case of the TDW with 'favourable chirality' pinned at the single notch, the simulation results indicated the depinning fields $\mathbf{H_d}$ for +ve and −ve field directions to be equal to 95 and -85 Oe ± 2.5, respectively. Figure 5.7(a) suggests that the TDW is symmetrically pinned in this case, and so the slight differences in the +ve and −ve depinning fields were attributed to the asymmetry in the notch shape due to the mapping/meshing of the notch edges by the simulation software. Despite this, the similarity of the depinning fields for the two directions indicates that the notch presents a potential well to the DW (Figure 5.7(a)).

For the 'unfavourable chirality (Figure 5.7(b)), the depinning was more complex. The fields required to completely depin the TDW in both the +ve (through the notch) and −ve directions (away from notch) were symmetrical (±75 Oe), suggesting that the overall energy landscape was a potential well. However, when depinning at -75 Oe, the TDW went through an intermediate magnetisation state before completely depinning from the notch. This was clearly indicated by the kink in the $\mathbf{M\text{-}H}$ curve for $-75 \leq \mathbf{H_d} \leq -55$ Oe. This metastable state adds to the complexity of the switching energy landscape, and could potentially contribute to stochasticity if it was bypassed in a stochastic manner by thermal excitations.

In order to understand the intermediate state more fully, the simulation was repeated, but this time with TDW being nucleated at the right side of the notch and propagated to the left, to ensure symmetry. Figure 5.8 shows the magnetic evolution details. The results show the TDW depinned from the right edge of the notch into the left edge of it (Figure 5.8(2)). This state seems to be more energetically favourable than the complete depinning state as long as the applied field is between 55 and 75 Oe. The total energy showed a slight drop in that field range (inset in Figure 5.8). This suggests the presence of a small potential well; since the TDW will have to cross an energy gradient to go back to the original pinned state as it passes through the constricted region below the apex of the notch.
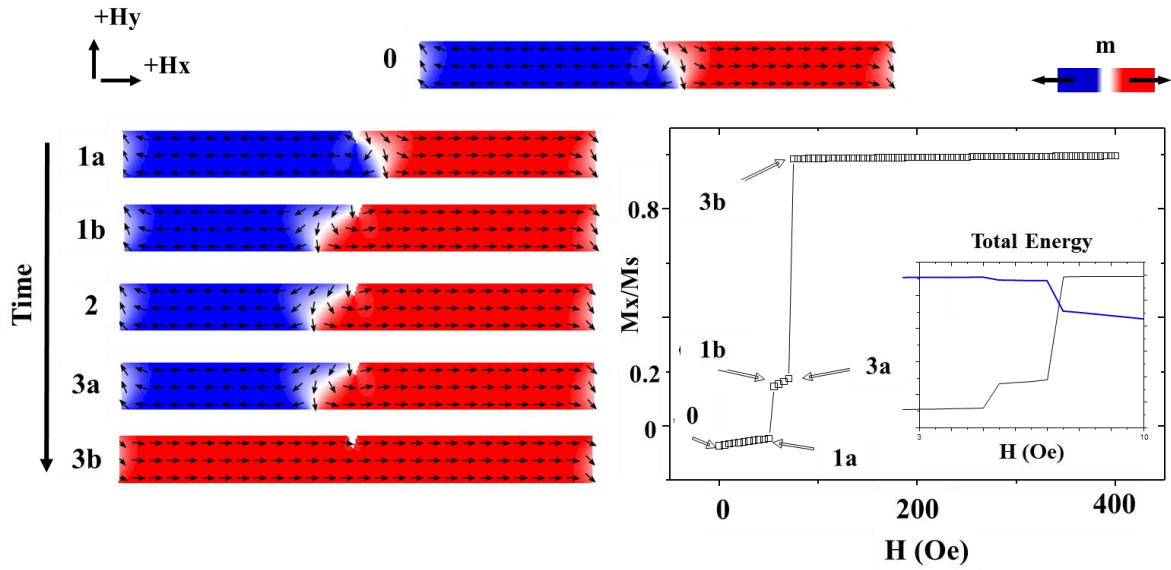
Figure 5.8: Simulation of 'unfavourable chirality' TDW depinning via a metastable state. TDW moves to the left side of notch while being pinned (1a-1b). DW remains pinned at (2) before depinning at (3). Kink between 1b-3a in M-H curve indicate the intermediate metastable stage. Inset shows total energy curve plotted on same graph as Mx/Ms.

While applied field was increased, the Zeeman energy continued to increase, and at H_d= 75 Oe ± 2.5, the TDW eventually surpassed the switching energy gradient and depinned the notch.

The results for this geometry were different from the results obtained in similar simulations performed by Hayashi *et al* [3], where H_d for crossing the notch was observed to be much higher than H_d for depinning in the opposite direction indicating the existence of a potential barrier. Such difference in behaviour could be attributed to the different nanowire geometry used by Hayashi *et al*.

In the case when the 'favourable chirality' VDW pinned at a single notch wire (Figure 5.7(e)) the field required to depin DW in the −ve direction (H_d=-215 Oe) was less than that needed to depin the DW in the +ve direction (H_d=310 Oe), suggesting the existence of an asymmetric potential well. However, for the vortex DW with 'unfavourable chirality' (Figure 5.7(f)) the field needed to depin it in the +ve direction (H_d = 365 Oe) was much greater than that required
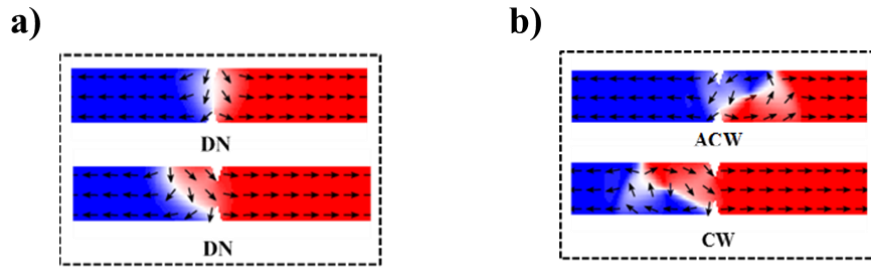
Figure 5.9: Snapshot of the simulation showing DW/notch interaction as it propagates from right to left of symmetric notches. The VDW remains pinned with bottom notch after crossing to the other side causing chirality reversal (right). The TDW depins from upper notch and remains pinned with bottom notch (left).

for depinning in the −ve direction, ($\mathbf{H_d}$= -90 Oe). This clearly suggests that the energy landscape resembles an energy barrier rather than a well.

For the nanowires with double notches, the depinning behaviour was similar to that observed for depinning of 'favourable chirality' DWs in single notches, and thus suggested a symmetric potential well for the TDWs and an asymmetric well for the VDWs (Figure 5.7(c)&(d) and Figure 5.7(g)&(h)). This similarity is attributed to the tendency of the DWs to primarily pin at the notch representing the "favourable" configuration in the single notch geometry, due to energitaclly favourable state, as was mentioned previously.

Interestingly, the simulation for the double notches showed that the DWs have remained pinned to one notch that represented the 'favourable chirality' configuration, when the DW passed one side of the notch. In the case of a VDW such asymmetric pinning behaviours have resulted in a reversal of VDW chirality. This observation will be utilized later, in chapter 9, where it is shown how this behaviour can be exploited as part of a chirality-based DW logic architecture.

In summary, from the simulations done above, the following may be concluded:

1) The depinning process of DWs in nanowire magnetic systems can be complex in nature even when considering defect sites with simple geometries. Such complexities can arise

due to DWs passing through intermediate states during their depinning process and/or the defects presenting asymmetric energy landscapes to the DWs.

2) DW depinning fields and depinning mechanisms depend strongly on DW spin structure, resulting in different forms of energy landscapes for vortex and transverse DWs. Asymmetric defect sites such as single notches are also highly sensitive to the chirality of the DWs.

3) Double notch defects are insensitive to DW chirality and might be good candidates for a nanowire magnetic system that exhibits single-mode DFD.

5.2 Experimental measurement of VDW depinning in Py nanowires

The simulation results done in the previous section showed that the chirality of the DW can have a strong effect on the field required to depin it from a defect site. To produce single-mode DFDs from defect sites it is therefore important to select a defect geometry that can either filter, or is insensitive to the DW chirality. The aim of this section is to experimentally investigate whether nanowires with double notch geometries of various sizes, which were shown to be chirality insensitive in the previous section, can be produce a single-mode DFD nanomagnetic system. This system can then be used in further stochastic studies.

5.2.1   Nanowire Designs

Two sets of nanowires with widths $w = 600$ nm and $w = 400$ nm, length l=20 µm and thicknesses t = 20 nm were fabricated. Each nanowire contained a double notch defect with depth $N_d = 0.2W$, $0.25W$ or $0.3W$. All the nanowires were connected to a rectangular nucleation pad of length $l = 5$ µm to act as a source of DWs [21, 22]. The end of the nanowire was designed to have narrow end to prevent nucleation due to its high shape anisotropy. A schematic diagram of the nanowire system is shown in Figure 5.10.
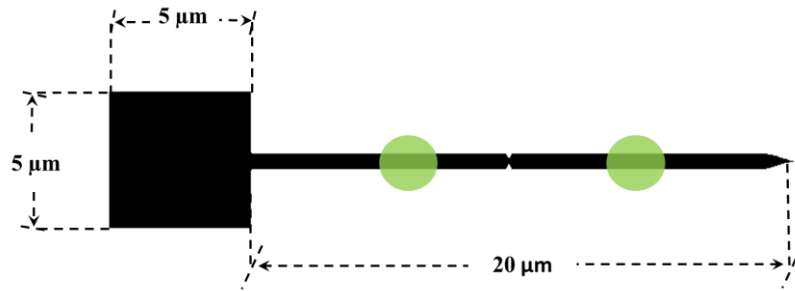
Figure 5.10: Schematic of designed double notch nanowire magnetic system with nucleation pad. Green circles indicate Laser spot indicating measured regions before and after the notches.

SEMs of the fabricated notch and nanowire geometries are shown in Figure 5.11. The nanowires designed to have $w=$ 600 nm had an average width of $w=$ 637 nm (6 % error). The nanowires with $w=$ 400 nm had an average width = 429 nm (7% error). The notches also have depths that are similar, but not identical to their design values.

The thickness and geometry of the wires were chosen to strongly favour the nucleation of VDWs, and to produce a large S/N ratio in the focused MOKE magnetometer (as higher thicknesses result in a stronger Kerr-angle rotation leading to clearer MOKE signal). VDWs were also selected as the simulation study above indicated that TDWs could form metastable states during depinning, a complex behaviour that was likely to cause additional stochasticity.
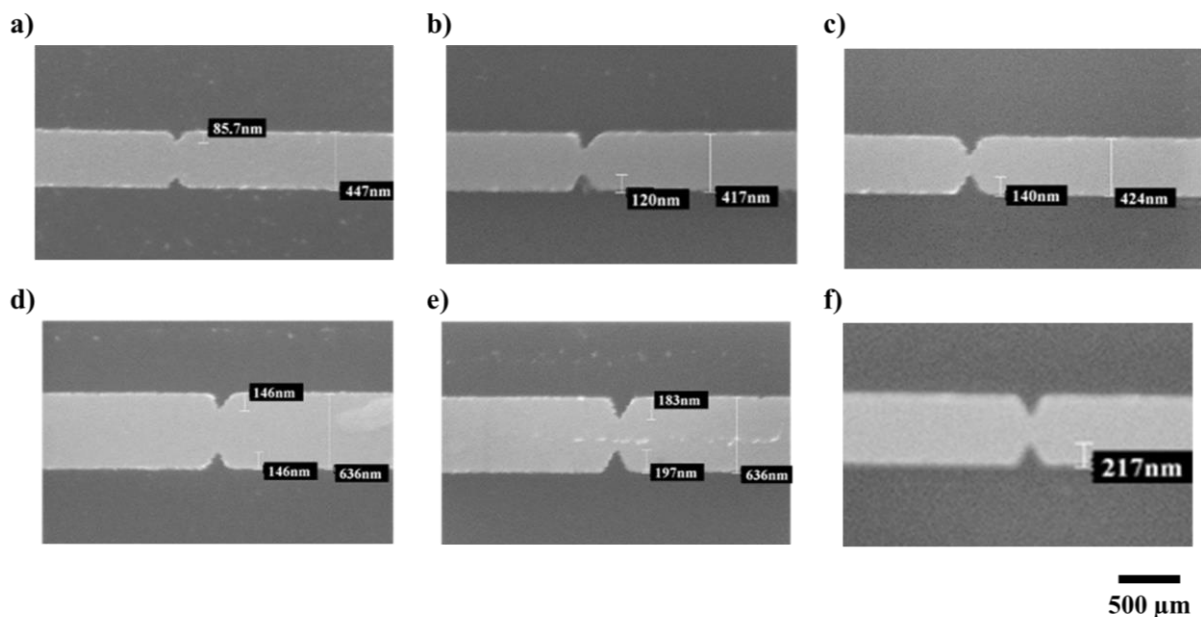
Figure 5.11: SEM images of Py nanowires with widths of 400 nm (a)-(c) and 600 nm (d)-(f). (a): N_d = 0.2W, (b): N_d = 0.25W, (c): N_d = 0.3W, (d): N_d = 0.2W, (e): N_d = 0.25W, (f): N_d = 0.3W

In fact, the remaining studies carried in this thesis will all focus on thick nanowires that favour VDWs.

5.2.2 Focused MOKE measurements of DFDs

The six nanowire geometries were measured using the focused MOKE setup described in section 4.4.1 An alternating magnetic field $\mathbf{H_x}$ with a peak-to-peak amplitude of 350 Oe was applied to the nanowires in order to nucleate DWs from the pads, transport them to the notches and then depin them. One hundred single shot measurements of the nanowires' switching were measured before and after the notches by focusing the system's laser spot at the locations indicated in Figure 5.10, in order to measure the DW injection field's distributions (IFDs) and the notches' DFDs. An algorithm was implemented in C++ in order to read the coercivity in each file automatically and write it into a table.

Figure 5.12 plots the IFDs and DFDs for each nanowire as histograms (Red: w=400 nm, Blue: w=600 nm). All of the nanowires' DFDs exhibited multiple peaks suggesting that the nanowires (of both widths) exhibited multiple switching modes to varying degrees.
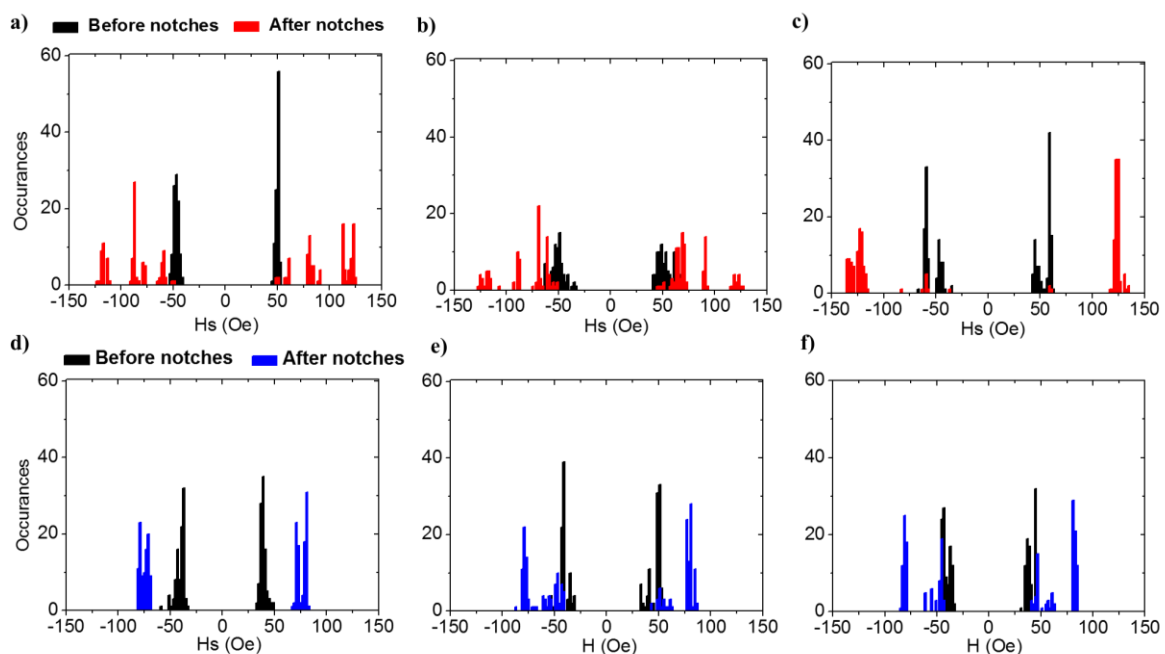

Figure 5.12: IFDs (black) and DFDs (red or blue) measured for nanowires with w= 400 nm (a)-(c) and w= 600 nm (d)-(f). (a): N_d = 0.2W, (b): N_d = 0.25W, (c): N_d = 0.3W, (d): N_d = 0.2W, (e): N_d = 0.25W, (f): N_d = 0.3W. Red is for w= 400 nm. Blue is for w= 600 nm.
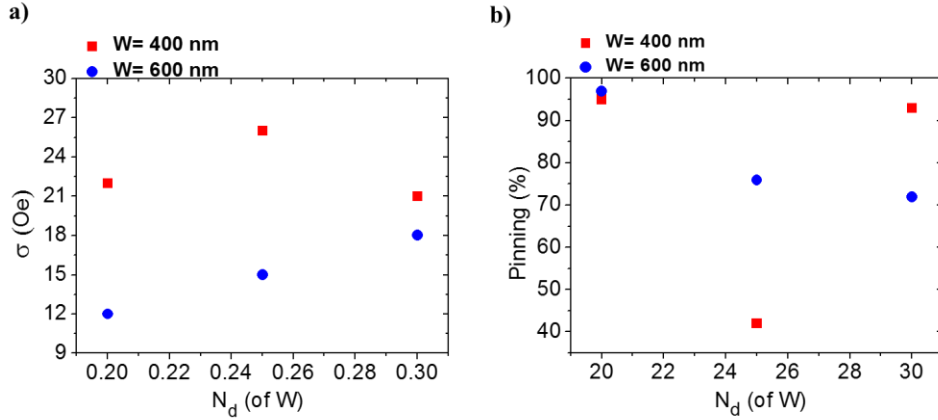
Figure 5.13 (a): Plot showing standard deviation (σ) of DFDs in measured histograms. (b): Plot showing pinning percentage of DFDs in measured histograms. w=400 nm (red) and w= 600 nm (blue).

Measurements were repeated for other copies of the nanowires with the same geometries and these also showed similar multi-mode DFDs. These results were unexpected as previous simulations have shown a single-mode behaviour at nanowires with double notches. This clearly indicate a complex behaviour counter-intuitive to the assumption that symmetrical notches will show simple depinning behaviour. This will be thoroughly investigated in the next chapter.

It can be deduced quantitatively from the standard deviation of the DFD (Figure 5.13), and the fraction of DWs that are pinned (as given by looking at the overlap between the DFD and IFD) that for nanowires with $w = 400$ nm pinning/depinning is best defined for $N_d = 0.3W$; while for nanowires with $w = 600$nm, switching is most reliable with $N_d = 0.2W$. These two metrics will be used frequently throughout this thesis to quantify the degree of stochasticity shown by a defect site.

The highly stochastic DFDs cannot be attributed to thermal activation as such effects are typically reflected in the width of Gaussian-like DFDs, and do not generally cause multiple depinning modes with widely spaced depinning fields [5]. However, the mean injection fields for all of the measured nanowires were in the range of 40-50 Oe which is above the typical Walker Breakdown (WB) field H_{WB} for Py nanowires [23, 24]. Hence, it is expected that the

DWs were undergoing WB transformations when they encountered the defect site. This suggests that stochasticity observed was of dynamical origin: i.e. it was caused by DWs arriving at the defect site in a range of configurations, and thus forming different pinned states with different depinning fields. A study of the WB process for this geometry was therefore required.

5.2.3   Studying WB in 400 nm wide Py nanowires

In this section dynamic micro-magnetic simulations were carried for domain wall propagation in nanowires with $w = 400$ nm and t = 20 nm. Unlike the simulations in section 5.1.2, these simulations used a realistic damping coefficient $\alpha = 0.02$ to allow WB dynamics to be simulated. This allowed the simulations to be representative of the manner in which the DWs approached the defect site in the focused MOKE measurements.

Published studies [9, 25] have indicated that DWs can undergo propagation in three different regimes: the linear regime, the periodic/oscillatory regime and the turbulent regime. As elaborated in section 3.3.3, the linear regime occurs below the Walker Breakdown field (H_{WB}) and domain walls propagate linearly at a velocity that increases linearly with the driving fields. At fields above H_{WB} the DWs enter the oscillatory regime and undergo periodic transformations of their spin structure. These in turn induce phases of retrograde motion that decreases the domain wall velocity. Beyond a further critical field the DW enters the turbulent regime of motion, where its velocity again begins to increase with applied field and the DW dynamics become increasingly complex.

Simulations were performed using the OOMMF's 3D simulator for a nanowire with dimensions 400 x 8000 x 20 nm^3. The mesh size was set to 4 x 4 x 20 nm^3. As mentioned earlier, this geometry favours VDW type. Propagation of DWs was simulated at H_x = -5, -10,

-15,-17, -20, -50, -100 and -200 Oe to investigate the three regimes. Figure 5.14 below shows the behaviour of the DW in each regime.

The simulation result showed that H_{WB} = -17.5 ± 2.5 Oe (a velocity vs field graph is provided in Appendix 2.3). This value is in agreement with reported H_{WB} values for similar nanowire geometries [25, 26].

The turbulent regime began at H = -75 ± 12.5 Oe. In the experimental measurements, the mean injection field was between -40 to -60 Oe for all of the nanowires, and hence it can be deduced that the DWs approached the notches within the oscillatory regime of motion.
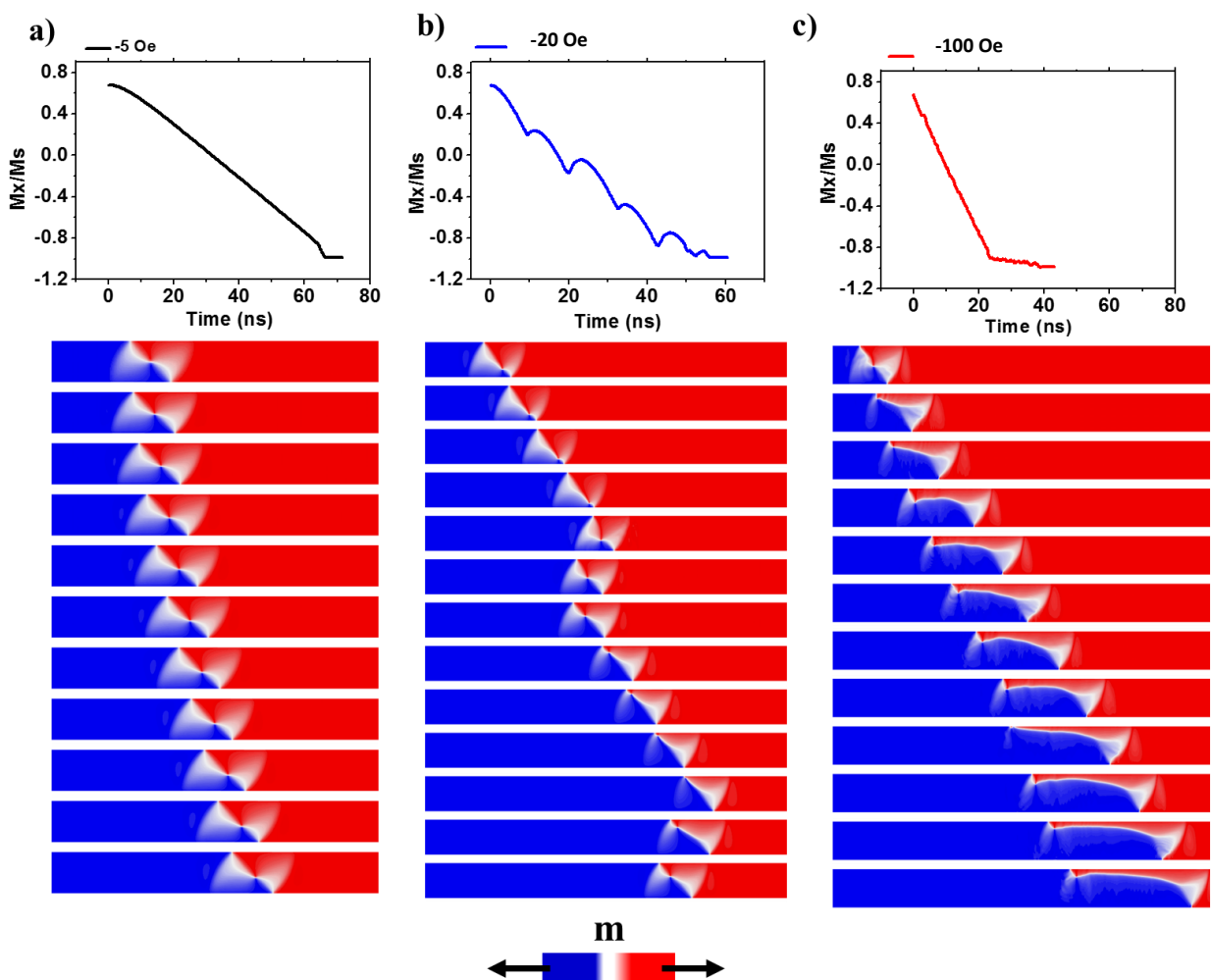
Figure 5.14: Micromagnetic simulation snapshots and magnetisation curves showing DW dynamics in nanowires of *w*= 400 nm and t= 20 nm when propagated at linear regime (H$_x$ = -5 Oe) (a), periodic regime (H$_x$ = -20 Oe) (b) and turbulent regimes (H$_x$ = -100 Oe) (c).

In all regimes, it was observed that the VDW preserved its chirality; however transformations and deformations of DW structure occurred in both the periodic and turbulent regimes. In the (experimentally relevant) periodic regime, it was observed that the core of the VDW translated in a transverse manner between the top and bottom of the nanowire, annihilating and reappearing at each edge. When the vortex core annihilated at the bottom edge, this resulted in the DW temporally assuming an UP TDW-like shape (Figure 5.15-1). The opposite mechanism occurred when the core moved to the top edge, with the DW assuming a DN TDW-like shape (Figure 5.15-4). The transverse translational movement of the core induced a periodic retrograde motion of the VDW.

The key finding here is that when the DWs were propagated towards the notch in the experimental measurements they were undergoing periodic transformations of their structures, and eventually arrived at the notches where they were pinned in completely different configurations in different field cycles. This offers an explanation of the multi-mode DFDs that were measured even for symmetrical double notches, which were predicted to show single mode DFDs due to their insensitivity to chirality. Direct simulation of the stochasticity induced by dynamic effects will be explored in later chapters.
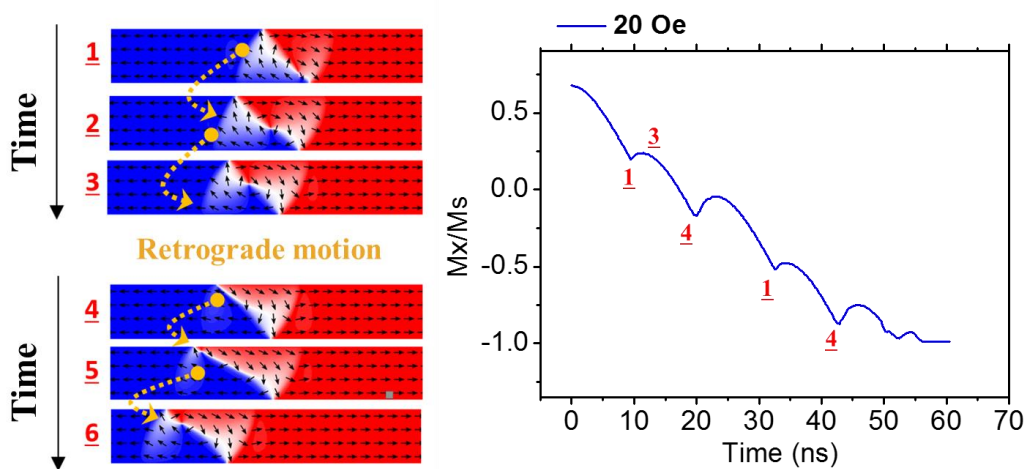

Figure 5.15: DW dynamics in the periodic regime of motion at H = 20 Oe in a 400 x 8000 x 20 nm³ Py nanowire. (1-3) and (4-6) showing the retrograde motion of the DW as the core moves away from the center to the nanowire edges.

5.2.4 Supressing WB induced stochasticity with transverse fields

In the previous section the high stochasticity of the DW pinning in the experimental measurements was attributed to DW propagation above WB. Therefore, one possible method to reduce the dynamically-induced stochasticity would be to attempt to modify or suppress WB. One method of achieving this has been modelled by Bryan *et al* [27] in thin nanowires with TDWs and verified experimentally by others [8, 28]. Bryan *et al*'s approach suggests using an external transverse field to make anti-vortex nucleation and attachment to the DW structure energetically unfavourable, thus hindering WB transformations. In this section, the method proposed by Bryan *et al* is applied to the nanowires measured and simulated here in order to try to suppress WB induced stochasticity for the aim of creating a single-mode DFD.

Initial micro-magnetic simulations were performed to investigate the effect of applying transverse field on the WB transformation. Since nanowires with w=200 nm and t = 20 nm produced the same WB behaviour as the w = 400 nm, t = 20 nm nanowires, simulations were performed on the 200 nm wide nanowires to save simulation time. Transverse fields, H_y = 30 Oe, 100 Oe and 150 Oe were applied in separate simulations. Magnetisation images and normalized M_s vs time graph are presented in Figure 5.16.

The effects of applying transverse fields can be clearly seen in the results presented in Figure 5.16, where the net forward motion and thus velocity of the VDWs increased with H_y. This can be seen in the extended duration of forward motion in each period, leading to an increase in the average slope of the graph (see for example between points 1 and 2 in each curve). Upon examining the magnetisation simulation snapshots, it was clear that the applied transverse field suppressed the transformations of the DW when it was in the DN TDW-like shapes.

This was due to the fact that the transverse field hindered (facilitated) the VDW cores' transverse movement between the top and bottom edge of the nanowire when the field applied was anti-parallel (parallel) to the magnetisation of the TDW-like state. This can be seen in the graph by the elongated and shortened parts of the WB cycle which correspond to the anti-parallel and parallel TDW-like configurations. The net effect was a temporary 'locking' of the DW into one of the TDW-like configurations. Interestingly, the TDW-like configuration that gets 'locked' is the one that is anti-parallel to the direction of the transverse field.
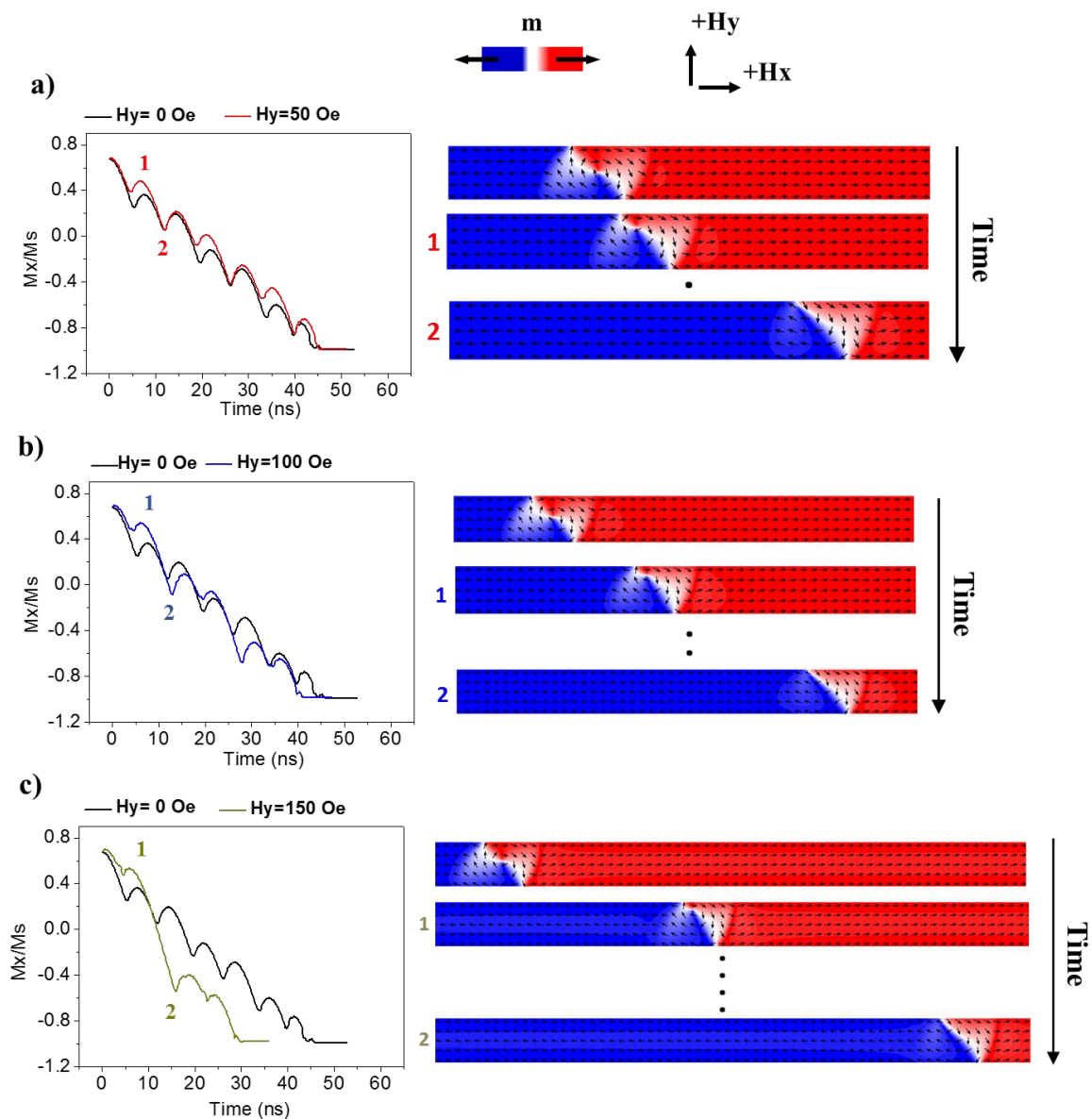
Figure 5.16: Micromagnetic simulations of DW propagation at the oscillatory regime in Py nanowire 200x 8000x20 nm³ when transverse field +Hy 50 Oe (a), 100 Oe (b) and 150 Oe (c) was applied.

114

In conclusion, the transverse field allows the DW to propagate with its TDW-like structure for longer time, leading to a partial suppression of WB transformations. As the DW then remains in a single state for a greater proportion of its propagation, one might therefore conclude that dynamic stochasticity would also be somewhat suppressed by the application of transverse field.

5.2.5 Revisiting MOKE measurement with transverse field

To examine whether dynamic stochasticity could be suppressed by transverse fields, the MOKE measurements of the $w = 400$ nm nanowires were repeated but with applying transverse fields, $H_y = 45$ Oe and 140 Oe. The results of these measurements are shown in Figure 5.17.
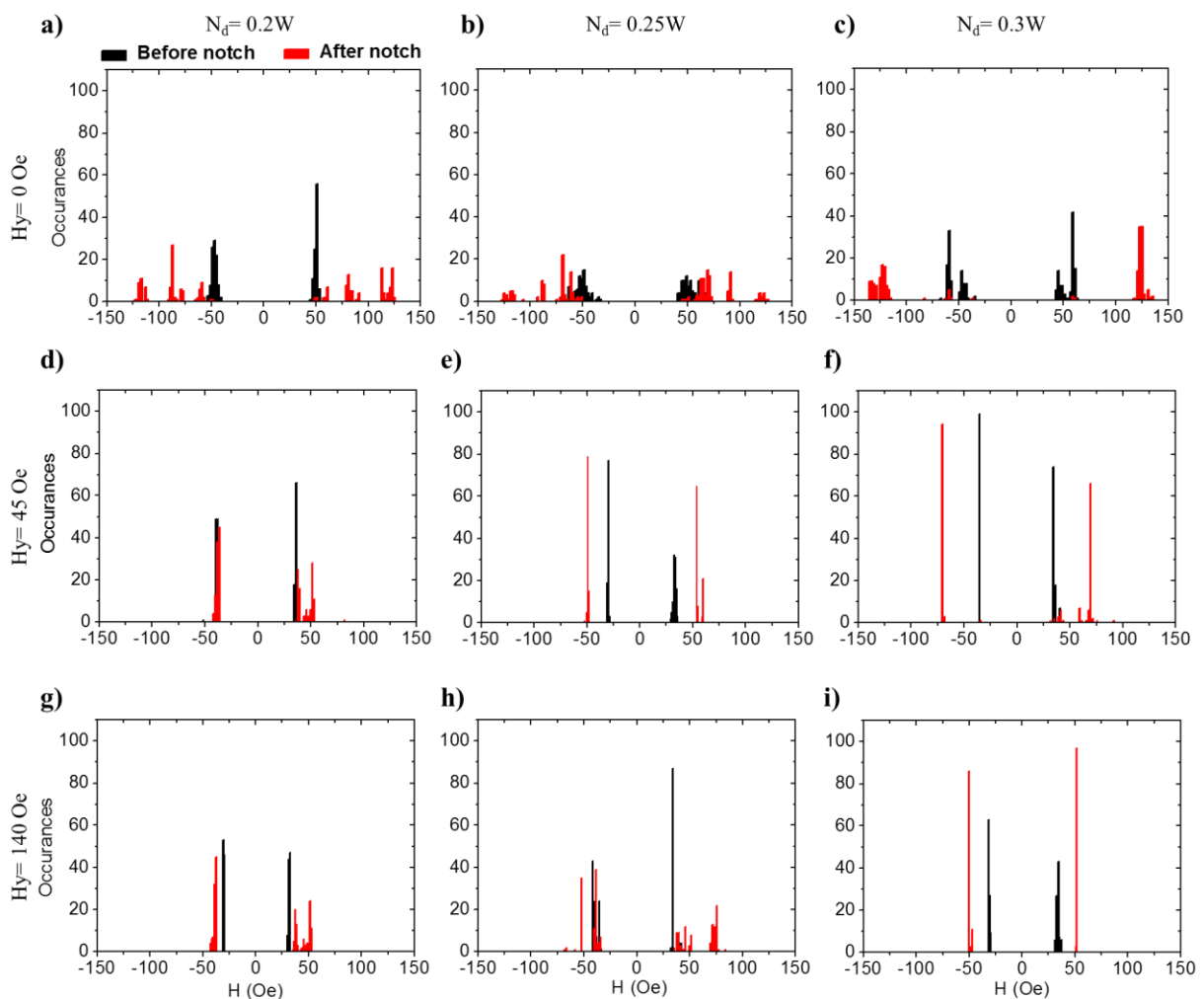
Figure 5.17: IFDs (black) and DFDs (red) measured for nanowires 400x20000x20 nm³ with transverse applied field Hy = 0 Oe (a-c), Hy= 45 Oe (d-f) and Hy= 140 Oe (g-i). Double notch with N$_d$= 0.2W (a,d,g), N$_d$= 0.25W (b,e,h) and N$_d$= 0.3W (c,f,i).

The results show that the transverse field has several effects: (1) a narrowing of the IFDs and DFDs, (2) reductions in injection and depinning fields and (3) reductions in the number of peaks in the DFD compared with that observed at $H_y = 0$. Point (3) in particular indicates that the transverse field managed to partially suppress dynamically induced stochasticity. The reduction in stochasticity can be further analysed quantitatively by calculating the standard deviation (σ_d) of the nanowires' DFDs (Figure 5.18(a)). This data shows a reduction in the σ_d, as H_y increases. Under transverse field the nanowire with $N_d = 0.3W$ seems to give the narrowest DFD and maximum pinning percentage. This is understandable as larger notches have been previously shown to produce large potential wells/barriers and high pinning probabilities [18, 29]. It would be expected that such strong pinning sites would confine the number of pinned DW configuration leading to few energetically feasible depinning modes (as will be discussed in the next chapter).

However, despite the improvements described above it is seen that the transverse field could not completely stabilize the DW depinning process into a single mode, with few multiple peaks being observed for all of the nanowires even at the highest transverse fields. This could suggest that the structure of the nucleated DW is reacting to the transverse field in a manner that reduces
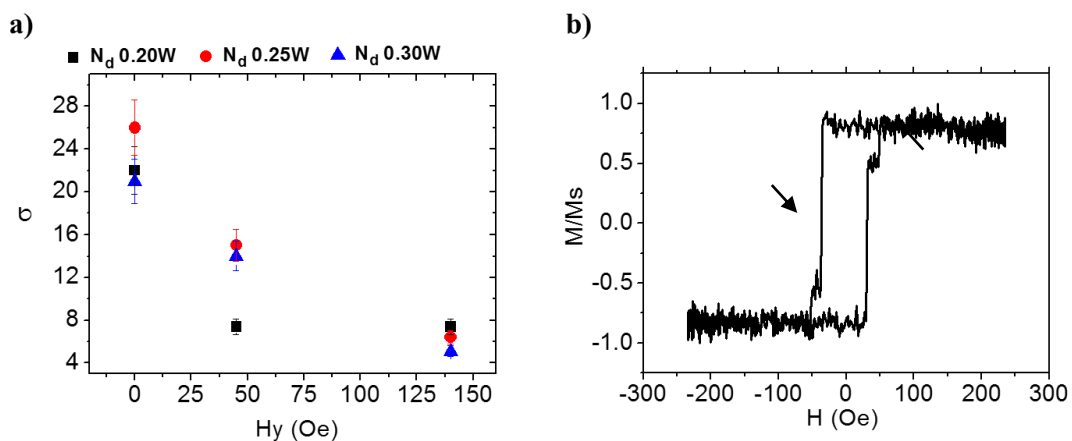

Figure 5.18: (a): Plot showing the change of the DFD standard deviation w.r.t increasing transverse field. (b): Single-shot M-H curve for a nanowire with $N_d = 0.3W$ measured in the region before notch. Arrows indicate the step in the loop that suggests DW deformation.

the WB transformations, resulting in a reduction in the depinning stochasticity. Such DW reaction could be in the form of delaying the DW core transversal movement as the simulation suggested previously (refer to Figure 5.16). It is important to mention that increasing the transverse field has resulted in the appearance of s step-response in the **M-H** curve for the region before the notch (indicated by arrows in Figure 5.18(b)). This might suggest some form of pinning being induced by the transverse field as hinted by Bryan *et al* [30]. Nevertheless, there seem to be good evidence that although a transverse field can't completely suppress WB, it can help reduce its induced stochasticity.

5.3 Conclusions

This chapter has compared the results of quasi-static simulations of DW pinning and depinning at artificial defect sites with experimental measurements of similar nanostructures, with the overall aim of identifying geometries that produce highly reliable, single-mode depinning field distributions.

In the quasi-static simulations performed with high damping coefficients (α=0.5), it was found that the energy landscapes for asymmetric notches could be complex for TDWs. VDWs pinned at the same defects in these nanowires showed less complexity in their depinning processes, but still experienced chirality dependent effects with the 'favourable chirality' viewing the defect site as an energy well, while 'unfavourable chirality' viewed it as an energy barrier, in agreement with published literature [3]. In symmetric notches, all DWs showed chirality independent behaviour, suggesting that double notches in thick nanowires might be good candidates for obtaining single-mode depinning behaviour.

The above hypothesis was then examined by performing experimental measurements of DW pinning at symmetrical double-notch defect sites. However, all of the measured nanowires exhibited highly stochastic, multi-peak depinning field distributions suggesting that the DWs

were pinning in a variety of magnetisation states. Dynamic micromagnetic simulations allowed this to be attributed to WB transformations that deformed and altered the spin structure of the DWs periodically as they propagated to the defect sites. These transformations can create stochasticity because they cause DWs to interact with and pin at defect sites in a range of spin configurations, each of which will have a different switching field.

Suppressing or mitigating the effects of WB transformations is clearly essential to obtaining a system with single mode switching. Attempts were made to achieve the latter by applying an external transverse field to supress the VDW core movement. Upon modelling and measuring magnetic switching with applied transverse field, it is concluded that the transverse field in VDW nanowires plays a role in improving DW propagation and partially suppressing WB transformation by 'locking' the DW into a single state for longer periods of time. However, this suppression is not enough to produce a system with a single-mode behaviour and could also result in substantially altering the DW structure leading to further complexities. A different approach was required, which will be the topic of the next chapter.

5.4. References

[1]   J. Akerman, M. Munoz, M. Maicas, and J. L. Prieto, "Stochastic nature of the domain wall depinning in permalloy magnetic nanowires," *Physical Review B,* vol. 82, Aug 31 2010.

[2]   J. Akerman, M. Muñoz, M. Maicas, and J. L. Prieto, "Selective injection of magnetic domain walls in Permalloy nanostripes," *Journal of Applied Physics,* vol. 115, p. 183909, 2014.

[3]   M. Hayashi, L. Thomas, C. Rettner, R. Moriya, X. Jiang, and S. S. P. Parkin, "Dependence of current and field driven depinning of domain walls on their structure and chirality in permalloy nanowires," *Physical Review Letters,* vol. 97, p. 4, Nov 2006.

[4]   M. Hayashi, L. Thomas, C. Rettner, R. Moriya, and S. S. P. Parkin, "Direct observation of the coherent precession of magnetic domain walls propagating along permalloy nanowires," *Nature Physics,* vol. 3, pp. 21-25, Jan 2007.

[5]   M.-Y. Im, L. Bocklage, P. Fischer, and G. Meier, "Direct Observation of Stochastic Domain-Wall Depinning in Magnetic Nanowires," *Physical Review Letters,* vol. 102, Apr 10 2009.

[6]   U.-H. Pi, Y.-J. Cho, J.-Y. Bae, S.-C. Lee, S. Seo, W. Kim*, et al.*, "Static and dynamic depinning processes of a magnetic domain wall from a pinning potential," *Physical Review B,* vol. 84, p. 024426, 2011.

[7]   R. Moriya, L. Thomas, M. Hayashi, Y. B. Bazaliy, C. Rettner, and S. S. Parkin, "Probing vortex-core dynamics using current-induced resonant excitation of a trapped domain wall," *Nature physics,* vol. 4, pp. 368-372, 2008.

[8]   D. Eastwood, J. King, L. Bogart, H. Cramman, and D. Atkinson, "Chirality-dependent domain wall pinning in a multinotched planar nanowire and chirality preservation using transverse magnetic fields," *Journal of Applied Physics,* vol. 109, p. 013903, 2011.

[9]   M. Munoz and J. L. Prieto, "Suppression of the intrinsic stochastic pinning of domain walls in magnetic nanostripes," *Nature Communications,* vol. 2, Nov 2011.

[10]   W. Wernsdorfer, E. B. Orozco, K. Hasselbach, A. Benoit, B. Barbara, N. Demoncy*, et al.*, "Experimental evidence of the Neel-Brown model of magnetization reversal," *Physical Review Letters,* vol. 78, pp. 1791-1794, Mar 3 1997.

[11]   W. Wernsdorfer, B. Doudin, D. Mailly, K. Hasselbach, A. Benoit, J. Meier*, et al.*, "Nucleation of magnetization reversal in individual nanosized nickel wires," *Physical Review Letters,* vol. 77, pp. 1873-1876, Aug 26 1996.

[12]   C. Wuth, P. Lendecke, and G. Meier, "Temperature-dependent dynamics of stochastic domain-wall depinning in nanowires," *Journal of Physics-Condensed Matter,* vol. 24, Jan 18 2012.

[13]   C. Wuth, L. Kolbe, and G. Meier, "Thermally activated stochastic domain-wall depinning in ferromagnetic nanowires," *Journal of Applied Physics,* vol. 114, Sep 14 2013.

[14]   J. Briones, F. Montaigne, M. Hehn, D. Lacour, J. R. Childress, and M. J. Carey, "Stochastic and complex depinning dynamics of magnetic domain walls," *Physical Review B,* vol. 83, Feb 10 2011.

[15]   J. P. Attane, D. Ravelosona, A. Marty, Y. Samson, and C. Chappert, "Thermally activated depinning of a narrow domain wall from a single defect," *Physical Review Letters,* vol. 96, Apr 14 2006.

[16]   R. D. McMichael and M. J. Donahue, "Head to head domain wall structures in thin magnetic strips," *Ieee Transactions on Magnetics,* vol. 33, pp. 4167-4169, Sep 1997.

[17]   *Object Orientated Micromagnetic Framework (OOMMF)* Available: http://math.nist.gov/oommf/.

[18]   D. Eastwood, L. Bogart, and D. Atkinson, "Scaling Behaviour of Chirality Dependent Domain Wall Pinning in Planar Nanowires," *memory,* vol. 3, p. 11, 2010.

[19]   D. Petit, A.-V. Jausovec, D. Read, and R. P. Cowburn, "Domain wall pinning and potential landscapes created by constrictions and protrusions in ferromagnetic nanowires," *Journal of Applied Physics,* vol. 103, p. 114307, 2008.

[20]   L. K. Bogart, D. Atkinson, K. O'Shea, D. McGrouther, and S. McVitie, "Dependence of domain wall pinning potential landscapes on domain wall chirality and pinning site geometry in planar nanowires," *Physical Review B,* vol. 79, Feb 2009.

[21]   R. P. Cowburn, D. A. Allwood, G. Xiong, and M. D. Cooke, "Domain wall injection and propagation in planar Permalloy nanowires," *Journal of Applied Physics,* vol. 91, pp. 6949-6951, 2002.

[22]   Y. Yokoyama, Y. Suzuki, S. Yuasa, K. Ando, K. Shigeto, T. Shinjo*, et al.*, "Kerr microscopy observations of magnetization process in microfabricated ferromagnetic wires," *Journal of Applied Physics,* vol. 87, pp. 5618-5620, 2000.

[23]   G. S. D. Beach, C. Knutson, C. Nistor, M. Tsoi, and J. L. Erskine, "Nonlinear domain-wall velocity enhancement by spin-polarized electric current," *Physical Review Letters,* vol. 97, Aug 4 2006.

[24]   M. T. Bryan, T. Schrefl, and D. Allwood, "Dependence of transverse domain wall dynamics on permalloy nanowire dimensions," *Magnetics, IEEE Transactions on,* vol. 46, pp. 1135-1138, 2010.

[25]   X. Jiang, L. Thomas, R. Moriya, M. Hayashi, B. Bergman, C. Rettner*, et al.*, "Enhanced stochasticity of domain wall motion in magnetic racetracks due to dynamic pinning," *Nature Communications,* vol. 1, Jun 2010.

[26]   A. Pushp, T. Phung, C. Rettner, B. P. Hughes, S.-H. Yang, L. Thomas*, et al.*, "Domain wall trajectory determined by its fractional topological edge defects," *Nature Physics,* vol. 9, pp. 505-511, 2013.

[27]   M. T. Bryan, T. Schrefl, D. Atkinson, and D. A. Allwood, "Magnetic domain wall propagation in nanowires under transverse magnetic fields," *Journal of Applied Physics,* vol. 103, p. 073906, 2008.

[28]   S. Glathe, R. Mattheis, and D. Berkov, "Direct observation and control of the Walker breakdown process during a field driven domain wall motion," *Applied Physics Letters,* vol. 93, p. 072508, 2008.

[29]   C. C. Faulkner, M. D. Cooke, D. A. Allwood, D. Petit, D. Atkinson, and R. P. Cowburn, "Artificial domain wall nanotraps in Ni81Fe19 wires," *Journal of Applied Physics,* vol. 95, pp. 6717-6719, 2004.

[30]   M. Bryan, D. Atkinson, and D. Allwood, "Multimode switching induced by a transverse field in planar magnetic nanowires," *Applied physics letters,* vol. 88, p. 032505, 2006.

Chapter 6:

The Effects of Nanowire Thickness and Notch Geometry on Dynamic Stochasticity

In the previous chapter it was concluded that a dominant source of stochasticity in DW depinning resides in the WB transformations that alter the spin structure of DWs as they propagate. Such alterations can affect the way DWs interact with defect sites, due to variations occurring in their spin structure.

Both H_{WB} and form of the WB transformations are strongly affected by a nanowire's width and thickness [1-3], with thickness having the stronger effect on H_{WB} (refer to eq. 3.13). Several studies [1, 2] have shown that increasing thickness would move H_{WB} to lower fields. However this does not necessarily result in an increase in the stochasticity of DW pinning/depinning, because a DW's dynamical interaction with a defect site also has a significant dependence on the geometries of both the defect and that of the nanowire [4, 5]. This interaction determines the pinning landscape and thus can have an effect on depinning stochasticity.

It is the aim of this chapter to investigate how changing the thickness of a nanowire and the depth and symmetry of notch-shaped defects can affect the dynamic pinning/depinning of DWs, and thus the stochastic nature of nanowire switching. Moreover, the possibility of finding a nanowire/notch system with geometrical parameters that can intrinsically produce single-mode pinning/depinning behaviours is explored. The studies presented will intrinsically explore the dynamic regime, as in all of the studied nanowires $H_{inj} > H_{WB}$, and thus DWs were always propagating above H_{WB}. Moreover, a simulation method has been devised to study how dynamic DW/notch interactions can yield depinning stochasticity in the same nanowire.

It is shown in this chapter that the vast majority of the nanowire/defect combinations studied show complex and highly stochastic pinning/depinning behaviours. It is also found that symmetrical (chirality-insensitive) pinning site does not necessarily result in a reduction in switching stochasticity, as might be assumed. On the contrary, such pinning sites can create complex interactions with the DW at the vicinity of the notch resulting in varying pinning configurations with distinct depinning fields. Therefore, a system that produces a single-mode switching behaviour should have a defect that interacts with the DW allowing it to have few DW pinning configurations that depin using the same depinning mechanism. Interestingly, it was found that thick nanowires with deep asymmetric defect can exhibit these features.

This study is essential in understanding how DW depinning behaviour gets altered due to different dynamical transformations occurring within DW structure. It also shows how several parameters such as the nature of DW transformation/deformation, shape of WB period, notch pinning strength and depinning mode can interact to influence stochastic switching and (in some cases) enhance it.

6.1. Methodology

Three sets of 400 nm wide Py nanowires were fabricated with thicknesses, $t = 10$ nm, 25 nm and 40 nm using electron beam lithography and lift-off processing. The widths of the nanowires were maintained at 400 nm in all cases. As mentioned earlier, thickness is expected to have a bigger effect on WB transformations than width; hence, the decision to focus on this parameter in the study. The 400 nm width was chosen to allow for good S/N ratio for single-shot MOKE measurements in all of the samples studied.

In each set of nanowires, two notch designs with varying depths (N_d) were studied. The first notch design was a single triangular notch, while the second notch design was a symmetrical

Figure 6.1: Schematic illustration of nanowire designs with double (top) and single (bottom) notch used throughout this chapter. The nanowires are of width w = 400 nm and thicknesses of t= 10, 25 and 40 nm.

double triangular notches. The N_d for the single notches was varied from 0.15W to 0.7W, and

for double notch, N_d was varied from 0.15W to 0.35W (for each notch). In all of the designs,

the notch depth was equal to notch width (N_w). Figure 6.1 shows a schematic diagram of the

two notch designs.

The switching behaviour for each nanowire was investigated by measuring the injection (H_{inj})

and depinning (H_d) field distributions using MOKE setup described in section 4.4.1. The

distributions were obtained by measuring 100 single-shot hysteresis loops, both before and

after the defect sites. The distributions were then plotted as histograms and the degree of

switching stochasticity was analysed using the following metrics:

(1) The form of the depinning field distribution and the visible number of clear depinning

modes (qualitative).

(2) The pinning probability (P_p), i.e. the faction of events in the depinning field distribution

that did not overlap with the injection field distribution (quantitative).

(3) The standard deviation of the depinning field distributions (σ_d) (quantitative).

It is important to note here that in this work σ_d is generally used as a generic measure of spread,

rather than to represent a characteristic shape of a Gaussian distribution, although the latter

analysis does apply to the few systems in which single mode depinning distributions were

observed. Values of σ_d were calculated both for distributions of all switching events, as well

as only for events where the DWs were pinned. This allowed situations with multiple depinning

modes to be differentiated from those with a single depinning mode, in systems where there exist passing DW incidents (i.e. $P_p < 1$). To gain insight into the DWs pinning and depinning mechanisms, micromagnetic simulations were performed for selected nanowire geometries using the MUMAX^3 software package [6]. Since these simulations will be performed to study the dynamical effects at different nanowire thicknesses, it is important that theses simulations be performed in three dimensional cell size and using realistic damping coefficient. Therefore, a cell size of 2.5x2.5x5 nm^3 have been used for nanowires of t=10 nm and t=25 nm while cell size of 2.5x2.5x10 nm^3 was used for t=40 nm. As for the damping coefficient, α was set to 0.02. Typical parameters were used to define the material parameters of NiFe: saturation magnetisation, exchange and magnetocrystalline anisotropy constant at Ms= 860 kA/m, A=13 pJ/m and K=0 J/m^3, respectively.

In order to simulate the range of possible pinning interactions for a dynamically transforming DW, propagating at fields above H$_{WB}$, a new simulation approach had to be developed. The method worked as follows:

1. For each of the nanowire thicknesses studied, the WB process was simulated at a propagation field equivalent to the average value of H$_{inj}$ measured in real nanowires of same thickness.

2. The distance travelled by the DW during a single WB cycle was calculated from the M$_x$/M$_s$ vs time graph generated by the simulation.

3. The length of the WB cycle was divided into ten intervals and simulations of DW pinning were performed with a notch placed in each of these locations (intervals). This allowed for the many possible configurations that the DW could arrive at the notch (under WB transformations) to be simulated. Figure 6.2 shows a schematic of this process.
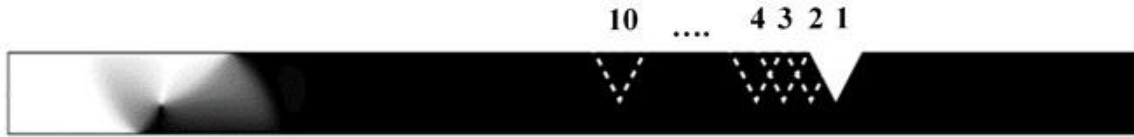
Figure 6.2: Schematic illustration showing how the single/double notch was moved in steps to cover the WB period, in order to simulate the different DW arrival states. Numbers 1-10 indicate the ten locations of the moved defect.

4. For each distinct pinned configuration observed, a quasi-static simulation was performed to calculate its depinning field and mechanism, thus allowing the range of potential depinning fields to be measured

For each nanowire thickness and notch type (single/double) this processes was performed for three different notch depths in order to give an indication of DW-notch interactions across the parameter space studied experimentally. All the simulations were done for both VDW chirality, the CW and ACW.

6.2. Nanowire of t=10 nm and single notch defect

For nanowires of t=10 nm with single notches, MOKE measurements were taken for ten nanowires with varying N_d in order to study their pinning/depinning behaviour over a wide range of notch depths. The analysis presented here will focus on five out of these nanowires that represent typical results and exhibit the overall trend observed for these nanowires. Nevertheless, all of the ten nanowires contributed to the quantitative metrics calculated, and the ten histograms will be available at Appendix 2.2 for reader's reference.

The depinning behaviour in this nanowire geometry, which has a chirality sensitive notch, is expected to show a minimum of two depinning modes, corresponding to pinned VDWs of both chiralities. Moreover, as H_{inj} is above H_{WB}, and since it was seen in chapter 5 that WB transformations can create a TDW-like structures, it is possible that the notches will exhibit a further two additional depinning modes corresponding to the two chiralities of TDWs. As N_d increases, one might expect to see a reduction in depinning stochasticity as depinning modes

may start to converge at strong pinning sites. However, the single notch nanowire is expected to maintain a multi-mode switching system due to its chirality sensitive feature.

6.2.1. Results and discussion of MOKE measurements

The results presented in the histograms (Figure 6.3) indicate a multi-mode depinning behaviour in all of the notch sizes. A strong stochastic component for all N_d was also evident from the plots of σ_d against N_d shown in Figure 6.4(a), which did not show any trend with notch size. A similar lack of systematic variation is seen in the plot of P_p against N_d shown in Figure 6.4(b). The latter is counter-intuitive, as it would be expected that increasing N_d would result in a stronger pinning potential. A possible explanation here may be that thermal excitation played a major role in assisting depinning in these thin nanowires, even for deep notches. Moreover, the fact that some modes were seen just above the injection field suggests that some modes were weakly pinned, or possibly pinned on the other side of the notch, making it easy for the applied field to depin them when thermally assisted. A similar observation for the weakly pinned DWs have been also reported by Bogart *et al* [4].
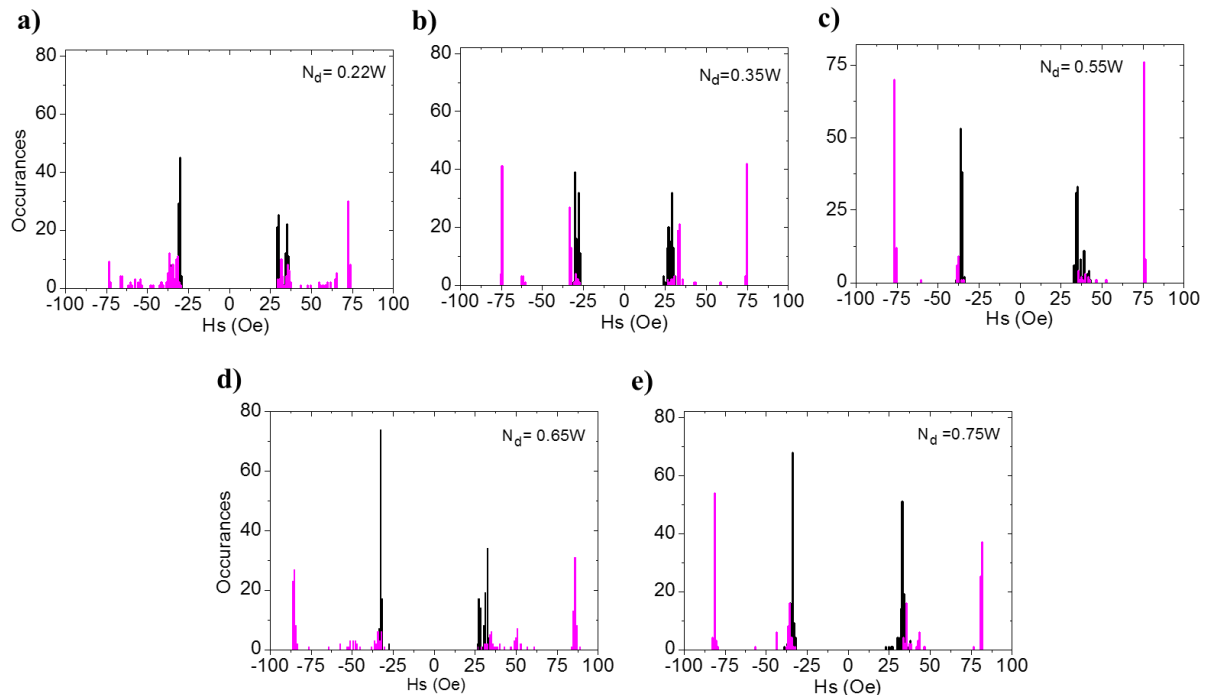
Figure 6.3: Switching field histogram plots of 100 single-shot measurements at region before the notch (black) and region after the notch (purple) for nanowires of t=10 nm and N_d=0.22W (a), N_d= 0.35W (b), N_d=0.55W (c), N_d= 0.65W (d) and N_d= 0.75W (e).
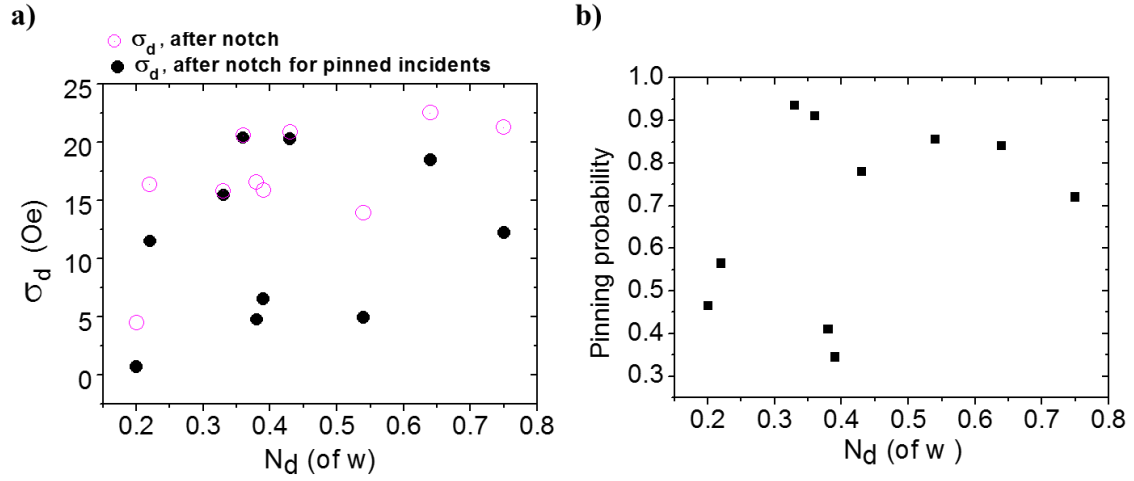
Figure 6.4: (a): Plot of depinning standard deviation versus notch depth for all switching attempts (solid circles) and for successfully pinned attempts only (open circles) (error= ± 1 Oe). (b): Plot of pinning probability Vs notch depth. Both plots are for nanowire with t=10 nm and with single notch defect.

Although there seem to be an overall lack of trend in the σ_d and P_p, it can be argued that as N_d increases there seem to be a reduction in switching stochasticity indicated by the reduction in the number of modes (in the form of convergence into a dominant mode). In addition, there seem to be one depinning mode dominating over the other modes (at around 75 - 85 Oe). This may suggest that increasing N_d might favour one particular DW pinning configuration, or that the other depinning mechanisms become energetically incapable of depinning and would converge toward a single mechanism. Another explanation for the presence of a dominating mode at high N_d might be that, for these notches, switching occurs only through DW re-nucleation at the other side of the notch, which would result in all pinned states switching at the same field. This has been previously suggested by Bogart *et al* [4].

6.2.2. 3D Simulation of nanowire of t=10 nm

To gain insight into the dynamic pinning/depinning process at different N_d, dynamic simulations were performed on nanowires with N_d =0.25W, 0.5W and 0.75W, using the methodology described in section 6.1.
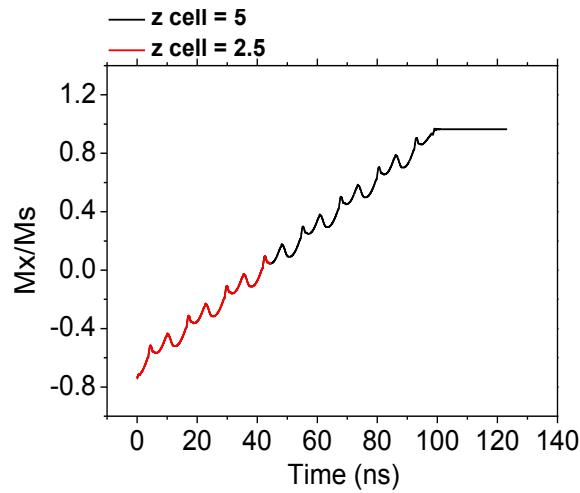
Figure 6.5: Magnetisation vs time curve showing WB oscillations at H=30 Oe for nanowire of t=10 nm obtained from MUMAX^3 simulation for cell size 2.5x2.5x5 nm^3 (black) and 2.5x2.5x2.5 nm^3 (red).

In these simulations, the z-component of the cell size was chosen to be 5nm to save simulation time after verifying that a negligible discrepancy exists between 2.5x2.5x2.5nm^3 and 2.5x2.5x5nm^3 cell sizes (refer to Figure 6.5).

The WB transformations simulated for nanowire t=10 nm at H_{inj}= 30 Oe, along with its corresponding magnetisation (M_x/M_s) vs time curve, are shown in Figure 6.6. It is clear from the periodic oscillations seen in the normalised magnetisation plot and the DW transformational cycles seen in the simulation snapshots that the DW is propagating within the oscillatory regime.

The WB transformations seen in Figure 6.6 are very similar to the transformation seen in section 5.2.3. The high-applied field results in transverse movement of the VDW core between the top and bottom edges of the nanowire. This results in the DW structure transforming between DN TDW (t=3ns and 17ns), ACW VDW (t=1,6 and 13 ns) and UP TDW (t=10 ns). Hence, the length of the WB period can be calculated as follows:

- Duration of period = 13 ns, DW travels distance $\Delta M_x/M_s$ = 0.2.
  - $\Delta M_x/M_s$ at full magnetisation for l= 6000 nm nanowire, is from (1 to −1) =2.
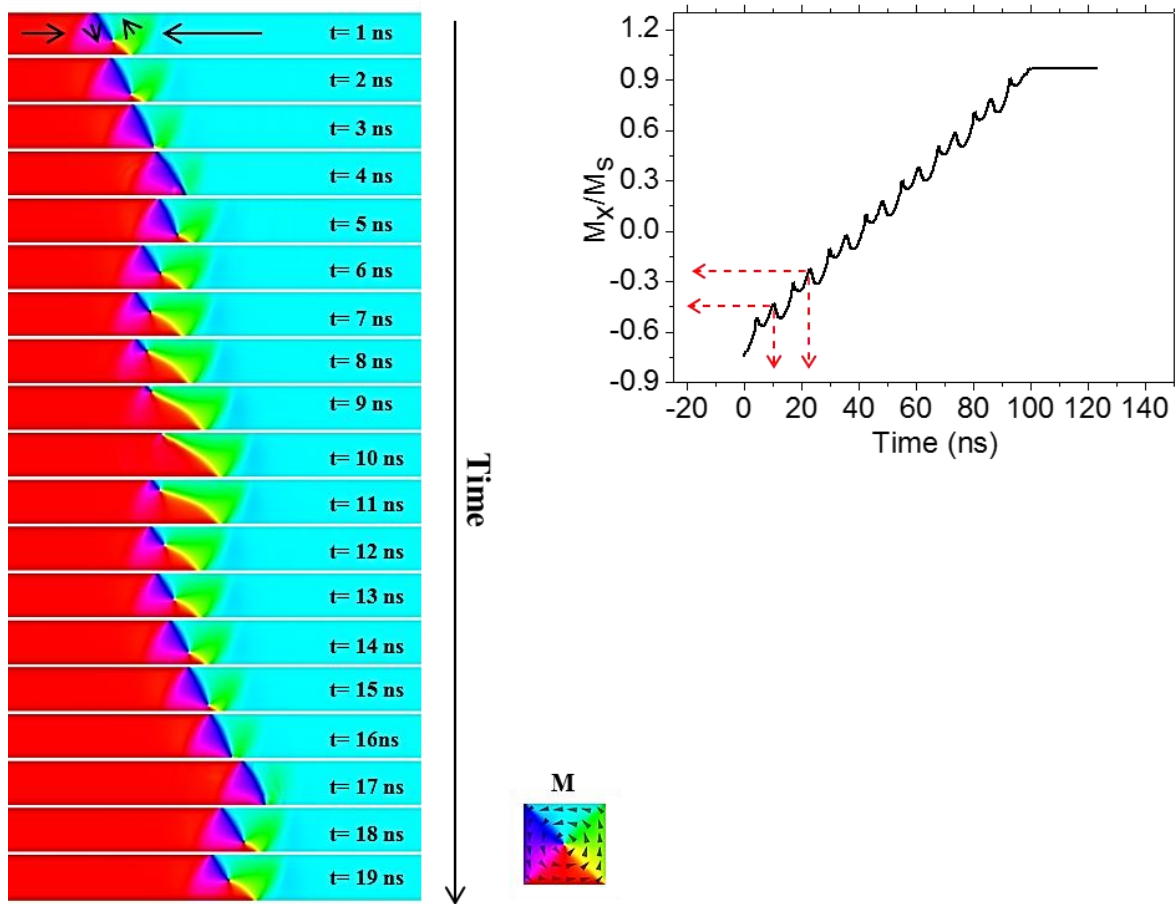   - Therefore, M_x/M_s of 0.2 is equivalent to (6000 × 0.2/2)= **600 nm**

Figure 6.6: Micromagnetic simulation of WB transformations of ACW VDW in nanowire of t=10 nm at H_p=30 Oe. Plot shows the magnetisation Vs time for the DW propagation.

To follow the simulation methodology in simulating different DW possible pinning states, the position of the notch was changed ten time. Each time the notch was moved 60 nm to cover the full 600 nm WB period.

In order to simulate ten intervals within a WB period, the notch in each nanowire should be horizontally moved in steps of 60 nm.

Figure 6.7 shows simulation results for $N_d = 0.25W$ simulated for ten different notch positions, once when an ACW VDW was relaxed and propagated from the left side to the right side of the nanowire, and another time when CW VDW was relaxed and propagated.

a)

Input DW: ACW

ACW: DW Pinning configuration #1

ACW: DW Pinning configuration #2

ACW: DW Pinning configuration #3
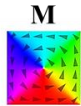
Table 6.7-a: Pinning states for ACW DWs in nanowire of t=10 nm and single notch with N_d=0.25W
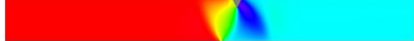
ACW Pinning State	H_d (Oe)	Probability (%)	Switching Method
Configuration #1	80 ± 2.5	50	Depinning
Configuration #2	115 ± 2.5	10	Depinning
Configuration #3	110 ± 2.5	40	Depinning
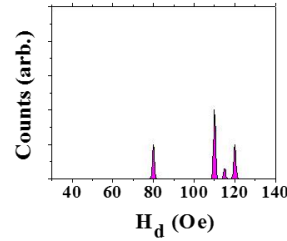
M

b)

Input DW: CW

CW: DW Pinning configuration #1

CW: DW Pinning configuration #2

CW: DW Pinning configuration #3

Table 6.7-b: Pinning states for CW DWs in nanowire of t=10 nm and single notch with N_d=0.25W

CW Pinning State	H_d (Oe)	Probability (%)	Switching Method
Configuration #1	120 ± 2.5	50	Nucleation
Configuration #2	110 ± 2.5	40	Depinning
Configuration #3	110 ± 2.5	10	Depinning

Figure 6.7: Micromagnetic simulation of DW pinning configurations for nanowire t=10 nm and single notch of N_d=0.25W for ACW (a) and CW (b) DWs. Tables summarize the switching outcomes for each pinned state. Plot shows constructed histogram for simulated DFD. H_{inj}= 30 Oe.

The results predicted that the notch would exhibit an H_d distribution consisting of four different depinning modes, and could support five distinct DW configurations. These five distinct DW configurations showed that the DW can be pinned in its normal VDW structure (CW: configuration #2) or stretched VDW structure, on the other side of the notch (ACW: configuration #2). Additionally, as the DW has undergone WB transformations, it has pinned in a normal TDW structure (CW: configuration #1) and in its stretched TDW-like structure on the other side of the notch (ACW: configuration #1&3 and CW: configuration #3).

It is important to mention that the presented pinning configurations are not necessarily the only possible configurations that can occur during real DW propagation. Moreover, although DWs
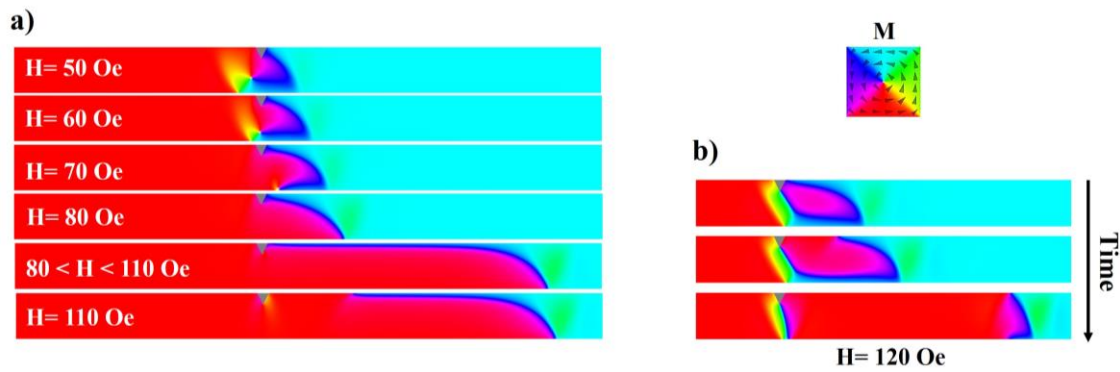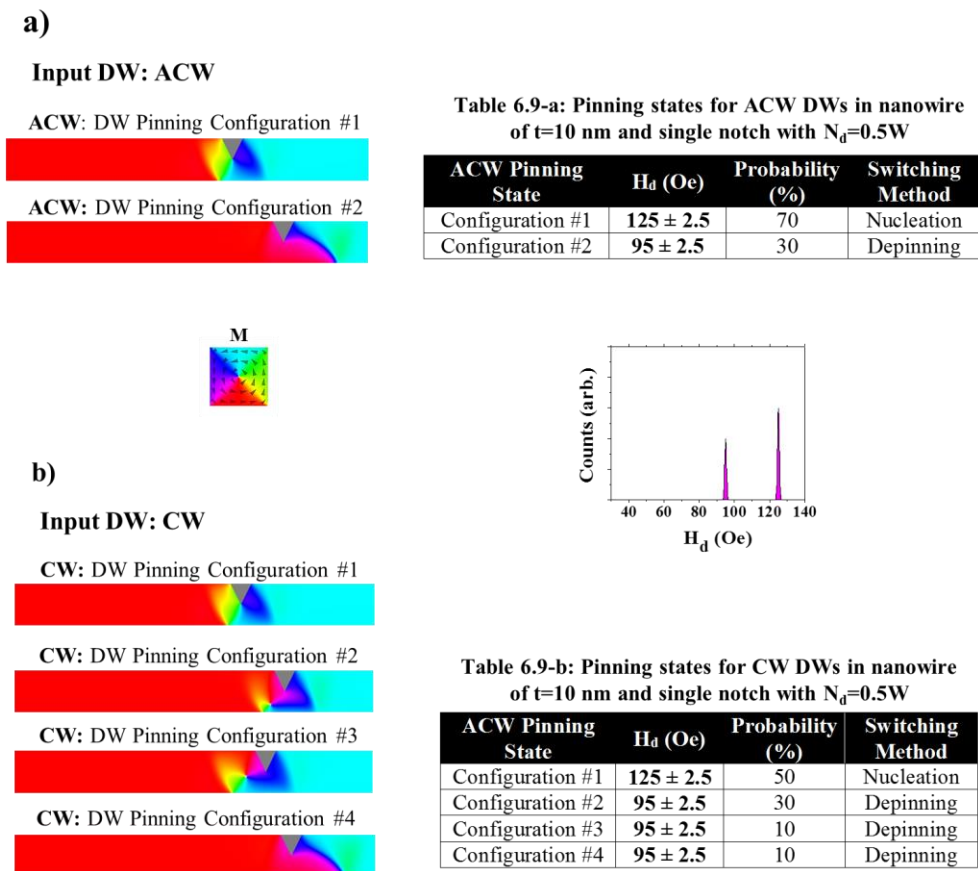
Figure 6.8: Micromagnetic simulation snapshots showing the depinning process of CW: configuration #2 with its elongated tail (a), and re-nucleation process for CW: configuration #1 (b).

can pin in different configurations, this does not necessarily mean that each will have a unique depinning field. For example, in the tables shown in Figure 6.7 ACW/CW configuration #3 and CW input configuration #2 both depin at the same field. This is explained by the fact that in some depinning processes the pinned DW evolved into another configuration prior to depinning. Here the pinned ACW VDW evolved into a downwards TDW when field was increased (Figure 6.8(a)), and thus the two states had a common depinning field. It was also noticeable that during half of this depinning processes, the DW became highly elongated during its attempt to depin. The elongated state remained stable over a relatively large range of fields (from 80 to 110 Oe) (Figure 6.8(a)). Similar highly elongated DW states were also reported by Akerman *et al* [7]. In a real experiment, it seems likely that elongated states like this would be highly susceptible to thermal activation, allowing the state to depin at any point in a large field range. Such phenomena might explain the small, highly distributed, peaks seen for $N_d = 0.22W$ (Figure 6.3).

Another explanation might relate to the presence of edge roughness, which might stabilise multiple similar DW states with slightly different depinning fields. In addition to this, it was notable that one depinning configuration (CW: configuration #1) has depinned through DW re-nucleation; in which, a new DW has nucleated on the other side of the notch and propagated to the other side causing nanowire switching. Figure 6.8(b) depicts the re-nucleation process.

131

More broadly comparing the simulation results with the MOKE measurement for small N_d (Figure 6.3(a)), it can be seen that there are qualitative behavioural similarities. Both the experimental data and simulations show a large number of depinning modes, which span a relatively large field range. This can be attributed to the varying possible pinning configurations as DWs can pin either in vortex or transverse-like states. On the other hand, the simulation does not show any passing incidents at H= 30 Oe although indications of weak pinning was seen where DWs were pinned on the other side of the notch. This could suggest that thermal activation in real experiments would have assisted the depinning of these pinned states which have contributed to increasing switching stochasticity seen in the histogram plot.

When N_d was increased to 0.5W, the simulation results (Figure 6.9) indicated a reduction in the number of depinning modes, with only two modes being observed at H_d = 125 Oe and H_d = 95 Oe respectively. This was in part caused by the quenching of configurations #1 and #2

a)

Input DW: ACW

ACW: DW Pinning Configuration #1

ACW: DW Pinning Configuration #2

Table 6.9-a: Pinning states for ACW DWs in nanowire of t=10 nm and single notch with N_d=0.5W

ACW Pinning State	H_d (Oe)	Probability (%)	Switching Method
Configuration #1	125 ± 2.5	70	Nucleation
Configuration #2	95 ± 2.5	30	Depinning

M

b)

Input DW: CW

CW: DW Pinning Configuration #1

CW: DW Pinning Configuration #2

CW: DW Pinning Configuration #3

CW: DW Pinning Configuration #4

Table 6.9-b: Pinning states for CW DWs in nanowire of t=10 nm and single notch with N_d=0.5W

ACW Pinning State	H_d (Oe)	Probability (%)	Switching Method
Configuration #1	125 ± 2.5	50	Nucleation
Configuration #2	95 ± 2.5	30	Depinning
Configuration #3	95 ± 2.5	10	Depinning
Configuration #4	95 ± 2.5	10	Depinning

Figure 6.9: Micromagnetic simulation of DW pinning configurations for nanowire t=10 nm and single notch of N_d=0.5W for ACW (a) and CW (b) DWs. Tables summarize the switching outcomes for each pinned state. Plot shows constructed histogram for simulated DFD. H_{inj}= 30 Oe.

seen for ACW injection in the previous smaller notch (Figure 6.7(a)). This quenching can be attributed to strong pinning encountered by the DW at the deep notch; such that, DW/notch interaction does not allow for the two quenched configurations to exist. Instead, they evolve into the other states during the pinning process. In other words, large notches seem to permit fewer metastable states to exist. Moreover, the UP TDW pinning configuration (configuration #1) increased its occurrence probability and continued to switch the nanowire through re-nucleation. This might suggest that the system is favouring this mode as N_d increases.

When comparing the results obtained in above simulations with the MOKE results for similar N_d (Figure 6.3(c)), it is clear that in both cases increasing N_d resulted in a reduced number of depinning modes. However, the simulations showed two clear modes, whereas in the MOKE data, one mode dominated. The latter suggests that in real experiment there are factors that seem to cause convergence of depinning modes that were absent in simulation. Such factors can be attributed to the edge roughness that may have assisted the re-nucleation switching process.

As N_d further increases to 0.75W, the simulation results begin to show clear dominance of a single, nucleation-based depinning mode at $H_d = 130$ Oe (Figure 6.10). This corresponds to an UP TDW, and was formed in 80 % of the total simulations indicating that this state was strongly favoured in large notches. The other states formed were CW VDWs, and a downward TDW pinned before the notch. Both of these states switched via a depinning, rather than nucleation-based process.

When compared with the MOKE measurements (Figure 6.3(e)) for larger notch depths, the simulation results seem to correlate well. Both results show tendency towards the dominance of a single depinning mode. Also the simulation results showed that the dominating depinning mode occurred through re-nucleation switching method and correlates with the dominating mode shown in MOKE histograms which has increased in dominance with increasing N_d.

a)

Input DW: ACW

ACW: DW Pinning Configuration #1

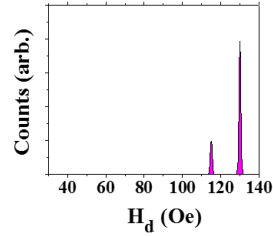**ACW:** DW Pinning Configuration #2

M

Table 6.10-a: Pinning states for ACW DWs in nanowire of t=10 nm and single notch with N_d=0.75W

ACW Pinning State	H_d (Oe)	Probability (%)	Switching Method
Configuration #1	130 ± 2.5	80	Nucleation
Configuration #2	115 ± 2.5	20	Depinning

b)

Input DW: CW

CW: DW Pinning Configuration #1

CW: DW Pinning Configuration #2

CW: DW Pinning Configuration #3

Table 6.10-b: Pinning states for CW DWs in nanowire of t=10 nm and single notch with N_d=0.75W

CW Pinning State	H_d (Oe)	Probability (%)	Switching Method
Configuration #1	130 ± 2.5	80	Nucleation
Configuration #2	115 ± 2.5	10	Depinning
Configuration #3	115 ± 2.5	10	Depinning

Figure 6.10: Simulation of DW pinning configurations for nanowire t=10nm and single notch of N_d= 0.75W for ACW (a) and CW (b) DWs. Plot shows constructed histogram for simulated DFD. H_{inj}= 30 Oe.

Therefore, it could be hypothesised that with further increase in N_d, it is expected that H_d will eventually saturate around nucleation field (H_N) as nanowire switching will only be achieved through DW re-nucleation. This is in agreement with the conclusions of Bogart *et al* when justifying why H_d will saturate for $N_d \geq 0.6W$ [4].

Summarising the simulation results obtained from all three nanowire depths (N_d =0.25W, 0.5W and 0.75W), it can be seen that several possible pinning configurations exist in each N_d which would justify the presence of multi-mode behaviours seen in the MOKE measurements. Furthermore, as N_d increases, the number of depinning modes in the constructed histogram plots (Figure 6.7, 6.9, 6.10) decrease, with nucleation-based modes becoming dominant for large notches. These broad trends are also observed in the experimental data.

Thus for single triangular notches, in nanowires of t = 10 nm, it can be argued that:

- Depinning stochasticity is particularly significant at small N_d due to presence of multiple pinning configurations that correspond to variants of four main DW structures (both chiralities of VDWs and TDWs) anticipated in the nanowire geometry. Contributions to the highly distributed H_d distributions may also be made by the thermal activation of highly elongated DW configurations formed prior to depinning, or the stabilisation of nominally similar DW configurations, with slightly different depinning fields, by edge roughness.

- As N_d increases, the H_d distributions exhibit a reduction in depinning modes, and trend towards a single, dominating depinning mode. The simulations suggest that this occurs because fewer DW configurations are stable as notch size increases, and that the trend towards a single mode occurs because switching via re-nucleation of the DW is strongly favoured in the largest notches.

- Dominance of a single mode was observed more prominently in the experimental data than the simulations, perhaps because edge roughness contributes to DW pinning, thus favouring re-nucleation processes over the depinning mechanisms observed in the simulations.

- Significant numbers of incidents where the DWs passed the notches at the injection field were observed in all experimental histograms, but not in the simulations. This suggests that thermal perturbations in thin nanowires are significant in assisting DW transmission even for deep notches. It is believed that the presence of such unsuccessfully pinned incidents is the reason for the lack of trend in σ_d even though a decrease in switching stochasticity can be inferred from the overall behaviour of the MOKE measurements and simulations.

6.3. Nanowire of t=10 nm and double notch defect

For the case of a double notch, where pinning site is chirality-insensitive, one would have expected to observe fewer depinning modes, and more deterministic switching than in the equivalent single notches. However, the experimental measurements showed more complex results:

6.3.1. Results and discussion of MOKE measurements

Figure 6.11 shows the H_d measured for whole set of the five nanowires with double notches.

The H_d distributions of all of the nanowires exhibit multi-mode switching behaviours. Unlike the nanowire with single notches, the multi-mode behaviour does not seem to converge towards a single mode as notch size increases. This suggests that a double notch geometry could be intrinsically stochastic in nanowires of t=10 nm, as opposed to the single notch where the data showed a tendency towards approaching single-mode-like system at large notch sizes.
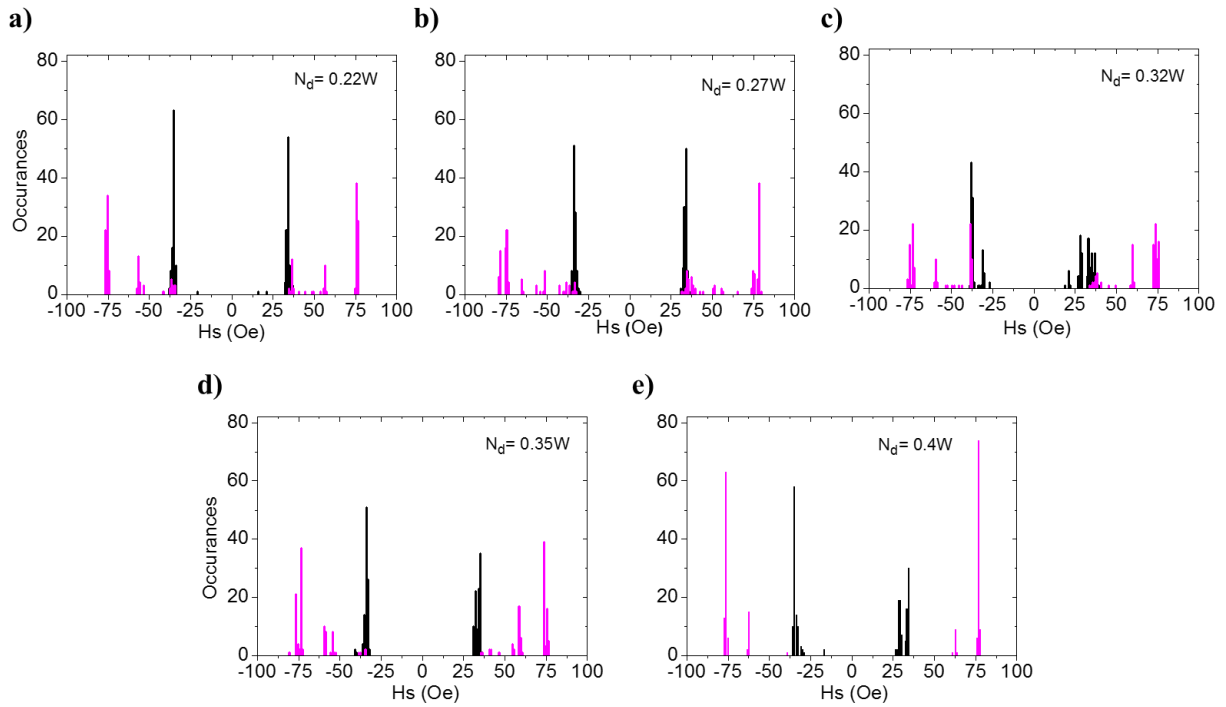
Figure 6.11: Switching field histogram plots of 100 single-shot measurements at region before the notch (black) and region after the notch (purple) for nanowires of t=10 nm and double notch of N_d=0.22W (a), N_d= 0.27W (b), N_d= 0.32W and (c), N_d= 0.35W (d), N_d= 0.4W (e).

These results are counterintuitive as double notches are expected to show chirality-insensitive pinning/depinning behaviours that should assist in limiting the number of discrete depinning modes. Akerman *et al* [8] also observed high stochasticity for double notch defects. They attributed this to pinning interactions that were very sensitive to the shape of the DW profile as it reached the double notch. This in turn is very sensitive to the propagation field, thermal activation and edge roughness.

Figure 6.12 shows plots of σ_d and P_p as a function of N_d. Both plots show trends that were not seen in single notch nanowires. As N_d increases, the pinning probability seems to increase while the σ_d decreases. This might be attributed to the reduced number of passing and weakly pinned incidents in double notches compared with single notch for the same notch gap depth. It also suggests that σ_d (or indeed any isolated metric) alone does not necessarily give an accurate estimate of how deterministic the system is. This is because despite the decrease in σ_d, the multi-mode switching behaviour remained, indicating undeterministic switching behaviour.

This observation is opposite to the previous study for the single notch nanowires where quantitative metrics did not show a trend for increasing N_d, whereas their histograms indicated clear signs of convergence towards a single mode.
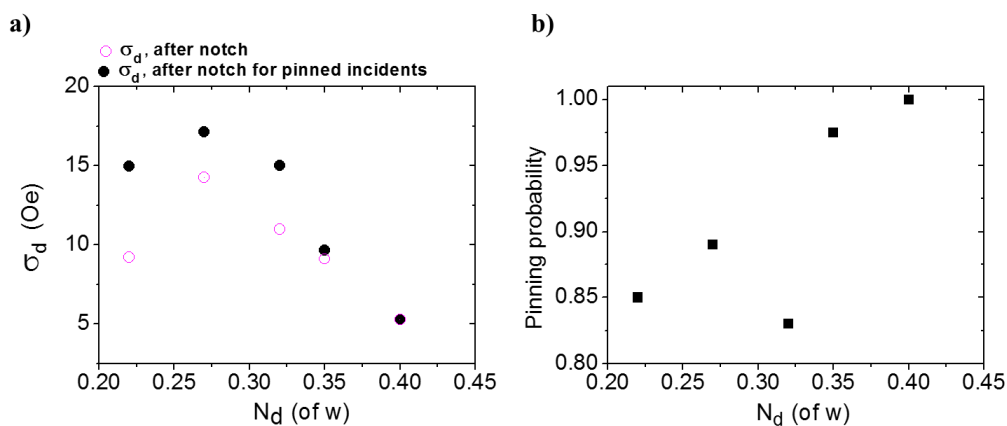
Figure 6.12: (a): Plot of depinning standard deviation versus notch depth for all switching attempts (solid circles) and for successfully pinned attempts (open circles). (b): Plot of pinning probability Vs notch depth. Both plots are for nanowire with t=10nm and with double notch defect.

In order to get an insight into the pinning and depinning processes at the double notch defect, dynamic simulations were performed for three double notch geometries: N_d= 0.2W, 0.3W and 0.4W.

6.3.2. 3D Simulation of nanowire of t=10 nm and double notch defect

Figure 6.13 presents the pinned DW and deduced depinning field distributions simulated for a nanowire with N_d = 0.2W configurations. Four unique pinning configurations were observed corresponding to VDW (ACW: configuration #4 and CW: configuration #2), TDW (ACW: configuration #1,3 and CW: configuration #1) and deformed TDW (ACW: configuration #2) pinned DW structures. However, only three unique depinning fields exist at H_d= 105, 120 and 125 Oe due to the symmetry of the double notch as will be explained below.

a)

Input DW: ACW

DW Pinning Configuration #1

DW Pinning Configuration #2

DW Pinning Configuration #3

DW Pinning Configuration #4

M
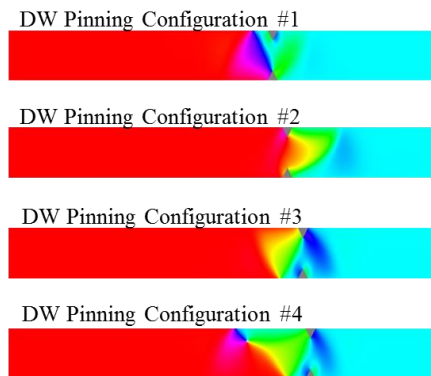
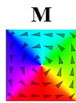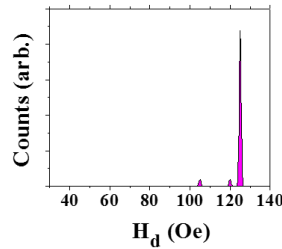**Table 6.13-a: Pinning states for ACW DWs in nanowire of t=10 nm and double notch with N_d=0.2W**

ACW Pinning State	H_d (Oe)	Probability (%)	Switching Method
Configuration #1	125 ± 2.5	20	Nucleation
Configuration #2	105 ± 2.5	20	Depinning
Configuration #3	125 ± 2.5	10	Nucleation
Configuration #4	120 ± 2.5	50	Depinning

b)

Input DW: CW

DW Pinning Configuration #1
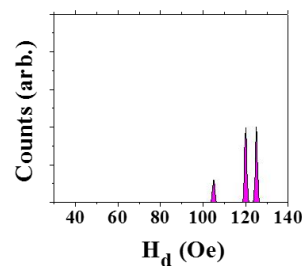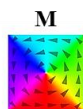
DW Pinning Configuration #2
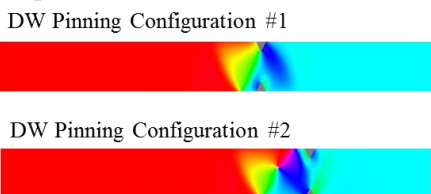
Table 6.13-b: Pinning states for CW DWs in nanowire of t=10 nm and double notch with N_d= 0.2W

CW Pinning State	H_d (Oe)	Probability (%)	Switching Method
Configuration #1	125 ± 2.5	60	Nucleation
Configuration #2	120 ± 2.5	40	Depinning

Figure 6.13: Micromagnetic simulation of DW pinning configurations for nanowire t=10 nm and double notch of N_d=0.2W for ACW (a) and CW (b) DWs. Tables summarize the switching outcomes for each pinned state. Plot shows constructed histogram for simulated DFD. H_{inj}= 30 Oe.

138

Interestingly, the magnetisation configurations of the ACW and CW DWs did not show exact symmetry in DW pinning configurations nor in their occurrence probability (configuration #1 and #2 in ACW case did not appear in the CW chirality set of simulations). This could be due to having a slightly different initial DW position (in the nanowire) that resulted in a different arrival probability to the notch. However, it can be seen that there exist some aspects of symmetry in the pinning states due to the nature of the double notch. For example, in the ACW case (Figure 6.13(a)), configuration #1 and configuration #3 are equivalent. The only difference is that configuration#1 shows a transverse-like DW with spins orienting downward, and DW pinning with the bottom notch, while configuration #3 shows a transverse-like DW with spins pointing upward and DW pinning with the top notch. The results also showed that although some depinning modes had similar H_d, their switching method could be radically different. This difference was seen for modes with $H_d=120$ Oe and $H_d = 125$ Oe; in which, modes with $H_d=125$ switched through re-nucleation while modes with $H_d=120$ Oe have switched through DW depinning.

When comparing the simulation results with the MOKE measurements (Figure 6.11(a)), it can be seen that both showed multi-mode switching behaviours with much smaller gap between the modes in the simulation result compared with histogram. Furthermore, two depinning modes seem to dominate in MOKE as well as in simulation. These two modes correspond to the different switching methods; in which, in one method (at $H_d=120$ Oe) switching of nanowire happened through DW depinning, while in the other method ($H_d= 125$ Oe), switching happened through re-nucleation.

When N_d was increased to 0.3W, the simulations showed a reduction in depinning stochasticity as indicated in the deduced depinning field distribution, which shows a dominating mode at H_d

a)

Input DW: ACW

DW Pinning Configuration #1

DW Pinning Configuration #2

DW Pinning Configuration #3
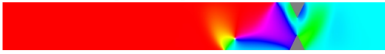
DW Pinning Configuration #4

M

Table 6.14-a: Pinning states for ACW DWs in nanowire of t=10 nm and double notch with N_d=0.3W

ACW Pinning State	H_d (Oe)	Probability (%)	Switching Method
Configuration #1	125 ± 2.5	20	Nucleation
Configuration #2	120 ± 2.5	10	Nucleation
Configuration #3	105 ± 2.5	10	Depinning
Configuration #4	125 ± 2.5	60	Nucleation

b)

Input DW: CW

DW Pinning Configuration #1

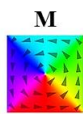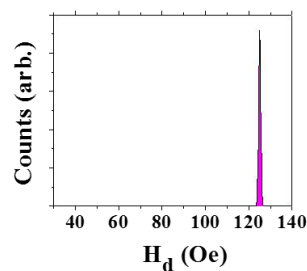DW Pinning Configuration #2
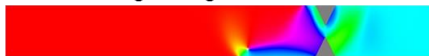
DW Pinning Configuration #3

Table 6.14-b: Pinning states for CW DWs in nanowire of t=10 nm and double notch with N_d=0.3W

CW Pinning State	H_d (Oe)	Probability (%)	Switching Method
Configuration #1	125 ± 2.5	50	Nucleation
Configuration #2	125 ± 2.5	10	Nucleation
Configuration #3	125 ± 2.5	40	Nucleation

Figure 6.14: Micromagnetic simulation of DW pinning configurations for nanowire t=10 and double notch of N_d=0.30W for ACW (a) and CW (b) DWs. Tables summarize the switching outcomes for each pinned state. Plot shows constructed histogram for simulated DFD. H_{inj}= 30 Oe.

= 125 Oe (Figure 6.14). This is expected to have occurred because the majority of both VDW

and TDW configurations now all switch by re-nucleation.

Moreover, it was noticed that the same depinning field values were seen for this notch as were

observed for N_d = 0.2W, unlike in the case of the single notch where H_d varied with N_d. In

particular it is notable that the field required for re-nucleation remains constant at H_d = 125 Oe.

This behaviour seems to be consistent with the MOKE measurements (Figure 6.11) where the

depinning fields stayed almost the same for all of the histograms regardless of the notch size.

The probability of each depinning mode, however, has changed.

When comparing the simulations with the MOKE measurements, the MOKE result does not

seem to conclusively suggest a movement towards a single-mode behaviour for this N_d, unlike

the case inferred from the simulation results. This might suggest that other depinning processes are occurring due to edge roughness or imperfect symmetry in double notches.

As N_d increases further to 0.4W, the simulations showed a convergence of the depinning field distribution into a single mode. This can be explained by the fact that the high N_d resulted in strong pinning, leading to switching through nucleation for all DW configurations.

When comparing the simulation with MOKE measurements, both results imply a decrease in depinning stochasticity at the largest notch depths as indicated by the continuous reduction in σ_d value from 15 Oe to 9.5 Oe to 5 Oe at N_d= 0.32W, 0.35W and 0.4W, respectively. This decrease in σ_d can be attributed to the increase in successful pinning events with increasing N_d which caused a reduction in the overall distribution of H_d. Moreover, although there seem to

a)

Input DW: ACW

DW Pinning Configuration #1

DW Pinning Configuration #2

DW Pinning Configuration #3

M

Table 6.15-a: Pinning states for ACW DWs in nanowire of t=10 nm and double notch with N_d= 0.4W

ACW Pinning State	H_d (Oe)	Probability (%)	Switching Method
Configuration #1	120 ± 2.5	30	Nucleation
Configuration #2	120 ± 2.5	10	Nucleation
Configuration #3	120 ± 2.5	60	Nucleation

b)

Input DW: CW

DW Pinning Configuration #1

DW Pinning Configuration #2

DW Pinning Configuration #3

Table 6.15-b: Pinning states for CW DWs in nanowire of t=10 nm and double notch with N_d= 0.4W

CW Pinning State	H_d (Oe)	Probability (%)	Switching method
Configuration #1	120 ± 2.5	50	Nucleation
Configuration #2	120 ± 2.5	10	Nucleation
Configuration #3	120 ± 2.5	40	Nucleation

Figure 6.15: Micromagnetic simulation of DW pinning configurations for nanowire t=10 nm and double notch of N_d= 0.4Wfor ACW (a) and CW (b) DWs. Tables summarize the switching outcomes for each pinned state. Plot shows constructed histogram for simulated DFD. H_{inj}= 30 Oe.

be a movement towards favouring a single mode in the MOKE measurements, there still exist two depinning modes, suggesting that other depinning processes occur in real nanowires with double notches. As for simulation results, the decrease in stochasticity is seen in the dominance of one depinning mode. Moreover, the appearance of a dominating mode in the MOKE and simulation result supports this observation.

In conclusion, for nanowires of t= 10 nm with double notches:

- Multi-mode depinning/switching was seen in all of the nanowires indicating that double notch systems strongly exhibit stochastic switching behaviour. While the simulations indicated that notches could support a range of DW configurations with both TDW and VDW structures, the major cause of the multi-mode behaviour appeared to be a splitting of the switching field distribution into configurations that could switch by depinning (at a lower field), and those that required re-nucleation to occur (at a high field).

- In the simulations a strong convergence towards a single re-nucleation-based mode was observed as N_d increased. This was less apparent in the experimental data, but a decrease in σ_d with an increase in N_d provided evidence of a small population shift towards the re-nucleation mode. However, in contrast to what might be expected for this geometry, the results have shown that single-mode switching could not be achieved in double notches. This conclusion is in agreement with Akerman et al [8], and could be attributed to fabrication limitation factors such as imperfection in the double notches symmetry and edge roughness that seem to trigger additional depinning modes

- It was observed that the pinning probability in the double notch is higher than the probability seen in the single notch. This might indicate that the pinning potential well of the double notch is higher than the pinning landscape produced by the single notch for the same gap depth.

6.4. Nanowire of t=25 nm and single notch defect

After studying the results for single notch nanowire of t=10 nm, it would be expected from single notch nanowire systems of t=25 nm to show multi-mode behaviour corresponding to the two chiralities of the VDW, quenching of the TDW-like states at thicker wires, and stronger pinning site with increased thickness which would result in higher P_p compared with thinner nanowires. Four MOKE measurements with N_d=0.15W, 0.25W, 0.55W and 0.75W will be presented (refer to Appendix 2.5 for full set of measurements), and nanowires of $N_d = 0.25$W, 0.5W and 0.75W will be presented in the 3D simulation.

6.4.1. Results and discussion of MOKE measurements

Results in Figure 6.17 show multi-peak histograms for all notch depths for nanowires of t=25nm.

For small notches (less than N_d=0.55W), unexpected low pinning probability is noted which might be attributed to thermal activation and possibly other unknown factors. Two dominant
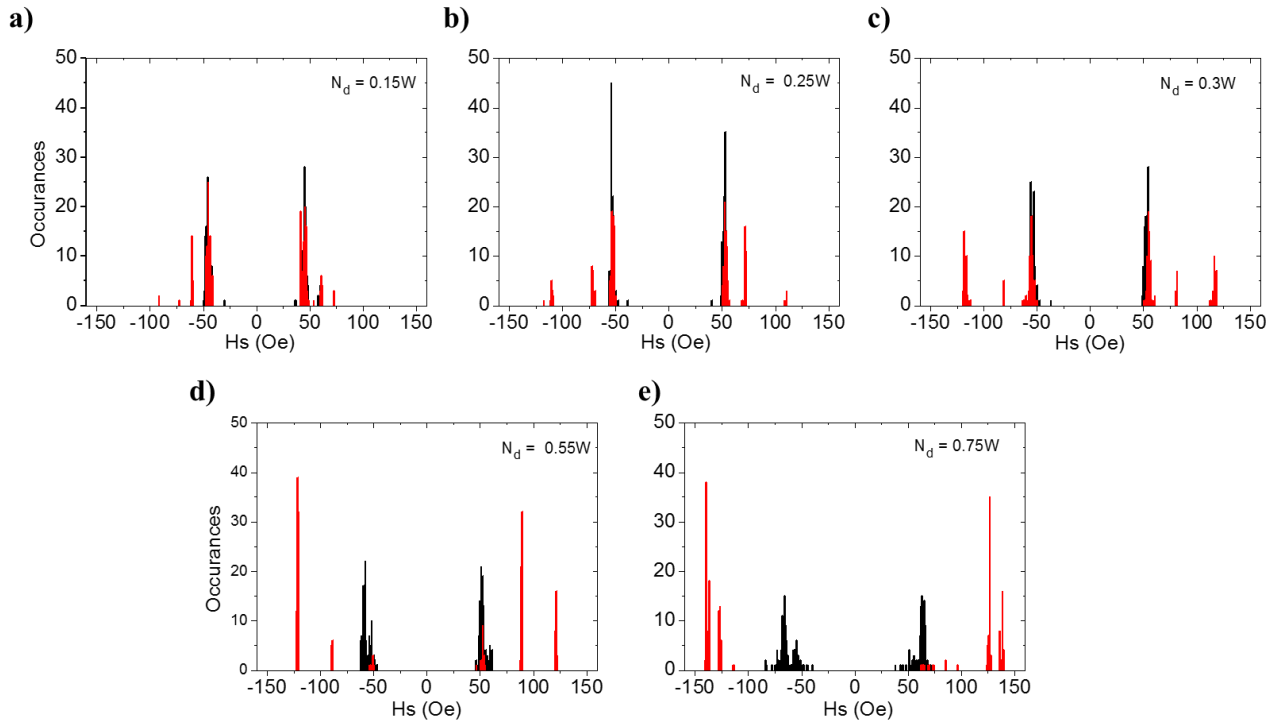
Figure 6.17: Switching field histogram plots of 100 single-shot measurements at region before the notch (black) and region after the notch (red) for nanowires of t=25 nm and single notch N_d=0.15W (a), N_d= 0.25W (b), N_d=0.3W (c), N_d=0.55W (d) and N_d=0.75W (e).

143
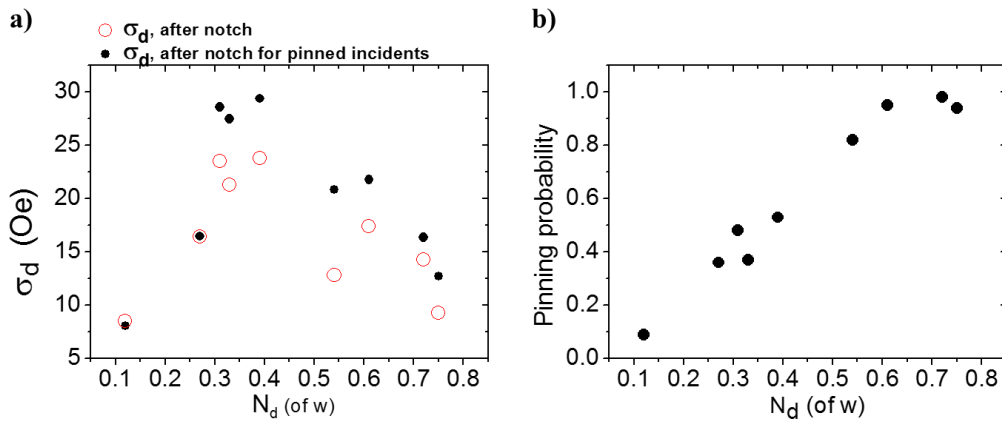
Figure 6.18: (a): Plot of depinning standard deviation versus notch depth for all switching attempts (solid circles) and for successfully pinned attempts (open circles). (b): Plot of pinning probability Vs notch depth. Both plots are for nanowire with t=25 nm and with single notch defect.

depinning modes appear in all histograms which are expected to resemble the two chiralities due to the asymmetry of the notch. This is unlike t=10 nm where more than two modes was seen.

Furthermore, the two modes seen in histograms did not seem to successfully converge into one mode as N_d is increased. This suggests that switching via re-nucleation does not seem to occur significantly in comparison with 10nm thick wires (this has been verified later by simulation).

Unlike nanowires of t=10 nm, the P_p vs N_d shows a positive trend suggesting that thermal activation might be playing smaller role than that played in t=10 nm nanowire at big N_d. This suggests that factors other than thermal activation are responsible for the high passing events seen above.

As for switching stochasticity, the number of peaks and σ_d value do not seem to have an overall systematic change in response to change in N_d. However, as N_d increases above 0.3W, depinning modes seem to start converging and σ_d starts showing a negative sloping trend.

In order to verify our explanation, 3D simulation was done for three N_d sizes: 0.25W, 0.5W and 0.75W.

6.4.2. 3D Simulation of nanowire of t=25 nm

Plot in Figure 6.19 shows the magnetization evolution of DW as it propagates across the nanowire at H_p=50 Oe. The magnetisation process seems to go through a form of periodic oscillations as the VDW core moves in a transverse motion. This suggests that the DW is in the periodic regime. However, the graph shows a level of turbulence within the same period suggesting that the DW could be oscillating at the margin of the oscillatory regime, and would explain the weak retrograde motion compared with WB transformations seen in Figure 6.6 for nanowire with t=10 nm at H_p=30 Oe.

This assumption has been verified when checking the WB velocity graph in Appendix 2.3. Nevertheless the period was identified by the highest crest of the normalized M_x curve.
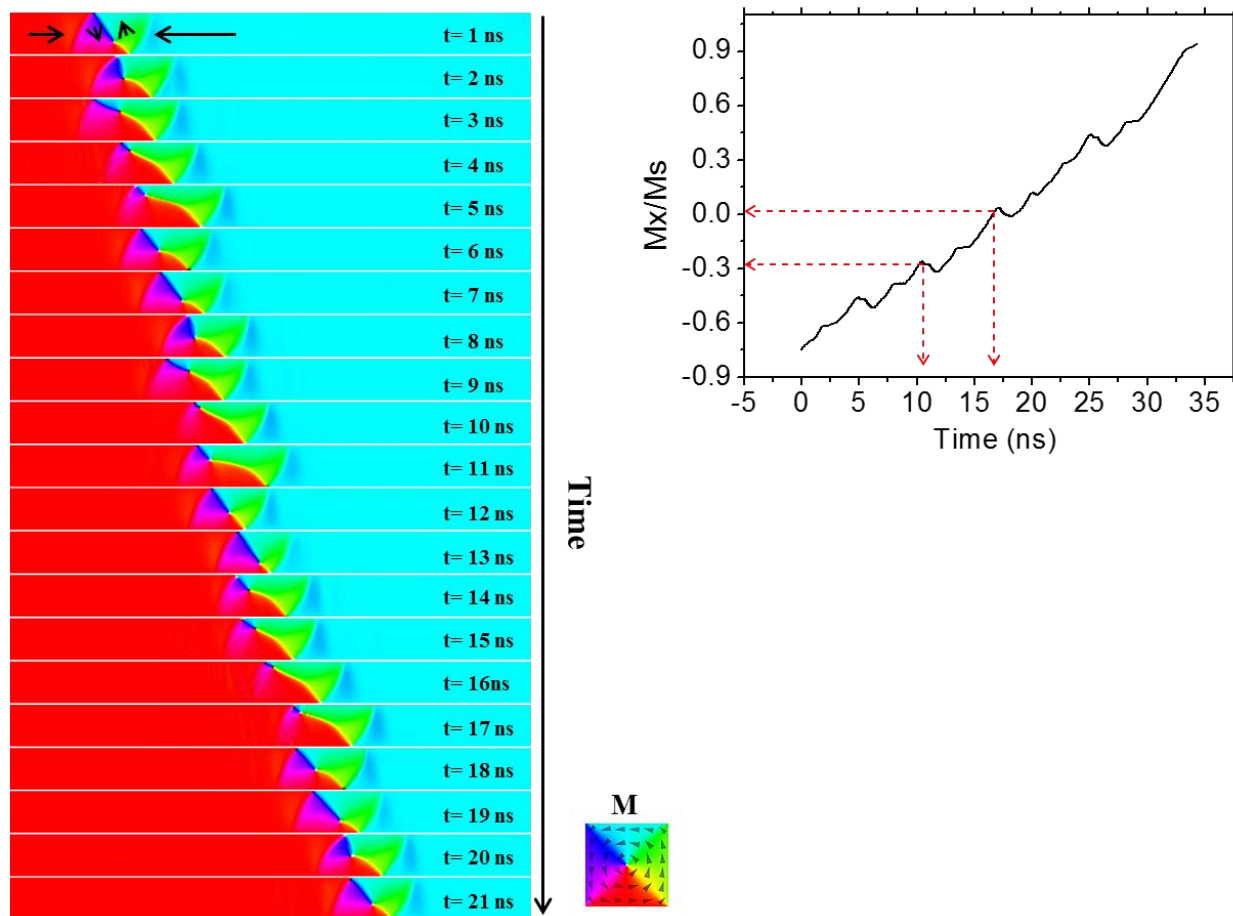
Figure 6.19 Micromagnetic simulation of WB transformations of ACW VDW in nanowire of t=25 nm at H_p=50 Oe. Plot shows the magnetisation Vs time for the DW propagation.

Snapshots of Figure 6.19 show that the transverse-like structures are weakly formed throughout the transformation compared with the transverse-like structure for t=10 nm in Figure 6.6, suggesting that it is less favourable than in nanowires with t=10 nm.

The period was calculated to be around 1050 nm and takes around 7ns, v = 150m/s. Hence, the notch position was shifted by 105 nm.

Results and discussion of simulation

As expected, simulation results (Figure 6.20) show a two-mode corresponding to the ACW and CW VDW chiralities. It is also indicative that TDW pinning configuration doesn't seem to exist at small notches for t=25 nm.

The ACW VDW is pinned more strongly at the notch when the core and the leading edge are pinned outside the notch, forming an energy barrier due to its unfavourable chirality (as discussed in the previous chapter).

a)

Input DW: ACW

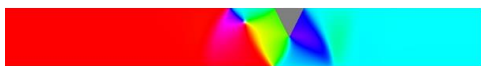DW Pinning Configuration #1
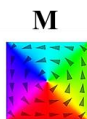
Table 6.20-a: Pinning states for ACW DWs in nanowire of t=25 nm and single notch with N_d=0.30W

ACW Pinning State	H_d (Oe)	Probability (%)	Switching method
Configuration #1	170 ± 2.5	100	Depinning

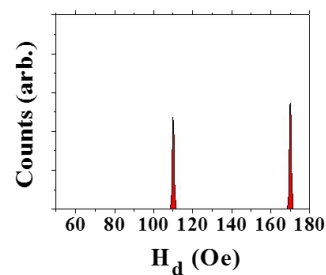**b)**
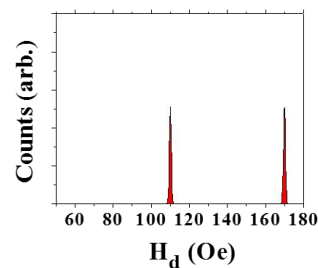
Input DW: CW

DW Pinning Configuration #1

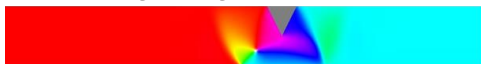**Table 6.20-b: Pinning states for CW DWs in nanowire of t=25 nm and single notch with N_d=0.3W**

CW Pinning State	H_d (Oe)	Probability (%)	Switching method
Configuration #1	125 ± 2.5	100	Depinning

Figure 6.20: Micromagnetic simulation of DW pinning configurations for nanowire t=25 nm and single notch of N_d=0.3W for ACW (a) and CW (b) DWs. Tables summarize the switching outcomes for each pinned state. Plot shows constructed histogram for simulated DFD. H_{inj}= 50 Oe.

The simulation for small N_d of 0.3W does not show that DW gets pinned with a transverse-like state. This is in contrary with the study made by Pi *et al* [9] which showed a high affinity for transverse-like structure to get pinned at notch.

When compared with relevant MOKE measurement (Figure 6.17(c)), simulation results seem to agree very well with it. The histogram and simulation showed two different depinning fields corresponding to the two different VDW chiralities. Hence, it could be concluded that in this geometry stochasticity is a result of VDW chirality.

As N_d increases to 0.5W, simulation results (Figure 6.21) showed the existence of a new pinning configuration; in which the DW is pined in a transverse-like structure (CW: configuration #2). However, the H_d for this configuration is the same as H_d for the ACW: configuration #1. Upon checking the simulation process it was verified that both have very

a)

Input DW: ACW

DW Pinning Configuration #1

M

b)

Input DW: CW

DW Pinning Configuration #1

DW Pinning Configuration #2

Table 6.21-a: Pinning states for ACW DWs in nanowire of t=25nm and single notch with N_d=0.5W

ACW Pinning State	H_d (Oe)	Probability (%)	Switching method
Configuration #1	170 ± 2.5	100	Depinning

Table 6.21-b: Pinning states for CW DWs in nanowire of t=25nm and single notch with N_d=0.5W

CW Pinning State	H_d (Oe)	Probability (%)	Switching Method
Configuration #1	140 ± 2.5	90	Depinning
Configuration #2	170 ± 2.5	10	Depinning

Figure 6.21: Micromagnetic simulation of DW pinning configurations for nanowire t=25 nm and single notch of N_d=0.5Wofw for ACW (a) and CW (b) DWs. Tables summarize the switching outcomes for each pinned state. Plot shows constructed histogram for simulated DFD. H_{inj}= 50 Oe.

similar depinning process. Moreover, in all configuration, depinning occurred through DW depinning, unlike the case for nanowire of t=10 nm.

When compared with the MOKE results (Figure 6.17(d)), results seem to agree to a good extent. MOKE measurements and simulation results showed two distinct depinning modes, each of which are expected to correlate with each DW chirality

As N_d increases even further to 0.75W (Figure 6.22), the same pinning configurations were seen as the previous N_d but at higher H_d value. This is understandable as increasing N_d will result in reducing the size of the constricted region leading to a deeper and higher potential barrier/well. Nevertheless, switching continues to happen through depinning not re-nucleation. It is important to mention here that re-nucleation switching method is referred to the nucleation of a new DW core on the other side of the notch that evolves into a DW and depins while the first DW remains pinned at the notch [8].

a)

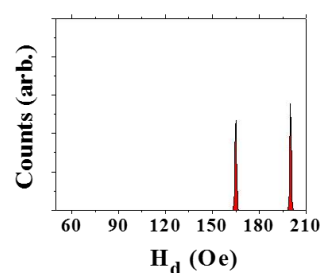**Input DW: ACW**

DW Pinning Configuration #1

M
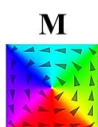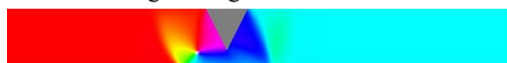
Table 6.22-a: Pinning states for ACW DWs in nanowire of t=25 nm and single notch with N_d=0.75W

ACW Pinning State	H_d (Oe)	Probability (%)	Switching Method
Configuration #1	200 ± 2.5	100	Depinning

b)

Input DW: CW

DW Pinning Configuration #1

DW Pinning Configuration #2

Table 6.22-b: Pinning states for CW DWs in nanowire of t=25 nm and single notch with N_d=0.75W

CW Pinning State	H_d (Oe)	Probability (%)	Switching Method
Configuration #1	165 ± 2.5	90	Depinning
Configuration #2	200 ± 2.5	10	Depinning

Figure 6.22: Micromagnetic simulation of DW pinning configurations for nanowire t=25 nm and single notch of N_d=0.75W for ACW (a) and CW (b) DWs. Tables summarize the switching outcomes for each pinned state. Plot shows constructed histogram for simulated DFD. H_{inj}= 50 Oe.

Results of MOKE measurements for $N_d = 0.75W$ (Figure 6.17(e)) agree to good extent with simulations. Histogram and simulations show two depinning modes. These two modes can either be attributed to the two VDW chiralities or to the emergence of a new nucleating mode at around 140 Oe.

It can be deduced from above studies on single notch at t=25 nm, that

- There will always exist two depinning modes in this geometry due to the sensitivity of the single notch to DW chirality. When N_d is small, only two pinning configurations are seen in the MOKE measurements and in simulation. These two configurations correspond to CW and ACW chirality. As N_d increases, a third pinning configuration arises where DW is pinned with transverse-like structure. However, TDW-like configuration depinned using the same depinning mechanism for the ACW DW.

- The fact that in all N_d sizes, switching happened through DW depinning and not re-nucleation, suggests that the switching for such systems are very unlikely to converge towards a single-mode switching behaviour. This is unlike t=10nm and in agreement with expectations.

The next section presents a study of the switching behaviour in symmetrical notches in nanowires of t=25nm.

6.5. Nanowire of t=25 nm and double notch defect

The magnetisation measurements for nanowires of t=25 nm and N_d=0.2W, 0.3W, 0.33W and 0.35W have been measured using MOKE. Results are presented in Figure 6.23.

Since previous study for t= 25 nm indicated less pinning configurations compared with thinner wire (with the small occurrence of TDW-like configurations at t= 25 nm), it is expected to see single-mode behaviour due to the chirality-insensitive notch.

6.5.1. Results and discussion of MOKE measurements

Histograms for double notch defect in nanowires of t= 25 nm and varying N_d showed an existence of multi-peak distributions indicating multi-mode switching behaviour in most of the nanowires.

At small N_d ($N_d \leq 0.33W$), most histogram plots show multi-peak distributions. This is similar to the unexpected result seen in double notch nanowires of t=10 nm; verifying that DW/notch interaction does not intuitively rely on the DW chirality, but also on the complex interactions with defects. Complexities are indicated by DW chirality having different pinning configurations.

However, as N_d increases beyond 0.33W, switching behaviour seem to have converged towards a single mode behaviour nanowire system at H_d= 117 Oe. This is supported by the decrease in σ_d and increase in P_p seen for $N_d \geq 0.3W$.
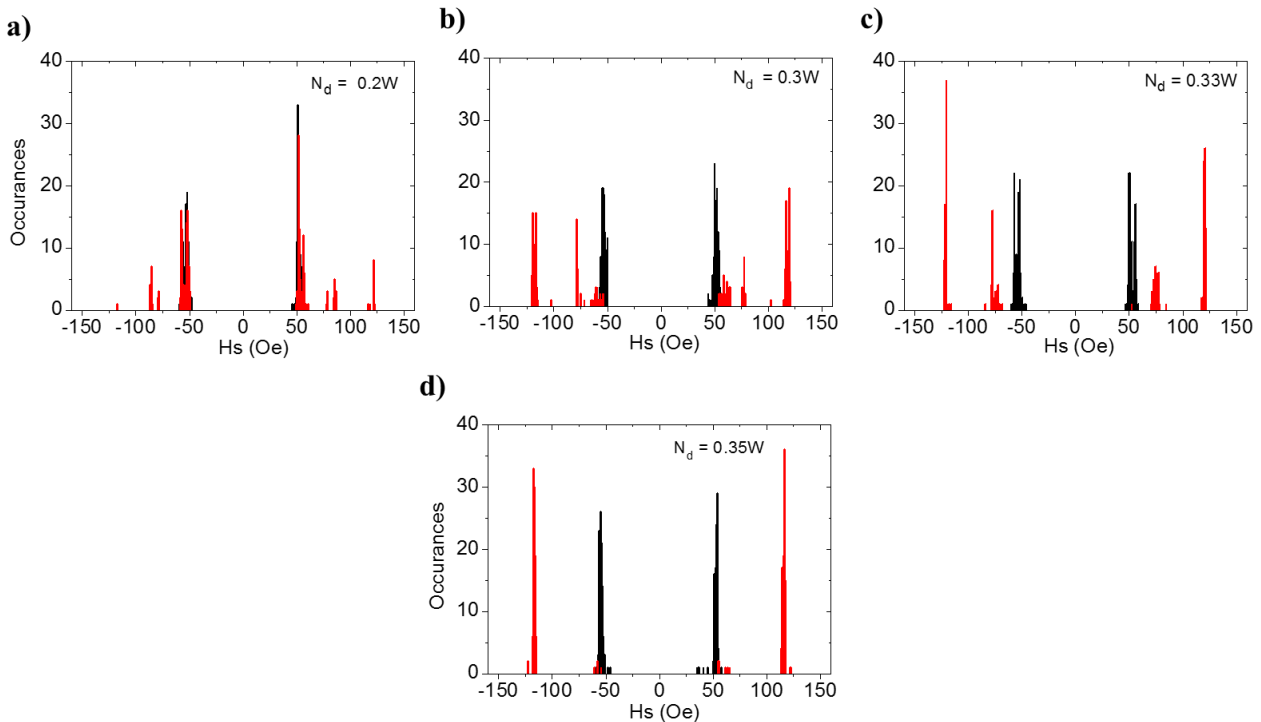
Figure 6.23: Switching field histogram plots of 100 single-shot measurements at region before the notch (black) and region after the notch (red) for nanowires of t=25 nm and double notch of N_d=0.22W (a), N_d= 0.2W (b), N_d= 0.3W (c), N_d= 0.33W (d) and N_d=0.35W (e).
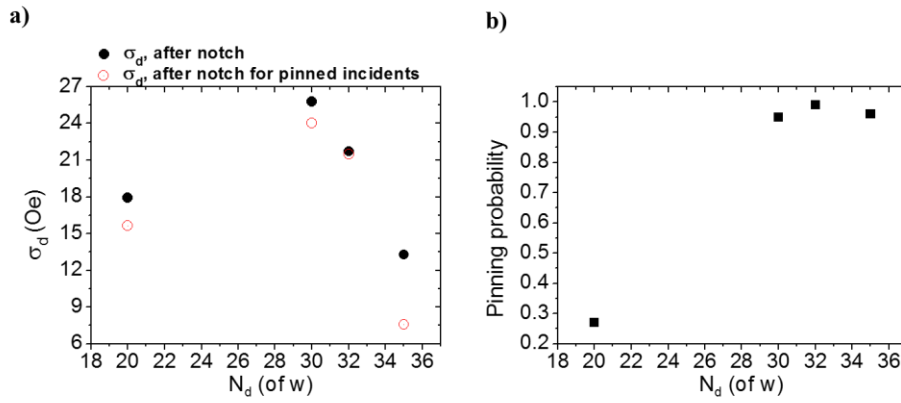
Figure 6.24: (a): Plot of depinning standard deviation versus notch depth for all switching attempts (solid circles) and for successfully pinned attempts (open circles). (b): Plot of pinning probability Vs notch depth. Both plots are for nanowire with t=25 nm and with single notch defect.

The next simulation investigates the depinning processes in nanowires of t=25 nm and for N_d=0.2W, 0.3W and 0.35W.

6.5.2. 3D Simulation of nanowire of t=25 nm and double notch defect

Simulation results for nanowires with double notch with N_d= 0.2W (Figure 6.25) show the existence of two unique pinning configurations with two depinning modes. Interestingly, both

a)

Input DW: ACW

DW Pinning Configuration #1

DW Pinning Configuration #2

Table 6.25-b: Pinning states for ACW DWs in nanowire of t=25 nm and single notch with N_d= 0.2W

ACW Pinning State	H_d (Oe)	Probability (%)	Switching Method
Configuration #1	185 ± 2.5	30	Depinning
Configuration #2	145 ± 2.5	70	Depinning

b)

Input DW: CW

DW Pinning Configuration #1
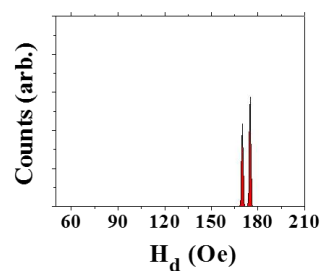
DW Pinning Configuration #2

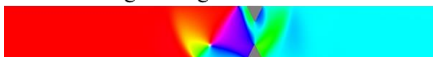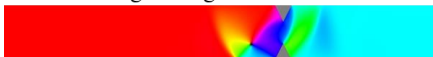**Table 6.25-b: Pinning states for CW DWs in nanowire of t=25 nm and single notch with N_d= 0.2W**

CW Pinning State	H_d (Oe)	Probability (%)	Switching Method
Configuration #1	185 ± 2.5	50	Depinning
Configuration #2	145 ± 2.5	50	Depinning

Figure 6.25: Micromagnetic simulation of DW pinning configurations for nanowire t=25 nm and single notch of N_d=0.2W for ACW (a) and CW (b) DWs. Tables summarize the switching outcomes for each pinned state. Plot shows constructed histogram for simulated DFD. H_{inj}= 50 Oe.

unique modes belong to the same chirality; in which in one of the two VDW pinning configuration, the leading edge of the VDW pins outside the double notch as it encounters what seems like an energy barrier pinning site. The other configuration, however, pins inside the double notch forming an energy well. This can be attributed to the shape of the DW structure as it encountered the double notches as it underwent WB transformations.

The two modes are of vortex structure. Unlike nanowire with t=10 nm, simulation results did not show any transverse-like pinned structures, and the two modes are of vortex structure.

As expected, the symmetrical nature of the double notch has resulted in producing the same pinning configurations and depinning modes for the ACW and CW chirality. Simulation results for N_d= 0.2W seem to be in agreement with MOKE measurements (Figure 6.23(a)). The histogram for nanowire with N_d=0.2W showed multi depinning modes.

a)

Input DW: ACW

DW Pinning Configuration #1

DW Pinning Configuration #2

Table 6.26-a: Pinning states for ACW DWs in nanowire of t=25 nm and single notch with N_d= 0.3W

ACW Pinning State	H_d (Oe)	Probability (%)	Switching Method
Configuration #1	175 ± 2.5	40	Depinning
Configuration #2	170 ± 2.5	60	Depinning

M

b)

Input DW: CW

DW Pinning Configuration #1

DW Pinning Configuration #2

Table 6.26-a: Pinning states for ACW DWs in nanowire of t=25 nm and single notch with N_d=0.3W

ACW Pinning State	H_d (Oe)	Probability (%)	Switching Method
Configuration #1	175 ± 2.5	70	Depinning
Configuration #2	170 ± 2.5	30	Depinning

Figure 6.26: Micromagnetic simulation of DW pinning configurations for nanowire t=25 nm and single notch of N_d=0.3W for ACW (a) and CW (b) DWs. Tables summarize the switching outcomes for each pinned state. Plot shows constructed histogram for simulated DFD. H_{inj}= 50 Oe.

As N_d is increased to 0.3W (Figure 6.26), results suggested the convergence of the two modes into a single-mode. Switching of the nanowire, however, remained to occur through DW depinning.

As N_d is further increased to 0.35W, results (refer to Figure 6.27) showed that the pinning configurations remained the same, but their H_d has converged into a single mode. Although this is similar to simulation result of t=10 nm, switching in t=25 nm occurred only through depinning, with no transverse-like structures; in which the two pinning configurations depinned following the same depinning mechanism.

When compared with MOKE measurements, results (Figure 6.23(d)) seem to be in agreement with simulation. Both histograms showed a single dominating peak indicating that the behaviour has converged towards a single depinning mode.

a)

Input DW: ACW

DW Pinning Configuration #1
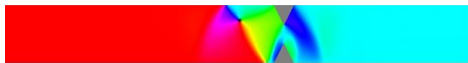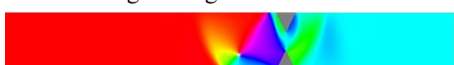

DW Pinning Configuration #2
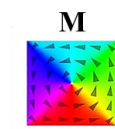
Table 6.27-a: Pinning states for ACW DWs in nanowire of t=25 nm and single notch with N_d=0.35W

ACW Pinning State	H_d (Oe)	Probability (%)	Switching Method
Configuration #1	170 ± 2.5	80	Depinning
Configuration #2	170 ± 2.5	20	Depinning

M

b)
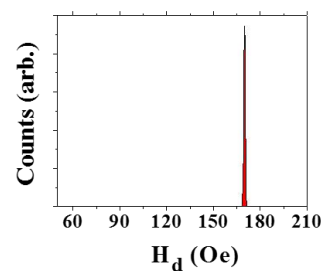
Input DW: CW

DW Pinning Configuration #1
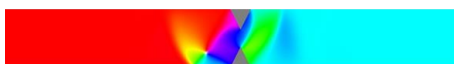
DW Pinning Configuration #2

Table 6.27-b: Pinning states for CW DWs in nanowire of t=25 nm and single notch with N_d= 0.35W

ACW Pinning State	H_d (Oe)	Probability (%)	Switching Method
Configuration #1	170 ± 2.5	60	Depinning
Configuration #2	170 ± 2.5	40	Depinning

Figure 6.27: Micromagnetic simulation of DW pinning configurations for nanowire t= 25 nm and single notch of N_d= 0.35W for ACW (a) and CW (b) DWs. Tables summarize the switching outcomes for each pinned state. Plot shows constructed histogram for simulated DFD. H_{inj}= 50 Oe.

In conclusion, it was observed that in nanowires of t=25 nm:

- A single notch system did not produce a single depinning mode behaviour, unlike the case of double notch where it is possible to produce a single-mode system due to chirality insensitivity.

- In the double notch case for nanowires of t=25 nm, switching of DWs happened only through DW depinning not re-nucleation (unlike in nanowires of t=10 nm).

- Results seem to hint that in a symmetrical notch, depinning modes is insensitive to DW chirality, however, different vortex structure pinning configurations resulted from the interaction of the double notch and the transformed VDWs.

- Simulation for double notch nanowires showed a gradual convergence toward single mode as N_d increases. In MOKE results, a sudden convergence toward single mode was seen at deepest notch only.

6.6. Nanowire of t= 40 nm and single notch defect

As nanowire thickness increases to t=40 nm, the depinning behaviour at single notches is expected to show only vortex structure with no transverse-like DW pinning structures, due to high thickness. Moreover, existence of two-mode depinning behaviour due to the CW and ACW chirality of VDWs would be expected.

While investigating eight nanowires with eight different N_d, the analysis presented is for the nanowires with N_d=0.15W, 0.25W, 0.35W, 0.5W and 0.7W that are believed to represent the trend for nanowires of t=40 nm with single notch. However, all the analysis will include the eight nanowires (histograms of all eight nanowires can be found in Appendix 2.7).

6.6.1. Results and discussion of MOKE measurements

MOKE results seem to agree to some extent with expectations. At small N_d, two multi-mode behaviours are seen which are expected to correlate with the ACW and CW VDW chiralities.

However, as N_d increases, the two-modes start converging until the system becomes a single-mode behavioural system. This suggests that as N_d increases, either the depinning mechanisms for the two DW chiralities become extremely similar yielding a single depinning mode, or that DWs interact with the pinning site and pin at it with the same pinning configurations. Such convergence behaviour can explain the suppression of depinning stochasticity indicated by the decreasing trend in σ_d as N_d increases (Figure 6.29).

As energy barrier increases with increasing notch depth, the P_p increases and converges to 1 for $N_d>0.25W$ indicating full pinning incidents in nanowires of t=40 nm. Results indicated a promising nanowire geometry for obtaining a single-mode nanowire system.
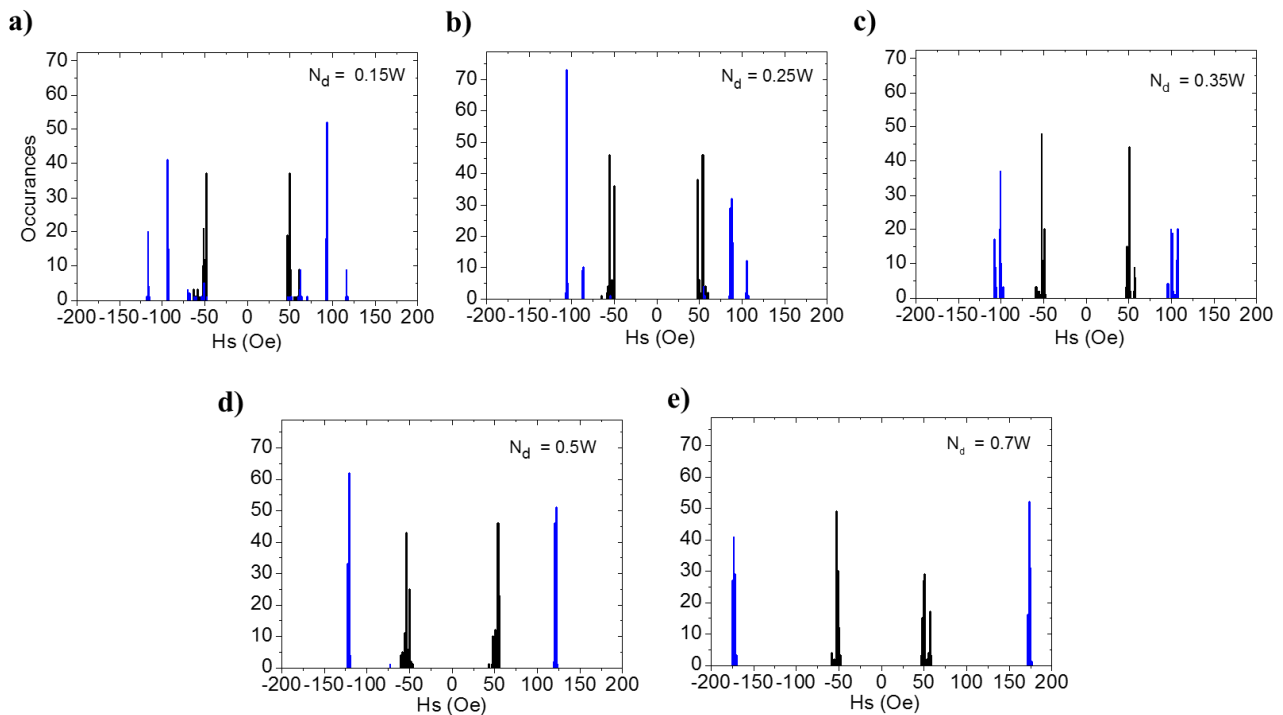
Figure 6.28: Switching field histogram plots of 100 single-shot measurements at region before the notch (black) and region after the notch (blue) for nanowires of t=40 nm and single notch of $N_d=0.15W$ (a), $N_d=0.25W$ (b), $N_d=0.35W$ (c), $N_d=0.5W$ (d) and $N_d=0.7W$ (e).
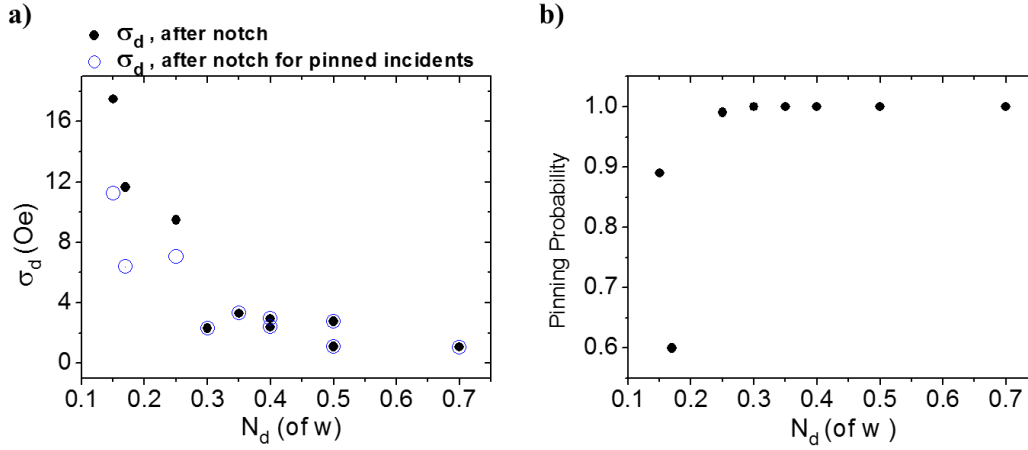
Figure 6.29: (a): a): Plot of depinning standard deviation versus notch depth for all switching attempts (solid circles) and for successfully pinned attempts (open circles). (b): Plot of pinning probability Vs notch depth. Both plots are for nanowire with t=40 nm and with single notch defect.

6.6.2. 3D Simulation of nanowire of t=40 nm

From plot in Figure 6.30, it is shown that the WB for nanowire of t=40 nm at H_p=50 Oe seems to be happening at the beginning of the turbulent regime. This is indicated by the lack of periodicity in the plot, and from WB velocity graph in Appendix 2.3. However, when examining the simulation snapshots, it can be assumed that a pseudo-periodic transformation occurred every 5 ns. For instance, the DW structure at t=1 ns and t=6 ns are very similar, the same can be said about t=2 ns and t=7ns, t=3 ns and t=8 ns. Therefore, the duration of period =5 ns, M_x/M_s for l=6000 nm.

Therefore the pseudo-period can be determined at 400 nm, and the position of the notch is moved 40 nm in order to simulate the possible pinning states in ten different notch positions along the WB cycle.

In the WB transformation presented in Figure 6.30 below, the DW does not seem to go through a transverse-like structure transformations. This is understandable as the demagnetisation energy produced from having a TDW in thick nanowires would be very high and hence would be highly unfavourable. Instead, the DW undergoes an elongation and contraction of its DW width.
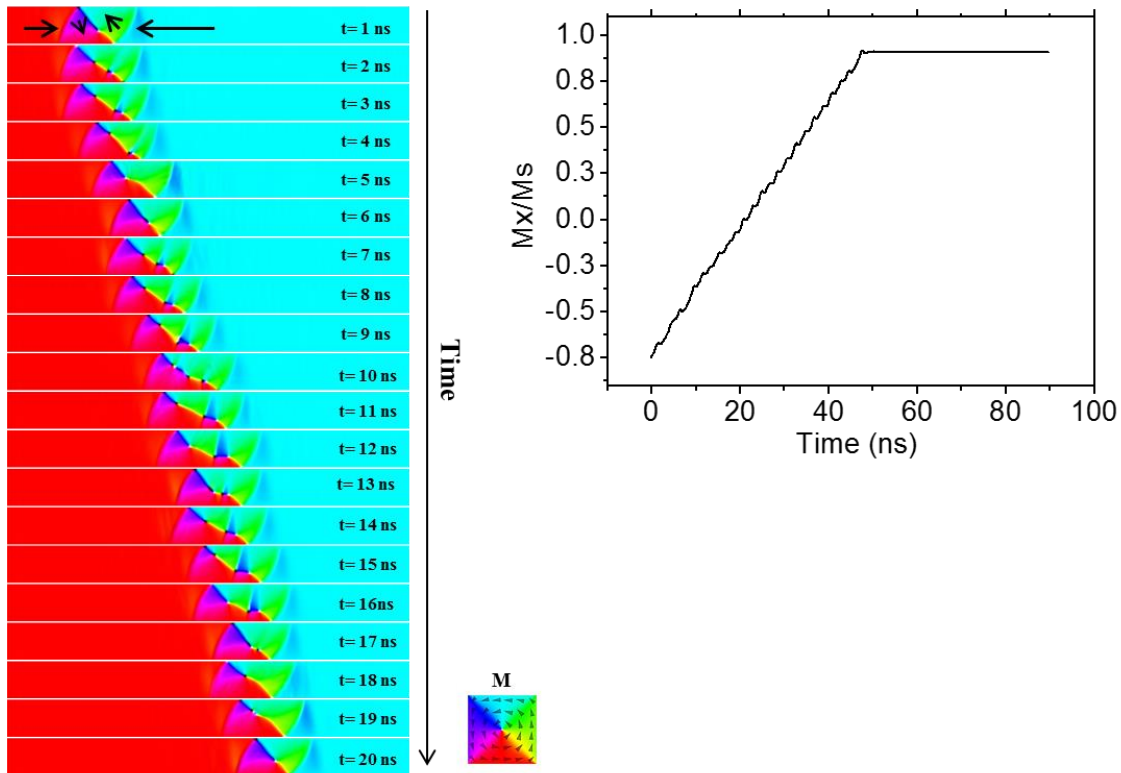
Figure 6.30: Micromagnetic simulation of WB transformations of ACW VDW in nanowire of t=40nm at H$_P$=50 Oe. Plot shows the magnetisation Vs time for the DW propagation.

The WB transformation for thick nanowires can be summarized as follows: As propagating field is applied above H$_{WB}$ (estimated at 15 ± 5Oe from simulation) the core will start moving in the transverse direction. However, since the vortex shape of the DW is highly favourable, the energetic cost for transforming the DW into a transverse-like structure is very expensive. As a result of the competition between the high **M$_z$** component that pushes the core towards the edge (as explained in section 3.3.3), on one hand, and the expensive energetic cost of losing the vortex shape on the other hand, the vortex core is elongated and splits to two cores and an anti-vortex core between the two cores [2] (refer to Figure 6.31). This splitting results in the elongation of DW as one core moves in the +y direction, but does not annihilate at the edge of
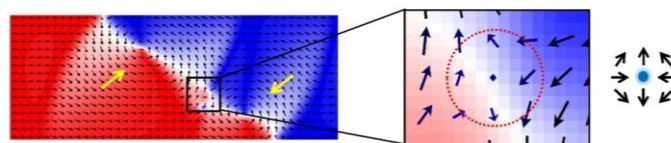

Figure 6.31: Simulation snapshot showing two vortex cores splitting with an anti-vortex in-between. Yellow arrows pointing at the two cores.

157

the nanowire. Eventually the two cores approach each other and annihilate into one core causing the DW to contract.

Simulations of the possible pinning configurations were done for nanowires with N_d= 0.15W, 0.5W and 0.75W.

Results and discussion of Simulation

Simulation results for single notch of N_d= 0.15W (Figure 6.32) showed two configurations, one for each chirality. As expected, transverse-like pinning configurations were not seen in any of the N_d due to the high nanowire thickness. This would justify why thick nanowires can result in less switching stochasticity [10]. Furthermore, result may suggest that interactions at single notches in thick nanowires are relatively insensitive to DW states compared with small N_d at nanowires of t=10 nm, especially when the associated WB transformation preserves the basic form of the VDW, leading to a more deterministic pinning states for each chirality.
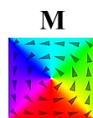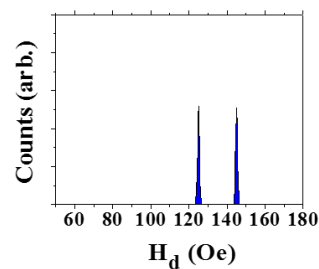
a)

Input DW: ACW

DW Pinning Configuration #1

M

Table 6.32-a: Pinning states for ACW DWs in nanowire of t=40 nm and single notch with N_d=0.15W

ACW Pinning State	H_d (Oe)	Probability (%)	Switching method
Configuration #1	**145 ± 2.5**	100	Depinning

b)

Input DW: CW

DW Pinning Configuration #1

Table 6.32-b: Pinning states for CW DWs in nanowire of t=40 nm and single notch with N_d=0.15W

CW Pinning State	H_d (Oe)	Probability (%)	Switching method
Configuration #1	**125 ± 2.5**	100	Depinning

Figure 6.32: Micromagnetic simulation of DW pinning configurations for nanowire t=40 nm and single notch of N_d=0.15W for ACW (a) and CW (b) DWs. Tables summarize the switching outcomes for each pinned state. Plot shows constructed histogram for simulated DFD. H_{inj}= 50 Oe.

When compared with MOKE measurements, simulation results seems to be in very good agreement with measurements. Both results showed two peaks in the histogram which can be attributed to the two chiralities. This observation implies that a single-mode behaviour system can be built if a mechanism to rectify the chirality of the propagating VDW can be innovated and integrated with this single notch system (this will be the topic of Chapter 8).

As N_d increases, simulations showed some unique interactions (refer to Figure 6.33 & 6.34). Some of the propagated CW VDWs have interacted with the deep notch of N_d=0.5W, and produced in a chirality flipping behaviour in which the VDW has transformed into an ACW VDW before pinning at the notch. This pinning configuration (CW: configuration #2), is the same as ACW: configuration #1, and is expected to play a role in reducing depinning stochasticity in this nanowire geometry. A similar result showing the flipping has been recently reported by Brando *et al* [5].

According to the simulation snapshots, flipping happened when the 'topological defect' of the leading edge of the DW interacted with the extended spin frustration area near the very edge of the nanowire (Figure 6.34(a-2)). Such interaction has caused nucleation of a new DW core
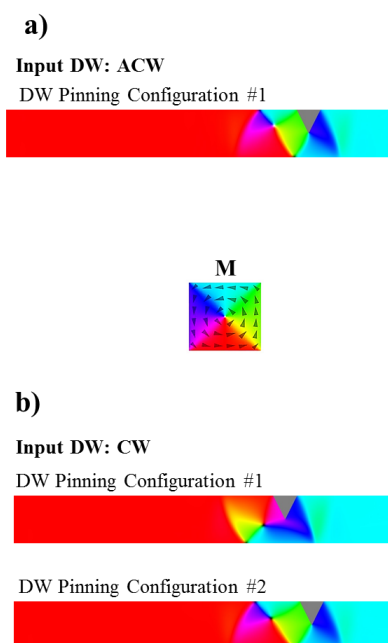

a)

Input DW: ACW

DW Pinning Configuration #1

M

b)

Input DW: CW

DW Pinning Configuration #1
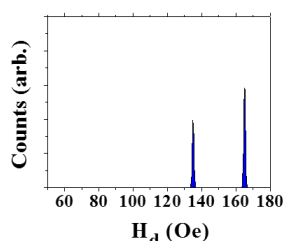
DW Pinning Configuration #2

Table 6.33-a: Pinning states for ACW DWs in nanowire of t=40 nm and single notch with N_d= 0.5W

ACW Pinning State	H_d (Oe)	Probability (%)	Switching method
Configuration #1	165 ± 2.5	100	Depinning

Table 6.33-b: Pinning states for CW DWs in nanowire of t=40 nm and single notch with N_d= 0.5W

CW Pinning State	H_d (Oe)	Probability (%)	Switching method
Configuration #1	135 ± 2.5	80	Depinning
Configuration #2	165 ± 2.5	20	Depinning

Figure 6.33: Micromagnetic simulation of DW pinning configurations for nanowire t= 40 nm and single notch of N_d= 0.5W for ACW (a) and CW (b) DWs. Tables summarize the switching outcomes for each pinned state. Plot shows constructed histogram for simulated DFD. H_{inj}= 50 Oe.

with ACW chirality. Although Brando *et al* [5] explained that the flipping occurs when DW arrives with its elongated structure, our simulation showed flipping incidents that happened at elongated and non-elongated DW structure indicating a more complex process.

The number of incidents in which the CW VDW was successfully flipped into an ACW VDW at the notch were 2 out of 10 (refer to Table 6.33-b in Figure 6.33). This indicates that the overall probability for the whole system to have a pinned ACW VDW at the notch is 60% (i.e: 100% when input DW: CW and 20% when input DW: ACW ((100% + 20%) /2 = 60%)). For the other eight CW states, an attempt to flip to ACW has occurred but was unsuccessful (Figure 6.34(b)) since the DW/notch-spins interaction occurred above the bottom edge of the nanowire (Figure 6.34(b-2).

When compared with MOKE results (Figure 6.28(d)), an interesting correlation was seen. The MOKE results showed a single peak distribution with σ_d of 3, indicating that the system is approaching a single-mode behavioural system with low depinning stochasticity.

Since simulation results did not show a clear indication of convergence of the two depinning modes that would explain the MOKE results, it was important to try to investigate how the single mode behaviour was obtained.
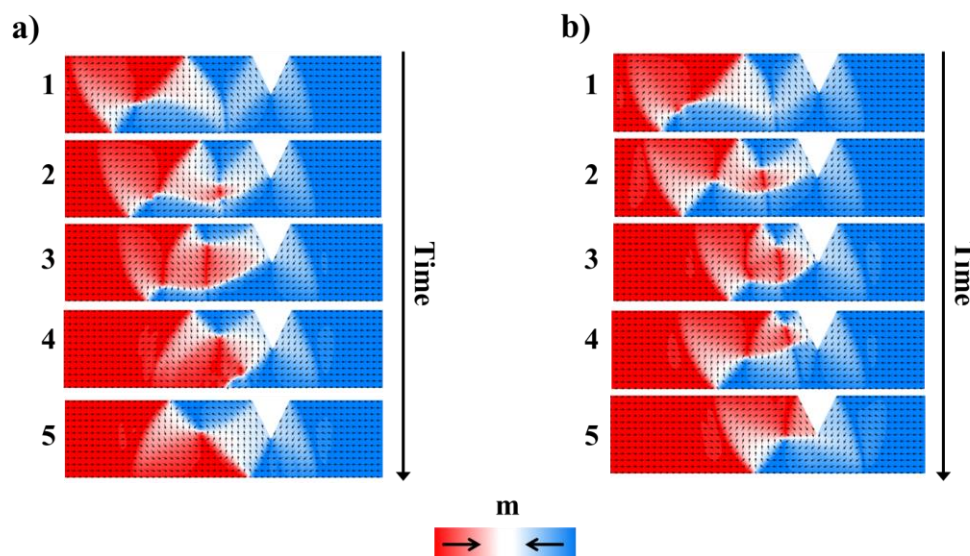

Figure 6.34: Micromagnetic simulation showing the successful flipping of CW chirality (a) and unsuccessful flipping attempt (b) in nanowires with of t=40 nm and N_d=0.5W .
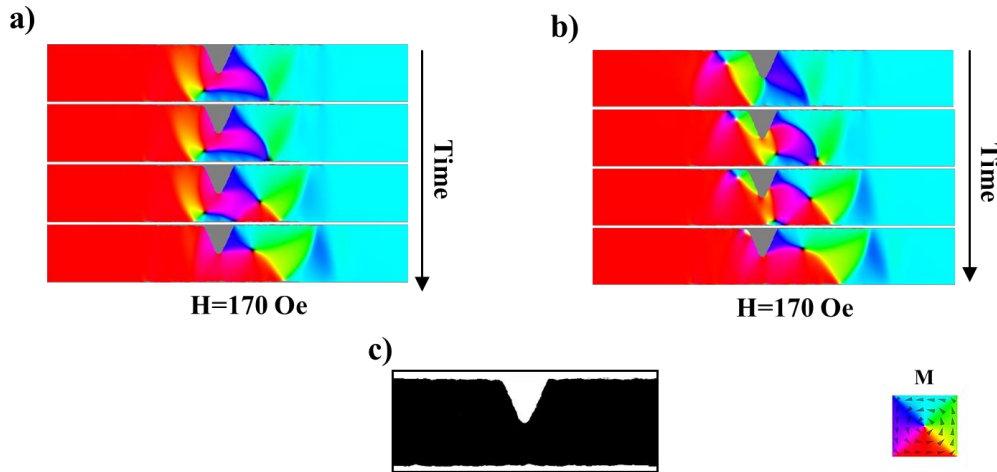
Figure 6.35: Micromagnetic simulation of nanowires of N_d=0.5W in rough nanowires. (a): CW chirality. (b) ACW chirality. (c): Schematic of imported roughness from SEM image.

Therefore, a more realistic simulation was performed by importing the edge roughness from the SEM image of the real nanowire (Figure 6.35(c)) and repeating the simulation.

The results in Figure 6.35 revealed that the edge roughness has enforced a consistent switching mechanism through re-nucleation at H_s= 170 ± 2.5 Oe. This switching mechanism was not seen in the first simulation where switching has occurred through depinning. Therefore, the single-mode behaviour seen in the MOKE measurements can be mainly attributed to the re-nucleation process that occurred in thick nanowires with rough edges. It is important to mention that the re-nucleation process here is different than the re-nucleation process seen previously in t=10nm nanowires. The flipping feature seen in Figure 6.34, however, is expected to play a secondary role in justifying the single-mode behaviour.

As N_d increases further to 0.7W, simulation results (Figure 6.36) showed similar results to N_d=0.5W. The flipping of the CW DW to ACW at the vicinity of the notch in certain cases has increased to 3 successful flipping attempts. Switching continues to happen through DW depinning affirming that in thick and smooth nanowires, depinning field is less than nucleation field even at deep notches. When compared with MOKE results (Figure 6.28(e)), measurements showed a single-peak distribution indicating a well-defined single mode switching system.

a)

Input DW: ACW

DW Pinning Configuration #1

M

b)
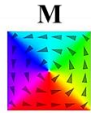
Input DW: CW

DW Pinning Configuration #1
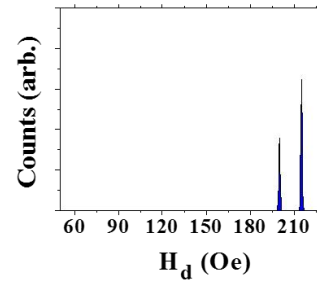

DW Pinning Configuration #2

Table 6.36-a: Pinning states for ACW DWs in nanowire of t=40 nm and single notch with N_d=0.7W

ACW Pinning State	H_d (Oe)	Probability (%)	Switching method
Configuration #1	**215 ± 2.5**	100	Depinning

Table 6.36-b: Pinning states for CW DWs in nanowire of t=40 nm and single notch with N_d= 0.7W

CW Pinning State	H_d (Oe)	Probability (%)	Switching method
Configuration #1	**200 ± 2.5**	70	Depinning
Configuration #2	**215 ± 2.5**	30	Depinning

Figure 6.36: Micromagnetic simulation of DW pinning configurations for nanowire t=40 nm and single notch of N_d=0.7W for ACW (a) and CW (b) DWs. Tables summarize the switching outcomes for each pinned state. Plot shows constructed histogram for simulated DFD. H_{inj}= 50 Oe.

Similar to the previous case, simulation was done on nanowire after introducing edge roughness to explore if this is a factor in having a single-mode behaviour system.

Results were consistent with the MOKE measurement, showing that H_s for both the CW and ACW pinning configurations has converged towards a single value of H_s= 250 Oe which resulted in a single-mode behavioural system due to re-nucleation switching, justifying the single-mode behaviour seen in MOKE.

It can be concluded that for single notches in nanowires of t=40 nm, the nature of the WB transformation in thick nanowires does not seem to allow for transverse-like DW structures to occur; hence, reducing the number of allowed pinning states to VDW shapes leading to reduction in switching stochasticity. Moreover, a new chirality flipping mechanism was seen at the notch which would help reduce the different pinning states. However, it is believed that

the main reason for the single-mode behaviour seen in real measurements comes from the re-nucleation process forced by the rough edges of the nanowire that seem to create strong pinning site. This conclusion seems to be very similar to the conclusion deduced by Im *et* al [10] where it was found that switching is deterministic in thick nanowires.

6.7. Nanowire of t=40 nm and double notch defect

For nanowires of t=40nm MOKE measurements will be presented and analysed for nanowires with N_d=0.2W, 0.3W, 0.35W, and 0.37W. As for simulation, 3D simulation for nanowire of $N_d = 0.15W$, 0.25W and 0.35W will be then presented.

6.7.1 Results and discussion of MOKE measurements

MOKE measurements for double notches show a multi-peak distribution behaviour with no indication of any convergence towards a single mode with increasing N_d.

This suggests that the DW/double- notch interaction is sensitive and will produce different pinning configurations similar to what was seen in the double notch case for t=25 nm, yielding a stochastic switching system.
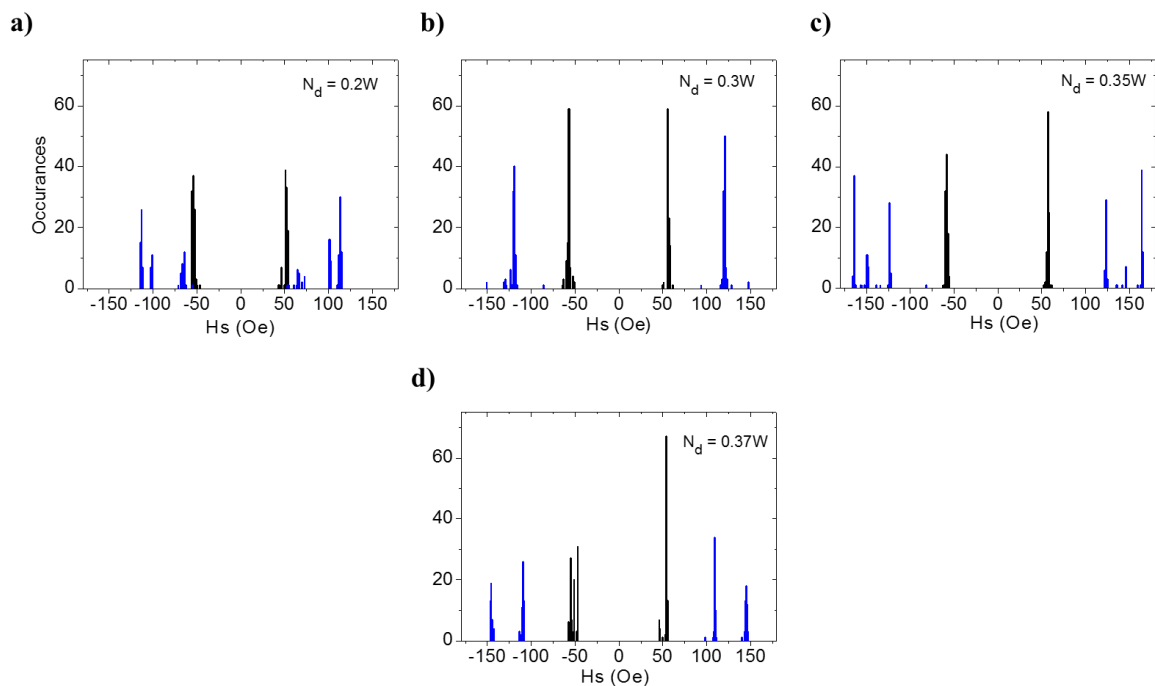

Figure 6.37: Switching field histogram plots of 100 single-shot measurements at region before the notch (black) and region after the notch (blue) for nanowires of t=40 nm and double notch N_d= 0.20W (a), N_d= 0.3W (b), N_d=0.35W (c), N_d=0.37W (d).
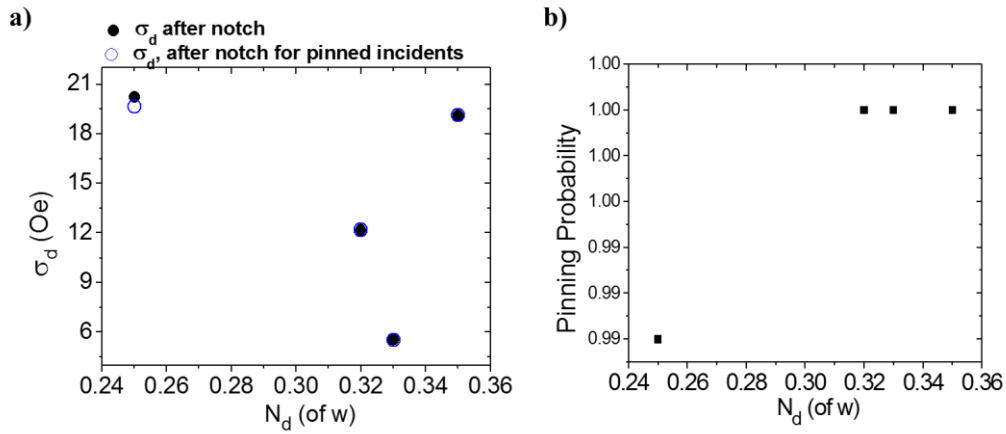
Figure 6.38: (a): Plot of depinning standard deviation versus notch depth for all switching attempts (solid circles) and for successfully pinned attempts (open circles). (b): Plot of pinning probability Vs notch depth. Both plots are for nanowire with t=40 nm and with double notch defect.

Moreover, the σ_d vs N_d plot (Figure 6.38) did not seem to produce a conclusive trend, affirming the presence of high switching stochasticity in the thick nanowires with double notch.

On the other hand, the P_p vs N_d plot showed an increase in pinning as N_d increases, with the least pinning probability of 98%. This is ascribed to the high energy barrier produced in thick nanowires, and the strong pinning at double notches compared with the single notch. Furthermore, the high P_p compared to nanowires of t=25 nm and 10 nm for the same N_d might suggest that the effect of thermal activation that assists depinning is less than that seen in thinner nanowires. This is expected since in thick nanowires, higher energy barriers are present due to the bigger volume (E_b α V), which means that the same amount of thermal energy (~KT) will be less effective on thick nanowires compared with thin nanowires.

6.7.2. 3D Simulation of nanowire of t=40 nm and double notch defect

Simulation has been conducted for nanowires with N_d= 0.15W, 0.25W and 0.35W.

Based on the MOKE result, it would be expected to see a stochastic behaviour due to the DW/double-notch interaction. On the other hand, the preservation of the vortex shape by the
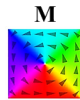
164

a)

Input DW: ACW

DW Pinning Configuration #1

DW Pinning Configuration #2

M

b)

Input DW: CW

DW Pinning Configuration #1

DW Pinning Configuration #2

Table 6.39-b: Pinning states for CW DWs in nanowire of t=40 nm and double notch with N_d = 0.15W

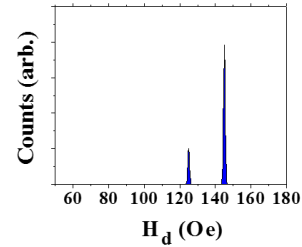| ACW Pinning State	H_d (Oe)	Probability (%)	Switching method
Configuration #1	145 ± 2.5	90	Depinning
Configuration #2	125 ± 2.5	10	Depinning

Table 6.39-b: Pinning states for CW DWs in nanowire of t= 40 nm and double notch with N_d = 0.15W

CW Pinning State	H_d (Oe)	Probability (%)	Switching method
Configuration #1	145 ± 2.5	70	Depinning
Configuration #2	125 ± 2.5	30	Depinning

Figure 6.39: Micromagnetic simulation of DW pinning configurations for nanowire t=40nm and double notch of N_d=0.15W for ACW (a) and CW (b) DWs. Tables summarize the switching outcomes for each pinned state. Plot shows constructed histogram for simulated DFD. H_{inj}= 50 Oe.

WB transformation in thick nanowire might lead to reduced pinning configuration and reduced stochasticity.

Results for N_d= 0.15W show two pinning configurations for different vortex shape. As expected, transvers-like structures are not favourable in thick nanowire. There exist one dominating mode out of the two depinning modes with vortex structure pinning outside the notch.

When compared with MOKE results, both results showed the presence of more than one depinning mode. However, the simulation results indicated only two peaks with one mode dominating.

As N_d increases, results for double notch with N_d=0.25W showed a single-mode behaviour system at H_d=130 Oe. This indicated that the other pinning configuration seen in N_d=0.15W are no longer stable.
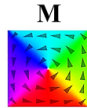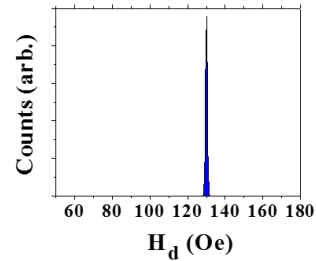
a)

Input DW: ACW

DW Pinning Configuration #1

M

ACW Pinning State	H_d (Oe)	Probability (%)	Switching method
Configuration #1	**130 ± 2.5**	100	Depinning

b)

Input DW: CW

DW Pinning Configuration #1

Table 6.40-b: Pinning states for CW DWs in nanowire of t=40 nm and double notch with N_d= 0.25W

CW Pinning State	H_d (Oe)	Probability (%)	Switching method
Configuration #1	**130 ± 2.5**	100	Depinning

Figure 6.40: Micromagnetic simulation of DW pinning configurations for nanowire t=40nm and double notch of N_d=0.25Wofw for ACW (a) and CW (b) DWs. Tables summarize the switching outcomes for each pinned state. Plot shows constructed histogram for simulated DFD. H_{inj}= 50 Oe.

When compared with MOKE measurements, there seem to be some inconclusive results to correlate with. However, for nanowire of N_d=0.25W, MOKE measurements showed an unexpected drop in distribution and spreading to around σ_d=5.5, and a convergence toward a single mode depinning behaviour.

Interestingly, this seems to be the only geometry in the double notch case that showed a single depinning behaviour. Therefore, it might be the case that for a certain double notch geometry (around 0.25W) in nanowires of t=40 nm, there might exist a system that exhibits a single-mode switching behaviour, due to reduced number of pinning configurations. This observation requires further verification by measuring different samples of similar N_d.

a)

Input DW: ACW

DW Pinning Configuration #1

DW Pinning Configuration #2

DW Pinning Configuration #3
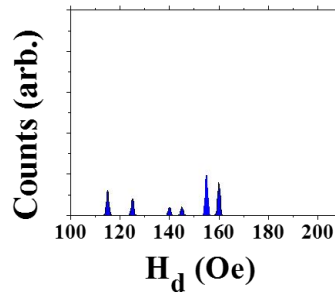

DW Pinning Configuration #4

DW Pinning Configuration #5

Table 6.41-a: Pinning states for ACW DWs in nanowire of t=40 nm and double notch with N_d=0.35W

ACW Pinning State	H_d (Oe)	Probability (%)	Switching method
Configuration #1	**145 ± 2.5**	10	Depinning
Configuration #2	**160 ± 2.5**	20	Depinning
Configuration #3	**160 ± 2.5**	40	Depinning
Configuration #4	**155 ± 2.5**	20	Depinning
Configuration #5	**125 ± 2.5**	10	Depinning

b)

Input DW: CW

DW Pinning Configuration #1

DW Pinning Configuration #2

DW Pinning Configuration #3

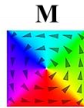DW Pinning Configuration #4

DW Pinning Configuration #5

Table 6.41-b: Pinning states for CW DWs in nanowire of t=40 nm and double notch with N_d=0.35W

ACW Pinning State	H_d (Oe)	Probability (%)	Switching method
Configuration #1	**155 ± 2.5**	20	Depinning
Configuration #2	**125 ± 2.5**	10	Depinning
Configuration #3	**155 ± 2.5**	30	Depinning
Configuration #4	**115 ± 2.5**	30	Depinning
Configuration #5	**140 ± 2.5**	10	Depinning

Figure 6.41: Micromagnetic simulation of DW pinning configurations for nanowire t=40 nm and double notch of N_d=0.35Wofw for ACW (a) and CW (b) DWs. Tables summarize the switching outcomes for each pinned state. Plot shows constructed histogram for simulated DFD.

As N_d increases furthermore to N_d= 0.35W, results (Figure 6.41) indicate very stochastic switching behaviour for deep double notches. All the pinning configurations showed a VDW shape where the DW leading edge pins at the notch, inside the double notch or attempts to form a new core near one of the notches. Upon studying the simulation snapshots, it was seen that

the DW first pins with one of the notches normally and then interacts in a complex manner with the other notch. For instance the ACW DW leading edge pins with the top notch first and then interacts with the bottom notch. The opposite is seen for the CW DW. This might justify the complexity seen at the vicinity of the double notches but not in the single notches.

It can be concluded that double notch design in thick nanowires:

- Produced a highly stochastic depinning behaviour as having double notches seem to trigger interactions between DW and double notch which can become complex in deep notches.

- Vortex structure is the only pinning structure that is present in t=40 nm nanowire

- Based on simulation, switching occurs through depinning (not re-nucleation) for all notch sizes and shapes.

- It is difficult to draw any conclusion on the trend by which double notches will react to the DW in t=40 nm, where either the notches stabilise the complex interactions at the notch or produce different pinning modes. This is unlike the single notch case, where the interaction seems to be more deterministic and would result in converging the depinning modes.

- The unpredictable stochastic switching behaviour of double notches was unexpected for nanowires with t=40 nm since transverse shapes of DW is not allowed in thick nanowires which would imply less number of possible pinning configurations and a deterministic switching behaviour.

6.8. Conclusion

It can be concluded that nanowire thickness and notch depth are major factors in affecting the interaction of DW at vicinity of notch, as well as the depinning mechanism, which in turn affects switching stochasticity.

It was generally seen that DW depinning mechanism from single and double notches is stochastic. This is due to the varying DW structures that can arrive to the notch due to WB transformation resulting in varying interactions with the pinning site, and yielding different pinning configurations. Nevertheless, certain geometries of nanowires have shown a convergence of depinning behaviour towards a single-depinning mode at deep notches (t=10 nm with single notch, t=25 nm with double notch and t=40 nm with single notch). This convergence occurred because either there are limited number of different DW transformations arriving to the notch due to the nature of WB at that nanowire geometry, or because the geometry and in some cases the edge roughness force the different DW pinned configuration to depin following the same depinning mechanism (usually this happens via re-nucleation). Furthermore, other geometries (t=40 nm and single notch with small N_d) have shown two-mode behaviour that simply correspond to simple ACW and CW VDW pinning configurations. These geometries can produce a single-mode behavioural system if the input DW chirality can be controlled or its chirality rectified before reaching the notch while conserving its WB transformation (this will be the topic of Chapter 8).

Interestingly, it was noticed that a nanowire with symmetrical defect does not necessarily produce a deterministic switching system. This observation is counter-intuitive to the basic assumption that symmetrical notches with chirality-insensitive feature will mitigate stochasticity. This is because symmetrical notches seem to trigger complex DW/notch interaction, and can hence stabilize multiple DW configurations. In fact, it was found that thick nanowire with single deep notch produced the most deterministic magnetic system.

In addition to the nanowires depinning behaviours, it was observed that many of the above studied systems exhibited a DW passing (non-pinning) behaviour, or weakly pinned configurations that were not indicated in the simulation. This observation highly suggests that thermal activation is playing a major role in assisting DW passing events; especially that such

passing behaviour was seen to be the least in thick nanowires. The latter is justified by the fact that the energy barrier is proportional to the nanowire volume (in this case thickness); hence, the same amount of thermal energy will be able to assist DW passing in thin (t=10 nm) nanowires where energy barrier is smaller than that found in thick nanowires (of t=40 nm). Furthermore, it was noticed that double notches seem to produce a higher pinning probability compared with single notches of the same notch gap size, suggesting that the pinning energy landscape at double notches is difficult to surpass. However, this suggested conclusion would require additional experimental/modelling work to be verified.

Finally, this study have shown the validity of the simulation method created in providing qualitative predictions and understanding of the different possible DW pinning configurations. There is room for optimization, and additional modification would be needed to gain a modelling methodology that would provide quantitative data that matches real measurements. Nevertheless, this method can be used to further explore phase space models to find reliable switching geometries to be used in reliable future magnetic applications.

6.9. References

[1]   M. T. Bryan, T. Schrefl, and D. Allwood, "Dependence of transverse domain wall dynamics on permalloy nanowire dimensions," *Magnetics, IEEE Transactions on,* vol. 46, pp. 1135-1138, 2010.

[2]   S.-M. Seo, K.-J. Lee, W. Kim, and T.-D. Lee, "Effect of shape anisotropy on threshold current density for current-induced domain wall motion," *Applied physics letters,* vol. 90, p. 252508, 2007.

[3]   J. Yang, C. Nistor, G. S. D. Beach, and J. L. Erskine, "Magnetic domain-wall velocity oscillations in permalloy nanowires," *Physical Review B,* vol. 77, Jan 2008.

[4]   L. K. Bogart, D. S. Eastwood, and D. Atkinson, "The effect of geometrical confinement and chirality on domain wall pinning behavior in planar nanowires," *Journal of Applied Physics,* vol. 104, p. 033904, 2008.

[5]   J. Brandao, R. L. Novak, H. Lozano, P. R. Soledade, A. Mello, F. Garcia*, et al.*, "Control of the magnetic vortex chirality in Permalloy nanowires with asymmetric notches," *Journal of Applied Physics,* vol. 116, Nov 21 2014.

[6]   A. Vansteenkiste, J. Leliaert, M. Dvornik, M. Helsen, F. Garcia-Sanchez, and B. Van Waeyenberge, "The design and verification of mumax3," *AIP Advances,* vol. 4, p. 107133, 2014.

[7]   J. Akerman, M. Muñoz, M. Maicas, and J. L. Prieto, "Selective injection of magnetic domain walls in Permalloy nanostripes," *Journal of Applied Physics,* vol. 115, p. 183909, 2014.

[8]   J. Akerman, M. Munoz, M. Maicas, and J. L. Prieto, "Stochastic nature of the domain wall depinning in permalloy magnetic nanowires," *Physical Review B,* vol. 82, Aug 31 2010.

[9]   U.-H. Pi, Y.-J. Cho, J.-Y. Bae, S.-C. Lee, S. Seo, W. Kim*, et al.*, "Static and dynamic depinning processes of a magnetic domain wall from a pinning potential," *Physical Review B,* vol. 84, p. 024426, 2011.

[10]   M.-Y. Im, L. Bocklage, G. Meier, and P. Fischer, "Magnetic soft x-ray microscopy of the domain wall depinning process in permalloy magnetic nanowires," *Journal of Physics: Condensed Matter,* vol. 24, p. 024203, 2012.

Chapter 7:

The Effect of DW Injection Method on Stochastic Pinning/depinning

From the previous chapter, it was concluded that DW depinning stochasticity is strongly affected by the interaction of DWs with pinning sites. This, in turn, is a product of the intrinsic dynamic transformations that DWs undergo when propagating above H_{WB}. Furthermore, this interaction is affected by the shape of the WB cycle that is determined by both the initial structure of the DW and propagation field [1].

As deduced from the previous chapter and as reported in literature [2], any small change in the DW profile can create large difference in the depinning mode. This may suggest that the method used to nucleate DWs can play a role in DW stochasticity, as it can have an effect on both the initial DW structure and the propagation field. Hence, it is important to investigate how different injection methods affect stochastic depinning behaviours.

There are two main injection methods used to inject DWs into a nanowire. The first method employs a nucleation pad of low coercivity, designed to switch at low field and inject the DW into the nanowire using a global external field (H_{ext}) [3, 4]. The other method utilizes the induced magnetic field from electric pulses flowing in a strip line perpendicular to the nanowire device [5, 6].

In the nucleation pad method, the nucleated DW gets pinned at the junction between the pad and the nanowire and is injected to the nanowire when $H_{ext} \geq H_{inj}$ [7]. Experimental evidence has shown that the value of H_{inj} can have a distribution affected by thermal perturbations [8]. Moreover, the magnetisation state of the nucleation pad can also play a role in affecting H_{inj}

distribution, especially when a small transverse field is applied [9]. These factors can result in adding a level of stochasticity to the DW transformation process. This method of nucleation will be referred to as 'pad nucleation' (PN) in this chapter.

On the other hand, in the current pulse nucleation method, DWs are nucleated within nanoseconds from the current pulse [5]. Upon DW nucleation, the external field (H_{ext}) can hypothetically be utilized to propagate DWs at any value of $H_{ext} > 0$. Moreover, when voltage and duration of the current pulse are set to sufficient values, nucleation of DW is considered to be deterministic [6]. Throughout this chapter, this method will be referred to as 'current pulse nucleation' (CN).

It is the aim of this chapter to explore the role of the injection method in affecting DW stochasticity. This will be done by designing a method for directly comparing the two methods of PN and CN to investigate if there exist intrinsic differences that can affect DW propagation and depinning. However, a study will first be done to investigate how DW depinning modes and stochasticity are affected when DWs are nucleated using CN method, and propagated at different fields.

7.1. Propagation of DWs in different regimes

Previous studies have shown that DWs can propagate in three regimes depending on their propagation field [10-12]. In each regime, the DW exhibits different dynamical characteristics that affect its affinity to pin at intrinsic defects (edge roughness) as well as artificial defects [13], in addition to altering its velocity.

As mentioned in section 3.3.3, at low propagation fields (less than H_{WB}), the DW is expected to maintain its structure without deforming, and may propagate rigidly with low pinning stochasticity. This is known as the viscous regime. As H_p exceeds H_{WB}, DW enters the

oscillatory/periodic regime where its internal structure undergoes periodic transformations that cause a decrease in DW velocity and an increases in its depinning stochasticity. As H_p continues to increase, the DW enters the turbulent regime where it undergoes unstable transformations and its velocity increases with H_p again [11].

Although DWs in the viscous regime are expected to show a regular motion with zero pinning probability, it has been reported that such behaviour can only happen in high quality nanowires at very low H_p [10]. In other more common nanowires, intrinsic defects result in H_p exceeding H_{WB}.

Therefore, in order to study the effect of CN on the depinning stochasticity, it is important to start by investigating the different propagation regimes that are accessible in our nanowire devices using the CN method.

7.1.1. Experimental setup for CN measurements

Py nanowires of widths w=500, 400, 300, l=20μm and t=20nm were fabricated using EBL followed by thermal evaporation. Electric contacts were fabricated by depositing Ti (20 nm)/Au (200 nm) metals perpendicular to the Py nanowires to form a 2 μm wide strip line used for passing the electric current pulses. The strip line was patterned using photolithography. Figure 7.1 shows a schematic of the fabricated sample.

A voltage signal of 4.5 V and pulse duration of 50 ns was injected in the 2 μm wide strip line to nucleate the DW. From eq. 3.10 ($\mathbf{H} = I/2w$) the field induced from the electric pulse was calculated to be around 280 Oe which is higher than the nanowire coercivity (H_c=140 Oe). The coercivity was determined by measuring the field needed to switch the nanowire without injecting a DW via CN method. The pulse generator was 'synchronised' with external field (generated by the electromagnet), H_{ext}, and programmed to allow the nucleating signal to be
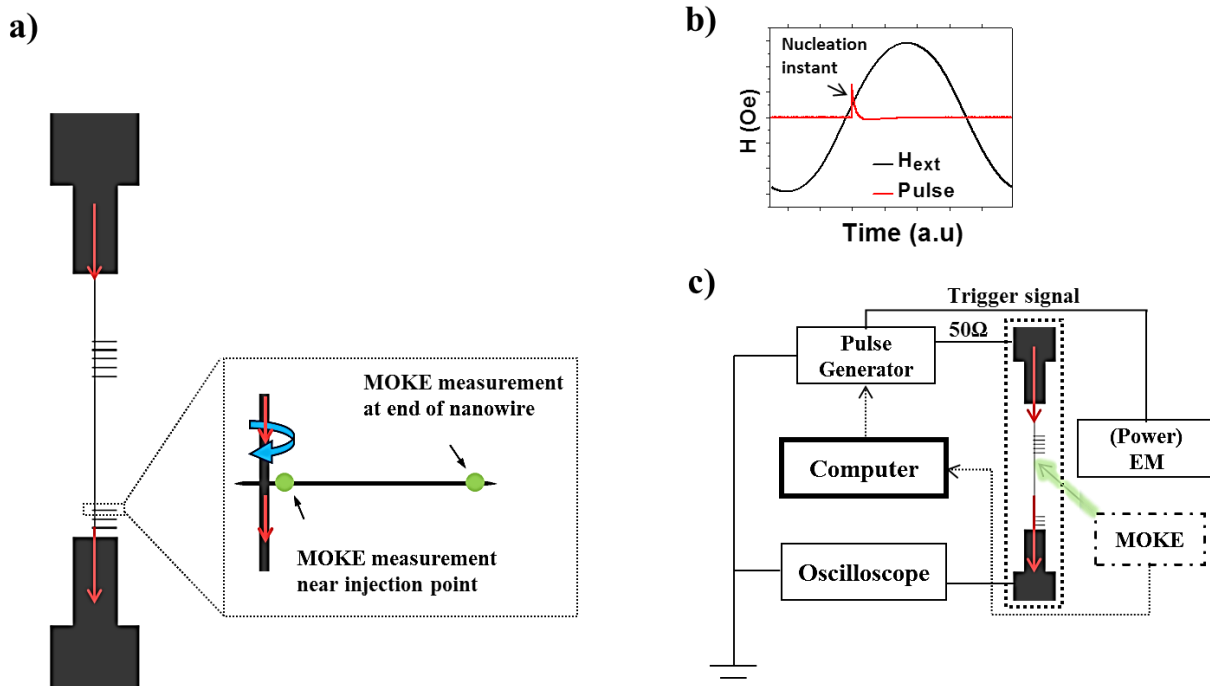
Figure 7.1: Schematic of the current pulse nucleation nanowire experimental setup. (a): Schematic showing the contacts, strip line and nanowires. Enlarged image shows the direction of pulse, induced magnetic field (blue arrow) and location of MOKE laser spots at regions near the start and end of the nanowire. (b): Plot of input signal sent to pulse generator and electromagnet showing time of pulsing (DW nucleation) wrt H_{ext}. (c): Overall schematic showing how MOKE system is interconnected in the experimental setup.

injected when H_{ext} reaches a specific value (Figure 7.1(b)). For instance, to propagate the DW at 50 Oe, the input program of the pulse generator was modified to send a pulse at the same time instant when the H_{ext} sinusoidal signal reaches 50 Oe. This external field will be referred to as nucleation field (H_N) as it reflects the field value at the instant of DW nucleation.

Magnetisation measurements were taken using the MOKE setup (described in section 4.4.1) at the region close to the nucleation point, near strip line (refer to Figure 7.1(a)) in order to investigate the switching behaviour close to the point of DW nucleation. Nucleation of DWs was induced at a range of nucleation fields varying from H_N=0.5 Oe to H_N=180 Oe in increments of 10 Oe. At each H_N, one hundred single-shot measurements were taken and the switching field was recorded for the statistical analysis. The same experiment was then repeated after focussing the laser spot at the end of the nanowire in order to test the ability of DWs to propagate through the nanowire at a given field. Results are then used to investigate

how stochastic switching is affected. The results of these measurements are shown in Figure 7.2.

Results and Discussion

Figure 7.2(a) shows a scatter plot of the switching fields H_s as a function of H_N in nanowire of w= 500nm. In an ideal nanowire with no edge roughness all injected DWs would be expected to propagate at H_N. However, in real nanowires with edge roughness, it is expected that switching can become stochastic at low H_N (except in very high quality nanowires [10]).

From the plot in Figure 7.2(a), it is indicated that a relatively high level of stochasticity existed with a spread of fields at H_N<10 Oe before the switching behaviour became more deterministic with tight distribution at $H_N \geq 10$ Oe. For instance, when nucleating at H_N= 0.5 Oe, H_s was detected to be ranging from 1.5 to 16 Oe. This suggests that the DW is experiencing stochastic depinning as it propagates from the injection point to the 5 µm laser spot. The existence of a switching distribution at low values of H_N indicates that the perfectly smooth propagation regime found by Munoz *et al* [10] could not be seen in this nanowire. Since H_{WB} for nanowire of similar geometries were found to be ranging from around 5 Oe [14] to 15 Oe (refer to Appendix 2.3), it can be concluded that, for this nanowire, it is not possible to propagate
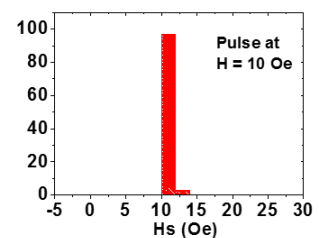
a)
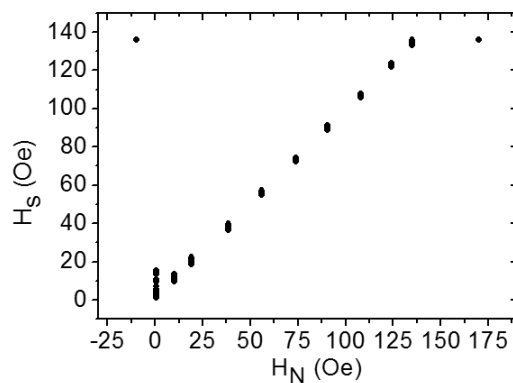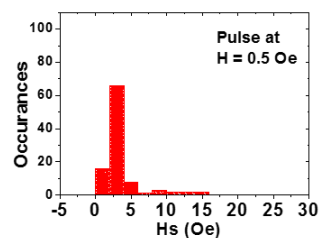
Figure 7.2: (a): Scatter plot showing H_s with respect to H_N field applied during DW injection in nanowire of w= 500nm. (b): Detailed histograms for the hundred single-shot measurements taken at H_N= 0.5 Oe (below WB). (c): Histograms for the hundred single-shot measurements taken at H_N=10 Oe (above WB).

reliably below H_{WB} due to finite edge roughness. Another factor that could make propagation below H_{WB} difficult to achieve might come from the high localized field that is generated by the nucleating pulse current. This localized field is added to H_{ext} resulting in the DW being propagated by a high propagation field (above H_{WB}) from the instant it got nucleated [15].

It can be seen from histograms in Figure 7.2(b) and (c) that a drop in switching stochasticity occurred at H ≥ 10 Oe, where σ_d dropped from 2.8 to 0.6 Oe when DW was nucleated at H_N= 0.5Oe and 10 Oe, respectively. This verifies that deterministic switching started at H_N=10 Oe. Based on the estimated WB field for this nanowire, it can be deduced that the reliable and controlled propagation seen at H_N≥10 Oe is most likely to be occurring because the DW is now propagating at a field sufficient to overcome intrinsic defects; hence, producing a deterministic switching behaviour even though DW propagation is in the oscillatory regime.

When studying the switching stochasiticity near the end of the nanowire (Figure 7.3(a)), at H_N =0.5 Oe, H_s was in the range of 10 to 41 Oe. This observation revealed that higher switching stochasticity behaviour occurred when DW had to propagate along the full length of the nanowire compared with the measurements taken when laser spot was focussed near the injection strip.
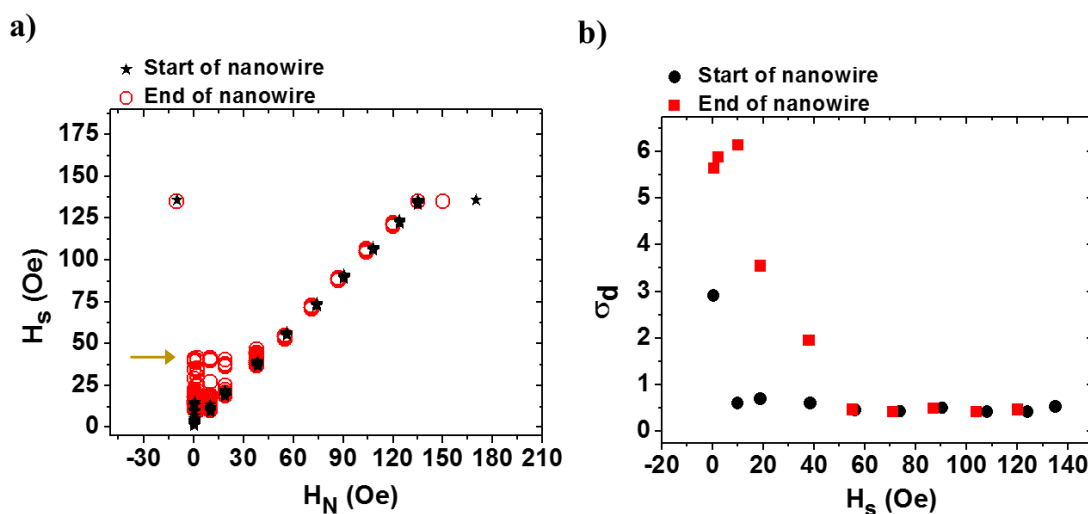

Figure 7.3: (a): Scatter plot showing distribution of H_s at different H_N measured near current line (black) and at 20 μm from current line (red) in nanowire of w= 500 nm (error = ± 2 Oe). Arrow points at maximum H_s value at lowest H_N. (b): Standard deviation for values of H_s that were measured near the current line (black) and at 20 μm from the current line.

In order to get a more quantitative measure of stochasticity, the σ_d of all sets of single-shot measurements taken for both laser spot locations were calculated and plotted as function of H_N in Figure 7.3(b). The plot showed a rise of switching stochasticity for measurements done at end of nanowire compared with those done near nucleation point. This was indicated by the rightward shift of the σ_d curve. This rise in σ_d is justified by the fact that the further the DW propagates along the nanowire, the more defect sites it will encounter. As a result, it is more probable for the DW, as it undergoes dynamical transformations, to reach an edge defect with a different and stronger pinning configuration. Moreover, high values of σ_d were seen for $H_s \leq 40$ Oe as the propagation field is not sufficient enough to overcome all defects.

From Figure 7.3(a) it can be seen that deterministic switching; where DWs propagated all the way along the nanowire without pinning, occurred at $H > 40$ Oe. This suggests that the strongest pinning site encountered by DW can be dynamically depinned when $H_{ext} = 45$ Oe $\pm$ 5 Oe leading to deterministic and controlled switching. For the purpose of comparison, the same experiments were repeated for nanowires with $w = 300$ nm and 400 nm.
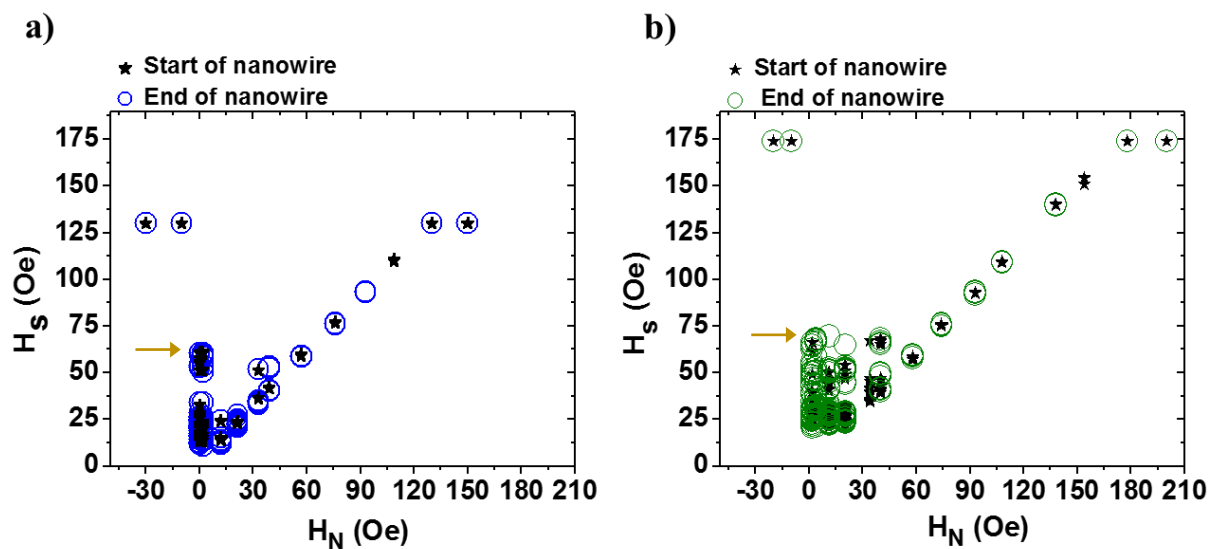

Figure 7.4: Scatter plots showing distribution of H_s at different H_N measured near injection point (black/blue) and at 20μm from injection point (green) in nanowire of $w= 400$ nm (a) and $w=300$ nm (b). (error = ± 2 Oe). Arrow points at maximum H_s value at lowest H_N.

The results of these measurements, as shown in Figure 7.4, showed few differences in the stochastic H_s range where the maximum switching occurred at 43 Oe, 63 Oe and 72 Oe for $w=$ 500, 400 and 300 nm, respectively, when nucleation occurred near 0 Oe. However, results for the three nanowires seem to affirm that deterministic switching happens above the same value of H = 45 Oe ± 5 Oe, suggesting that the source of this limit could be due to the fabrication limitations.

From the above experiment, it was concluded that stochasticity in magnetic switching is affected by the applied field as well as the length of the DW propagation distance. It would be interesting as well as valuable to further investigate the dependence between DW propagation distance and switching stochasticity. Hence, further investigation was done in the next section.

7.2. The effect of DW propagation distance on switching stochasticity

In order to further investigate how pinning stochasticity changes as DWs propagate farther, magnetic measurements were taken at regularly spaced intervals along the nanowires. This was done by nucleating DW at $H_N \approx 0$ Oe and applying a sweeping field from -300 Oe to 300 Oe to propagate DWs. The laser spot was focussed at the injection point (close to the current line), and then at a distance of 4, 8, 12 and 16 μm away from the injection point. Nanowires of $w=$ 300, 400 and 500nm were measured by taking 50 single-shot measurements and calculating the average H_s as well as the minimum and maximum H_s in each nanowire at each distance.

Results and Discussion

Figure 7.5 and 7.6 show the histogram plots measured at each position for the three nanowires (w=300, 400 and 500 nm nanowires) along with plots showing changes in the average value of H_s and σ_d as a function of propagation distance. Additionally, Figure 7.6 shows a plot for the maximum and minimum values of H_s as a function of distance.

All the histograms (Figure 7.5(a)) showed an increase in the spreading/distribution of H_s as well as in the maximum value of H_s as measurements are taken farther away from injection point. This is understandable as increasing the propagation distance means that DWs will have a higher probability of encountering strong pinning sites and getting pinned with a strongly pinned configuration. This is also verified by the average H_s vs distance plot (Figure 7.5(b)) that shows an increase in H_s with increasing distance from nucleation point. Additionally, the histograms showed an increase in switching stochasticity indicated by the positive slope in the σ_d plots (Figure 7.5(c)). From this, it can be deduced that increasing DW propagation distance will lead to an increase in switching stochasticity. This conclusion verifies the one deduced in the previous section when magnetisation was measured at the end of the nanowire at $H_N \approx 0$ Oe (Figure 7.3 and Figure 7.4).

Furthermore, a plot that shows the changing trend in the maximum and minimum H_s values with respect to distance from nucleation point has been drawn (Figure 7.6). The plots suggest that both values eventually reached saturation. However, minimum switching fields show very little variation as a function of distance, meaning that the minimum H_s value measured near the nucleation point was close to the minimum value measured near the end of nanowire. This suggests that there will always exist a probability for the DW to pass without experiencing strong pinning, even in long nanowires.

On the other hand, maximum H_s seems to increase abruptly with increasing propagation distance, before reaching saturation (with a slope > 2 Oe/μm compared with slope < 1 Oe/um for minimum H_s). This indicates that the DWs only had to travel a certain distance before they encountered the maximum strength defect site for the nanowires. This also indicates that strong DW pinning at edge defect site does not seem to occur gradually, but rather abruptly at a critical distance. From Figure 7.5(c), it can be deduced that this distance is between ~5-10 μm for the given nanowires.
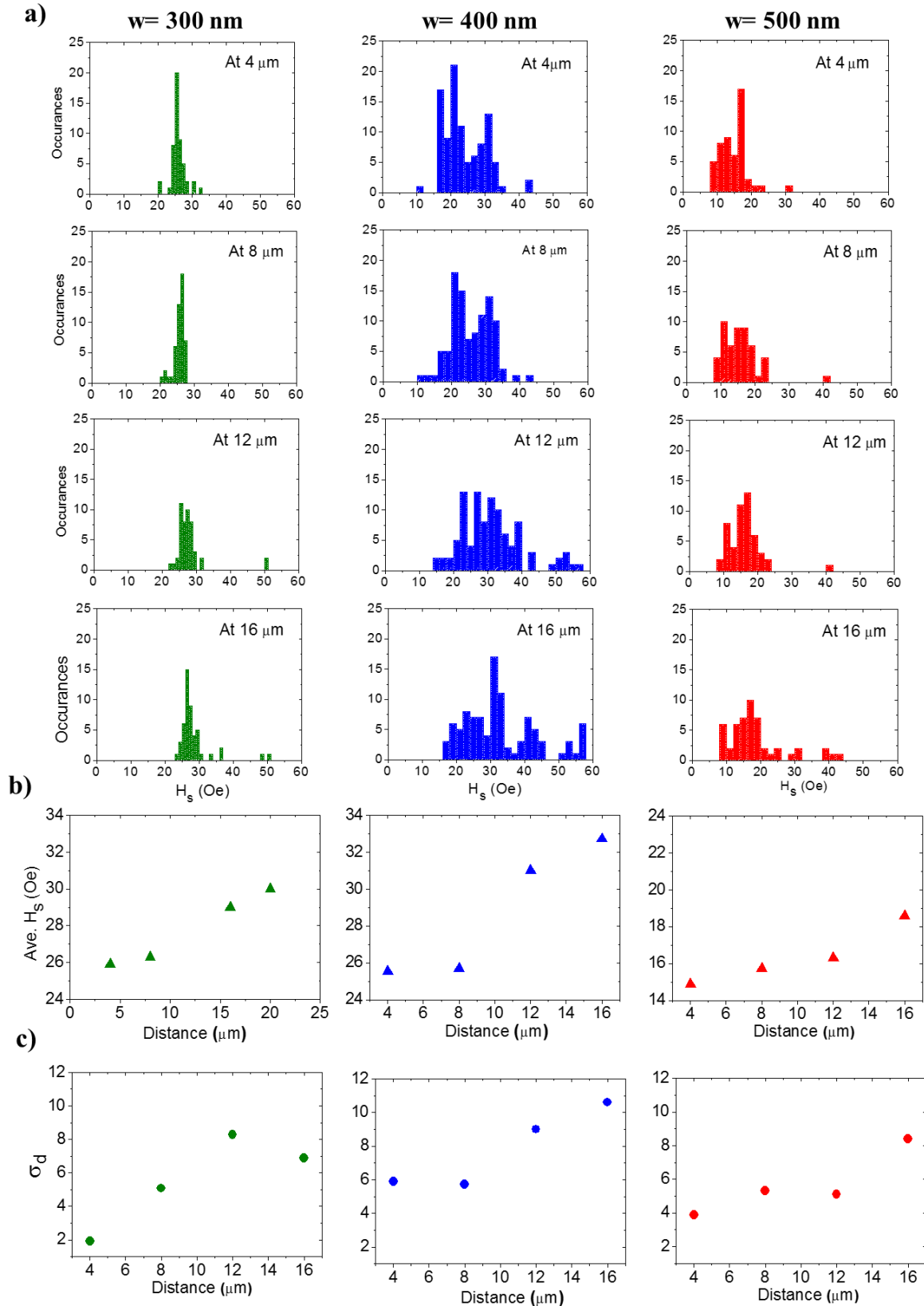
Figure 7.5: Analysis data of position resolved single shot MOKE measurement for nanowires of w=300 nm (green), w=400 nm (blue) and w= 500 nm (red). (a): H_s distribution Histograms of 50 single-shot measurements taken at 4, 8, 12 and 16 μm from nucleation point. (b): Plots of average H_s as a function of DW propagation distance. (c): Plots of σ_d as a function of DW propagation distance.
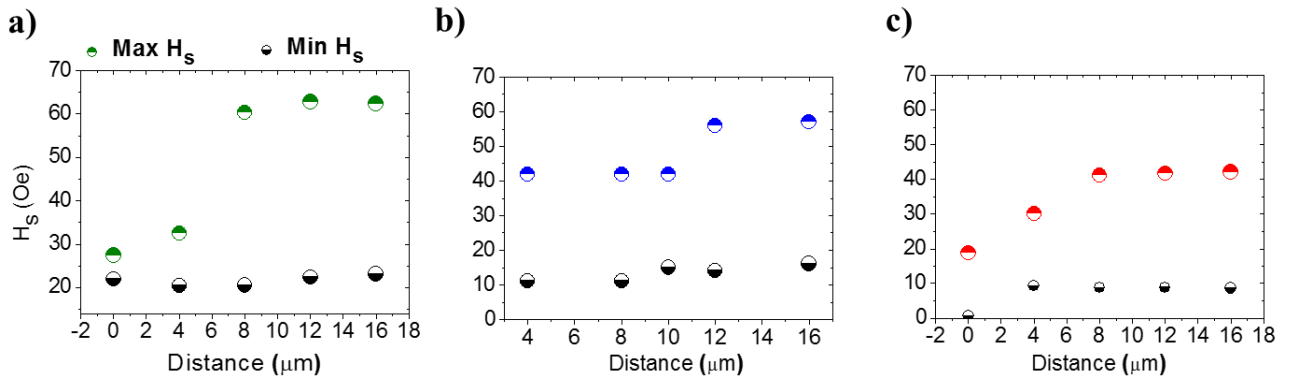
Figure 7.6: Plot of maximum (colored circles) and minimum (black circles) Hs as a function of DW propagation distance from nucleation point for nanowires of w=300nm (a), w=400nm (b) and w=500 nm (c).

Finally, when comparing the saturated value of maximum H_s in each nanowire with the scatter plot in Figure 7.3 & 7.4, it can be seen that the value of H_N where deterministic switching started to occur in the scatter plots are similar to the values of the maximum H_s found in the position-dependent measurements of each nanowire. This is understandable since in the deterministic regime it is expected that all pinning sites can be surpassed.

In addition to providing interesting information on the stochastic switching behaviour of nanowires, the methods presented in this section can be applied on nanowires to test their fabrication quality. Similar suggestion have also been made by Prieto *et al* [5] based on their own measurement methodologies.

After characterising DW propagation as a function of H_N in defect-free nanowires, it is now possible to carry on a study to understand the pinning/depinning behaviour of DWs propagated at different fields, in nanowires with artificially introduced defects. Such understanding is vital for completing a full study of DW propagation under CN.

7.3. The effect of propagation field on DW pinning/depinning mode

In the section above, it was shown that nanowire switching at low propagation field can suffer an unavoidable level of stochasticity, due to pinning at edge defects. On the other hand, as the

propagation field increases, switching becomes more deterministic, since the driving field is sufficient to overcome all defect sites. However, this pattern will not hold for larger artificial pinning sites, as here DWs are more likely to pin at all fields. In such case, the depinning stochasticity becomes strongly dependent on the specific nature of the pinning.

Therefore, in this section, the CN method of DW injection is used to study how changing the propagation field, and altering the dynamical transformations of DWs will alter the pinning and depinning behaviour from artificial defect sites. Such study will provide great understanding of the interaction of DWs with pinning sites, and may also provide a level of selectivity over the stochastic depinning behaviour of DWs at a particular defect by controlling the DW propagation field.

In order to perform this study, a Py nanowire of w=400 nm, l=20 μm and t=20 nm was fabricated using EBL and thermal evaporation. The nanowire contained a double notch of N_d=N_W= 0.25W at which to probe pinning/depinning behaviours. As in the previous experiments, a Ti(20 nm)/Au(200 nm) strip line was added to the nanowire in order to allow injection of DWs by the CN method. DWs were nucleated and propagated to the notch at propagation fields (H_p) of 25, 30, 40, 50 and 60 Oe, where DWs are pinned and then depinned using an incrementing external field, H_{ext}, from 0 – 300 Oe. One hundred single-shot measurements were taken at each field using focused MOKE measurements. The measurements were taken both; before and after the notch in order to measure the distribution of both injection and depinning fields. In addition to the MOKE measurements, the DW trajectory was simulated for the same range of propagation fields using OOMMF software. The simulation results will provide us with information regarding the nature of the WB cycle.

Results and Discussion

Figure 7.7 shows the results of the MOKE measurements presented as histogram plots along with their corresponding simulated magnetisation curve. The magnetisation curve is proportional to the DW trajectory curve, and would provide information on DW motion.

The results show a clear change in the depinning behaviour of the DWs when the applied field was changed. Two major depinning modes (Mode 1 and Mode 2) seem to exist in most of the cases. However, their level of occurrence seems to strongly depend on H_p.

Since H_{WB} for nanowires with similar geometries is estimated at around 15 Oe , it is expected that DW motion in this experiment was occurring within the oscillatory regime. This means that the DW is undergoing periodic transformations determined by the value of H_p. This is verified by the WB cycle plot shown for each H_p.

From previous chapter, it was concluded that DW depinning behaviour depends on the pinning configuration of the DWs as they pin at a defect. Figure 7.7(b) shows normalized M_x vs time plots for each H_p. Plots clearly show that the nature, length and slope (proportional to velocity) of oscillations change with changing H_p. Hence, at different applied fields, the "average" configuration that the DW arrives with at the pinning site will change as a function of applied field.

Moreover, small perturbations from thermal and edge roughness will alter the DW pinning configuration resulting in stochastic pinning [11]. Both factors justify the changes seen in the histograms at different fields
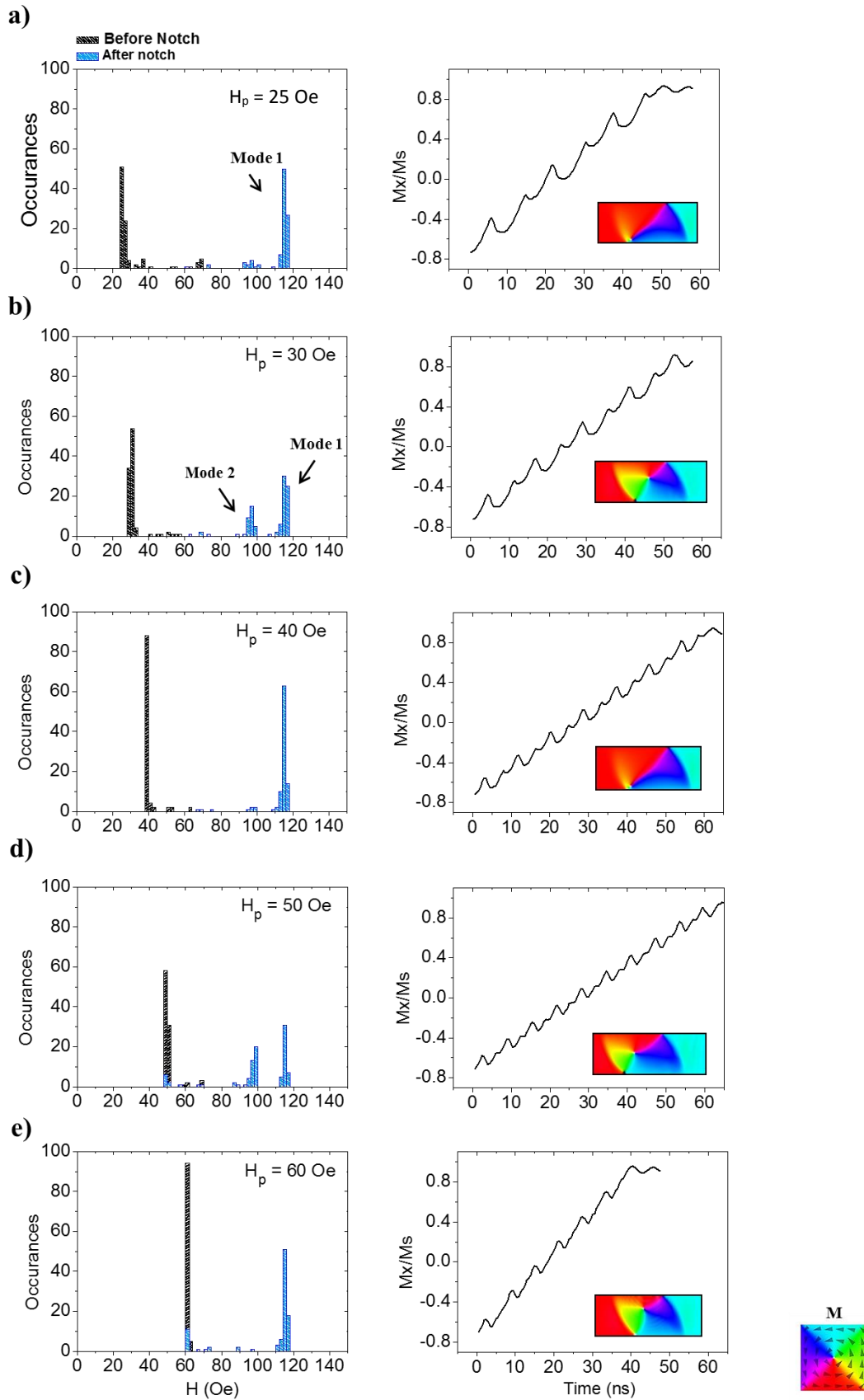
Figure 7.7: IFD and DFD Histograms of 100 single-shot MOKE measurements for region before (black) and after double notch (blue) at varying H_p. Plots of magnetisation curves showing WB cycle at each H_p are also shown. Inset shows the DW shape at middle (at $M_x/M_s=0$) of nanowire. Measurements were taken at $H_p = 25$ Oe (a), 30 Oe (b), 40 Oe (c), 50 Oe (d) and 60 Oe (e).

The switching behaviour seen in the histograms can be explained *qualitatively* by the help of the simulations done for each examined H_p. Upon examining the simulated magnetisation curve that reflects the DW trajectory, it was seen that DW trajectory is different at every H_p value. This is expected, as WB period depends on the velocity of the DW which depends on the driving field (as explained above). Furthermore, upon checking the DW structure at $M_x/M_s = 0$ (at mid of the nanowire) for each H_p values, it was seen that the structure differs substantially. Such observation affirms that the DWs are very likely to have different structures as they arrive the defect, resulting in a different pinning configuration and different depinning modes.

The same experiment was repeated several times on nanowires of similar geometries on different devices. Results were very similar to one obtained in Figure 7.7, in which, the depinning behaviour showed one or two modes oscillating at different values of H_p. Moreover, a similar experiment was conducted by Akerman *et al* [1] on nanowires with single notches and they observed also that different depinning modes can exist at different H_p. Therefore, it can be concluded from the above experiment that stochastic DW depinning behaviour depends strongly on the propagation field since it affects the structural transformation of the DW during its propagation.

If engineered carefully, this approach can provide us with a level of control in selecting between different DW depinning processes, including the possibility of tailoring a system with single-mode behaviour (similar to histogram in Figure 7.7(e)). Such control was not possible with the pad nucleation method. However, the question remains whether injection from a pad intrinsically produces less reliable DW pinning than when using deterministic CN injection method. This will be the focus of the final section of this chapter.

7.4. Comparing Pad nucleation with controlled nucleation

From the previous section, it is clear that the CN method can be used to manipulate the oscillatory trajectory taken by DWs during their propagation, and thus the DWs' interaction with defect sites. Moreover, it was observed that the CN method can be used to produce highly deterministic and reproducible DW propagation before the notch. This could be attributed to the fast generation of DWs by the CN method [16]. This is not the case for the PN method where the injection field is part of a less deterministic distribution as H_{inj} can be affected by the pad magnetisation state [9, 17], hence, producing stochastic DW injection and propagation behaviour. Therefore, it is important to investigate how these intrinsic differences in the stochasticity of injection process from a pad, when compared to the CN method, are reflected in DW pinning/depinning behaviours. In this section, the effects of different nucleation methods on DW stochasticity will be explored by comparing the DW depinning behaviour when nucleation happens through PN method and CN method.

To achieve this, two sets of five nanowires with nominally identical dimensions and defect sites were fabricated. Nanowires in the first set had nucleation pads, while those in the second set had a perpendicular Ti/Au strip line added for CN DW injection. Both nanowire sets had dimensions: w= 400 nm, l= 20µm, t= 20 nm and a double notch of depth N_d= 0.25W at the middle of each nanowire.

Magnetization switching measurements were taken using focused MOKE for both sets of nanowires in order to conduct a statistical analysis and compare the sets collectively. In each measurement, one hundred single-shots were taken both before and after the double notches in order to study the injection and depinning behaviours, respectively. Histograms of the depinning fields from CN and PN nanowires were then compared.

Figure 7.8 compares the histograms of injection and depinning fields for the PN and CN DW injection methods. Each set of histograms was analysed in a holistic and collective manner, and then two whole sets were compared qualitatively.

It can be seen that in the CN set (Figure 7.8(f)-(j)), the histograms indicate the dominance of a single mode switching behaviour in four out of five nanowires (with nanowire (j) being the exception). In these four nanowires, the dominating mode encompassed > 85% of switched events. In nanowire (j), the highest switching mode encompassed ~55% of the events.
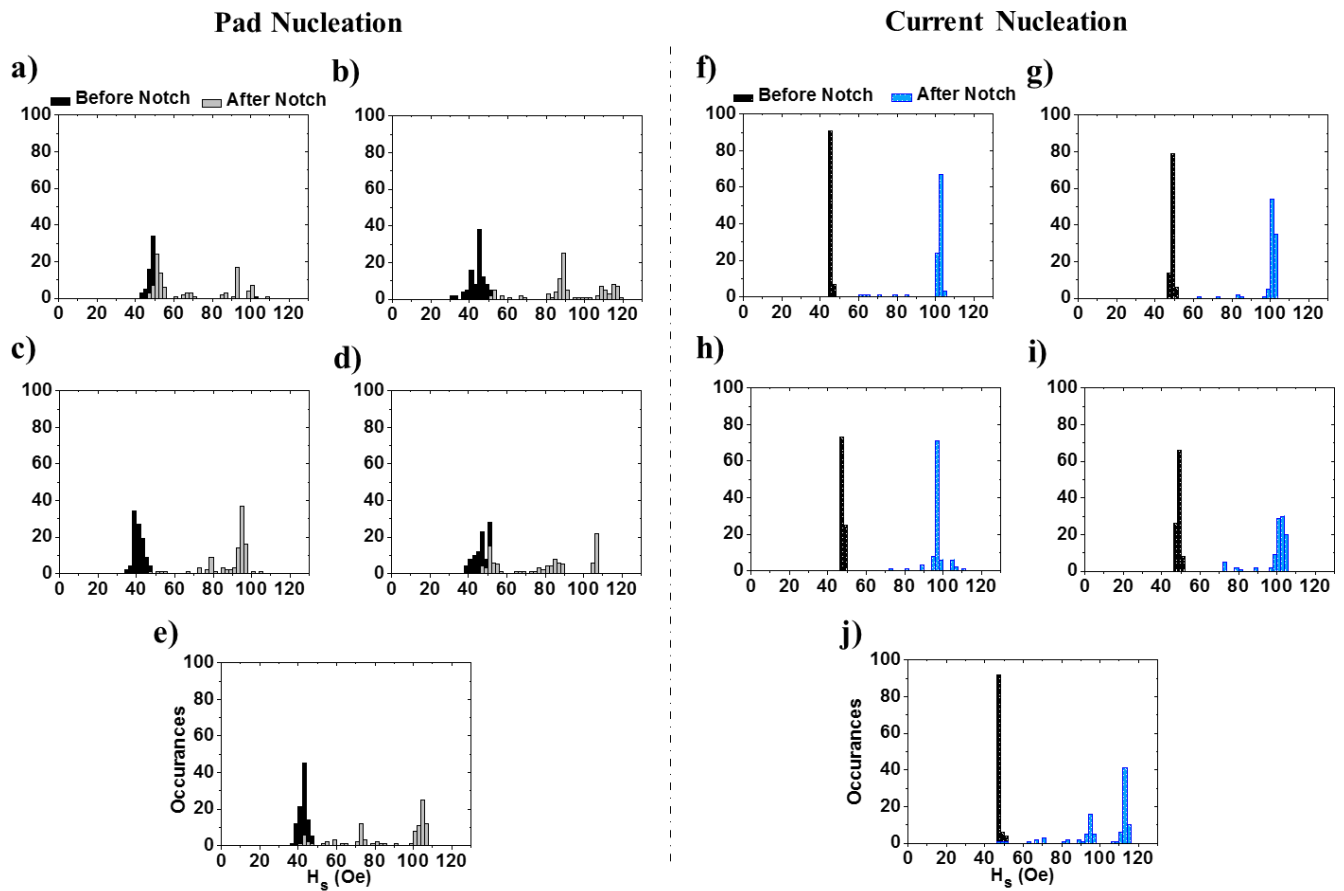

Figure 7.8: IFD and DFD Histograms showing depinning behaviour for nanowires (w=400 nm) with double notch of N_d= 0.25W for PN nucleation method (a)-(e), and CN nucleation method (f)-(j). 100 single-shots were taken in each histogram using MOKE. (Black columns) represent H_s before the double notch, (grey, blue columns) represent H_s after the double notch.
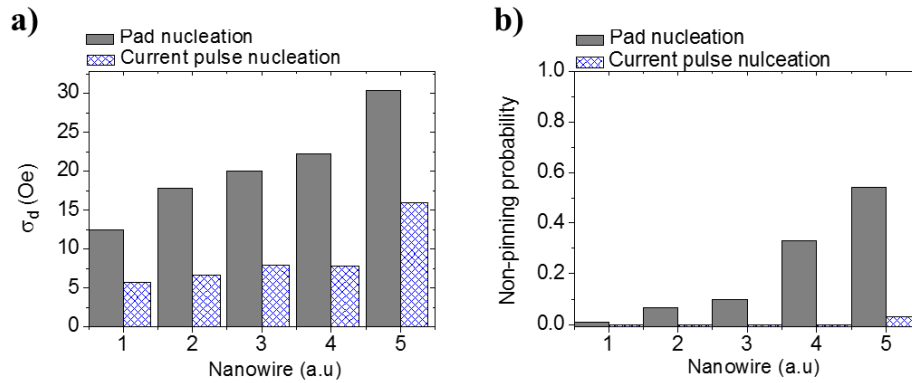
Figure 7.9: (a): Chart showing standard deviation for each nanowire nucleated using PN and CN methods shown in Figure 7.8. (b): Chart showing non-pinning (passing) percentages for nanowire where DWs were nucleated using PN and CN. (Solid grey columns): Nanowires with PN method. (Patterned blue columns): Nanowires with CN method. Values of plots are plotted in an ascending order.

On the other hand, the switching behaviour in nanowires that followed the PN method (Figure 7.8 (a)-(e)), did not show a clear indication of a single dominating mode in any of the nanowires except for nanowire (c); where the highest probability of switching to occur along the dominating mode was calculated to be less than 65% (refer to nanowire (c)).

To verify this analysis and to get a sense of the distribution of the H_s, σ_d was calculated and plotted for each set of nanowires (Figure 7.9 (a)). The σ_d was plotted in an ascending order for both sets as the study is taken in a holistic sense where the order is irrelevant. In addition to analysing the distribution, the pinning percentage was calculated for each nanowire (Figure 7.9(b)).

 The data presented in Figure 7.9 should be considered collectively to compare the behaviour of the whole set of PN nanowires with the whole set of CN nanowires. From the σ_d graph (Figure 7.9(a)), it is clear that the values of σ_d measured for the CN set are generally lower than those of the PN set. This is further evidenced by the fact that the calculated average σ_d for PN set was = 21 Oe while for the CN it was = 9 Oe. Furthermore, the passing percentage plots (Figure 7.9(b)) indicate a higher probability for non-pinning (passing) in the PN method than the CN method. The calculated average passing probability for PN versus CN was 20% to 1%, respectively. Therefore, from these qualitative and quantitative analyses, it can be deduced that

PN method is producing more stochastic DW than the CN method; where more controlled nucleation and less stochastic depinning behaviour was observed.

As discussed and shown earlier, in the PN method, DW injection occurs within a range of injection fields (**PN**: $\overline{H}_{inj}$= 47 Oe, $\bar{\sigma}_{inj}$= 4 Oe), (**CN**: $\overline{H}_{inj}$= 48 Oe, $\bar{\sigma}_{inj}$= 0.5 Oe). In other words, an injection field distribution always exists when a nucleation pad is used. This is not usually the case in the CN method where propagation field can be very deterministic, as indicated by the narrow shape of the histogram column at the region before the notch (Figure 7.8(f)-(j)), where the width of the bar represents the error of the fitting algorithm that is used to read the MOKE files (error = ± 2 Oe). As shown in the previous section, the pinning/depinning behaviour of the DWs at a notch is strongly dependent on H_p, and hence it could be hypothesised that distribution of the injection field seen in the PN is dominant factor in creating the higher level of depinning stochasticity compared to the CN method with well-defined H_p.

In order to investigate this claim, the CN method was utilized to emulate the injection field distribution produced by the PN method, thus making the distribution of fields at which DWs were injected equivalent in the two methods.

To achieve this, 50 single-shot MOKE measurements were taken for a randomly chosen nanowire in the CN set. In this case, nanowire (h) was chosen (refer to Figure 7.8). The single shots were taken at successive values of H_N from 37.5 Oe to 54 Oe with an incrementing field of 1.5 Oe. The sets of depinning field measurements which were taken at different H_N were then assigned a statistical weight that would correspond to the same H_{inj} probability produced by a randomly chosen PN nanowire. Nanowire (d) was chosen for this experiment. The statistical data produced from each measured H_N and its corresponding weight (numbers above histogram bars in inset of Figure 7.10) were then assembled to form a composite DFD that emulates the IFD of the PN nanowire (d).
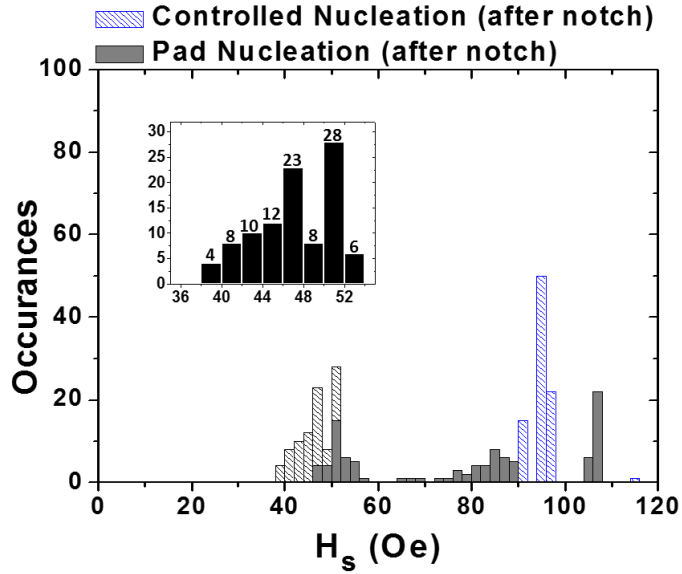
Figure 7.10: Histograms comparing DFD of PN and CN method when both have same IFDs. (Black patterned) columns show the assembled IFD of nanowires (h) using CN method. (Blue patterned) columns show composite depinning field histogram assembled using CN method. Solid grey column shows depinning field histogram measured for nanowire (d). Inset shows the injection profile of PN nanowire (d). Numbers above histogram bars are the probabilities of each injection field which were used to weigh the CN data in the composite plots.

 Figure 7.10 compares the depinning field distribution from the PN nanowire, with the composite depinning field distribution from the CN nanowire. The graph shows clear differences between the DFD of both methods. These differences can be seen in the shape of the distribution profile, number of passing events and in number of modes. The PN nanowire (solid grey columns) showed a DFD range of around 50 Oe compared with 40 Oe for CN (blue patterned columns), and a passing probability of 30% compared to 0% in the controlled case. The σ_d for pad nucleation was calculated to be 22 Oe while for CN was only 3 Oe. A full comparison of quantitative metrics is shown in Table 7.1.

These data indicate that even after emulating the range of injection fields produced using the PN method, the CN method still produced a less stochastic depinning behaviour.

Table 7.1: Statistical analysis for PN vs CN nucleation experiment for the same injection field profile

	σ_d	σ_d (for Pinned)	Passing %	Average H_s (Oe)	Min H_s (Oe)	Max H_s (Oe)
Pad Nucleation	22	15	30	78	56	107
Current Nucleation	4	4	0	95	75	115

This suggests that the stochasticity in PN cannot be attributed to the H_{inj} distribution alone, and that our previous hypothesis was inaccurate. In fact, it seems that PN method is intrinsically stochastic; whereas CN method seems to produce more reliable and deterministic switching behaviour.

Such stochasticity could possibly be justified by the different processes the DW undergoes when being nucleated, injected and propagated in each of the two nucleation methods. In the CN method, the large electric current pulse passing above the nanowire creates a magnetic field greater than H_c, and is hence sufficient to nucleate DWs on both sides of the strip line. This process is expected to be fast and straightforward, and DWs will be nucleated almost instantly in the nanowire without suffering significant pinning. However, in the pad nucleation case, the magnetisation of the pad has first to be switched, forming a DW at the junction between the nanowire and the pad. The DW gets pinned in the junction until H_{ext} exceeds H_{inj} and the DW depins. However, during the junction depinning process, the DW would undergo elongations/deformations before the DW completely depins and is injected into the nanowire [18]. It can be hypothesised that this deformation alters the initial state of the DW each time in a random manner, giving an additional stochastic element to the structure of the DW as it propagates. This DW stochasticity would then result in having different pinning configurations, and a relatively high stochastic depinning behaviour.

To test this hypothesis, it must be shown through simulation that the DW trajectory for propagating DW through a nanowire is sensitive to the initial DW structure when the DW was depinned from the pad junction. This means that if the DW gets stretched/deformed during depinning from the pad junction, its propagation state will be affected resulting in a different trajectory. In order to simulate this, two identical nanowires with two injected DWs, each having a different structural elongation shape will be propagated at the same field. Their magnetisation curve (which is a reflection to their trajectory) will then be compared.

Hence, a challenge existed on how to simulate two injected DWs that have different deformed/stretched structures, but have the same injection field and are injected into two identical nanowires. Fortunately, it was found that by slightly altering the shape of the pad junction, the DW gets slightly elongated and the DW will depin in a slightly different shape, while maintaining the same injection field value. It is important to mention that the aim of this simulation test is not necessarily to test whether the DW gets stretched as it depins the pad junction or not, (this has already been verified by Bryan *et al* [18] in their MTXM imaging experiment); instead, the aim of this simulation is to test whether a deformed/stretched injected DW will retain its trajectory as it propagates, or will it have a different trajectory.

Hence, two designs have been created, in the first design the junction has a normal sharp shape, while in the second design the junction had a rounded shape (Figure 7.11). The other dimensions of the pads and nanowires were identical. Moreover, the injection fields for both designs were also identical and were equal to 50 Oe.

Simulation was performed using OOMMF in which DWs were injected into 400 x 4000 x 20 nm^3 nanowires by applying a ramping H_{ext} from 30 Oe to 60 Oe in order to magnetise each pad (1x1 μm^2), create a DW at the junction, inject the DW and switch the nanowire. The propagation trajectories for DWs in each design were then compared by comparing their magnetisation versus time plot. The cell size used was 2.5x2.5x20 nm^3 and the damping factor was set to $\alpha = 0.02$.

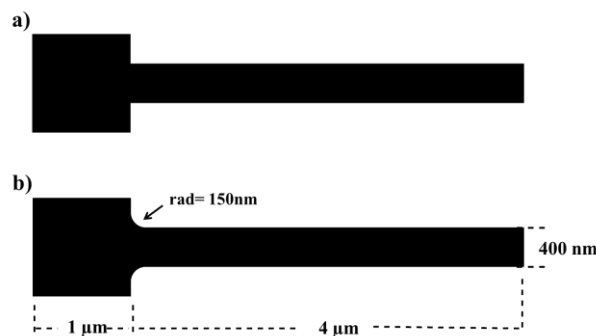**Figure 7.11: Schematic design of simulated systems with sharp shaped junction (a) and rounded shaped junction (b).**

a)

Junction with sharp angles

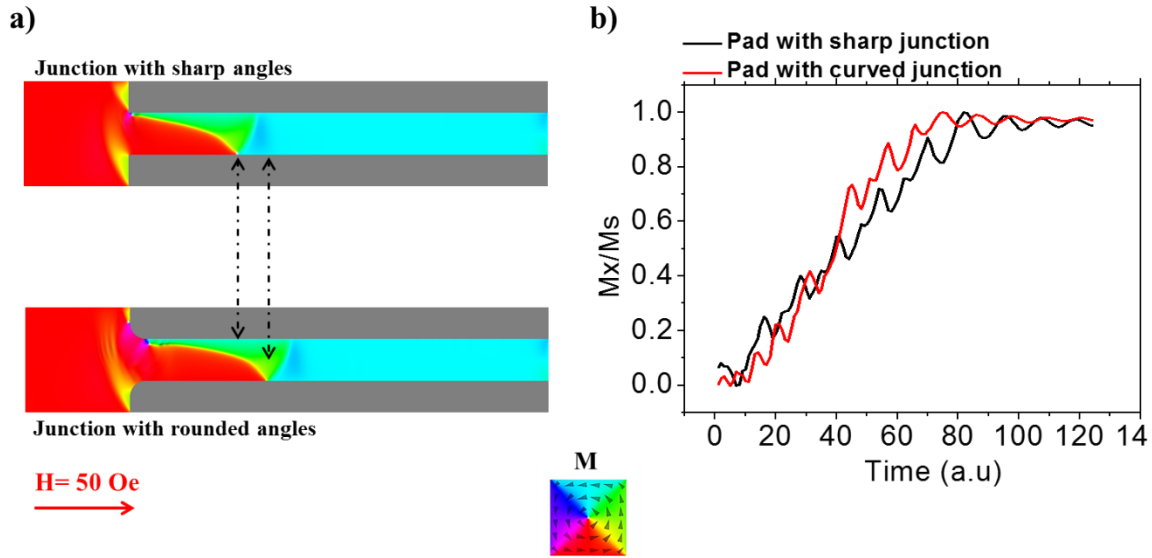**Junction with rounded angles**

H= 50 Oe

b)

M

Figure 7.12: Simulation results for different junction shapes and different DW deformed shapes. (a): Simulation snapshot for design of junction with sharp angles (top) and rounded angles (bottom) at the instant the DW depins the junction (at t=0 ns). (b): Normalized magnetisation versus time curves for DW propagation in nanowires (*w*= 400 nm) with sharp and rounded (curved) junction.

The simulation snapshots shown in Figure 7.12 indicate a deformed/stretched shape of the pinned DWs, at the instant just before depinning from the junction occurred. It can be seen that the deformed DWs in the two nanowires have different lengths as indicated by the dashed arrows in Figure 7.12(a).

In order to examine the trajectory and nature of propagation of the DWs under WB transformations, their normalized magnetisation curves (M_x/M_s) were plotted in Figure 7.12(b).

Form the normalized M_x versus time plot (Figure 7.12(b)), it can be clearly seen that DW trajectories taken by the two DWs are quite different. This is an interesting and important result as it suggests that when DWs depin with a deformed structure they may not retain their normal DW shape nor the same WB propagation cycle, even if their injection and propagation fields were the same each time.

In real experiments, it could be suggested that due to the edge roughness at the junction region between the pad and the nanowire, the DW could pin differently prior to its injection in each

switching event. As the DW pins differently, it is expected that its shape get deformed differently each time, resulting in stochastic propagation. This added stochasticity could then be the reason for the formation of additional pinning configurations at the notch, and could produce different depinning modes that were not observed when DWs were nucleated in a more deterministic manner using CN method. Therefore, it can be argued that the pinning caused by the junction (when a nucleation pad is used), will create an additional layer of stochasticity reflected in DW propagation and pinning/depinning behaviour, making the PN method *intrinsically* stochastic.

7.5. Conclusion

From above experiments, it is concluded that the DW nucleation method can have a strong effect on DW switching stochasticity. When using the CN method, it is difficult to achieve deterministic switching at very low fields due to intrinsic defects in the nanowire, which depends on the quality of fabrication. However, deterministic switching occurs above a critical H_p.

As a DW propagates through a nanowire under a sweeping external field, the probability for it to encounter different intrinsic defects increases with propagation distance. This results in increasing the distribution of depinning fields, as well as, increasing the average switching field with increasing propagation distance. However, when H_p is chosen to be higher than that sufficient to overcome intrinsic defects, DW propagation and nanowire switching become more reliable/controlled with stochasticity dropping significantly.

Moreover, in the CN method, the propagation of DWs can be controlled by controlling/selecting the H_p. Since the nature of WB oscillations depends on H_p, the DW structural transformations that occur as it propagates will also will be altered depending on H_p. This will result in the DW arriving at the pinning site with different structures, thus producing

different pinning configurations, depinning field distributions and depinning modes. If the switching behaviour of nanowires are studied as a function of H_p, then the CN method can be exploited to provide an additional level of control where certain depinning modes can be selected/favoured.

When comparing PN with CN method, it was concluded that PN method intrinsically produces more severe stochastic depinning/switching behaviours than the CN method, and that the causes of this extend beyond the fact that injection fields are poorly defined when using the PN method. This observation seen in the PN method could be attributed to the different injected DW deformed/stretched structures, which will result in different initial propagation states and trajectories. These different DW structures are formed as a result of DW pinning/depinning at different pinning sites at the junction, due to edge roughness. As the DW is injected with a different initial structure, its WB oscillation gets altered and the probability of it producing more pinning configurations at the pinning site (notch) increases, resulting in a significantly stochastic depinning behaviour.

While it has been demonstrated in this chapter that regulating injection can be used to control stochastic switching to some degree, the next chapter will demonstrate how an even greater control can be gained by a combination of regulating initial DW structures and careful selection of WB modes and defect geometries.

7.6. References

[1]   J. Akerman, M. Muñoz, M. Maicas, and J. L. Prieto, "Selective injection of magnetic domain walls in Permalloy nanostripes," *Journal of Applied Physics,* vol. 115, p. 183909, 2014.

[2]   J. Akerman, M. Munoz, M. Maicas, and J. L. Prieto, "Stochastic nature of the domain wall depinning in permalloy magnetic nanowires," *Physical Review B,* vol. 82, Aug 31 2010.

[3]   R. P. Cowburn, D. A. Allwood, G. Xiong, and M. D. Cooke, "Domain wall injection and propagation in planar Permalloy nanowires," *Journal of Applied Physics,* vol. 91, pp. 6949-6951, 2002.

[4]   K. Shigeto, T. Shinjo, and T. Ono, "Injection of a magnetic domain wall into a submicron magnetic wire," *Applied Physics Letters,* vol. 75, pp. 2815-2817, 1999.

[5]   J. L. Prieto, M. Muñoz, and E. Martínez, "Structural characterization of magnetic nanostripes by fast domain wall injection," *Physical Review B,* vol. 83, p. 104425, 2011.

[6]   L. Bocklage, F.-U. Stein, M. Martens, T. Matsuyama, and G. Meier, "Time structure of fast domain wall creation by localized fields in a magnetic nanowire," *Applied physics letters,* vol. 103, p. 092406, 2013.

[7]   D. Eastwood, L. Bogart, and D. Atkinson, "Scaling Behaviour of Chirality Dependent Domain Wall Pinning in Planar Nanowires," *memory,* vol. 3, p. 11, 2010.

[8]   K. Shigeto, K. Miyake, T. Okuno, K. Mibu, T. Ono, Y. Yokoyama, *et al.*, "Temperature dependence of switching field distribution in a NiFe wire with a pad," *Journal of magnetism and magnetic materials,* vol. 240, pp. 301-304, 2002.

[9]   M. T. Bryan, P. W. Fry, T. Schrefl, M. R. Gibbs, D. Allwood, M.-Y. Im, *et al.*, "Transverse field-induced nucleation pad switching modes during domain wall injection," *Magnetics, IEEE Transactions on,* vol. 46, pp. 963-967, 2010.

[10]   M. Munoz and J. L. Prieto, "Suppression of the intrinsic stochastic pinning of domain walls in magnetic nanostripes," *Nature Communications,* vol. 2, Nov 2011.

[11]   T. J. Hayward, "Intrinsic Nature of Stochastic Domain Wall Pinning Phenomena in Magnetic Nanowire Devices," *Scientific Reports,* vol. 5, p. 13279, 08/25/online 2015.

[12]   H. Tanigawa, T. Koyama, M. Bartkowiak, S. Kasai, K. Kobayashi, T. Ono, *et al.*, "Dynamical Pinning of a Domain Wall in a Magnetic Nanowire Induced by Walker Breakdown," *Physical Review Letters,* vol. 101, p. 207203, 11/12/ 2008.

[13]   U.-H. Pi, Y.-J. Cho, J.-Y. Bae, S.-C. Lee, S. Seo, W. Kim, *et al.*, "Static and dynamic depinning processes of a magnetic domain wall from a pinning potential," *Physical Review B,* vol. 84, p. 024426, 2011.

[14]   G. S. Beach, C. Nistor, C. Knutson, M. Tsoi, and J. L. Erskine, "Dynamics of field-driven domain-wall propagation in ferromagnetic nanowires," *Nature materials,* vol. 4, pp. 741-744, 2005.

[15]   F.-U. Stein, L. Bocklage, T. Matsuyama, and G. Meier, "Generation and annihilation of domain walls in nanowires by localized fields," *Applied Physics Letters,* vol. 100, p. 192403, 2012.

[16]   A. Pushp, T. Phung, C. Rettner, B. P. Hughes, S.-H. Yang, L. Thomas, *et al.*, "Domain wall trajectory determined by its fractional topological edge defects," *Nat Phys,* vol. 9, pp. 505-511, 08//print 2013.

[17]   M. Bryan, D. Atkinson, and D. Allwood, "Multimode switching induced by a transverse field in planar magnetic nanowires," *Applied physics letters,* vol. 88, p. 032505, 2006.

[18] M. T. Bryan, T. S. P. Fry, M. Gibbs, D. Allwood, M. Im, and P. Fischer, "Transverse field-induced nucleation pad switching modes during domain wall injection," ed, 2010.

Chapter 8:

Mitigating DW Depinning Stochasticity Using Chirality Rectification in Sharp Bent Nanowires

In the previous two chapters, it was demonstrated that DW depinning stochasticity in nanowires depends highly on the spin structure of a DW as it arrives at a defect site. The two main factors that determine this are the initial DW structure and the WB transformations that occur during propagation.

It was seen in chapter 6 that, when using a chirality-insensitive double notch, depinning stochasticity remains a major problem since even DWs with the same chirality can relax at the double notch in varying pinning configurations, resulting in a multi-mode switching system. On the other hand, it was seen that deep single notches in thick nanowires can reduce depinning stochasticity resulting in a single-mode switching system. However, this decrease in depinning stochasticity is limited only to deep single notches ($N_d > 0.4W$), with very high depinning fields. In smaller single notches, the DW chirality remains the major factor in limiting the creation of a single-mode switching system, where two modes corresponding to each DW chirality are created. However if a method to rectify the chirality of a propagating DW before reaching the notch could be found it might be possible to produce a highly deterministic depinning system with a relatively low depinning field.

Only a few methods to rectify a VDW as it propagates have been proposed [1, 2]. In these methods, an asymmetric notch [2] (as discussed in section 3.3.2), or perpendicular lines that can filter the DW chirality [1] have to be introduced in order to achieve rectification. However,

these methods require the addition of pinning sites that can be undesired; hence, limiting the functionality of the system.

A recently published method that uses a high frequency rotating magnetic field in a ring-shaped nanowires [3] to rectify DW chirality would be difficult to integrate into nanowire networks, and the requirement of a high frequency rotating field may increase system design complexity. Furthermore, although various methods have been proposed to bias the chirality of DWs at the point of nucleation [4-6], these methods can't be used to modify propagating DWs. Rectifying propagating DWs can be useful in resetting DW chirality as they get altered during their propagation because of WB or because of other defects. Moreover, rectifying DWs during propagation can be useful in future proposed DW-based applications such as chirality-based logic [7].

In this chapter a simple and effective method of rectifying VDWs as they propagate is proposed. The method is based on propagating VDWs ballistically into sharp corners in continuous nanowires, and does not need the introduction of a defect or a complex rotating magnetic field. Instead, it uses the spin alignment of the bend to produce a magnetically frustrated region that will interact with the DW spin structure and rectifies its chirality through DW re-nucleation. This rectification method will then be exploited to demonstrate that a single-mode depinning system can be created by propagate deterministic DW types in the presence of a single small notch (of $N_d=0.15W$) in nanowire geometries where the nature of WB transformation does not change the DW chirality.

The rectifier has been studied using OOMMF micro-magnetic simulation software, and was then verified experimentally using magnetic transmission soft X-ray microscopy (MTXM) at the Advanced Lawrence Berkeley Labs to image the rectified vortex DWs.

8.1. Magnetic simulation of VDW rectifier

DW rectifiers work by breaking the symmetry of a nanowire in order to favour the propagation of DWs of a certain chirality over the other. A simple way to achieve this was to attach a bend to the end of the nanowire and study the DW propagation through it. Both, the upward (UP) and downward (DN) pointing directions of the bend design (Figure 8.1(b)) were investigated as they were expected to show rectification to opposite chiralities.

The thickness of the nanowire was chosen to be 40 nm as chapter 6 and other studies [8, 9] indicated less dynamic and depinning stochasticity in thick nanowires. The simulated nanowires had width of $w=375$ nm, length of nanowire $l=3.2$ μm and outer UP bending radius $r=1$ μm. A schematic in Figure 8.1(a) shows the design of the nanowire.

Initially, simulations were performed with a high damping parameter $\alpha = 0.5$ in order to investigate the rectification process without the effect of dynamical factors and WB transformations. A mesh cell size of 4 x 4 x 40 nm^3 was used.

The simulations were performed in a ballistic manner in which $\mathbf{H_x}$ was applied at a fixed value after relaxing the DW on the left side of the nanowire in a T2T configuration. Simulations were performed with $\mathbf{H_x} = 50, 100, 120, 150, 200$ and 300 Oe. The results for $\mathbf{H_x} = 50$ and 150 Oe will be presented here as they are sufficient to demonstrate the rectification process.
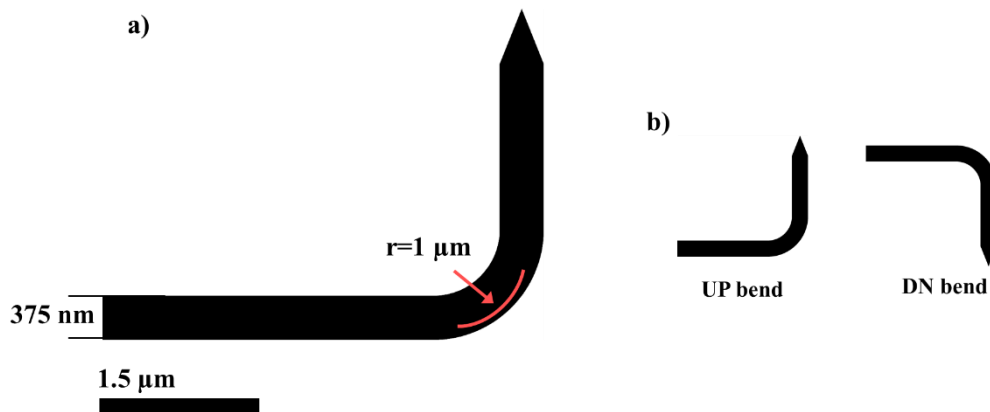

Figure 8.1: (a): Schematic illustrating the details of the UP bend nanowire design used in micromagnetic simulation (b): Schematic describing the UP and DN bend conventions used in this chapter.

Results for the simulation with $\mathbf{H_x}$ =50 Oe and at $\mathbf{H_x}$ =150 Oe are shown in Figure 8.2 and 8.3, respectively. The results from both input chiralities showed that bends could successfully rectify the DW chirality; however, this rectification process occurred only above a critical field (H_{rec}) of 150 Oe, indicating the existence of two modes of functioning for UP and DN bends. For $\mathbf{H_x}$ < 150 Oe (Figure 8.2), the bend did not rectify the DWs, and they propagated smoothly through it.

On the other hand, for $\mathbf{H_x}$ ≥150 Oe (Figure 8.3), the bend functioned as a chirality rectifier; in which, CW (ACW) VDW in a T2T configuration was rectified to ACW (CW) chirality in the UP (DN) bend. Rectification occurred through DW re-nucleation, as will be elaborated below.

In order to understand the cause of rectification, close-up snapshots of the simulation have been studied during the rectification process for nanowires of r= 1 μm. From the simulation results shown in Figure 8.4, it could be deduced that rectification depends on the relative spin orientation of the leading edge of the DW and the magnetisation of the vertical part of the bend. When the DW approaches the bend, the spins at the DW leading edge start interacting with the magnetic spins in front of them. In the case of the UP bend and ACW DW (Figure 8.4(a)), the spins of the leading edge of the vortex DW are oriented in parallel with the magnetisation state of the bend section aligned along the +y direction (refer to dotted circle in Figure 8.4(a)). Since both spin structures are aligned in parallel, there are no points of magnetic frustrations and the DW propagates smoothly along the nanowire bend without flipping its chirality.
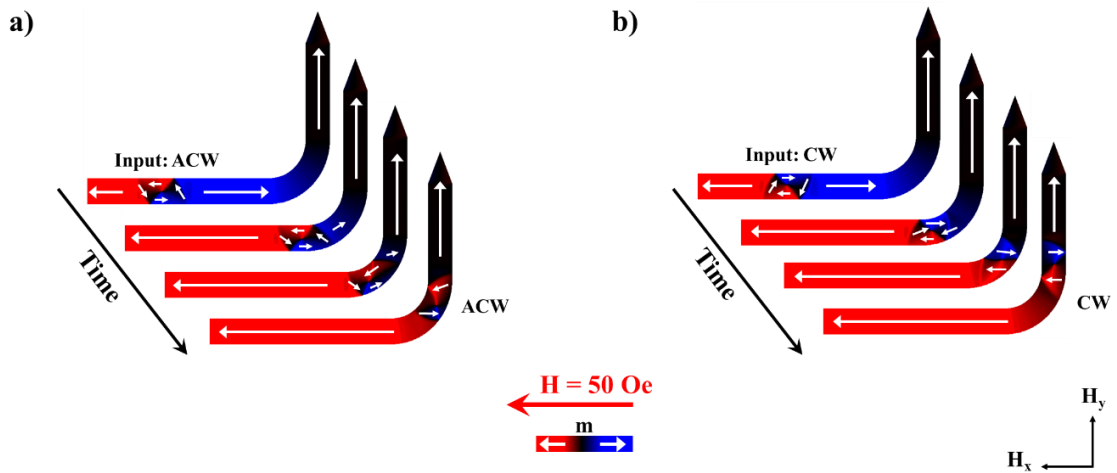
Figure 8.2: Micromagnetic simulation snapshots of bend with *r*= 1 μm in a T2T configuration at H= 50 Oe. H< H$_{rec}$ and the bend works in the non-rectifying regime. (α=0.5) (a): Input VDW: ACW chirality. ACW VDW passes to the output of rectifier without changing its chirality (b): Input VDW: CW. CW VDW passes to the output of bend without changing its chirality.
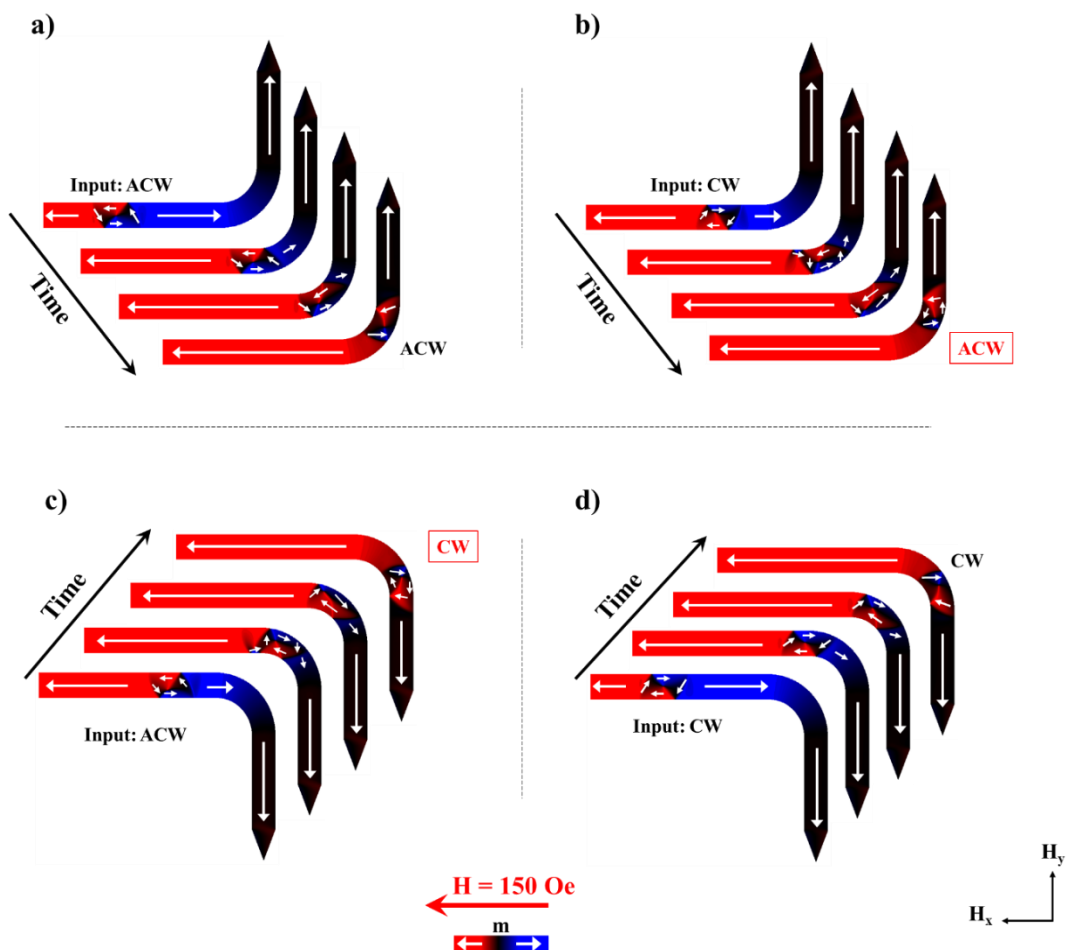

Figure 8.3: Micromagnetic simulation snapshot of rectifier in a T2T configuration for UP and DN rectifier at H= 150 Oe. H > H$_{rec}$ (rectifying regime). (α=0.5) (a): Input VDW: ACW. ACW passes to the output without changing its chirality. (b) Input VDW: CW. CW is rectified to ACW. (c): Input VDW: ACW. ACW is rectified to CW VDW at the output. (d): Input VDW: CW. CW passes to the output without changing its chirality.
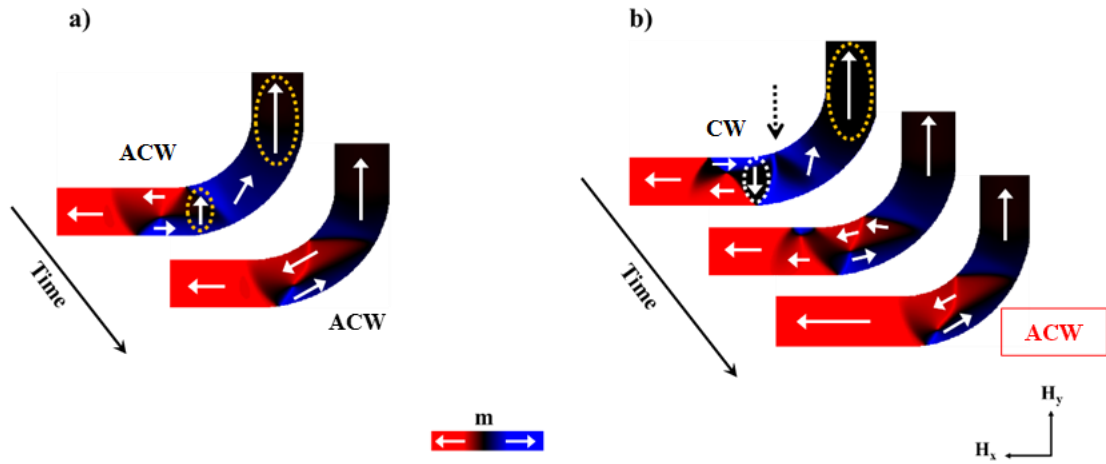
Figure 8.4: Micromagnetic simulation snapshots showing the working process of the UP bend rectifier of *r*=1 μm (α= 0.02). (a): ACW VDW with spins at leading edge parallel to magnetisation of bend can propagate smoothly to the bend output. (b): CW VDW with spins at leading edge anti-parallel to magnetisation of bend as indicated by dotted circles. H= 150 Oe.

On the other hand, for the CW DW case (Figure 8.4(b)), as the DW approaches the bend, the Zeeman energy continues to push the DW to propagate through the bend section of the nanowire, a point of magnetic frustration at the edge of the nanowire is created (refer to dotted arrow in Figure 8.4(b)). This is because spins at the leading edge of the DW are oriented anti-parallel with the +y magnetisation state of the UP bend. The point of magnetic frustration is very energetically unfavourable due to the resulted high exchange energy. While the high field was still applied, the frustrated region becomes a nucleation point, and a new DW was nucleated in order to resolve the frustrated region. The newly nucleated DW will have its leading edge aligned parallel to the UP bend section, resulting in an ACW DW each time such nucleation occurs. This latter behaviour causes the DW rectification, and occurs every time a T2T CW DW passes an UP bend at $\mathbf{H_x} \geq 150$ Oe (this is for α= 0.5).

The same process occurs in the DN bend design. However, in this case, the ACW DW gets rectified to CW. This is because contrary to the ACW DW in the UP bend case, in the DN case, the spins at the leading edge of the ACW DW are oriented anti-parallel with the –y

magnetization alignment of the bend section, leading to the creation of magnetic frustration point and re-nucleation of a CW DW.

It can be seen that the rectification process depends on the nucleation of a new DW core. It is expected that such nucleation is facilitated when DWs are not very stable due to dynamical effects. At low propagation fields (below 150 Oe), the DW propagates in a stable manner with low dynamics resulting in smooth propagation without being rectified. As the applied field increases, it is reasonable to expect that the dynamical effects increases too, and DW interaction with the bend becomes more sensitive. Such interaction would facilitate the re-nucleation process that results in rectification. This explanation would provide a justification on why rectification occurs only above a certain field.

After understanding the rectification process at high damping conditions, it was important to run simulation at real damping conditions to see if the rectification can still function in realistic damping conditions. Therefore, the same simulations were repeated; however, this time using a more realistic damping coefficient of $\alpha=0.02$. Results of simulations are shown in Figure 8.5.

With realistic damping, the DW propagation was much more complex as DW were propagating in the turbulent regime. The DW structure underwent different deformations due to the nucleation of vortices/anti-vortices and the elongation of its structure as it attempts to dissipate its energy. As it entered the bend section, its leading edge suffered from magnetic frustration, which resulted in the creation of a new core (indicated by green arrow in Figure 8.5), which evolved into a new DW with ACW chirality. Eventually, the core of the first CW VDW annihilated at the inner edge of the bend. The same process was seen in the DN bend design where ACW VDWs were rectified to CW VDWs
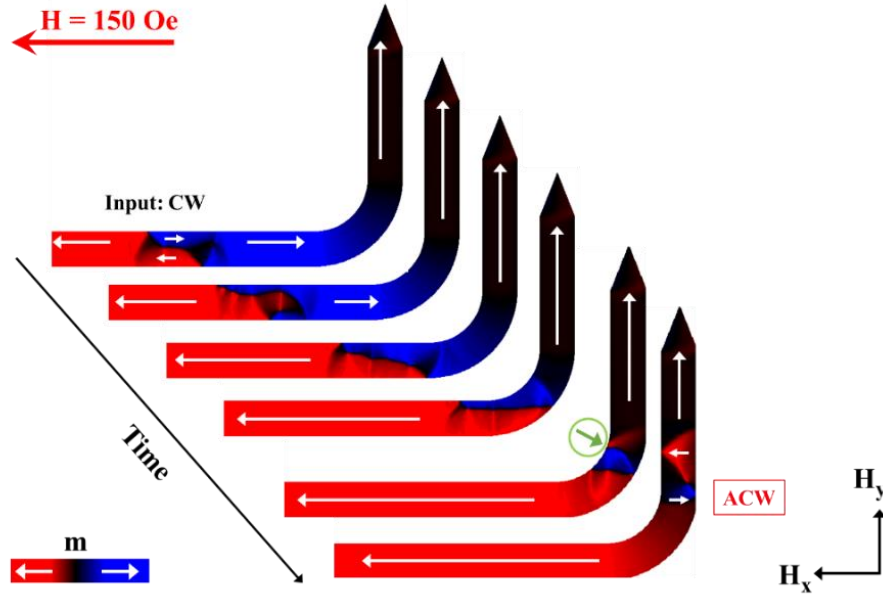
Figure 8.5: Micromagnetic simulation snapshot for UP bend rectifier of *r*= 1µm (α=0.02) showing rectification process at H$_x$=150 Oe (H> H$_{rec}$). Green arrow indicate point of magnetic frustration and core nucleation.

This result clearly suggests the high possibility of the rectifier conceptual design to function in reality. However, before experimentally testing its functionality, it was important to study how the radius of the bend can affect the rectification process. It could be hypothesised that as the radius of bends increase, the point of magnetic frustration becomes less energetically unfavourable (more tolerable) due to the longer bend angle causing less abrupt changes in the angles between spins. This should result in these configurations having lower exchange energies in wide bends than in sharp bends, leading to increases in H$_{rec}$.

Therefore, to investigate this hypothesis, the simulations for α= 0.5 and α=0.02 were repeated for bends of radii 2 µm and 5 µm, in order to determine their corresponding values of H$_{rec.}$ Results are plotted in Figure 8.6.
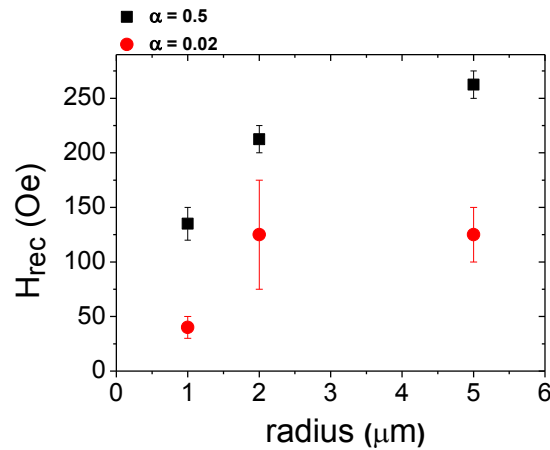
Figure 8.6: Plot showing simulated values of propagation field where rectification process starts to occur (H_{rec}) as a function of bend radius for nanowire of w=375 nm for α= 0.5 (black) and α= 0.02 (red)

As expected, the overall results of these simulations showed that H_{rec} increases with increasing bending radius. However, it was noticed that for radii 2 µm and 5 µm at α=0.02, values of their corresponding H_{rec} were not conclusively determined, as sporadic values of H_{rec} were seen during simulation (as indicated by error bars in Figure 8.6). It was noticed that the highly turbulent propagation of DWs through the relatively long bends has increased the sensitivity of interaction between the DW spins and the edge of the bend where core nucleation would occur, resulting in sporadic rectification. Such complexity in the dynamic transformations can be attributed to the low damping coefficient, and is expected to be reduced in nanowires doped with rare earth materials [11, 12] that would increase damping coefficient.

Nevertheless the rectification process was observed for α= 0.02. Furthermore, it was observed from plot in Figure 8.6, that at the higher damping coefficient of α=0.5, H_{rec} was higher in value compared to that at the low damping coefficient of α=0.02. This indicates that the dynamics of the DW play a major role in assisting the vortex re-nucleation that leads to rectification. It can be argued that at high damping, the spins around the DW has relaxed at a faster rate, thus, inhibiting the rapid and dynamical interactions with the spins at the point of magnetic frustration that cause the nucleation of a new core. In that sense, the evolution of magnetic

spins can tolerate higher values of **H** and can magnetically stabilize before such interaction occurs and a new core is nucleated.

8.2. Experimental testing of rectifier using MTXM

After finishing the simulation study that indicated successful functionality of the rectifier at realistic damping, the rectifying behaviour of corners was experimentally tested at the Advanced Light Source Labs (ALS) using MTXM method described in section 4.4.1. This was done by directly imaging the DWs in bend sections of nanowires before and after the bend.

Samples were fabricated on Si_3N_4 membranes using EBL, thermal evaporation and lift-off of Py material. The thickness of deposited material was chosen to be 40 nm to be in agreement with the simulation study, and to show a good contrast image. The designs included nanowires of w=400 nm, a horizontal extended nanowire section of l=23 µm, and a curved bent section of radii r=1, 2, 5 and 10 µm. The extended section of the nanowire was attached to a 5 µmx5µm rectangular nucleation pad on its left side.

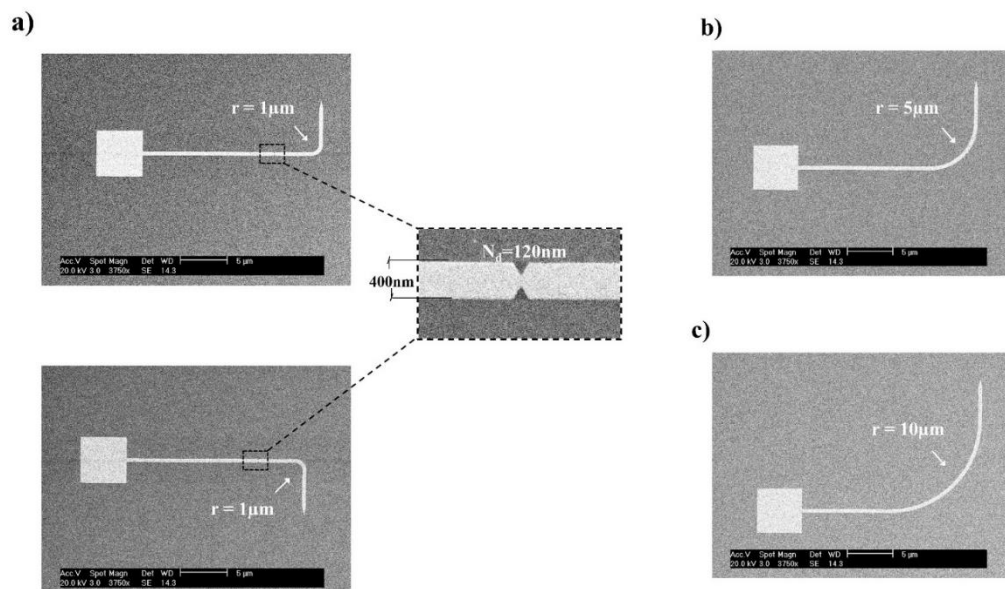**Figure 8.7: SEM images of rectifier designs with UP and DN bends of w=400 nm and t= 40 nm (a): UP bend rectifier (top) and DN bend rectifier (bottom) with double notch of N_d= 120 nm and r= 5µm (b): UP bend with r=5 µm (c): UP bend with r=10 µm.**

One set of nanowires had UP bends (Figure 8.7(a)-top) nanowires while the other set had DN bends (Figure 8.7(a)-bottom) in order to verify that complementary rectification processes occurred for each bend direction. Additionally, for the design with bend of $r=1$ μm and 2 μm, a double notch ($N_d= 0.35W$) was introduced 5μm before the bend in order to trap the DW and determine its initial chirality (refer to enlarged inset in Figure 8.7(a)).

The experiment was carried out first on the UP and DN bend designs with $r=1$ μm (Figure 8.7(a)). The nanowires were first saturated by applying a DC field of $\mathbf{H_x}= 1000$ Oe and $\mathbf{H_y}=$ 150 and -150 Oe for the UP and DN nanowires, respectively. The applied field was then turned off allowing the magnetisation of the nanowires to relax. An injection field (ranging from -150 to -225 Oe) was then applied to inject a VDW into nanowire in a H2H configuration and pin it at the notch. Upon injecting a VDW, the field was removed to allow it to relax in order to image its chirality. Then, $\mathbf{H_x}$ was applied in order to depin the VDW and propagate it through the bend section. The VDW was eventually stabilized at the top vertical part of the bend as $\mathbf{H_x}$ does not apply an effective torque to move the VDW at the top of the vertical part of the bend. The field was then removed to allow the VDW to completely relax before taking an image of the DW at the bend "output". The measurements were taken 16 and 20 times for $r= 1$ and 5 μm bends, respectively, in order to measure the robustness of the rectifier at the UP and DN bend.

Results and Discussion for UP and DN bend design with r=1 μm

Results of VDW images shown in Figure 8.8 and Figure 8.9 indicate successful rectification process as shown in the simulation study. Two image examples for each VDW chirality were presented in Figure 8.8 and 8.9 to demonstrate the basic trend of the rectification process. Unlike in the simulations done above, in these measurements, the nanowires were magnetised in a H2H magnetic configuration. Hence, it is expected to show an opposite chirality-rectification process to the one shown in the simulation.

With agreement to the expectation, the UP bend nanowire (Figure 8.8) resulted in the rectification of VDWs to CW chirality. The same logic described above can be followed: in the H2H configuration the vertical part of the bend is aligned in the –y direction in a manner anti-parallel to the spins of the leading edge of the ACW DW. This creates frustration between the anti-parallel spin alignments (between VDW leading edge and bend magnetisation) resulting in the re-nucleation of VDW with CW chirality at the bend.

The experiment with the UP bend nanowire was repeated 16 times to test the device's robustness. Out of these 16 attempts, ACW chirality was injected 6 times from the nucleation pad, and in all of these attempts, CW DW was produced at the output end of the UP bend, indicating 100% rectification. The 10 attempts where the input was of CW chirality, the output was also of CW chirality as expected.

For the DN bend case (Figure 8.9), the opposite chirality rectification process was achieved, in full agreement with simulation study. For this design, the experiment was repeated 9 times. Out of these 9 attempts, CW chirality was injected 3 times, and in all of these attempts ACW DW was produced at the output of the DN bend, indicating 100% rectification.
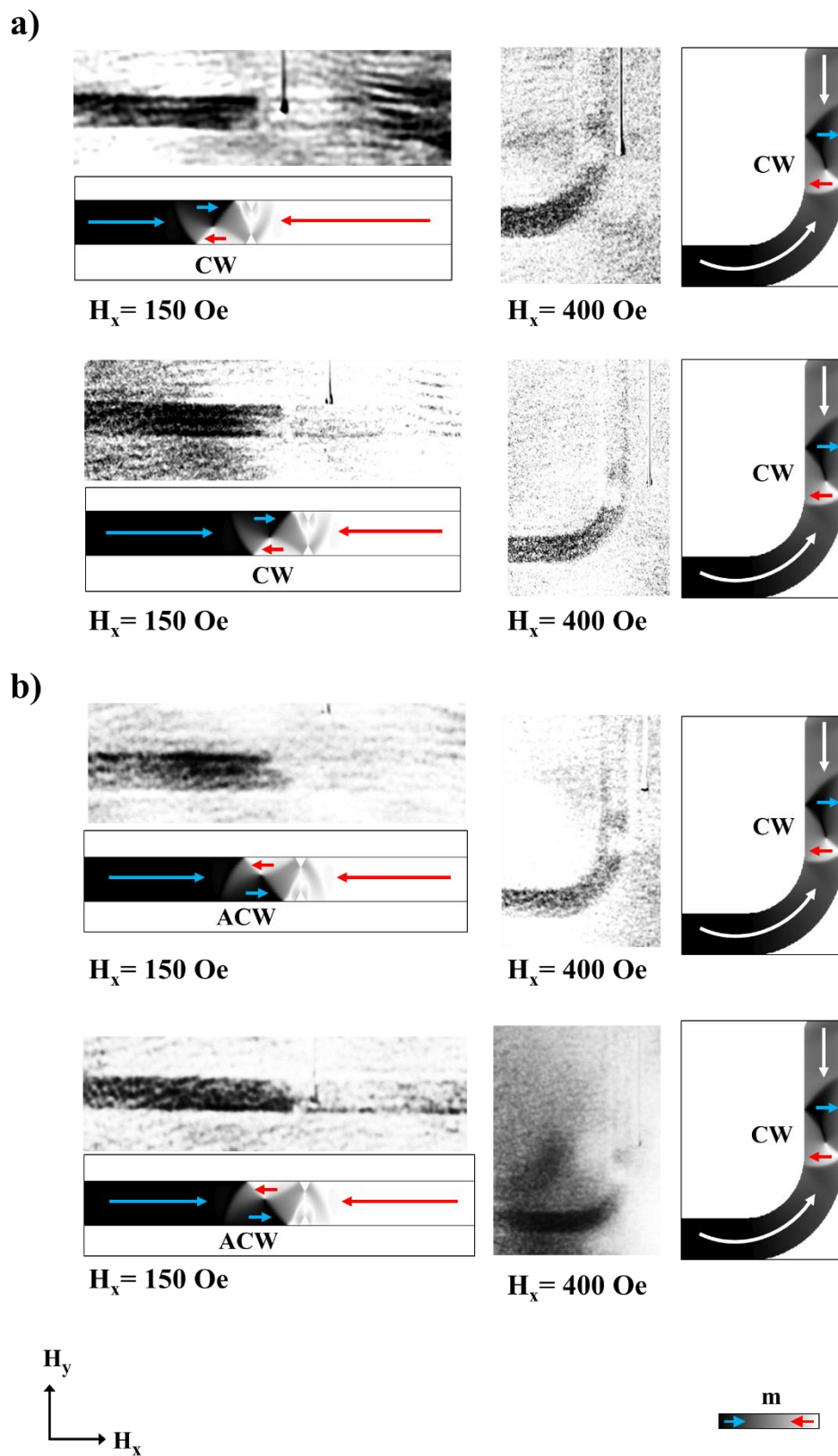
a)

H$_x$= 150 Oe   H$_x$= 400 Oe

H$_x$= 150 Oe   H$_x$= 400 Oe

b)

H$_x$= 150 Oe   H$_x$= 400 Oe

H$_x$= 150 Oe   H$_x$= 400 Oe

H$_y$

H$_x$

m

Figure 8.8: MTXM images of the UP bend rectifier of *r*= 1um. Images show DW chirality before and after passing the bend, along with equivalent simulation results. (a): CW VDW is injected. (b): ACW VDW is injected and is rectified.
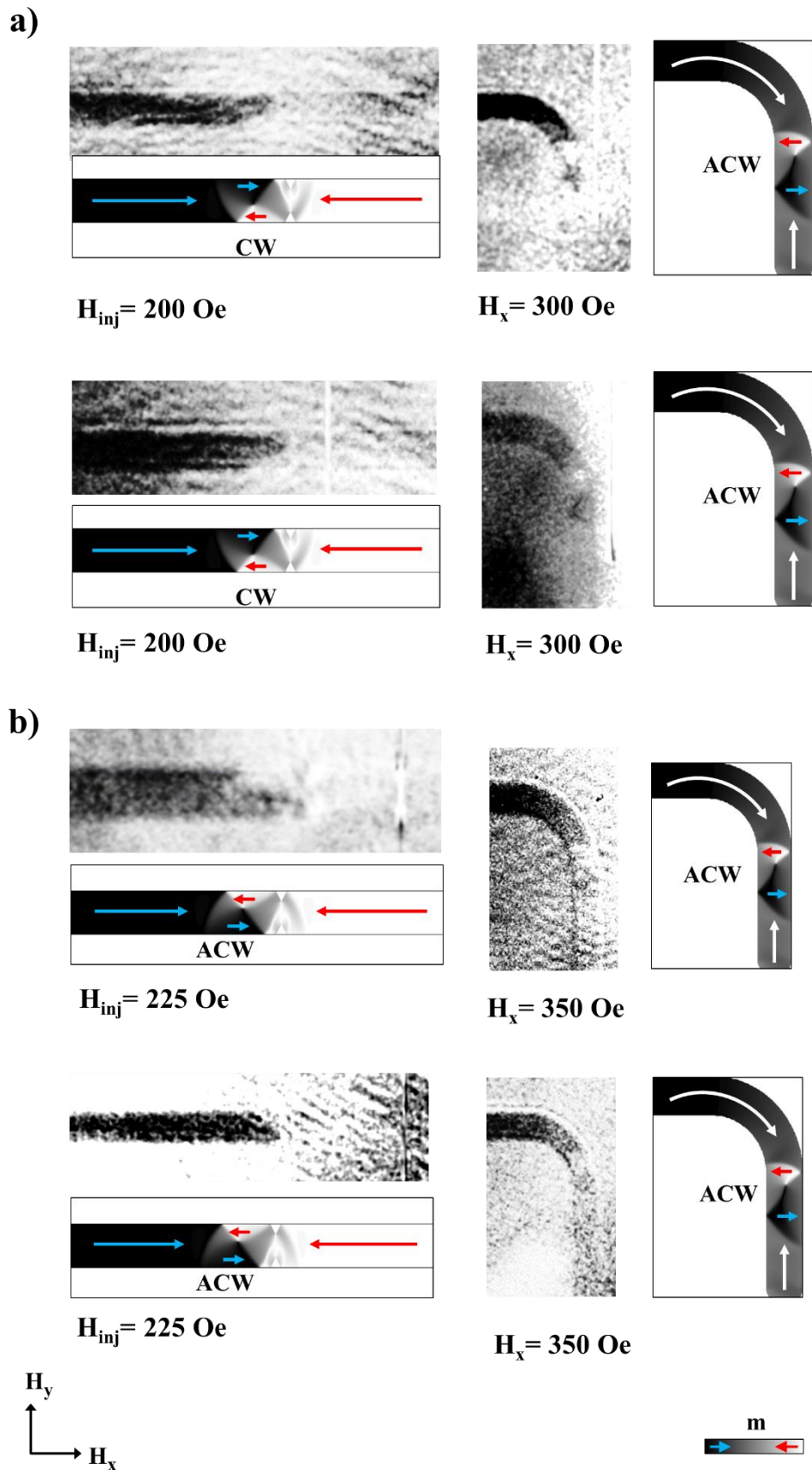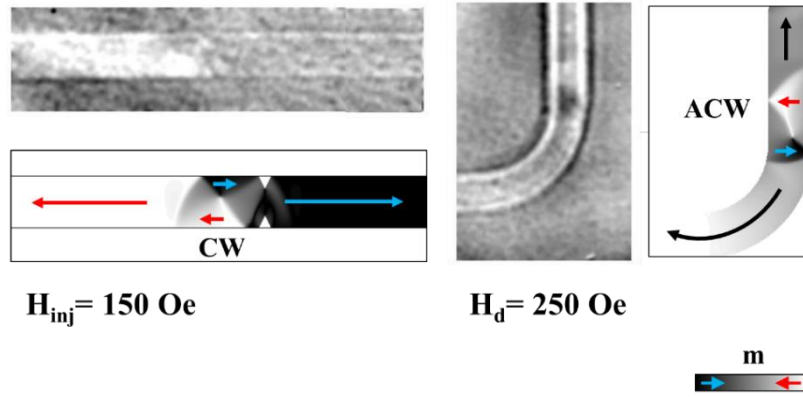
a)

H_{inj}= 200 Oe

H_x= 300 Oe

H_{inj}= 200 Oe

H_x= 300 Oe

b)

H_{inj}= 225 Oe

H_x= 350 Oe

H_{inj}= 225 Oe

H_x= 350 Oe

H_y

H_x

m

Figure 8.9: MTXM images of the DN bend rectifier of *r*=1 μm. Images show DW chirality before and after passing the bend, along with their simulation results. (a): CW VDW is injected and is rectified. (b): ACW VDW is injected.

Figure 8.10: MTXM images of chirality rectifier in UP bend in a T2T configuration with equivalent simulation snapshots.

In order to verify the logic of operation explained previously i.e. that the rectification process depends on the VDWs H2H/T2T nature and the spin orientation of the leading edge of the DW, the magnetization configuration of the VDW was changed from H2H to T2T, and the experiment was repeated. Results are shown in Figure 8.10. As expected, changing the magnetization configurations of the nanowire bend has changed the rectification process; in which, the UP bend of $r=1$ μm was rectifying VDWs into ACW as opposed to the CW rectification that was seen for the H2H configuration. This result verifies our explanation of the rectifier.

Following the experiments on nanowires with $r = 1$μm, the same experiment was repeated for the 2, 5 and 10 μm bends. However, for the bend design with $r = 5$ μm and $r = 10$ μm, the design did not include a notch before the bend, and the DW was injected directly into the bend section. The reason for not including the notch, is to try to propagate the VDW at a low propagation field below H_{rec} (round 125 Oe, as indicated in Figure 8.6) in order to test if the bend stops rectifying when propagation is below H_{rec}, as indicated in the simulation. If a notch was included before the bend, the VDW will get pinned by the notch, and field needed to depin the VDW will most probably exceed H_{rec} as shown in the previous example. This test was not possible for the bend of $r= 1$ μm, since its corresponding H_{rec} was at 30 Oe which is below H_{inj}, hence it won't be possible to achieve such low propagation field.

Therefore, the sole purpose of the latter test was to see if the rectification process became weakened at wide bending radii as indicated by the simulation, and thus if both VDW chiralities could be seen after the bend.

Results and Discussion for UP bend design with r=2μm, 5μm and 10μm

When investigating the UP bend of $r = 2$ μm, the VDWs in Figure 8.11 showed same behaviours as in bend with $r = 1$ μm (Figure 8.8): i.e. CW DW chiralities at the output of the bend when ACW or CW VDW was propagating at the input, indicating 100% rectification. In these measurements, 10 switching attempts were studied, in which, ACW VDW was seen at the input in 3/10 attempts, and the CW was seen in 7/10 attempts.

The rectification observed in the $r=2$ μm experiment can be justified by the fact that H_d from the pinning site was ~300 Oe, a value that is high enough to exceed the expected $H_{rec} = 200$ Oe for bend of $r = 2$ μm (Figure 8.6). As a result, all of propagated VDWs inside the bend had a CW chirality.

Interestingly, it was noticed that some of the output VDWs have shown double VDW structure (Figure 8.11(c)) that was not observed for the nanowires with $r = 1$ μm. These double VDW structures were seen 5/10 times.

Since the UP bend did not show a break or weakening in the rectification process, the complementary DN bend for radius 2μm was not investigated, and experimental measurement proceeded to test for the robustness of the rectification process in nanowires of larger bends with radius 5 μm and 10 μm. As mentioned earlier, both designs did not have a double notch before the bend, and all images were taken at the output section of the bend. Figure 8.12 shows the images for $r=5$ μm.

a)

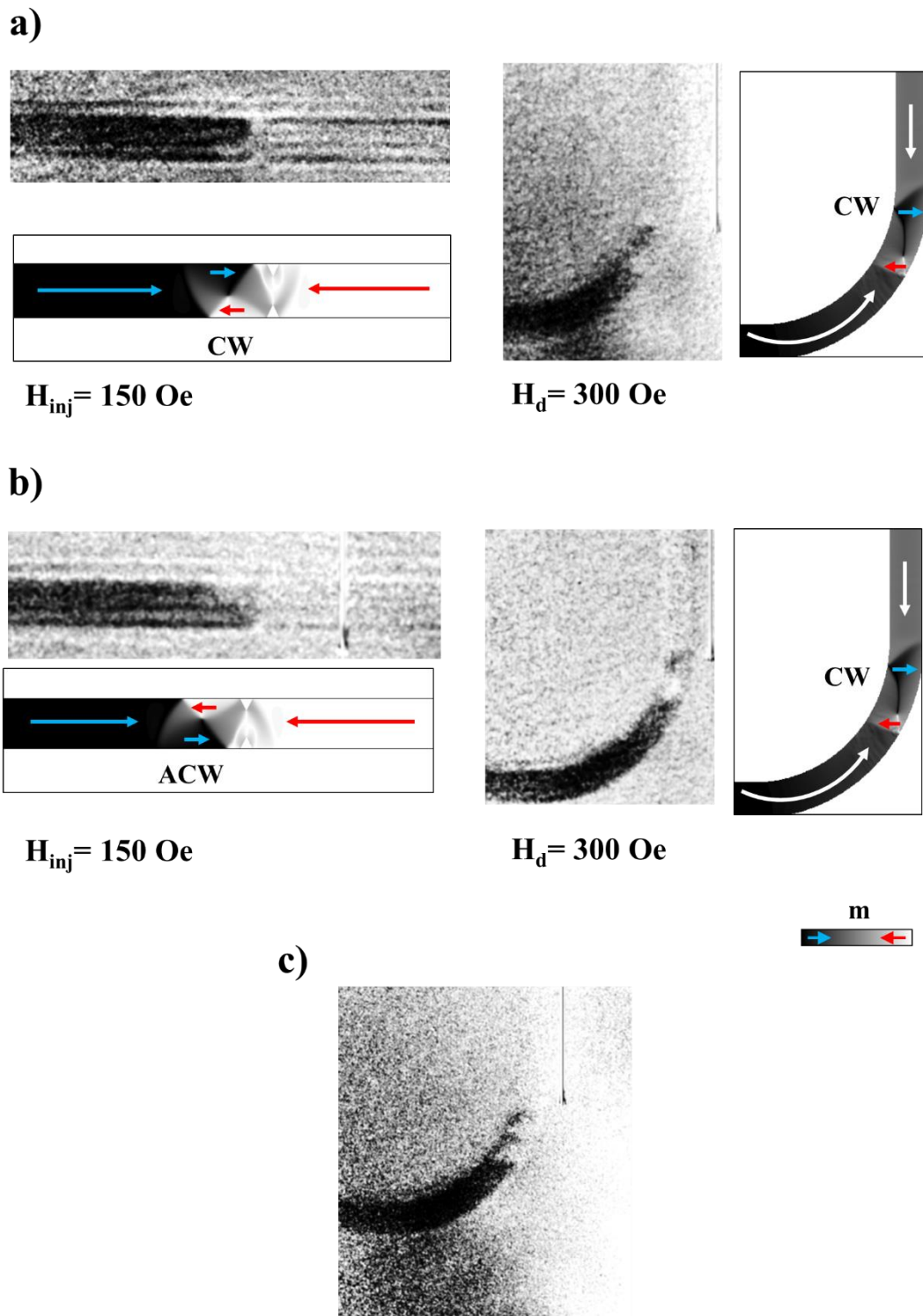

H_{inj}= 150 Oe

H_d= 300 Oe

CW

b)

ACW

H_{inj}= 150 Oe

H_d= 300 Oe

CW

m

c)

Figure 8.11: MTXM images of the DN bend rectifier of *r*=2 μm. Images show DW chirality before and after passing the bend, along with their simulation results. (a): CW DW is injected. (b): ACW DW is injected. (c): Image showing the double VDW structure seen 5/10 of the times.
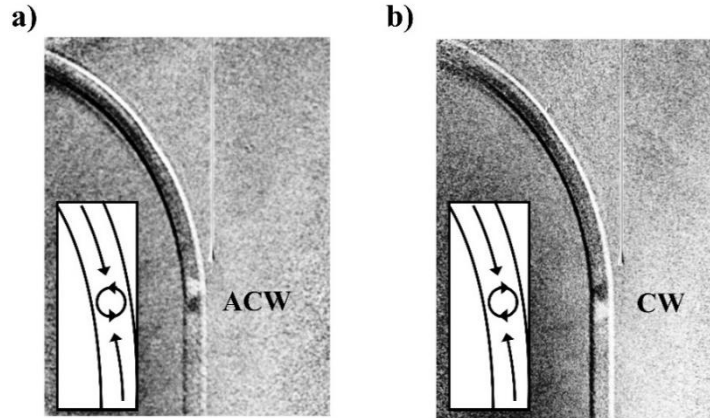
Figure 8.12: MTXM images of DW propagation along the 5 μm bend at H=180 Oe. (a): ACW chirality was seen 90% of the time. (b): CW DW was seen 10% of the time.

In the nanowire with $r = 5$ μm, the measurements indicated the presence of DWs with both ACW and CW chiralities at the output of the bend section of the nanowire (Figure 8.12). As explained earlier, the DN bend with H2H magnetisation configuration is expected to rectify VDW chiralities into an ACW DWs. In the previous bend geometries ($r = 1$ μm and $r = 2$ μm) not a single unrectified DW was observed in more than 50 total attempts. However for the bend with $r = 5$ μm, an unrectified DW chirality (i.e: CW DW) was observed in 2 of 20 repeats of the experiment times. This clearly suggests that the rectification process has been weakened at this bend geometry. Nevertheless, the high occurrence of the ACW chirality at the output of the bend (90% of the time) could be attributed to the relatively high propagating field (H_x= 180 Oe) which exceeds H_{rec} for this geometry (H_{rec}=100 Oe) according to simulation study (Figure 8.6) suggesting that the r= 5um bend could be performing rectification but with less reliability than smaller bends. Moreover, since the chirality of the input DW cannot be known (as there is no pinning site before the bend), it would be difficult to determine the strength and percentage of the rectification process.

For the nanowire with $r = 10$ μm, results in Figure 8.13 seem to hint that rectification has been further weakened. However, the limited contrast of the images makes the results less conclusive.
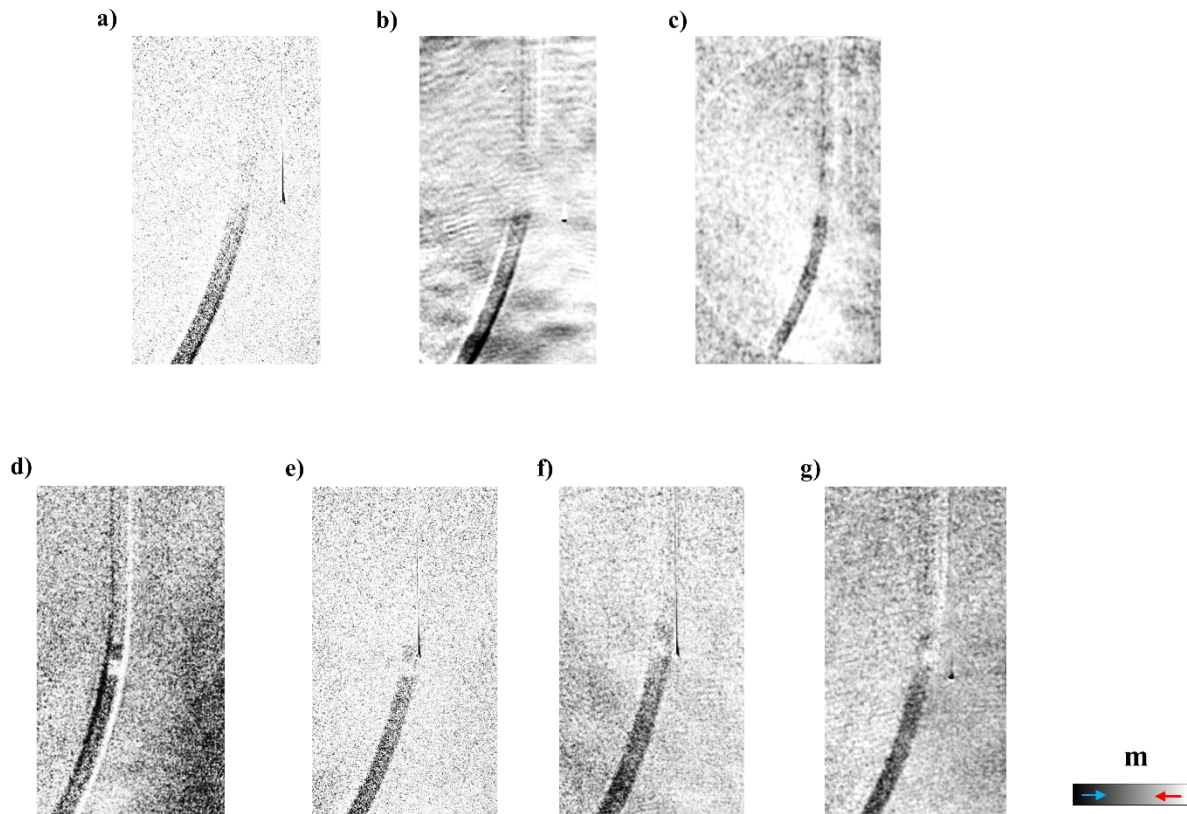
Figure 8.13: MTXM images of DW propagation along the 10 μm bend at H_x=250 Oe. (a)-(c): ACW chirality was seen 25% of the time. (d)-(g): CW DW was seen 75% of the time. H_p = 250 Oe.

Nonetheless, if our interpretation of the images is accepted (despite the images' poor acquired contrast); where images in Figure 8.13(a)-(c) were interpreted to indicate an ACW VDW, and Figure 8.13(d)-(g) were interpreted to indicate a CW VDW, the results would verify our hypothesis that wide bends will have weak rectification ability, and that bends with r=10 μm have shown CW VDW 25% of the time (4 out of 16 attempts). The field by which DWs were propagating across the 10 μm bend was $\mathbf{H_x}$=250 Oe.

The above experiments have verified the simulation study indicated in Figure 8.6. Results have shown that the VDW chirality rectification process of the nanowire bend is reliable at sharp bends and is weakened when the bend radius is increased (in this case at r ≥ 5 μm) and the injection field is lowered. However, further future work is needed to accurately determine experimentally the boundaries of the rectification process.

Upon reaching the end of this section it was experimentally evident that a sharp bend of r =1µm showed a rectification process with high robustness. Hence, the second aim would be to attempt to exploit this rectification process to mitigate stochasticity in a notch system where poorly defined VDW chirality was a primary cause of the system's depinning stochasticity. If this attempt was successful, it would result in establishing a deterministic switching device with a single-mode switching behaviour. This aim will be investigated in the next section.

8.3. Mitigating depinning stochasticity through DW rectification

In chapter 6, the depinning behaviour of DWs propagating across a single notch with depth N_d= 0.15W, in nanowire with t = 40 nm and w = 400 nm was investigated (refer to Figure 6.32). The results indicated that this geometry exhibited only two depinning modes, where each mode correspond to the pinning of one VDW chirality. This suggests that if propagation was limited to only one VDW chirality it would be possible to create a highly deterministic system with one depinning mode.

To achieve a chirality-biased DW propagation the rectifier discussed above was integrated into the nanowire system. Three designs of Py nanowires with t = 40 nm, w = 400 nm were fabricated and a single triangular notch of N_d = 60 nm was created.

The first nanowire was straight nanowire of l=20 µm, and was attached to a rectangular pad of size = 5 µm x 5 µm (Figure 8.14(a)). This nanowire was used as a 'control' device to compare the response of the other two nanowire systems. The second nanowire system contained an UP bend (radius r = 1 µm) connected to the nucleation pad with the straight nanowire (Figure 8.14(b)). As for the third nanowire system, it was designed to be identical to the second nanowire; however, the nucleation pad was connected to the straight section of the nanowire through a DN bend (Figure 8.14(c)). Schematics of the three nanowire devices are shown in Figure 8.14 below.
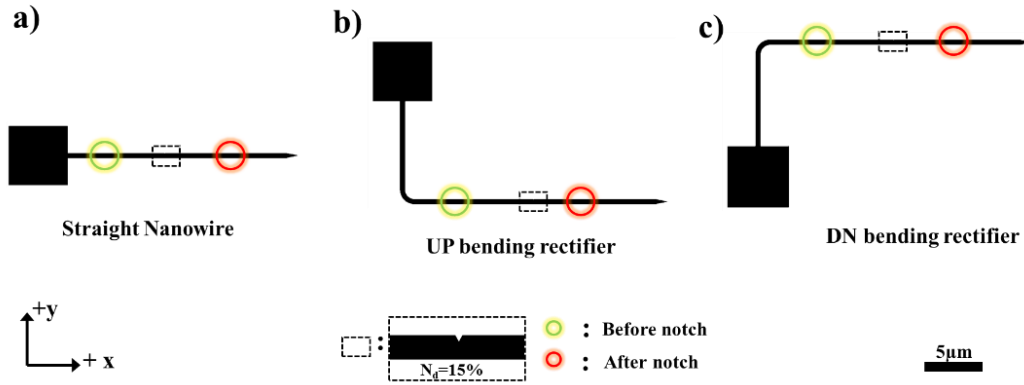
Figure 8.14: Schematic of the three nanowires used in the 'mitigating stochasticity' experiment. (a): Straight nanowire of w=400 nm and t=40 nm is used as a control. (b): UP bend rectifier (rotated -90°). (c): DN bend rectifier (rotated -90°). Single notch of N_d=0.15W is included in all nanowires.

The aim of the experiment was to investigate the depinning behaviour of the three nanowire systems by measuring their switching behaviour before and after the notches using the focused MOKE.

To do this, the straight nanowire was first saturated in the +x direction by applying H_x= 300 Oe. The field was then ramped to a maximum of H_x= -300 Oe in order to switch the pad and inject a DW into the straight nanowire. This will produce a T2T VDW which will propagate to and then depin from the notch. One hundred single shot measurements were taken both before and after the notch in order to characterise the injection and depinning field distributions, which are presented in Figure 8.16(a).

For the UP (DN) bend designs, the nanowires were first saturated by applying H_x= 300 Oe and H_y= - (+)100 Oe. T2T VDWs were then injected by sequentially applying a ramping field of H_y= +(-) 100 and then H_x=- 300 to drive VDWs around the bends and through the notches. As for the straight wire, one hundred single-shot measurements were taken before and after the notch. Results for these nanowires are plotted in histograms in Figure 8.16(b)&(c). Figure 8.15 shows examples of the voltage signals sent to the electromagnet in order to saturate and switch in the UP bend nanowire system.
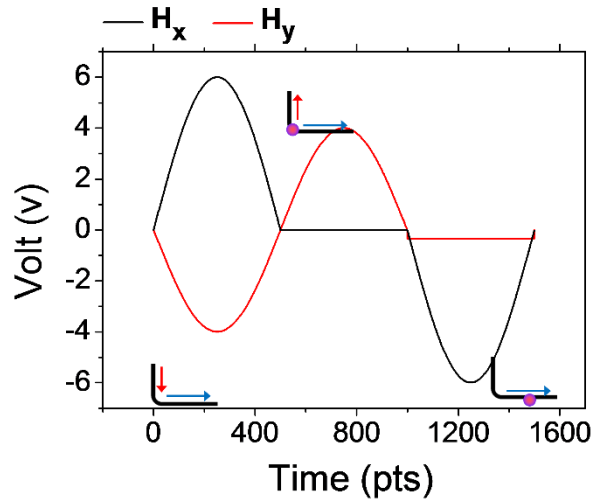
Figure 8.15: Output voltage signal sent to electromagnet in order to switch the UP bend nanowire. Small figures indicate the position of DW and magnetisation along the bend rectifier.

Results and discussion

The result of the IFDs and DFDs from the MOKE experiments were plotted in histograms as shown in Figure 8.16. The histograms of the UP and DN rectifiers reveal successful rectification process, and thus suppression of stochasticity for both bend directions.

The histogram of straight nanowire (Figure 8.16(a)) showed two depinning modes at H_d= -160 Oe and -95 Oe. In this nanowire, the ACW VDW occurred 45% while the CW VDWs occurred 55% of the time, indicating random nucleation of CW and ACW VDWs.

It was concluded from the previous section that the UP (DN) bend will rectify the DWs into a CW (ACW) chiralities when the DWs are in H2H configurations. This automatically entails that the rectification process will reverse for T2T VDWs. This means that the UP bend with a T2T configuration will rectify the VDWs into an ACW chirality (also indicated in Figure 8.10) and the DN bend (with T2T configuration) will rectify the VDWs into a CW chirality. This analysis is consistent with the experimental results. The nanowire system with the UP bend have rectified the DW into an ACW chirality, and the DN bend have rectified the VDW into a CW chirality. The CW VDW resembled the 'unfavourable' VDW when pinned at a single notch, as shown in the simulation snapshot in Figure 8.16(c).
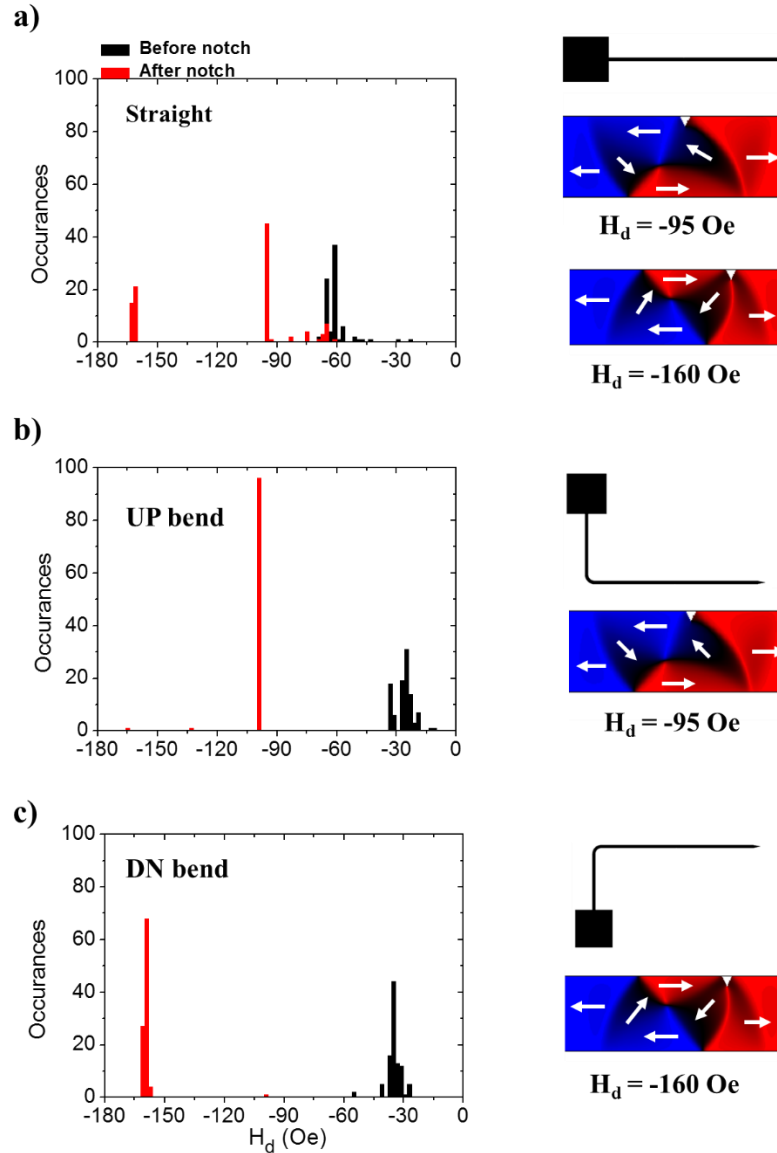
Figure 8.16: Histograms of switching fields before (black) and after (red) single notch pinning site obtained from 100 single-shot measurements using MOKE setup. (a): Histograms obtained for straight 'control' nanowire. (b): UP bend rectifier. (c): DN bend rectifier. Snapshot to the right of histogram show the chirality of VDW pinned at the pinning site and schematic of rectifier

In this example, the unfavourable chirality faced a high energy barrier at the notch, resulting in a high H_d value of -160 Oe. As for the DN bend, the ACW VDW was pinned in a 'favourable' chirality resulting in a relatively small energy well at the pinning site, where depinning occurred at H_d= -95 Oe (Figure 8.16(b)). These results are in general agreement with the simulation discussed in Figure 6.32; however, in this experiment a T2T rather than a H2H magnetisation configuration was set, resulting in an opposite chirality response to the single notch.

As the bends have managed to rectify the VDW chirality, both rectifiers have managed to suppress the depinning stochasticity by limiting the number of DW pinning configurations to a single one. This has resulted in establishing a system with a single-mode switching behaviour.

The experiment was repeated with 5 other duplicates of the UP bend as well as DN bends nanowires, and results were generally consistent with presented data in Figure 8.16. In two of these nanowires, the DFD histograms showed two modes: 75% (successfully rectified chirality) and 25% (non-rectified chirality) occurrence rate indicating less reliable rectification than seen in the other rectifiers. This has been attributed to the edge roughness of the bend that would have altered their rectification process.

From this experiment it can be concluded that sharp bend section of nanowires with $t = 40$ nm can act as DW chirality rectifiers and these can be successfully utilized to mitigate DW depinning stochasticity at artificial defects where DWs having ill-defined chiralities is a primary cause.

8.4. Conclusion

In this chapter, a new DW chirality rectification function using Py nanowires has been proposed and was successfully tested. The rectification feature can be used to manipulate VDW chirality in motion for DW logic applications as well as to mitigate depinning stochasticity.

From the first section where the reliability of rectification was investigated, it can be concluded that a sharp bend of $r = 1$ μm has the ability to rectify the VDW chirality in a manner depending on the nanowire magnetisation configuration and the spin orientation of the leading edge of the nanowire. Simulation and experimental results have shown that the H2H UP (DN) bend rectified VDWs to CW (ACW) chirality with a very high reliability when **H** is $\geq$ **H**$_{rec}$. For a

T2T magnetisation configurations, the opposite chirality rectification occurred; in which, DWs propagating through UP (DN) bend were rectified into ACW (CW) chirality.

The rectification process was due to magnetic frustration between the leading edges of the DWs and the magnetisation configuration of the vertical sections of the nanowires when the ACW (CW) VDW started propagating through the bend. The experimental tests also indicated very high robustness for sharp bends with $r \leq 2$ µm, even when dynamical effects dominated the propagation process. At bends of $r \geq 5$ µm, rectification seemed to get weakened and DWs were less likely to rectify their chirality.

Such functionality could be useful for chirality-based logic applications in which a rectifier can act to reset the DW chirality. Moreover, the study highlights an important limitation to the use of bend regions in applications where chirality of DWs is required to be preserved.

Another equally important outcome of the rectification functionality of sharp bend nanowires was explored in the second section where it was concluded that the DW chirality rectifier can limit the number of pinning configurations, when used before chirality-sensitive defects. This has resulted in a mitigation of depinning stochasticity as less possible depinning modes are available. The results presented here showed that in magnetic nanowire systems where switching exhibits two switching modes (such as in nanowires of t=40 nm and single notch of N_d=0.15W) that are due to VDWs pinning in two chiralities, the rectifier bend can transform the behaviour of this system to exhibit a single depinning mode. Such systems can be highly beneficial in DW applications as well as in further experiments studying DW behaviour.

8.5. References

[1]   E. R. Lewis, D. Petit, L. O'Brien, A. Fernandez-Pacheco, J. Sampaio, A. V. Jausovec, *et al.*, "Fast domain wall motion in magnetic comb structures," *Nat Mater,* vol. 9, pp. 980-983, 12//print 2010.

[2]   J. Brandao, R. L. Novak, H. Lozano, P. R. Soledade, A. Mello, F. Garcia, *et al.*, "Control of the magnetic vortex chirality in Permalloy nanowires with asymmetric notches," *Journal of Applied Physics,* vol. 116, Nov 21 2014.

[3]   A. Bisig, M.-A. Mawass, M. Stärk, C. Moutafis, J. Rhensius, J. Heidler, *et al.*, "Dynamic domain wall chirality rectification by rotating magnetic fields," *Applied Physics Letters,* vol. 106, p. 122401, 2015.

[4]   D. McGrouther, S. McVitie, J. Chapman, and A. Gentils, "Controlled domain wall injection into ferromagnetic nanowires from an optimized pad geometry," *Applied physics letters,* vol. 91, p. 022506, 2007.

[5]   K. Sentker, F.-U. Stein, L. Bocklage, T. Matsuyama, M.-Y. Im, P. Fischer, *et al.*, "Fast generation of domain walls with defined chirality in nanowires," *Applied Physics Letters,* vol. 104, p. 172404, 2014.

[6]   A. Pushp, T. Phung, C. Rettner, B. P. Hughes, S.-H. Yang, L. Thomas, *et al.*, "Domain wall trajectory determined by its fractional topological edge defects," *Nat Phys,* vol. 9, pp. 505-511, 08//print 2013.

[7]   K. Omari and T. Hayward, "Chirality-based vortex domain-wall logic gates," *Physical Review Applied,* vol. 2, p. 044001, 2014.

[8]   M.-Y. Im, L. Bocklage, P. Fischer, and G. Meier, "Direct Observation of Stochastic Domain-Wall Depinning in Magnetic Nanowires," *Physical Review Letters,* vol. 102, Apr 10 2009.

[9]   M.-Y. Im, L. Bocklage, G. Meier, and P. Fischer, "Magnetic soft x-ray microscopy of the domain wall depinning process in permalloy magnetic nanowires," *Journal of Physics: Condensed Matter,* vol. 24, p. 024203, 2012.

[10]   E. Lewis, D. Petit, L. Thevenard, A. Jausovec, L. O'Brien, D. Read, *et al.*, "Magnetic domain wall pinning by a curved conduit," *Applied Physics Letters,* vol. 95, p. 152505, 2009.

[11]   G. Woltersdorf, M. Kiessling, G. Meyer, J.-U. Thiele, and C. Back, "Damping by Slow Relaxing Rare Earth Impurities in Ni 80 Fe 20," *Physical review letters,* vol. 102, p. 257602, 2009.

[12]   W. Bailey, P. Kabos, F. Mancoff, and S. Russek, "Control of magnetization dynamics in Ni 81 Fe 19 thin films through the use of rare-earth dopants," *Magnetics, IEEE Transactions on,* vol. 37, pp. 1749-1754, 2001.

Chapter 9:

Chirality-based Vortex Domain Wall Logic Gates

The studies described in the preceding chapters have provided important insight into origins and characteristics of stochastic DW pinning and propagation in Py nanowires. Such understanding is vital for building DW-based spintronic applications that need to be robust, efficient and reliable. These spintronic applications, have gained huge interest in the last decade [1, 2]. Part of that interest comes from the promising properties of proposed information storage applications. These properties include non-volatility, solid-state operation leading to low power consumption, high data densities and fast propagation of DWs [3-6].

The "race-track" memory concept, proposed by IBM, uses spin-polarized currents to synchronously move DWs, and is considered one of the promising DW-based magnetic memory technologies [4, 7]. Furthermore, recent developments of this architecture using magnetic materials with perpendicular anisotropy may allow increases in data density to the point where it is competitive even with magnetic disk drives [4]. Moreover, similar DW-based memory technologies that use an applied field to drive DWs in a ratchet-like scheme to obtain synchronous DW motion have been proposed [8, 9], providing magnetic memory technology that can be integrated with nanomagnetic applications that uses field (rather than current) for magnetic switching.

In addition to storing information, magnetic domains/DWs in nanowires have been utilized to perform logical operations [10-12]. The famous DW-logic scheme [13] uses the direction of magnetisation of small regions in Py nanowires (separated by DWs) to represent bits of '1' and '0'. However, such data representation depends on the length of the magnetized region. Moreover, in such schemes, it is difficult to change intermediate bits (for example: '1 1 1' to

'1 0 1') as two DWs have to be nucleated for switching of intermediate bit (domain) to occur, rather than being able to switch the individual bit only, such as in the TDW chirality-based logic architecture described in section 3.5.1 [14]. Moreover, this scheme requires a fully rotating magnetic field for the logic gates (especially the NOT gate with its cusp shape (refer to DW-logic in section 3.5.1) to function, adding more complexity to its architecture.

In this chapter, a novel DW logic scheme is presented where a further degree of freedom of the VDW is being exploited to represent data. This additional degree of freedom is the VDW chirality. As has been explored throughout this thesis, the internal magnetisation of VDWs can rotate either clockwise (CW) or anticlockwise (ACW), and these two states can be used to represent digital binary data to build a chirality-based logic architecture.

In this chirality-based logic architecture, designs are proposed for NOT, NAND, AND, NOR, OR and FAN-OUT gates. All of these gates manipulate the chiralities of VDWs by propagating them through an interconnected network of nanowires that contain engineered notches. These gates have been proved to be cascadable. Moreover, upon tackling the stochasticity challenges and innovating a cross-over gate, the chirality-based logic gates can be interlinked to build any logical operation.
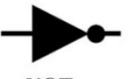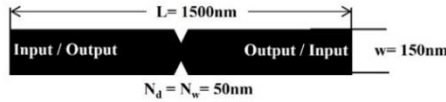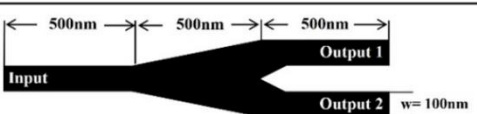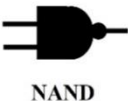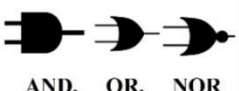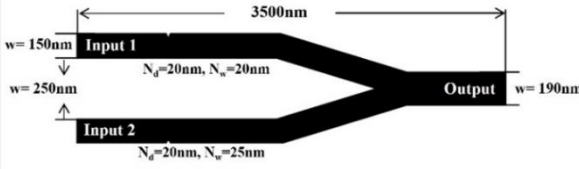
The chirality-based logic architecture proposed here is presented as a full simulation study using OOMMF simulation package [15] as a proof-of-concept. Moreover, the challenges that needs to be tackled before implementation will also be discussed. Finally, initial investigations into experimental realisations of the logic gates have been carried as well as suggestions on how future experiments could be improved.

9.1. Simulation method

Simulations were performed for 40-nm thick Py nanowires. Standard parameters of Py materials were used to model the nanowires magnetic properties as explained in section 4.5. A damping coefficient of $\alpha = 0.5$ was used in order to supress dynamical effects as the primary purpose was to study the phenomenological behaviour of interacting DWs in interconnected nanowires. However, high damping values such as these can also be obtained experimentally when Py is doped with rare-earth metals such as Terbium (Tb) or Holmium (Ho) [16, 17].

The cell size for the NOT and FAN-OUT gates was chosen to be $5 \times 5 \times 40$ nm^3, while a cell size of $2.5 \times 2.5 \times 40$ nm^3 was chosen for the AND, OR, NOR and NAND gates in order to
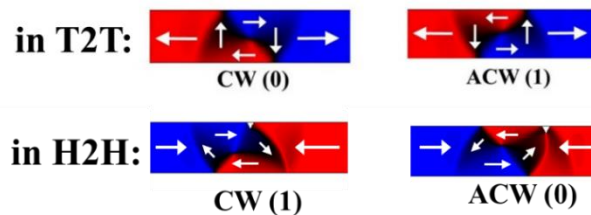

Figure 9.1: (a): Table showing schematic of the NOT, FAN-OUT and NAND, AND, NOR, and NOR logic gates. (b): Representation of '1' and '0' using ACW and CW chirality conventions for T2T and H2H.

obtain higher resolution of small notch features, which are integral to their designs. Table 9.1 shows a full schematic for the logic gates used in the chirality-based logic architecture.

In all of the logic gates, simulations were performed for all input combinations of both T2T and H2H magnetic configurations. The results presented here focus on the T2T configuration; nevertheless, results can be extended to include also the H2H configuration. However, when applying logic operations in a H2H configuration, the VDW chirality binary convention has to be reversed in order to exploit the symmetry of the VDW spin configuration which depends also on the monopole character [18].

In the T2T configuration, the ACW DW chirality was assigned as binary '1' and the CW chirality as binary '0'; whereas to obtain the same functionality for the same gate in the H2H configuration, the ACW chirality should be defined as '0' and the CW chirality to '1' (refer to DWs convention in Figure 9.1(b)). Since the T2T results will be presented throughout this chapter, the ACW and CW chiralities will represent '1' and '0', respectively.

The following sections will describe the design and operating principles of NOT gates, FAN-OUT gates and NAND, AND, OR and NOR gates. Simulations showing the behaviours of all the gates will be presented in detail.

9.2. NOT gate

The NOT gate (or invertor) is one out of the three basic logic gates needed to perform any logic operation. In the NOT gate, the input signal gets inverted at the output. In other words, if a binary '1' flows through the NOT gate, a binary '0' is seen at the output, and vice-versa. Equivalently, in the chirality-based NOT gate, an ACW VDW will invert into a CW VDW and a CW VDW will invert into an ACW VDW at the output.

Interestingly, the idea of the NOT was developed after observing the inversion behaviour of the double notch in thick nanowires while performing simulation study presented in chapter 6.

The chirality-based NOT gate developed here is simply composed of a nanowire of w= 150nm, t = 40 nm and contains a double triangular notch. The notches have depth $N_d = N_w = 50$ nm (0.33W) as shown in table of Figure 9.1.

The simulation was initialised by relaxing an ACW DW at the input side of the NOT gate in a T2T configuration. A propagating field H_x was increased quasi-statically from H_x= 100 Oe to 400 Oe in steps of 5 Oe in order to propagate the DW across the double notches. Results of the simulation are presented in Figure 9.2

Results and Discussion of NOT gate

As the VDW propagated from the input to the output channels, it encountered an energy gradient causing the DW to pin at the double notch. During this process, the leading edge of the VDW relaxed to pin centrally at the bottom notch allowing for a parallel alignment of DW spins with the edges of the notch and nanowire.

As H_x increased further, the bottom half of the VDW (that has spins parallel to the applied field) expanded in an attempt to depin through the double notch. However, due to the strong pinning site, the DW remained pinned, and at H_x= 380 Oe a new DW core was nucleated at the left side of the double notch (Figure 9.2(a)-4). This nucleation is the cause of the inversion process: as the new vortex was nucleated, the spins at its trailing edge had to be parallel to those in the leading edge of the initial vortex in order to prevent magnetic frustration (refer to yellow arrows in Figure 9.2(a)-4). Such alignment led to the creation of a CW VDW at the left side of the notch. Eventually the core of the first DW annihilated at the top edge of the nanowire while the second DW depinned from the double notch and continued its propagation. The
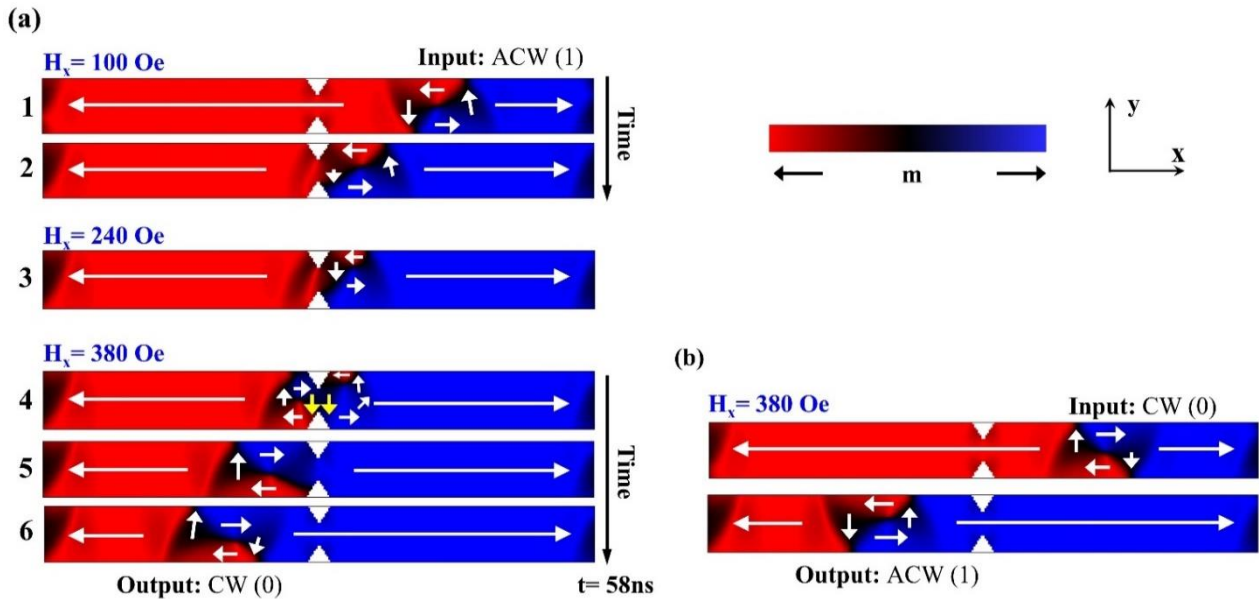
Figure 9.2: Micromagnetic simulation snapshots illustrating the inversion process of a NOT gate. (a): Snapshots of the inversion process of an ACW DW into CW chirality. (b): Inversion of CW ('0) chirality into ACW DW.

result, is a CW VDW at the output section of the NOT gate. The propagation of the VDW at H_x= 380 Oe is noted to be smooth as the WB transformation at high damping of α=0.5 starts at 500 Oe.

An analogous process occurred when the input VDW was of CW chirality. In the CW case, the VDW was initially pinned near the top notch, and the top half of the VDW expanded while a new core was nucleated on the other side of the double notch. Eventually an ACW DW was formed at the output channel, demonstrating the role of a NOT gate.

The results seemed to indicate that the inversion process occurred due to two factors: the reversal process occurring through the nucleation of a new VDW, and the symmetric shape of the notches that prevented any biasing by the pinning site, hence, leaving the initial VDW to control the chirality of the new VDW by aligning the spins of its leading edge parallel to the spins of the lagging edge of the newly nucleated VDW (refer to yellow arrows in Figure 9.2-4). The first factor may be attributed to the strong pinning potential of a deep notch in a thick nanowire, and so an investigation of the reliability of the inversion process in nanowires with

lower thicknesses was performed. It was observed that the same inversion process occurred only for t > 25nm. However, for 25 nm < t < 32 nm, inversion occurred through a different depinning process where the VDW transferred into a transverse-like structure before depinning, and the newly VDW core appeared only after the complete depinning of the DW (refer to Figure a3.1 in Appendix 3.1).

Since the inversion process in this latter method seemed to be highly dependent on the manner by which the DW detached from the pinning site, it is expected that this would be highly susceptible to thermal perturbation, and hence less reliable than the case for nanowires of t>32nm. For t < 25 nm, the inversion process did not work and the VDW depinned smoothly preserving its chirality.

Finally, the NOT gate functionality was tested in a ballistic manner; in which a constant magnetic field of $\mathbf{H_x}$ = 385 Oe was set to drive the DW through the gate under constant field, without a quasi-static field ramp. Results revealed a successful inversion process that proceeded in a manner very similar to the inversion process that occurred in the quasi-static simulations above. This feature suggests a fast and efficient functionality of NOT gate when successfully implemented in real devices.

9.3. FAN-OUT gate

The purpose of the FAN-OUT gate is to duplicate the input value at the output channels. In the two way FAN-OUT gate presented here, the VDW chirality at the input is duplicated at the two output channels by propagating the input VDW and nucleating an additional new VDW with the same chirality. The shape and dimension of junction connecting the input and the two-way output channels were designed carefully to allow the duplication process to occur as shown in Figure 9.1. The input and output nanowire channels have the same width of w=100 nm.

The simulation was initialised by relaxing a CW VDW at the left side of the gate and then increasing H_x from 0 Oe to -400 Oe in steps of 10 Oe in a quasi-static manner until the two nanowires at the output channels have switched and two DWs have appeared at the output channels. Figure 9.3 shows the results of the simulations.

Results and Discussion of FAN-OUT gate

It was observed from the simulation that the VDW propagated and reached the junction at H_x = -200 Oe. Upon increasing the field further, the VDW started to expand inside the junction while preserving its chirality. As the field continued to increase, the VDW core continued its upward motion by expanding the bottom half region of the VDW that has spins aligned parallel to the direction of the field (Figure 9.3(a) at H_x=-220Oe). This behaviour is similar to the behaviour seen in Dirac spin-ice networks where the chiralities of VDWs determine the path taken in a Y-shaped junction [19].

As the initial VDW core was displaced, an elongated DW was formed between the apex of the junction and output 2 with magnetisation pointing along –y. At H_x= -230 Oe, the leading edge
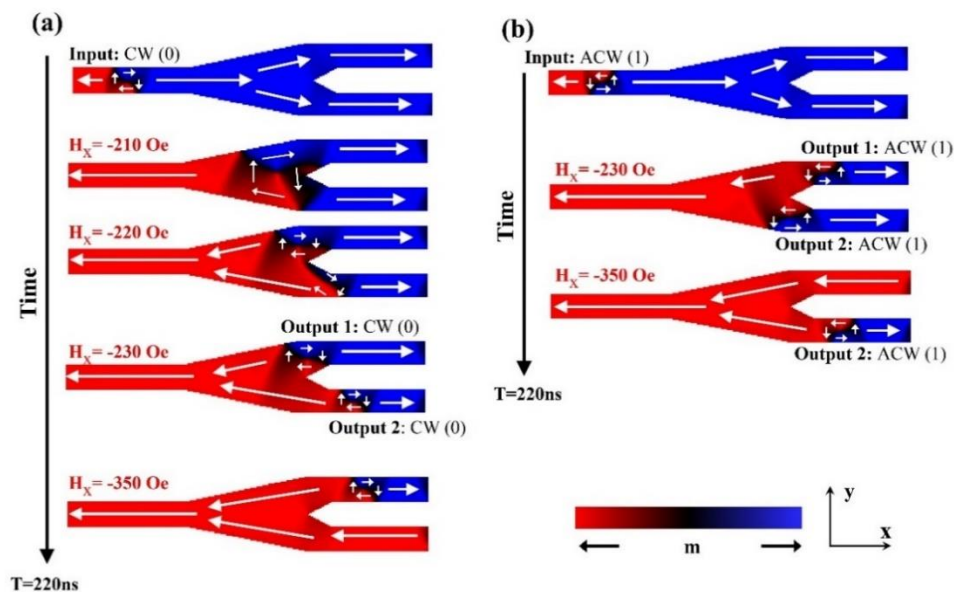

Figure 9.3: Micromagnetic simulation of FAN-OUT gate. (a): Detailed process of duplicating input in a FAN-OUT gate for a 'CW' DW input. CW VDW expands at the junction, moves towards output 1, and a new CW VDW is nucleated at output 2. (b): Input DW with ACW chirality

depinned from the apex and became the leading edge of the new VDW formed that, consequently, has the same chirality as the initial VDW. At the same instance, the VDW that propagated towards output 1 retained its vortex shape, and at H_x =-350 Oe depinned and propagated towards output 1. As a result, two CW VDWs were formed in the two output channels. An analogous process occurred for an initial ACW VDW, however, the initial VDW propagated towards output 2, while the new VDW is formed at output 1 Figure 9.3(b).

It is important to mention that the process that allows for the formation of a second VDW that has the same chirality depends mainly on the sequence and manner by which the leading edge of the second nucleated DW detaches from the apex. This method may be susceptible to stochasticity triggered by edge roughness and thermal activation.

Moreover, the fact that each output DW reaches the output channel at a different field (the first at -230 Oe and the second at -350 Oe) suggests that an additional method to synchronize the VDWs propagation might be needed. Nevertheless, the main aim of duplicating the VDW chirality was successfully achieved.

9.4. NAND, AND, NOR and OR gates

The basic logic gates that are used to build logic architectures are the NAND, AND, NOR, and OR gates. It is widely known that all of the basic logic gates can in principle by derived from the NAND gate alone. However, in this chapter a method to build each of the four basic gates separately will be discussed. The simulation details will be discussed for the NAND gate and then generalized to include the rest of the logic gates.

In the NAND, AND, NOR and OR gates two input channels produce one output that relates to the two inputs by a certain logical operation as shown in the truth table (Table 9.2). In the case of the chirality-based VDW gates, the two inputs are formed by a horizontal Y-shaped network

233

Table 9.2: Truth table for basic logic gates for T2T magnetic configuration

Logic Gate	Input 1	Input 2	Output
NAND	ACW (1)	ACW (1)	CW (0)
	ACW (1)	CW (0)	ACW (1)
	CW (0)	ACW (1)	ACW (1)
	CW (0)	CW (0)	ACW (1)
AND	ACW (1)	ACW (1)	ACW (1)
	ACW (1)	CW (0)	CW (0)
	CW (0)	ACW (1)	CW (0)
	CW (0)	CW (0)	CW (0)
NOR	ACW (1)	ACW (1)	CW (0)
	ACW (1)	CW (0)	CW (0)
	CW (0)	ACW (1)	CW (0)
	CW (0)	CW (0)	ACW (1)
OR	ACW (1)	ACW (1)	ACW (1)
	ACW (1)	CW (0)	ACW (1)
	CW (0)	ACW (1)	ACW (1)
	CW (0)	CW (0)	CW (0)

of nanowires that merge together at the junction to produce an output DW at the output nanowire channel. Schematic of gate is as shown in Figure 9.1.

First, it was important to study and understand how the chirality of a VDW in the output channel was determined by the switching of the two Y-shaped nanowires. Faulkner *et al* [12] have reported that in a similar Y-shaped structure; in which, the DW that arrives first to the junction will wait for the other DW to merge together in order to switch the junction. Therefore, it was important to know if the arrival sequence of the DWs had an effect on the chirality of the output DW. In order to investigate this, a Y-shaped network was designed, and a triangular notch of $N_d = N_w = 50$ nm was introduced at one of the input nanowire channels in order to manipulate the DW arrival sequence by creating a pinning site at one of the input channels. This caused the pinned DW to arrive at a later point in the applied field sequence. The notch was introduced in the other nanowire input channel and the same simulation was repeated. In both designs, the two possible sets of inputs (ACW, ACW) and (CW, CW) were simulated to investigate if the chirality of the input VDW had an effect on the chirality of the output VDW. The simulations were initialised by creating a VDW at each input and applying a ramping field

H$_x$ from -150 Oe to -300 Oe in steps of 10 Oe. Results of these simulations are shown in Figure 9.4

Results and Discussion of Arrival Sequence Test

Figure 9.4 shows the results of two sets of simulations. In the first set (Figure 9.4(a)), the top channel has a pinning site and hence in all cases the bottom VDW will arrive first to the junction. It can be deduced from these results that, irrespective of the chirality of the DWs, if the VDW in the bottom channel arrives first to the junction, the output VDW will always be of CW chirality for T2T DWs (and ACW in H2H), as shown in Figure 9.4(a). Equivalently, when a DW in the top channel arrives first to the junction, the output DW will always be of ACW chirality in a T2T magnetisation (and CW in H2H), as shown in Figure 9.4(b).

The reason for such observation can be explained as follows: as the VDW from top nanowire channel got pinned at the notch (Figure 9.4(a)), the VDW from the bottom channel propagated towards the junction and pinned just before it; between the internal apex of the Y-shaped junction and the corner between the two input channels (refer to green arrows in Figure 9.4(a)). This resulted in the magnetization of the junction obtaining component along the −y direction (indicated by two small arrows between the green arrows). This −y magnetisation component has set the leading edge of the VDW that will be nucleated later to be pointing also along the −y direction. As the field was further increased, the VDW in the top nanowire channel depinned from the notch and propagated toward the junction. As the VDW propagated toward the first DW, the magnetic tension form the propagating VDW caused the first DW to depin from the apex and merge with the propagating DW. This resulted in forming a new VDW with its leading edge pointing along the −y direction, resulting in a CW VDW. Therefore, it can be deduced that anytime the bottom channel switches first, the resultant VDW will be of a CW chirality.
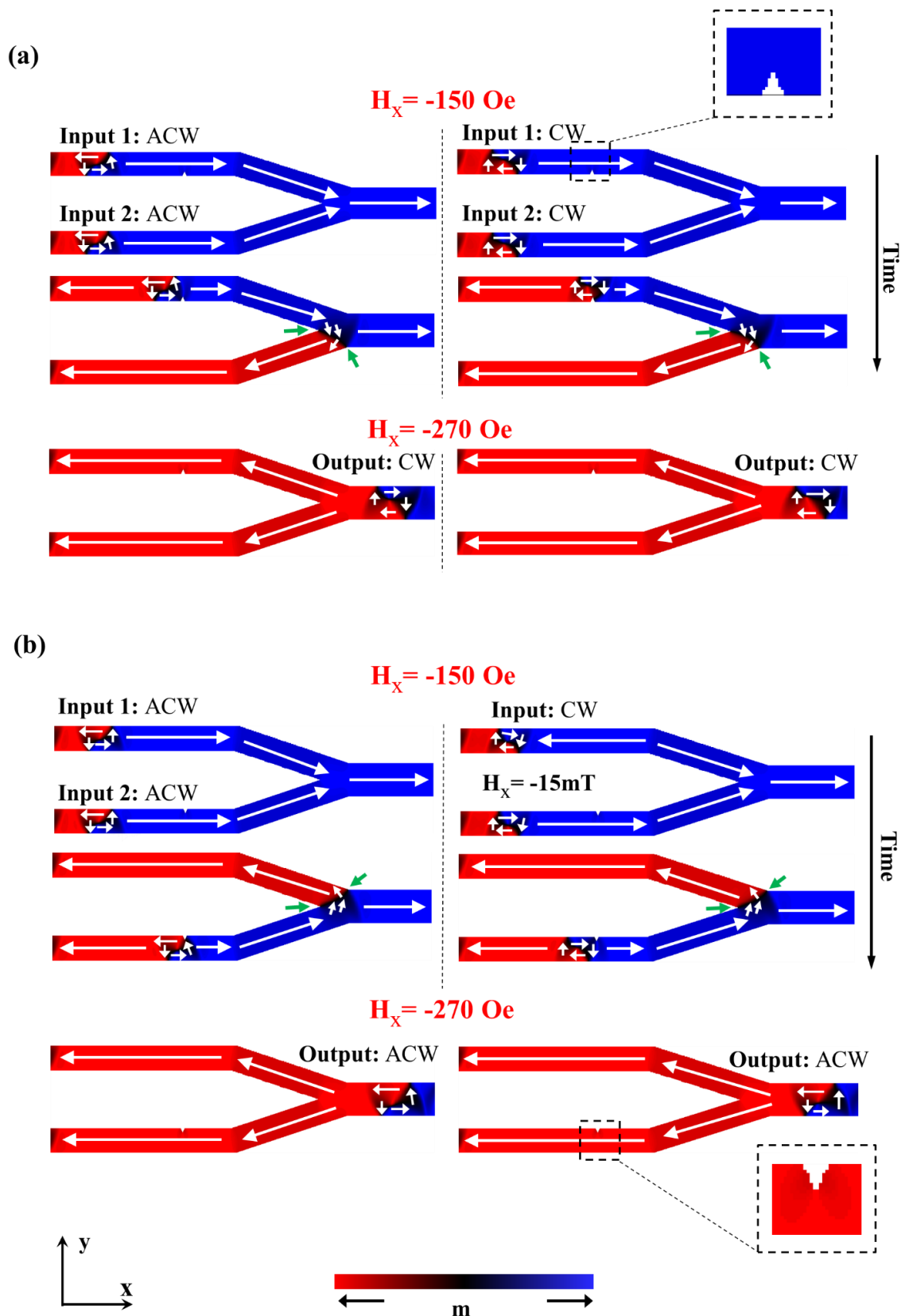
Figure 9.4: Micromagnetic simulations investigating how the chirality and arrival sequence of VDW affects the output VDW chirality in a Y-shaped junction. (a): A notch is designed in "input 1," delaying the arrival of the VDW in this wire. (b): The notch is designed in "input 2.". Green arrows show the pinning location between internal apex and corner between the two input channels. Images enclosed in dashed frames are an enlargement of the notch area.

A mirrored behaviour occurred for the other scenario, where the VDW in the top nanowire channel has reached the junction first (Figure 9.4(b)). In this case a +y magnetisation component was added to the junction (indicated by green arrows in Figure 9.4 (b)) before the second VDW from the bottom channel arrived. After the two DWs merged an ACW was produced.

The above simulation clearly indicates that the chirality at the output is determined by the sequence of arrival of the DW from the top or bottom channel. Therefore, in order to build a NAND, AND, NOR and OR logic gate, the Y-shaped network should be engineered in a manner that allows for a desired arrival sequence to occur. Such engineered arrival sequence should produce the functionality of the desired logic gate.

For instance, in the case of the NAND gate (Table 9.1) the output state should always be a high state of '1' except for the case when both inputs are '1' and '1', then the output should be of a low state of '0'. In other words, the output should always be an ACW VDW except when both inputs contain ACW VDWs. Since the previous simulation in Figure 9.4 showed that an ACW VDW was produced at the output when the DW at input 1 (top channel) arrived first to the junction, for the Y-shaped network to function as a NAND gate, the input channels should be designed to favour switching of input 1 first except when both input 1 and input 2 contain ACW VDWs.

One method to achieve this is by introducing different triangular notches in the two input channels and exploiting the chirality/notch interactions explained by Hayashi *et al* [20]; where each chirality has a different depinning field depending on the energy landscape produced when pinned at the notch. In other words, each of the two VDWs will pin at their corresponding notches until a critical depinning field $H_{input\ 1\ or\ input\ 2}^{ACW\ or\ CW}$ is applied, where the upper suffix indicate the chirality of the VDW and bottom suffix indicate the input channel. From the truth
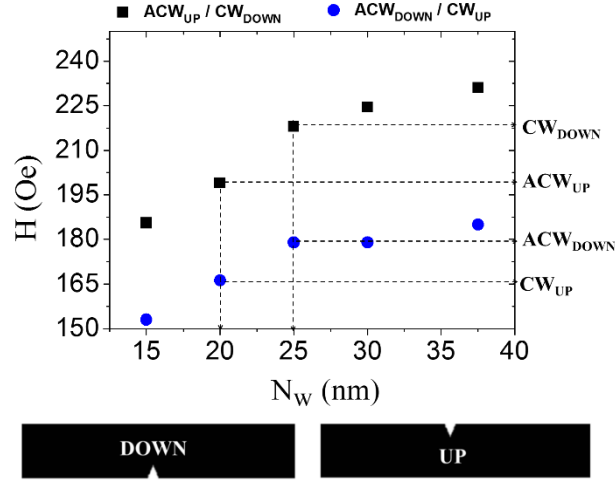
Figure 9.5: Plot showing different depinning fields for notches of varying notch widths. Schematic below plot shows UP and DOWN conventions used when notch is placed at top edge and bottom edge of nanowire, respectively.

table of the NAND gate (Table 9.2), it can be deduced that Y-shaped network of nanowires

will function as a NAND if the following inequality is satisfied:

$$H_{input\ 1}^{CW} <\ H_{input\ 2}^{ACW} <\ H_{input\ 1}^{ACW} <\ H_{input\ 2}^{CW} \qquad \text{(eq. 9.1)}$$

In order to design notches that can satisfy the above inequality, simulations were performed

for notches with different geometries in isolated Py nanowires with the same widths as the

input channels (w= 150 nm). Triangular notches of $N_d =$ 20 nm and varying N_w = 15, 20, 25,

30 and 35 nm were introduced at either the top edge of the nanowire (UP), or the bottom edge

of the nanowire (DOWN) as shown in inset of Figure 9.5. The aim of this simulation was to

find the depinning field associated with each VDW chirality and notch geometry in order to

choose the pair of notches that would satisfy the inequality in equation 9.1.

The simulated depinning fields are plotted in Figure 9.5. It can be seen that ACW VDW pinned

at the top edge are weakly pinned compared with CW VDW pinned at the same notch. The

opposite is seen for the case where the notch is located at the bottom edge of the nanowire.

This is a normal consequence to the reversal of VDW symmetry that results from reversing the

VDW chirality [18].

It can be deduced from the plot that placing a notch of $N_w = 20$ nm on the top edge of input 1 and a notch of $N_w = 25$ nm on the bottom edge of input 2 would satisfy the inequality.

The simulations described above were performed using 2.5 x 2. 5x 40 nm^3 cells. However, they were also repeated using cell size of 1 x 1 x 40 nm^3 in order to test the effect of resolution with these small notch dimensions. Both cell sizes produced similar results with a maximum of 6.5% error between the two sets of depinning fields.

In order to implement the NAND gate, the two notches: $N_d = 20$ nm and $N_d = 25$nm were added to input 1 (top) and input 2 (bottom), respectively. The four possible combinations of input VDW chiralities (ACW, ACW) (ACW, CW) (CW, ACW) and (CW, CW) were then simulated to verify the function of the NAND gate. This was achieved by relaxing two VDWs in the input 1 and input 2 nanowires and then increasing the applied field $\mathbf{H_x}$ from -100Oe to -400Oe in steps of 5 Oe in order to perform the simulation in a quasi-static manner. Results of these simulations are shown in Figure 9.6.

Results and Discussion of NAND gate

The simulation result indicated a successful implementation of the NAND functionality. Figure 9.6(a) presents results for the case where both input nanowires contain ACW VDWs. Both VDWs arrived and pinned at the notches in the input nanowires at $\mathbf{H_x}$= -150 Oe. As $\mathbf{H}$ increased to -190 Oe, the VDW in the bottom input nanowire (input 2) depinned and arrived at the junction, thus setting the junction's magnetisation to lie along –y. As $\mathbf{H_x}$ increased to -240 Oe the VDW from input 1 depinned and propagated toward the junction, before merging with the first VDW pinned to create a VDW in the output nanowire. The resultant output VDW was of CW chirality.
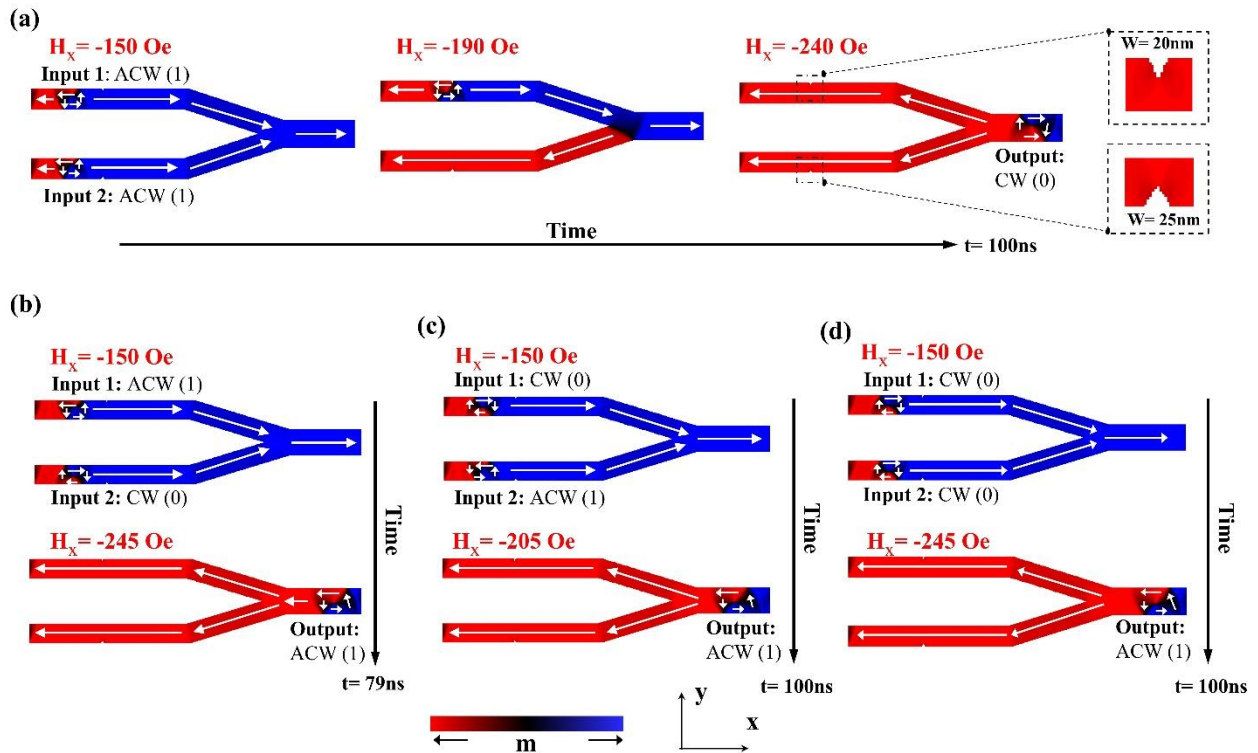
Figure 9.6: Micromagnetic simulation showing the NAND gate operation. (a): NAND gate with input 1 as ACW and input 2 as ACW. Framed images show shape of notches in each nanowire (N_d=20 nm). (b): Initial and final states for input 1 of ACW and input 2 of CW. (c): Initial and final states for input 1 of CW and input 2 of ACW. (d): Initial and final states for input 1 of CW and input 2 of CW.

The remaining input combinations are shown in Figure 9.6(b)-(d). In all of the remaining combinations, the top nanowire channel switched first, setting the magnetisation of the junction to the +y orientation, and creating an ACW VDW at the output.

It is important to note that when comparing the values of the depinning fields of the NAND gate notches with the values for isolated nanowires in Figure 9.5, it was observed that the depinning field values in the NAND structure were higher. This could be attributed to the monopole repulsion between the junction (after the first DW has entered it) and the second VDW, which would increase the pinning strength. Figure 9.7 depicts the monopole interaction.
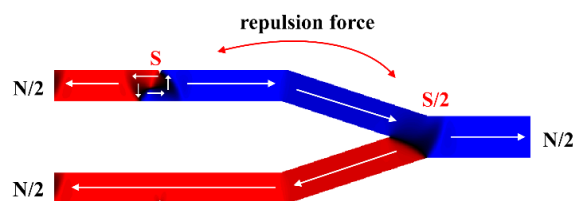

Figure 9.7: Schematic showing the monopole distributions 'south' (S) and 'north' (N) that results in a repulsive force from the Y-shaped network junction onto the pinned DW.

240

Table 9.3: Summary of switching field inequalities and notch location and width required to create NAND, AND, NOR and OR gate in a T2T magnetisation

Gate	Inequality	Notch at input 1 (location/width)	Notch at input 2 (location/width)
NAND	$H^{CW}_{input\ 1} < H^{ACW}_{input\ 2} < H^{ACW}_{input\ 1} < H^{CW}_{input\ 2}$	Top edge/20nm	Bottom edge/25nm
AND	$H^{CW}_{input\ 2} < H^{ACW}_{input\ 1} < H^{ACW}_{input\ 2} < H^{CW}_{input\ 1}$	Bottom edge/25nm	Top edge/20nm
NOR	$H^{ACW}_{input\ 2} < H^{CW}_{input\ 1} < H^{CW}_{input\ 2} < H^{ACW}_{input\ 1}$	Top edge/25nm	Bottom edge/20nm
OR	$H^{ACW}_{input\ 1} < H^{CW}_{input\ 2} < H^{CW}_{input\ 1} < H^{ACW}_{input\ 2}$	Bottom edge/20nm	Top edge/25nm

However, the location and orientation of the two notches used previously in input 1 and input 2 will have to change in order to fulfil the inequality that corresponds to each of the logic gates. Table 9.3 contains the depinning field inequalities that have to be fulfilled in order to obtain the correct DW arrival sequence that will produce each gate's functionality for the T2T magnetisation (same inequalities apply for H2H, but the binary convention should be reversed).

9.5. Engineering and feasibility analysis

After presenting the conceptual design of the logic gates, it is important to analyse the overall operational and engineering feasibility. For any logic gate architecture to function it should possess five essential features: Boolean operation, nonlinearity, gain, feedback elimination, and concatenability [21]. The boolean operation feature requires that the logical architecture can perform the basic logical operations such as NAND, AND, OR and NOT operations. This feature has been fully affirmed in the above sections that present conceptual designs of the NAND, AND, NOR, OR, NOT and FAN-OUT gates.

As for 'nonlinearity' to be achieved, the input signals should be of a digital nature where each state is completely discrete from the other binary state and does not show any intermediate analogue-like state between the different binary signals. This feature is present naturally in the

chirality-based logic architecture in which the VDWs can have either CW or ACW chirality with no intermediate states.

As for the 'gain' to be achieved, it is required that the power running the gates should not be supplied by the input signal; instead, it should be supplied by an external independent power source. This ensures that the signal does not decay as it propagates across cascaded gates. In the chirality-based architecture, the power supply is provided by an external magnetic field that is used to propagate the input signals. The FAN-OUT demonstrates a good example of this, as an input signal was duplicated in the two output by the application of an external magnetic field.

For 'feedback elimination', it is essential that the output signal is determined by the input signal and not vice-versa. In other words, the output signal should not affect the input signal. This can be achieved in the chirality-based logic by ensuring that the DWs propagate unidirectionally from the input to the output channel by proper control of the applied magnetic field. Similarly, it is important to innovate a technique that will ensure unidirectional propagation of DWs as they enter the next cascaded gate. One method to do that is by trapping the DWs at orthogonal sections of nanowire that would require a transverse field to move the DW before continuing its propagation. This method can also be used to synchronise the propagation of DWs coming from different output channels and entering the same multi-input gate. Figure 9.8 shows a schematic of how pulses of vertical and forward fields can be used to connect DWs in a unidirectional manner. However, care should be taken when designing the bend angle in order to prevent chirality rectification as discussed in chapter 8.
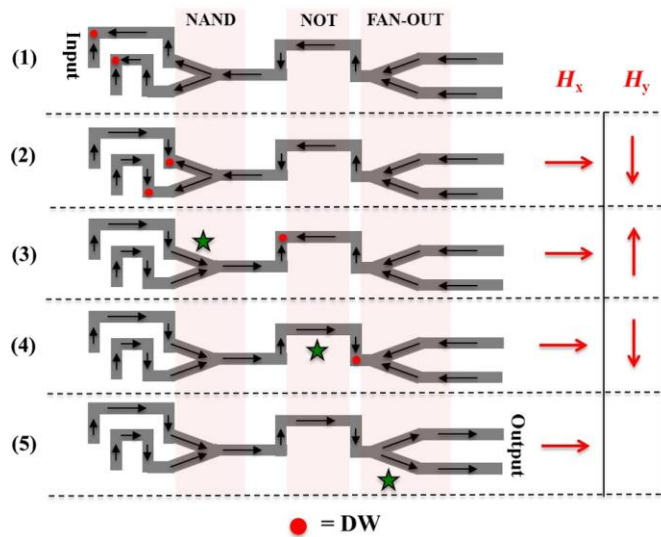
Figure 9.8: Schematic diagram depicting how a pair of DWs could be propagated through NAND, NOT, and FAN-OUT gates separated by vertical nanowire sections. Pulse along H_x and H_y can be used to propagate DW to the next. The star-shaped symbols indicate the points in the sequence where each gate has performed its operation

Other methods that could be used would be to either include features that induce "ratchet-like" movement of DWs as demonstrated in [8], or to introduce DW diode features [22, 23] that would prevent backward propagation of DWs. Furthermore, one could also employ a vertical bar perpendicular to the output channel that would act as a controllable pinning site [24] or switchable gate [11] to control the unidirectional movement of DWs.

Finally for the concatenability feature, the logic gate architecture should allow for multiple gates to be cascaded together; such that the output of one gate could be cascaded with the input of the next channel. Fundamentally, this can only be achieved if the output signal and the input signal are of the same type. In the chirality-based logic gate both input and output are VDWs. More practical concerns regarding the synchronisation of DWs passing through multiple gates have already been explored in the preceding paragraphs where 'feedback elimination' was described. Additionally, a simulation was performed for a cascaded NAND and NOT gate pair to verify that the principle of simple gate chaining can work. Figure 9.9 shows the successful simulation results.

NAND GATE   **NOT GATE**

Input1: ACW
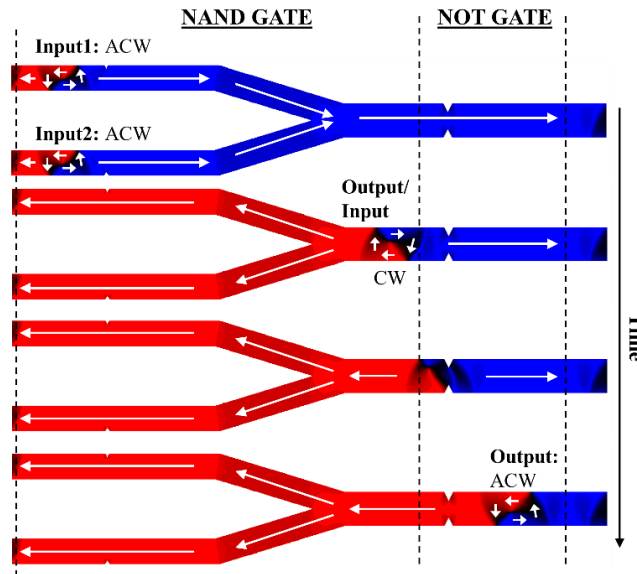Input2: ACW
Output/Input
CW
Output: ACW
Time

Figure 9.9: Micromagnetic simulation showing the feasibility of cascading NAND gate with a NOT gate by directly connecting the output of the NAND gate to the input of the NOT gate. This can be generalized for AND, OR, and NOR gates. Total simulation time was ~130ns.

9.5.1. Design and implementation challenges

While the simulation study indicated a promising conceptual design of the chirality-based logic gates, there exist few important challenges that would need to be tackled in order for a successful practical implementation to be achieved. These challenges are related to stochasticity, fabrication limitations, read/write methods and clock speed.

In most data storage and processing nanomagnetic application, switching stochasticity remains a critical problem. Stochasticity can arise due to both thermal activation [25] and dynamical DW transformations [26, 27]. Thermal activation can play a role in assisting the depinning of DWs when pinned at engineered notches. This can result in violating the inequality condition and disrupting the arrival sequence needed to ensure correct functioning of the gate. Although the thermal effects have not yet been investigated for the proposed logic geometry, as simulation were performed at 0 K, the study conducted in Chapter 6 suggested that thick nanowires (around 40nm) are less susceptible to thermal energy. Moreover nanowires with small widths are expected to have low susceptibility to thermal activation as they have relative high coercivity and bigger pinning energy barriers.

244

As for dynamically induced stochasticity, WB can result in flipping the chiralities of VDWs as they propagate through the nanowires. This can destroy the carried information and so disrupt the function of the logic gates. Therefore, suppressing WB in such applications is essential. In the simulation study, a high damping factor $\alpha = 0.5$ was used to achieve this. Such values have been experimentally demonstrated for Py nanowires by doping it with rare-earth materials [16, 17], thus indicating the possibility of stabilising VDW chirality in logic gates. Moreover, it was observed in the previous studies (Chapter 6) and in reported literature [19] that certain nanowire geometries can preserve VDW chirality even when WB occurs. Therefore, it can be argued that with proper nanowire design, problems relating to stochasticity can be circumvented.

As for problems related to fabrication limitations, it was shown that the function of the chirality-based logic gates depends strongly on the accurate fabrication of the notches that will control the arrival sequence of the DWs. The differences in notch sizes presented in Figure 9.6 for the NAND gate (and AND, OR, NOR gates as they use the same design but with different notch location) are small (around 5 nm) and it would be difficult in reality to obtain such high fabrication resolution. However, these small notches were used only as a 'proof of concept', and any alternative pinning method that would yield the desired arrival sequence of DWs (by satisfying the inequalities) is expected to produce the same function. Therefore, this limitation can be overcome by engineering pinning sites that can satisfy the desired arrival sequence.

As for writing data, it is important that a method to nucleate VDWs with desired chirality be devised. Several methods of controllable injection have been previously suggested, such as using current pulses in tilted strip lines above nanowires [28] or inserting an asymmetric notch below a strip line and controlling DW chirality by varying the current amplitude [19]. Moreover asymmetric nucleation pads can be used for controlled field induced nucleation [29].

On the other hand, reading data requires detection of VDW chirality. One method to achieve this is through sensing the stray field of the VDW and determining its chirality accordingly. This method has been proposed and simulated by Bashir *et al* [30] but has not yet been experimentally verified, although other experiments that detected the stray field of transverse DWs have been performed [31, 32]. Another method proposed by Moriya *et al* [33] can detect the chirality of a trapped DWs by measuring the nanowire resistance after resonantly exciting the DW with a spin-polarized AC current or a magnetic field. The resistance of the resonating VDW reflects the polarity and chirality of VDW.

Finally with regard to the speed at which such gates can switch, a preliminary study has been conducted to investigate if the gates can function at a competitive clock speed of 100 MHz. Therefore, instead of performing quasi-static simulation, the applied field was set to increase to the maximum field in 10 ns and then held constant. All the logic gates functioned well; however, minor modifications to the design of the FAN-OUT were needed in order to suppress any erroneous DW nucleation that occurred at the junction (refer to Figure a3.2 in Appendix 3.2 for simulation snapshots). Figure 9.10 shows the modification made. The time needed to duplicate the DW in the FAN-OUT was 20 ns. As for the NAND gate, the time for full functioning was only 10 ns when the maximum field was set to be at 350 Oe (to prevent further anomalous dynamical transformations of DWs). The NOT gate functioned very smoothly even with a DC magnetic field with a functioning time of 10 ns. Therefore, it can
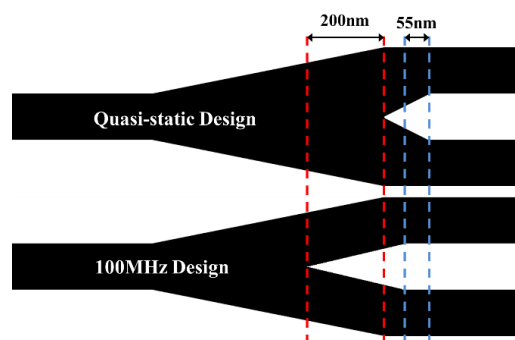

Figure 9.10: Schematic showing the design modification done for the FAN-OUT junction to prevent erroneous nucleation when performing at 100 MHz clock speed.

be concluded that the chirality-based logic-gates can function with a clock speed of 50-100 MHz if optimized properly.

9.6. Experimental verification of chirality-based logic gates

9.6.1. FAN_OUT gate

After performing the simulation study, a modest attempt has been made to fabricate and test the FAN-OUT gate using MTXM technique at the Advanced Light Source lab at Lawrence Berkeley Labs in USA.

In order to obtain good image contrast, the nanowires were designed to have a widths of 400nm and a total length of 17 µm. The input of the FAN-OUT was attached to a 5 x 5µm^2 nucleation pad, and double notches were designed at the output nanowires to pin the output DWs for imaging.

In the first attempt, the sequence of switching of the output channels was checked. Interestingly, it was found that half of the junction, then output 1 (top input) switched first before output 2 was switched. This can be inferred from Figure 9.11(a). This switching
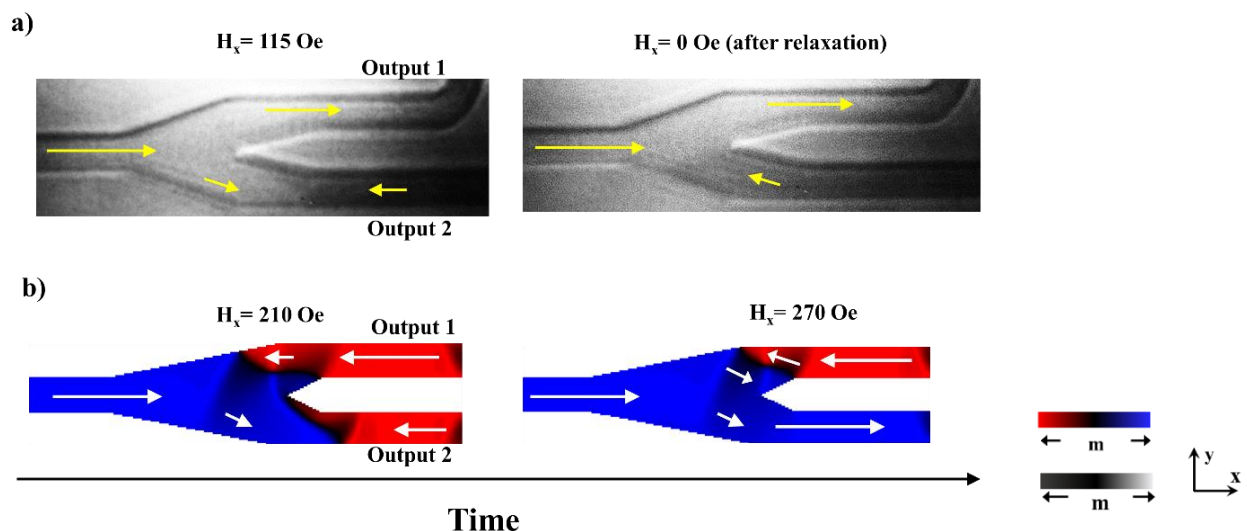

Figure 9.11: (a): MTXM image showing FAN-OUT output 1 switched and DW pinned unction when stretched at H$_x$= 115 Oe (left) and when relaxed (right). (b): Simulation snapshot showing DW at Hx= 210 (left) and at Hx = 270 Oe with output 2 being switched.

sequence was opposite to that occurring in the simulation where output 2 switched before output 1 (Figure 9.11(b)). This change in sequence is not expected to change the behaviour of the FAN-OUT gate. However, what was important was to ensure that the pinning/depinning of the DW occurs correctly between the apex of the junction and the output corner. Figure 9.11(a) seems to indicate promising results similar to the simulated snapshot below it. This image was taken while H_x was applied at 115 Oe, and the DW formed was not in its relaxed state. Therefore, in order to ensure that the DW is in fact pinned at the apex of the junction, the applied field was removed and the DW was left to relax before taking another image. Figure 9.11(b) clearly indicates that the DW was pinned at the apex before stretching toward output 2 indicating correct precursor state for this DW.

The next step was to image the two VDWs at output 1 and 2. At first (before discovering the role of the sharp bend in rectifying DWs) sharp bends were used to trap the DWs. However, all the output signals showed erroneous results mostly with filtered DWs. Another design was needed to trap the VDWs, and a decision was made to use deep double notches. Hence, in this second attempt, the same design of the FAN-OUT was fabricated but this time double notches were used to trap the DWs instead of a bend. The input DW was nucleated using a nucleation pad and was propagated towards the output nanowire channels. Some of the results are shown in Figure 9.12.
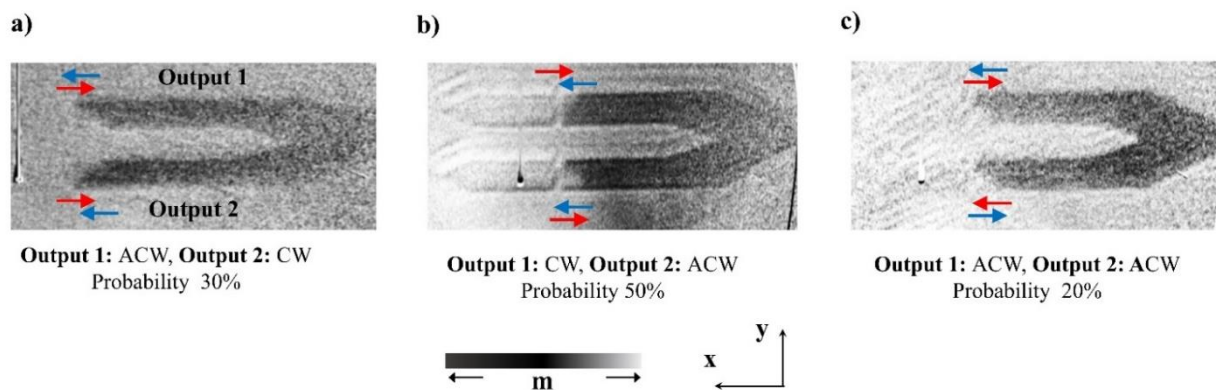

Figure 9.12: SEM images of FAN-OUT gate showing output results. (a): Output 1 with ACW and Output 2 with CW occurred 30% of the time. (b): Output 1 with CW and Output 2 with ACW occurred 50% of the time. (c): Output 1 with ACW and Output 2 with ACW occurred 20% of the time.

The results did not show a successful duplication of the VDW. Eight out of the ten attempts showed opposite VDW chiralities at the output. Such a high percentage of opposite VDW chirality would suggest a form of coupling which might occur between the two outputs due to the close vertical distance between the two nanowires (around 400nm, which is close to the output nanowire width). Therefore, it is important to have a widely separated nanowire inputs of a distance of at least 2xW clearance distance in order to ensure that there are no coupling induced.

9.6.2. Future work

For the NOT gates, since the double notches are required to be deep in order to produce strong pinning, it might be difficult to introduce a strong trapping site after the deep double notches. This is because the high depinning field needed to depin the VDW will be sufficient to dynamically pass the DWs through the second trapping site. Therefore, a different pinning method would be needed to trap the output VDWs in the NOT gate. One of the proposed idea to circumvent this problem is to fabricate a current-pulse strip line above the double notches, and to use the short pulsed localised field generated by the current pulses in order to depin the VDW through the double notch without using the external field. The depinned VDW can then be pinned again at any pinning site by applying small propagating field. Another idea would be to use nanobar strip placed perpendicularly above the secondary pinning site (on the same plane), in order to assist it in pinning of the VDW by using the nanobar's stray field [24].

As for the NAND, AND, OR and NOR gates, in order to verify their functionality in the future, it is important to first verify their working principle, that is, the dependence of the output VDW on the arrival sequence of the DW from the top and bottom input channels. This can be done by designing a Y-shape interconnected network of nanowires and propagating DWs in each input at a different time interval using perpendicular pulse currents, or by introducing a notch

at one of the channels and injecting DWs using nucleation pads. In both cases, the verification of the functionality of the chirality-based logic gate depends essentially on the verification of the output dependence on the arrival sequence of the VDWs to the junction. If the latter works fine, then any pinning site or method that can satisfy each gate inequality (Table 9.3) can be introduced to the design and is expected to create a functioning logic gate.

9.7. Conclusion

The simulations presented in this chapter propose a logic architecture that uses the chirality of VDWs as an additional degree of freedom to process information. This chirality-based logic has the feature of having a relatively simply architecture with straight or horizontal Y-shaped network of nanowires with engineered pinning sites. For instance, the NOT gate works simply by exploiting the DW/double notch depinning behaviour. The FAN-OUT gate exploits the propagation feature of VDWs in wide junction (in Y-shaped interconnected nanowires), in order to bias the nucleation of a second nucleated VDW to have the same chirality as the first VDW. The NAND, AND, NOR and OR gates function by manipulating the arrival sequence of DWs by exploiting chirality-sensitive pinning sites and the propagation feature of a 2-in-1-out junction.

Our proposed logic gates [34] resemble the first proposed architecture where chiral information is used in processing data. Recent publications [14, 35] demonstrated simulation studies that suggested the feasibility of chirality-based logic gates in TDWs, one of which was made in comparison to our VDW logic gate [14].

Despite the lack of a "cross-over" architecture, the NAND, AND, NOR, OR, NOT and FAN-OUT chirality-based gates studied have the potential to build complicated logic operations. Although challenges in suppressing stochasticity, innovating a reading/writing method, and building gates that perform at competitive clock speed still exist, there are several proposed

solutions to overcome these limitations, and a lot of room for optimization. For instance,

chapter 6 and 7 provide essential results that may be used to solve the stochasticity challenge.

9.8. References

[1] C. Liu, M. Östling, and J. Hannon, "New materials for post-Si computing," *MRS bulletin,* vol. 39, pp. 658-662, 2014.

[2] J. F. Gregg, "Spintronics: A growing science," *Nature materials,* vol. 6, pp. 798-799, 2007.

[3] S. Wolf, D. Awschalom, R. Buhrman, J. Daughton, S. Von Molnar, M. Roukes, *et al.*, "Spintronics: a spin-based electronics vision for the future," *Science,* vol. 294, pp. 1488-1495, 2001.

[4] S. Parkin and S.-H. Yang, "Memory on the racetrack," *Nature nanotechnology,* vol. 10, pp. 195-198, 2015.

[5] I. M. Miron, T. Moore, H. Szambolics, L. D. Buda-Prejbeanu, S. Auffret, B. Rodmacq, *et al.*, "Fast current-induced domain-wall motion controlled by the Rashba effect," *Nature Materials,* vol. 10, pp. 419-423, 2011.

[6] Y. Nakatani, A. Thiaville, and J. Miltat, "Faster magnetic walls in rough wires," *Nature materials,* vol. 2, pp. 521-523, 2003.

[7] S. S. Parkin, M. Hayashi, and L. Thomas, "Magnetic domain-wall racetrack memory," *Science,* vol. 320, pp. 190-194, 2008.

[8] J. Franken, H. Swagten, and B. Koopmans, "Shift registers based on magnetic domain wall ratchets with perpendicular anisotropy," *Nature nanotechnology,* vol. 7, pp. 499-503, 2012.

[9] R. Lavrijsen, J.-H. Lee, A. Fernández-Pacheco, D. C. Petit, R. Mansell, and R. P. Cowburn, "Magnetic ratchet for three-dimensional spintronic memory and logic," *Nature,* vol. 493, pp. 647-650, 2013.

[10] D. Allwood, G. Xiong, M. Cooke, C. Faulkner, D. Atkinson, N. Vernier, *et al.*, "Submicrometer ferromagnetic NOT gate and shift register," *Science,* vol. 296, pp. 2003-2006, 2002.

[11] S. Breitkreutz, G. Ziemys, I. Eichwald, J. Kiermaier, G. Csaba, W. Porod, *et al.*, "Domain wall gate for magnetic logic and memory applications with perpendicular anisotropy," in *Electron Devices Meeting (IEDM), 2013 IEEE International*, 2013, pp. 22.4. 1-22.4. 4.

[12] C. C. Faulkner, D. Allwood, M. D. Cooke, G. Xiong, D. Atkinson, and R. P. Cowburn, "Controlled switching of ferromagnetic wire junctions by domain wall injection," *Magnetics, IEEE Transactions on,* vol. 39, pp. 2860-2862, 2003.

[13] D. A. Allwood, G. Xiong, C. Faulkner, D. Atkinson, D. Petit, and R. Cowburn, "Magnetic domain-wall logic," *Science,* vol. 309, pp. 1688-1692, 2005.

[14] J. Vandermeulen, B. Van de Wiele, L. Dupré, and B. Van Waeyenberge, "Logic and memory concepts for all-magnetic computing based on transverse domain walls," *Journal of Physics D: Applied Physics,* vol. 48, p. 275003, 2015.

[15] *Object Orientated Micromagnetic Framework (OOMMF)* Available: http://math.nist.gov/oommf/.

[16] W. Bailey, P. Kabos, F. Mancoff, and S. Russek, "Control of magnetization dynamics in Ni 81 Fe 19 thin films through the use of rare-earth dopants," *Magnetics, IEEE Transactions on,* vol. 37, pp. 1749-1754, 2001.

[17] G. Woltersdorf, M. Kiessling, G. Meyer, J.-U. Thiele, and C. Back, "Damping by Slow Relaxing Rare Earth Impurities in Ni 80 Fe 20," *Physical review letters,* vol. 102, p. 257602, 2009.

[18] T. Hayward, M. Bryan, P. Fry, P. Fundi, M. Gibbs, D. Allwood, *et al.*, "Direct imaging of domain-wall interactions in Ni 80 Fe 20 planar nanowires," *Physical Review B,* vol. 81, p. 020410, 2010.

[19]   A. Pushp, T. Phung, C. Rettner, B. P. Hughes, S.-H. Yang, L. Thomas, *et al.*, "Domain wall trajectory determined by its fractional topological edge defects," *Nat Phys,* vol. 9, pp. 505-511, 08//print 2013.

[20]   M. Hayashi, L. Thomas, C. Rettner, R. Moriya, X. Jiang, and S. S. P. Parkin, "Dependence of current and field driven depinning of domain walls on their structure and chirality in permalloy nanowires," *Physical Review Letters,* vol. 97, p. 4, Nov 2006.

[21]   B. Behin-Aein, D. Datta, S. Salahuddin, and S. Datta, "Proposal for an all-spin logic device with built-in memory," *Nature nanotechnology,* vol. 5, pp. 266-270, 2010.

[22]   M. Bryan, T. Schrefl, and D. Allwood, "Symmetric and asymmetric domain wall diodes in magnetic nanowires," *Applied Physics Letters,* vol. 91, p. 142502, 2007.

[23]   A. Himeno, S. Kasai, and T. Ono, "Depinning fields of a magnetic domain wall from asymmetric notches," *Journal of applied physics,* vol. 99, p. 08G304, 2006.

[24]   S.-M. Ahn, K.-W. Moon, C.-G. Cho, and S.-B. Choe, "Control of domain wall pinning in ferromagnetic nanowires by magnetic stray fields," *Nanotechnology,* vol. 22, p. 085201, 2011.

[25]   C. Wuth, P. Lendecke, and G. Meier, "Temperature-dependent dynamics of stochastic domain-wall depinning in nanowires," *Journal of Physics: Condensed Matter,* vol. 24, p. 024207, 2012.

[26]   U.-H. Pi, Y.-J. Cho, J.-Y. Bae, S.-C. Lee, S. Seo, W. Kim, *et al.*, "Static and dynamic depinning processes of a magnetic domain wall from a pinning potential," *Physical Review B,* vol. 84, p. 024426, 2011.

[27]   M.-Y. Im, L. Bocklage, P. Fischer, and G. Meier, "Direct observation of stochastic domain-wall depinning in magnetic nanowires," *Physical review letters,* vol. 102, p. 147204, 2009.

[28]   K. Sentker, F.-U. Stein, L. Bocklage, T. Matsuyama, M.-Y. Im, P. Fischer, *et al.*, "Fast generation of domain walls with defined chirality in nanowires," *Applied Physics Letters,* vol. 104, p. 172404, 2014.

[29]   D. McGrouther, S. McVitie, J. Chapman, and A. Gentils, "Controlled domain wall injection into ferromagnetic nanowires from an optimized pad geometry," *Applied physics letters,* vol. 91, p. 022506, 2007.

[30]   M. Bashir, M. Bryan, D. Allwood, T. Schrefl, J. Claydon, G. Burnell, *et al.*, "Remote domain wall chirality measurement via stray field detection," *Journal of Applied Physics,* vol. 110, p. 123912, 2011.

[31]   S. Bowden and J. Unguris, "Field-driven sense elements for chirality-dependent domain wall detection and storage," *Journal of Applied Physics,* vol. 114, p. 223904, 2013.

[32]   L. O'Brien, A. Beguivin, A. Fernandez-Pacheco, D. Petit, D. Read, and R. Cowburn, "Magnetic domain wall induced, localized nanowire reversal," *Applied Physics Letters,* vol. 101, p. 062415, 2012.

[33]   R. Moriya, L. Thomas, M. Hayashi, Y. B. Bazaliy, C. Rettner, and S. S. Parkin, "Probing vortex-core dynamics using current-induced resonant excitation of a trapped domain wall," *Nature physics,* vol. 4, pp. 368-372, 2008.

[34]   K. Omari and T. Hayward, "Chirality-based vortex domain-wall logic gates," *Physical Review Applied,* vol. 2, p. 044001, 2014.

[35]   H. K. Teoh, G. Sarjoosing, and W. S. Lew, "Programmable logic operation via Domain Wall Profile Manipulation."

Chapter 10:

Conclusion

In this thesis dynamically-induced stochastic VDW pinning/depinning behaviours have been studied in nanowires both with and without artificial defects sites using experimental measurements and micromagnetic modelling. The results and methodologies presented combine to create a comprehensive understanding of stochastic DW behaviours in Py nanowires, and have allowed a number of methods to mitigate this stochasticity to be proposed. Moreover, a new method to rectify the chiralities of VDWs, and a conceptual design for a full chirality-based VDW logic architecture, have also been proposed

In Chapter 5 quasi-static micromagnetic simulations were initially used to attempt to identify nanowire/notch geometries that would exhibit single-mode depinning field distributions. However, experimental measurements indicated complex and stochastic pinning/depinning behaviours even for these nominally promising systems. This stochasticity was attributed to a combination of DWs undergoing WB transformations, and complex interactions between the DWs and the defect sites. A modest decrease in VDW stochasticity was observed under the influence of transverse field; however, complete suppression of stochasticity did not result, and single-mode depinning was not achieved. It was suggested that transverse field reduced the observed stochasticity by 'locking' the VDW into a single state for longer periods of time during its WB transformations.

To further understand the complexity of VDWs depinning behaviour, and to search for a single-mode depinning system, systematic study of the roles of thickness and pinning site geometry was conducted in Chapter 6. It was concluded that in the vast majority of geometries studied both symmetrical and asymmetrical notches produced stochastic DW pinning/depinning

distributions. A new simulation methodology was created to attempt to understand these results, and this allowed a direct demonstration of how WB transformations can result in stochastic DW behaviours over a large range of notch/nanowire geometries. Interestingly, it was found that deep, asymmetric pinning sites in thick nanowires are a rare example of a geometry that can produce single-mode switching behaviours. It was observed that thick nanowires (t = 40 nm) seemed to produce less DW dynamic stochasticity as WB transformations in such nanowires preserve the vortex shape of the DW, and also thermal perturbation seemed to be less effective in assisting DW depinning in thick nanowires, as the energy barriers presented by defect sites are expected to be larger than those seen in thinner nanowires. The results of this chapter thus contribute to two of the major aims of the thesis i.e. understanding and attempting to mitigate stochastic DW pinning.

In chapter 7 it was shown that, in addition to geometric parameters of the nanowires/defect sites, the method used to nucleate DWs can play a role in the stochasticity of DW pinning/depinning. It was found that a method where DWs were injected using orthogonal current lines seemed to produce more deterministic behaviour than when DWs were injected from a nucleation pad, even in cases where the current line was used to mimic the injection field distribution of the pad. This suggests that pad-based injection is intrinsically stochastic as it is believed that DWs nucleated by nucleation pad may experience different deformation/stretching as they are injected from the pad junction due to different pad magnetisation modes or rough edges at the junction. The different deformation/stretching of DW structure will alter DW motion trajectory and will add an extra element of stochasticity to the switching mechanism. Current-induced nucleation may also allow DW propagation modes that result in lower depinning stochasticity to be selected by propagating DWs at well-defined propagation fields. This is not possible with a pad-based nucleation method. In a further experiment exploiting current-line-based nucleation, it was observed that the average

propagation field measured in a nanowire increased with increasing DW propagating distance. Moreover, it was observed that the switching field distribution increased. Both observations demonstrated the significant role that edge defects play in affecting DW motion. Based on that, for deterministic DW behaviour to be achieved in nanowires, the propagation field should be chosen such that it is sufficient to depin from all edge defects.

In Chapter 8 a further approach that can be used to mitigate the stochasticity of DW pinning/depinning was proposed. Magnetic imaging was used to experimentally demonstrate that sharp nanowire bends in thick nanowires will rectify the chirality of VDWs to either CW or ACW depending on whether the corner turns left or right. Simulations showed that this occurs when the magnetisation of the vertical section of the bend interacts with the spins of the leading edge of a VDW. If both are parallel, propagation may occur smoothly without changing the DW chirality; whereas, if they are anti-parallel, magnetic frustration occurs and a new vortex will be nucleated with rectified chirality, while the original vortex be annihilated. This method allows for rectification of VDWs during propagation, and thus can be used to mitigate stochasticity at defect sites where poor definition of VDW chirality is its primary origin. This was demonstrated experimentally in nanowires where VDWs were passed through a rectifier before pinning at a single, chirality sensitive notch. In these devices single-mode, and thus relatively deterministic, switching behaviours were observed.

In Chapter 9 a chirality-based VDW logic architecture was proposed. A full simulation study was performed, suggesting the feasibility of chirality-based NAND, AND, NOR, OR, FAN-OUT and NOT logic gates. The NAND, AND, NOR and OR logic gates work by exploiting the interaction of two VDWs that merge together in the junction of a 2-in-1-out Y-shaped network of nanowires. The output VDW chirality is determined by the arrival sequence of the VDWs, which is in turn engineered by adding single notches on input channels and exploiting the chirality-dependent notch-DW interactions. FAN-OUT functionality is achieved by

256

propagating VDWs through a 1-in-2-out Y-shaped nanowire junction. The shape of the junction is engineered to allow for DW cloning; such that, the same chirality is cloned to the newly nucleated VDW. The NOT gate works by passing DWs through deep double notches. Here, depinning occurs through DW re-nucleation, and the newly nucleated VDW has an inverted chirality. The chirality-based logic architecture requires further experimental verification, which might require further design optimization (and further control of stochastic effects). Nevertheless, its simplicity, cascadability and relatively competitive speed make it a promising spintronic application. This conceptual spintronic application satisfies the third aim of the thesis.

In the thesis as a whole, it was demonstrated that the problems of DW stochasticity can be circumvented by proper device engineering and through understanding and exploiting the interactions between DWs and defects. With further development along these lines ferromagnetic nanowires may therefore yet prove to be reliable for creating new spintronic technologies.

Appendix

Appendix 1

GMR and TMR effect

The GMR effect is realized when current passes through a tri-layer (or multilayer) structure composed of a thin layer (spacer) of non-magnetic conducting material sandwiched between two ferromagnetic materials. When electrons pass through a polarized magnetic material, they experience different levels of scattering depending on the electron spin. The difference in scattering arises from the imbalance in the density of states (DOS) between the spin-up and spin-down electrons in ferromagnetic materials at the Fermi level.

Electrons passing through the first ferromagnetic layer become spin polarised [1]. As the spin-polarized current flows through the non-magnetic material and into the second ferromagnetic layer, the same process of spin-polarization occurs. Hence, if the two layers have parallel magnetisation, the current will flow through them with low resistance. However, if the layers have anti-parallel magnetisation alignment, the electrons will face significant scattering, resulting in high magnetoresistance (MR) [1]. The GMR value can reach up to 10% at room temperature [2], and is calculated by the expression [3]:

$$\text{MR} = \frac{R_{AP} - R_P}{R_P} \qquad \text{(eq A.1)}$$

Where R_{AP} and R_P are the electric resistance when ferromagnetic layers are anti-parallel and parallel, respectively. This layered structure is known as spin-valve.

Alternatively, if the spacer layer was replaced with an insulator ~1 nm thick, spin-polarized electrons can tunnel across the insulator barrier. If magnetisation of both ferromagnetic layers are parallel, then the majority of spins at the DOS of the first ferromagnetic layer will tunnel

to the DOS of majority spins in the second ferromagnetic layer. However, if the magnetisation of the ferromagnetic layers are anti-parallel, then the majority of spins in the first layer will tunnel to the DOS of minority spins of the second layer. Because conductance is proportional to the product of DOS of both ferromagnetic materials, then the tunnelling magneto resistance (TMR) is higher when the magnetisation of the two layers are anti-parallel [4]. The TMR effect can be used to build a magnetic tunnel junction (MTJ) device that is analogous to the spin-valve that uses GMR effect. In the MTJ, the MR ratio can reach up to 500% at room temperature [5] having a major advantage over spin-valves.

Usually, in the spin-valve and MTJ, one ferromagnetic layer is pinned using an anti-ferromagnetic material, while the other ferromagnetic layer can freely change its magnetisation along its long axis when a field is applied. Hence, the MTJ and the spin-valve can not only sense magnetisation, but also store magnetisation at the free layer. Using this feature, the MTJ and the spin-valve can be used as a magnetic storage bit [2].

a)

d)

b)

e)

c)

f)
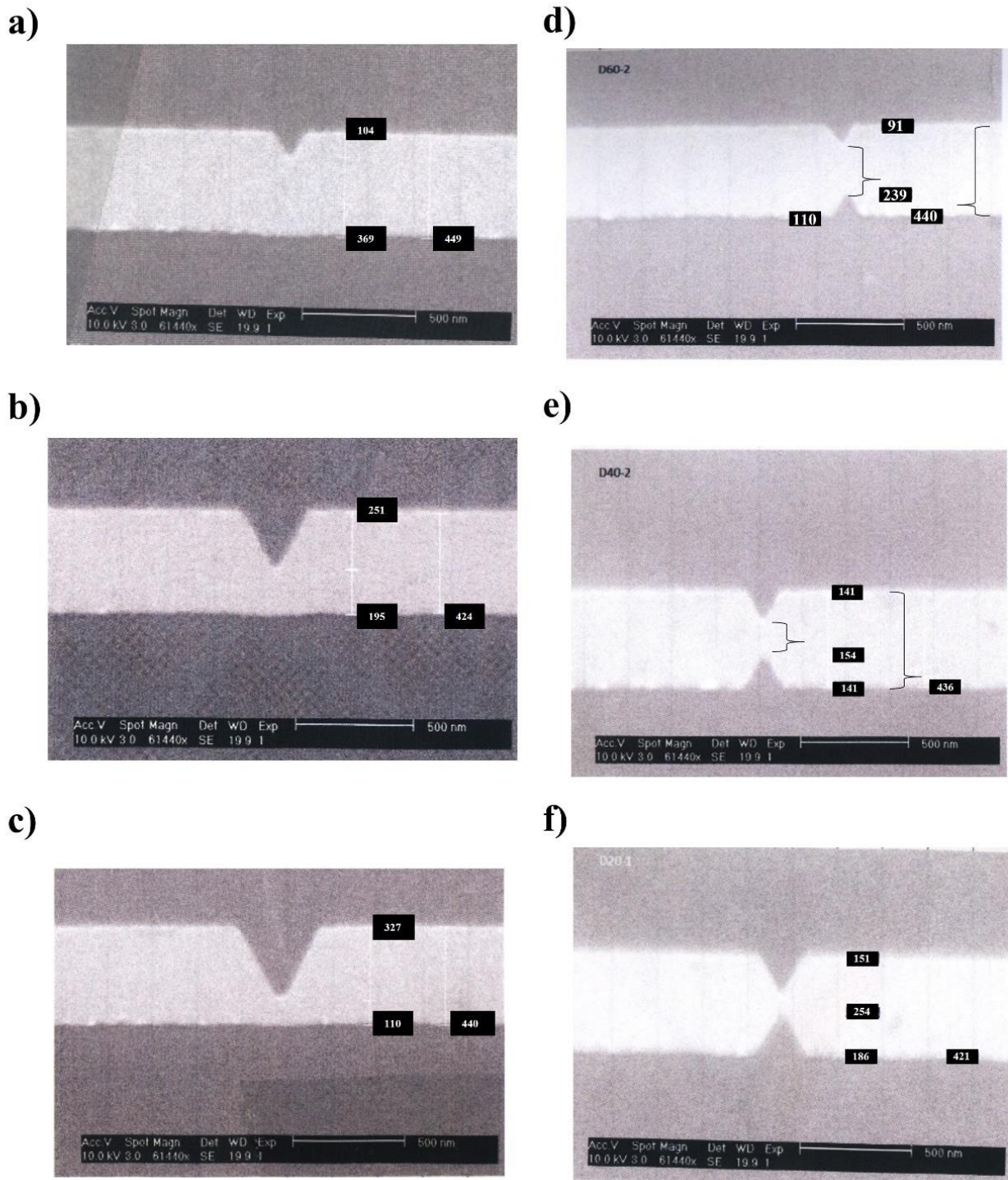
Figure a2.1: SEM images of nanowires with t=10nm. Single notch of N_d= 0.25W (a), 0.55W (b) and 0.75W (c). Double notch of N_d= 0.2W (d), 0.3W (e), 0.35W (f)

Appendix 2.2
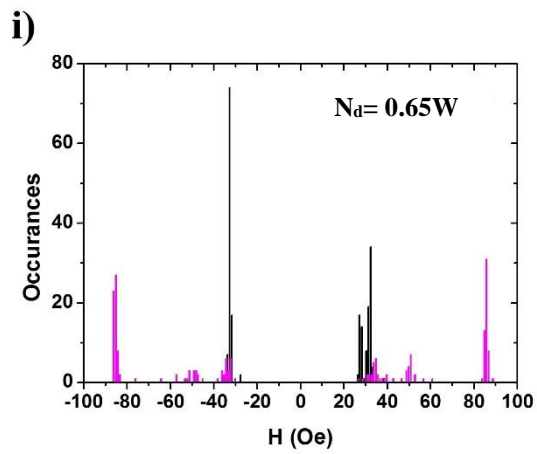
i)

$N_d = 0.65W$

j)

$N_d = 0.75W$
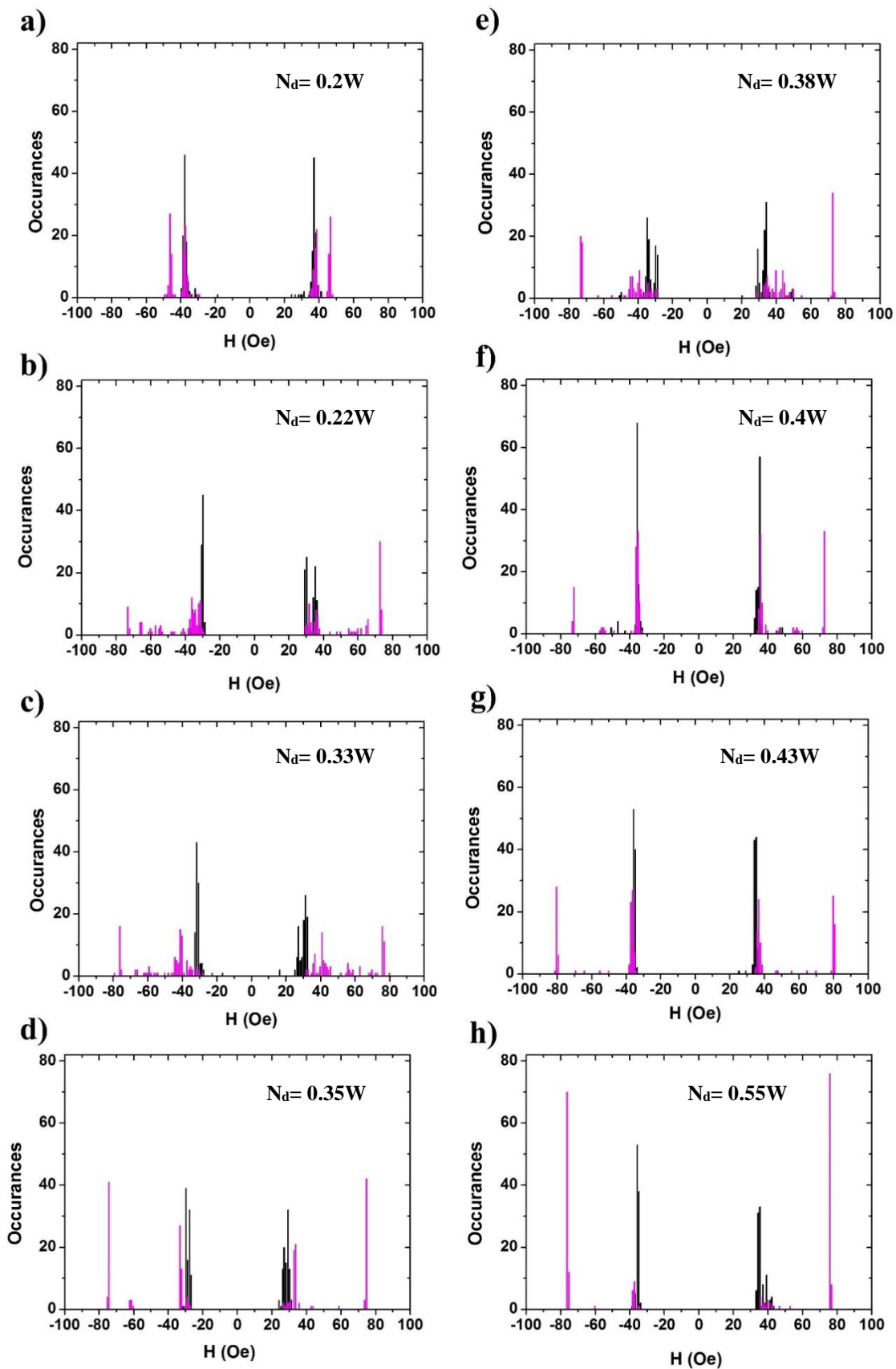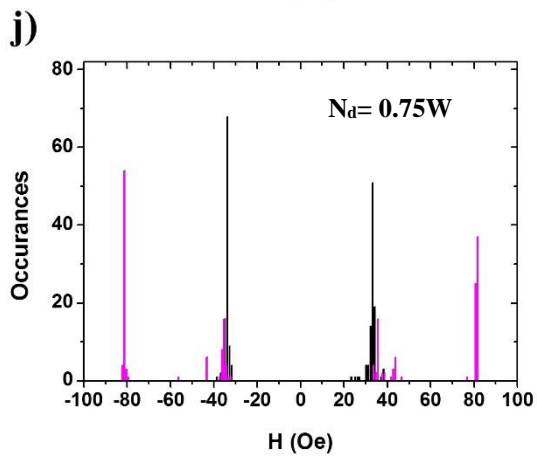
Figure a2.2: Histograms showing 100 single-shot measurements of the switching behaviour for nanowires of t=10 nm and single notch defect. 100 single shots measurements were taken using MOKE.
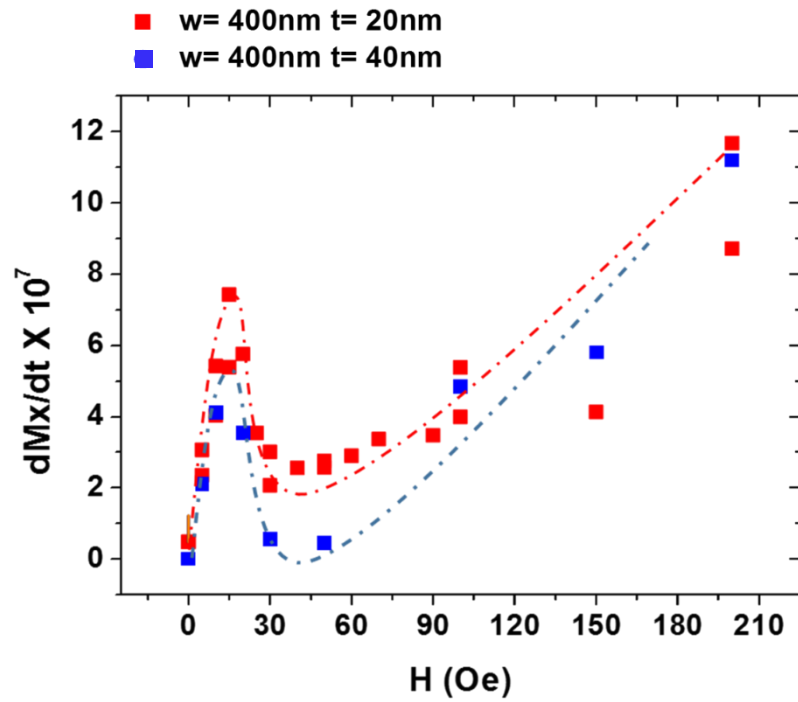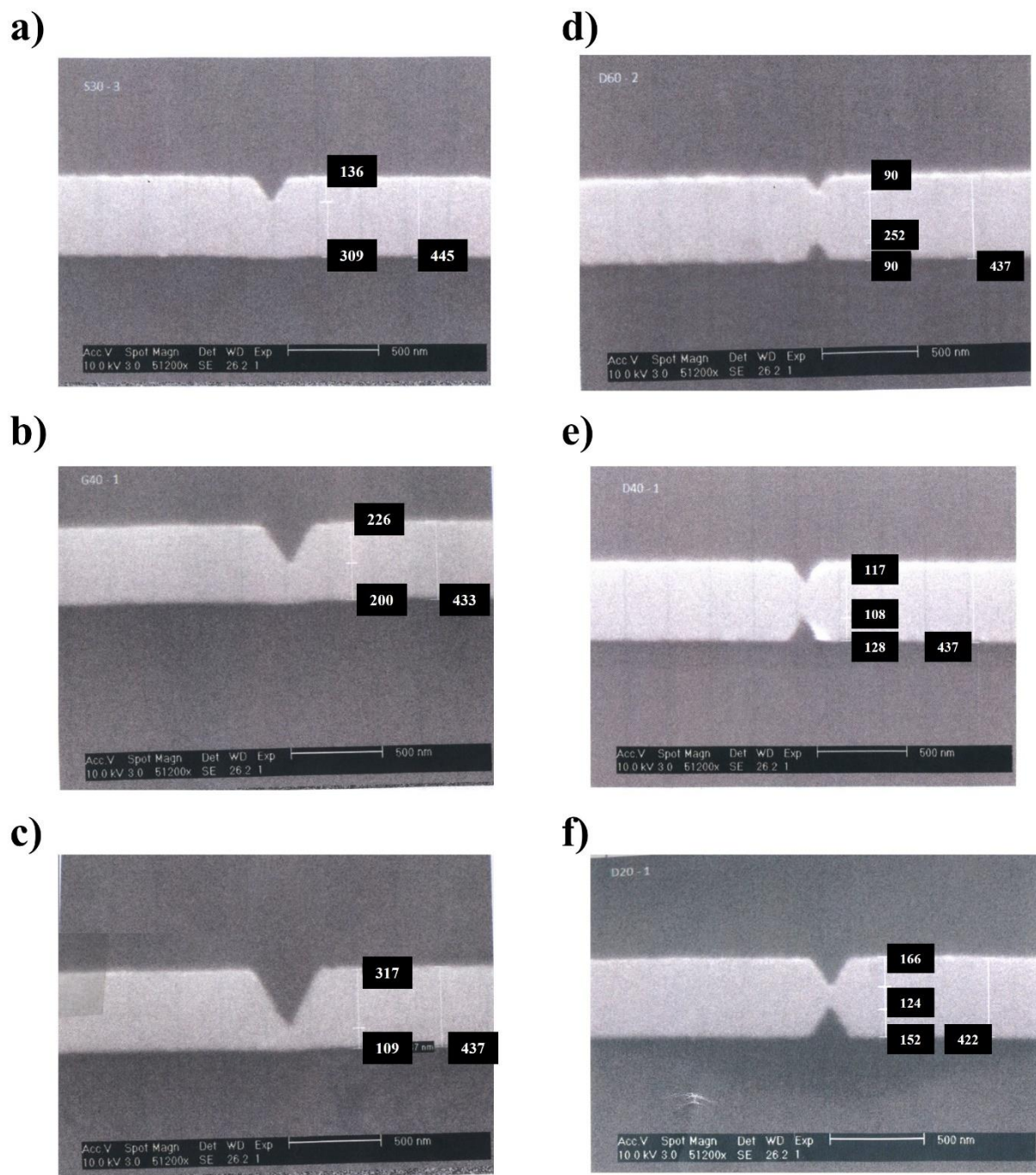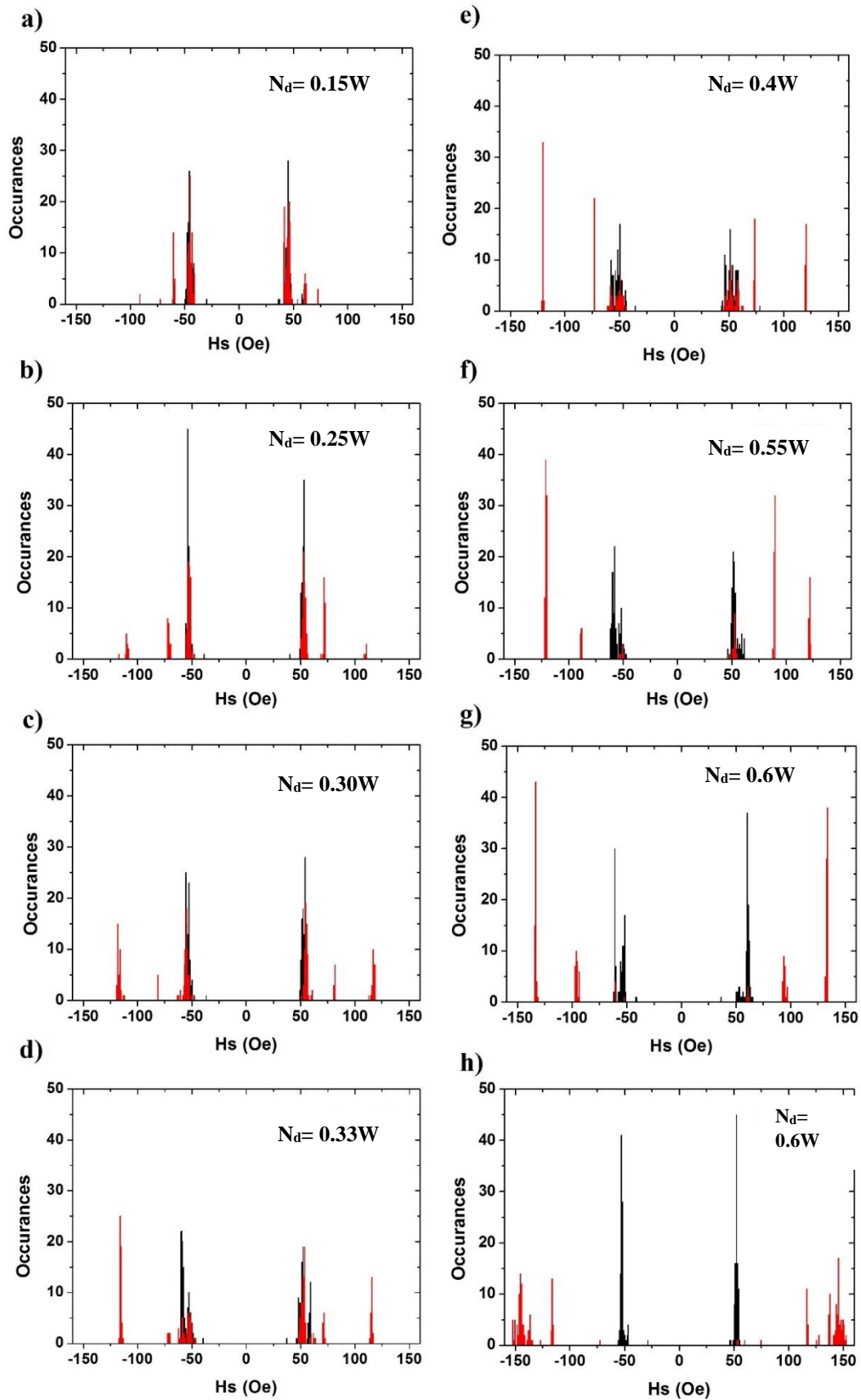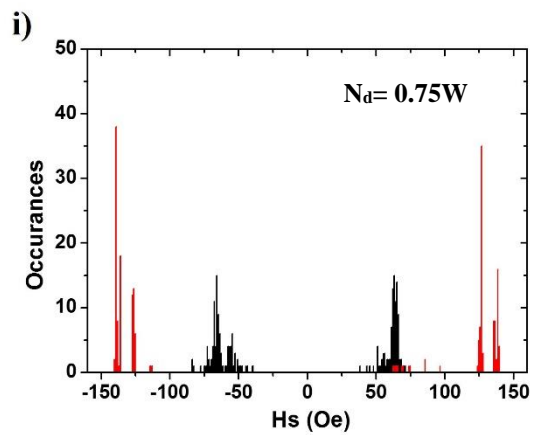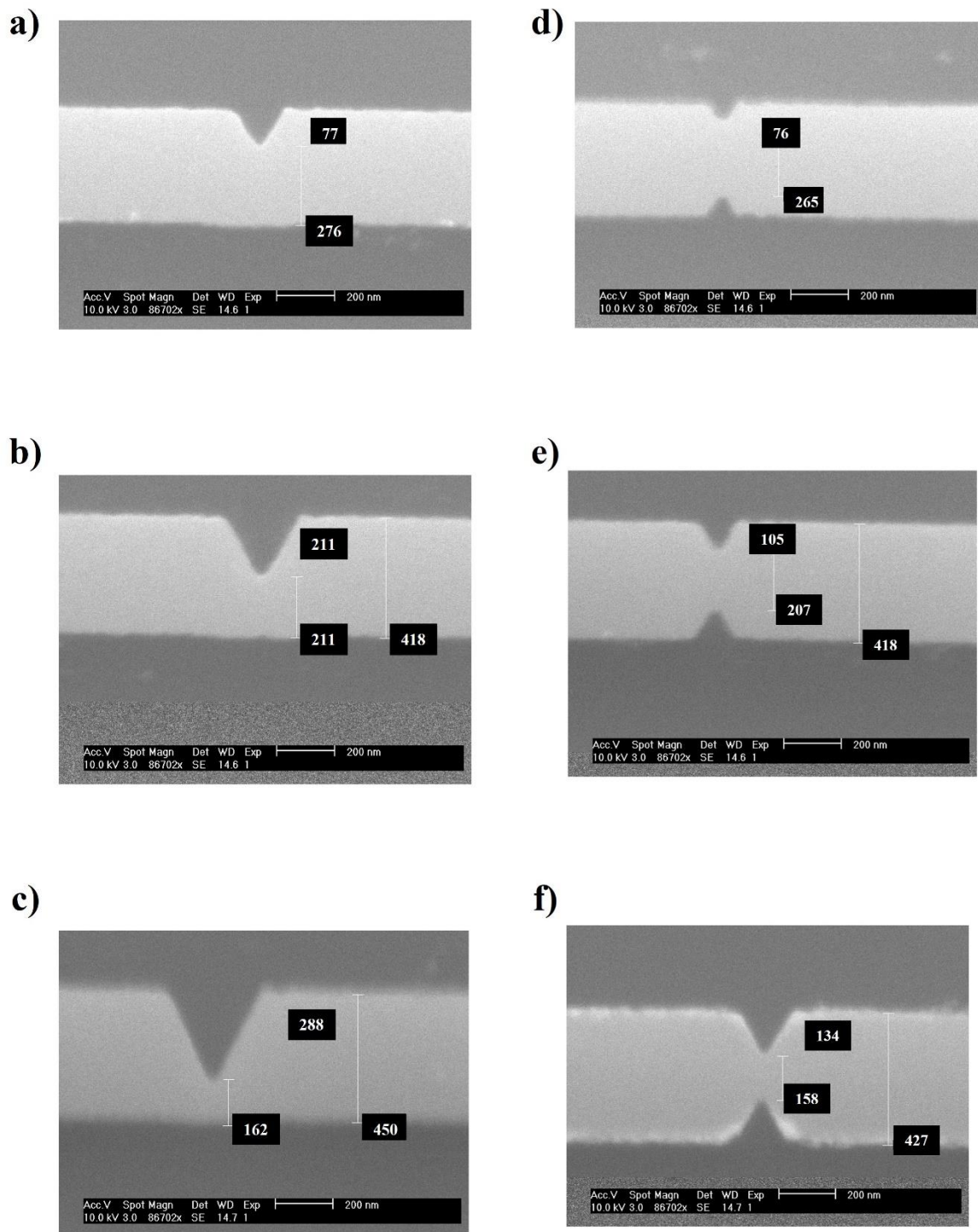
Appendix 2.3

Figure a2.3: Rate of change of Mx over time for nanowire 400x8000 nm² of t=20nm (red) and t=40 nm (blue). H$_{WB}$ is estimated at 22 Oe for t=20 nm and 15Oe for t=40nm, turbulent regime is estimated to start at 45 Oe. Dashed line is only a guide for the eye.

Appendix 2.4

Figure a2.4: SEM images of nanowires with t=25 nm. Single notch of N_d= 0.3W (a), 0.5W (b) and 0.7W (c). Double notch of N_d= 0.2W (d), 0.25W (e), 0.4W(f)
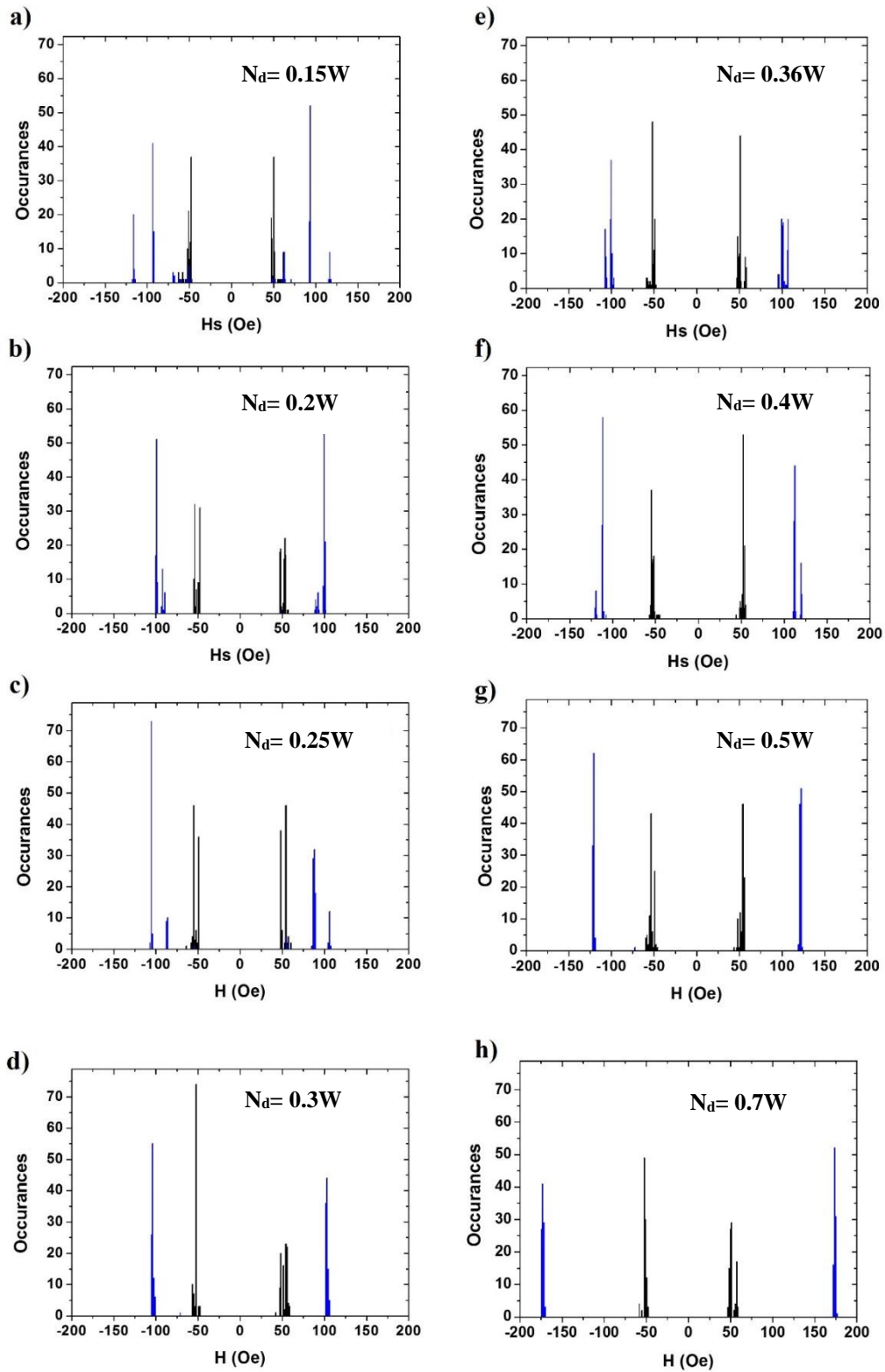
Appendix 2.5

i)

Figure a2.5: Histograms showing 100 single-shot measurements of the switching behaviour for nanowires of t=25 nm and single notch defect. 100 single shots measurements were taken using MOKE.

Figure a2.6: SEM images of nanowires with t=40 nm. Single notch of N_d= 0.18W (a), 0.5W (b) and 0.7W (c). Double notch of N_d= 0.18W (d), 0.25W (e), 0.33W(f)

Figure a2.7: Histograms showing 100 single-shot measurements of the switching behaviour for nanowires of t=40 nm and single notch defect. 100 single shots measurements were taken using MOKE.
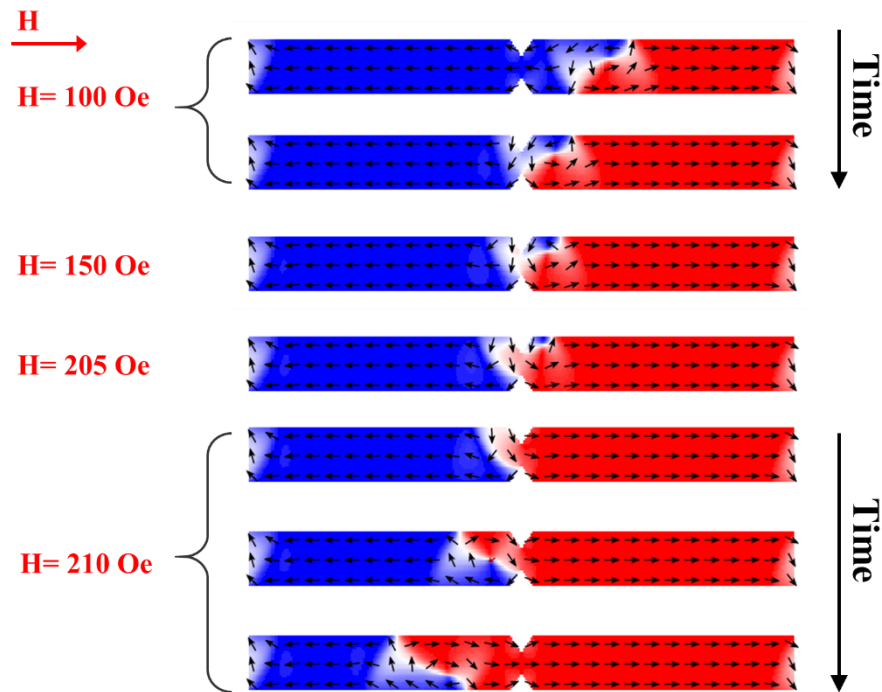
Appendix 3.1

Figure a3.1: Micromagnetic simulation snapshots for NOT gate showing the inversion process in t=26 nm at the boundary of the inversion regime. Nanowire is of w= 150 nm, N_d= Nw= 50 nm.
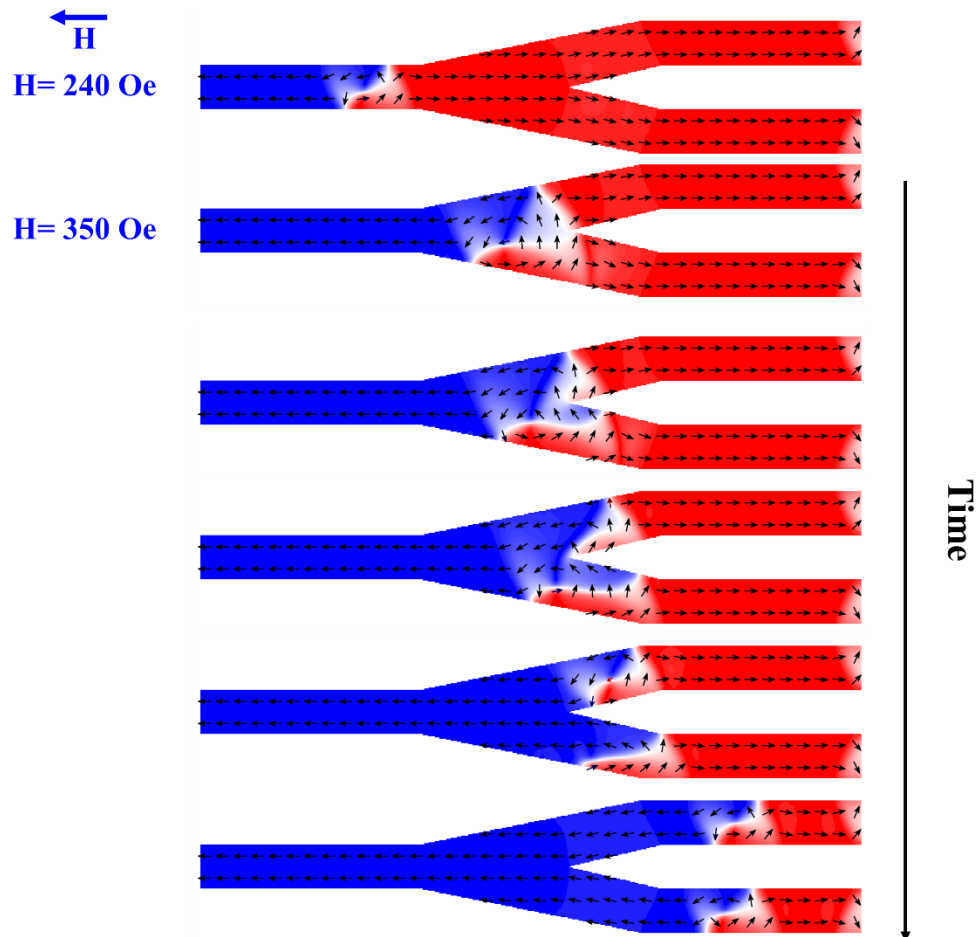
Figure a3.2: Micromagnetic simulation snapshots of modified FAN-OUT design functioning at an incrementing field from 0 to 350 Oe at a rate of 100 MHz.

References

[1]   N. A. Spaldin, *Magnetic materials: fundamentals and applications*: Cambridge University Press, 2010.

[2]   A. Hirohata and K. Takanashi, "Future perspectives for spintronic devices," *Journal of Physics D: Applied Physics,* vol. 47, p. 193001, 2014.

[3]   J. Slaughter, "Materials for magnetoresistive random access memory," *Annual Review of Materials Research,* vol. 39, pp. 277-296, 2009.

[4]   T. Shinjo, *Nanomagnetism and spintronics*: Elsevier, 2009.

[5]   Y. Lee, J. Hayakawa, S. Ikeda, F. Matsukura, and H. Ohno, "Effect of electrode composition on the tunnel magnetoresistance of pseudo-spin-valve magnetic tunnel junction with a MgO tunnel barrier," *Applied physics letters,* vol. 90, p. 2507, 2007.